Colloidal Cu_3N and Zn_3N_2 Nanoparticles: from the Single-Source Precursor Approach to Photocatalysis

by

Rudo Kadzutu-Sithole

Thesis submitted in partial fulfilment of the requirements for the degree of

Doctor of Philosophy in the Faculty of Science

Department of Chemistry

University of the Witwatersrand

Principal advisor: Prof Nosipho Moloto

Co-advisor: Dr. Juanita van Wyk

Declaration

I declare that the work furnished in this thesis is my independent work submitted for the degree of Doctor of Philosophy at the School of Chemistry, University of the Witwatersrand, Johannesburg. The contents herein have not been submitted for examination at any other institution.

Name: Rudo Kadzutu-Sithole Student no.: 445169

Signature:  Date: December 2019

Principal advisor: Professor Nosipho Moloto

Signature:  Date: December 2019

Abstract

Colloidal Cu_3N and Zn_3N_2 are one of the least studied nanocrystals in nanoscience. In general, much controversy exists on the optical properties of Cu_3N nanoparticles as evidenced by the great differences in the reported band gaps of Cu_3N that range from ~0.13 to ~2.06 eV and in the case of Zn_3N_2, band gaps range from 0.9 to 3.36 eV. Additionally, electrical properties vary due to great differences in percentage composition of Cu in different samples hence Cu_3N has been reported to be a metallic, semiconducting and insulating material. Furthermore, studies on the thermal stability have described the nitride nanoparticles as stable, metastable and unstable. Aspects such as reaction kinetics, magnetic properties, controlled size and dimensionality of colloidal Cu_3N and Zn_3N_2 nanoparticles are not yet well understood. Therefore, to better understand the chemistry of colloidal Cu_3N and Zn_3N_2 nanomaterials more studies must be performed on the synthesis, characterization and measurement of properties of the colloidal metal nitride nanoparticles.

Initially, 2-pyrrolecarbaldpropylimine ligand was prepared from a condensation reaction between 2-pyrrolecarboxaldehyde and propylamine. After characterization, the ligand was deprotonated and subjected to complexation by separately introducing copper and zinc salts. Complexation of mono-functional N, N pyrrolylaldimine Schiff-base ligand led to the formation of mononuclear Cu and Zn complexes, bis(2-pyrrolecarbaldpropyliminato) copper/zinc (II) complex. Three different methods were employed in the thermolysis of the Cu complex (PCC) and the Zn complex (PPZ) namely; the conventional colloidal method, microwave-assisted method and chemical vapor deposition (CVD). Zinc has a very high affinity for oxygen hence, despite the different synthetic methods that were employed to thermolyze the zinc complex, ZnO was always the resultant product. Changing the single-source precursor did not solve the problem until zinc powder was

ammonolyzed using chemical vapor deposition. Herein, we showed for the first time that as-synthesized single-source precursor (PPC) can be thermolyzed in organic solvents to give colloidal Cu_3N NPs. Of great importance was the introduction of the microwave-assisted method in the synthesis of Cu_3N nanocrystals. A comparative study was then carried out on the colloidal synthesis of Cu_3N nanoparticles using the as-synthesized Schiff-base complex and copper (II) nitrate trihydrate. In agreement with previous reports, thermolysis of $Cu(NO_3)_2$ resulted in the formation of Cu_3N nanocubes but the Cu complex produced spherical nanoparticles with a more blue shifted band gap than the nitrate compared to the bulk material.

The study then proceeded to investigate the morphological and crystal phase transformations that occur during the colloidal synthesis of Cu_3N at 260 °C using $Cu(NO_3)_2$ as the single-source precursor in octadecylamine and hexadecylamine coordinating ligands. A mixture of densely populated 'nuclei' and developing cubes was observed in the transmission electron microscopic images of the samples that were obtained after 5 min reaction time. Nanocubes and less of the nuclei were present after 10 min but only the cubes were detected at 15 min. Near-perfectly shaped nanocubes self-assembled into a brick-like wall pattern in both the octadecylamine and hexadecylamine capped nanoparticles. The cubes started to disintegrate at 20 and 30 min in octadecylamine and hexadecylamine respectively to eventually yield Cu nanoparticles after 60 min. We were intrigued by the changes that were detected in the organic ligands. Fourier-transform infrared and nuclear magnetic resonance spectroscopies indicated the presence of a nitrile group in the Cu_3N nanoparticles suggesting that the amine ligands had been deprotonated resulting in the formation of nitriles.

A one-pot colloidal synthesis of optically active Cu_3N, Cu_2S and Cu_9S_5 nanoparticles was then demonstrated by sulfidation of the nitride nanoparticles using a small amount of dodecanethiol. Previous studies have shown that the thiol ligand can act as a spectator solvent, capping and reducing agent but in this study, its introduction into a hexadecylamine-Cu_3N mixture led to the substitution of N atoms in the crystal structure of Cu_3N by S atoms leading to the formation of Cu_2S nanoparticles after 5 min of addition. With time, more S-rich nanoparticles were obtained as evidenced by the obtained powder X-ray diffractograms that matched with reported Cu_9S_5 patterns. X-ray photoelectron spectroscopy confirmed the substitution of N in Cu_3N that led to the detection of Cu^+ and S^{2-} ions in Cu_2S and ultimately Cu^{2+} and $(S_2)^{2-}$ species in Cu_9S_5 nanoparticles after 10 min of adding the thiol. Increasing reaction time did not lead to further sulfidation of the Cu_9S_5 nanoparticles.

The thesis culminates by testing the photocatalytic activities of the as-synthesized Cu_3N nanocubes, Cu_2S hexagons and Cu_9S_5 spherical to elongated nanoparticles with direct band gaps of 2.41, 2.75 and 2.36 eV respectively. Cu_3N proved to be the best (89%) photocatalyst in degrading methyl orange whilst Cu_9S_5 nanoparticles were the best (79%) in degrading methylene blue within a period of 3 hrs. Considering the best catalyst in each azo-dye, kinetic studies using the Langmuir–Hinshelwood model suggested that the photocatalytic reaction followed 1^{st} order and 2^{nd} order reaction pathways in methyl orange and methylene blue for Cu_3N and Cu_9S_5 nanoparticles respectively. Finally, high-performance liquid chromatography was employed in order to detect the reaction products of degrading each dye.

Dedications

Special dedication for your unwavering support:

Constance Kadzutu (Mother)

Osli Kadzutu (Daughter)

Gladys (Kadzutu) Maseko (Sister)

All my Siblings, Nieces and Nephews

Acknowledgements

‘… with men, this is impossible; but with God all things are possible.’

- All my gratitude goes to our Lord Jesus Christ for **everything**; for opening up this avenue and for taking care of me and renewing my strength every day.

- This project would not have been possible without the professional guidance of my supervisor, Prof. Nosipho Moloto and I cannot find the correct words to express my gratitude. Prof, you trusted me with this project and allowed me to venture into studying towards a PhD in Chemistry from an Education background. Thank you for supporting me academically and even financially till the completion of this project. I traversed through a lot of hiccups that made me want to give up but your patience and encouragement pushed me on till this day. Through the years, you have indirectly taught me that even if people have different personalities, there is always a way of bringing the best out of each and every one. To my co-supervisor, Dr Juanita van Wyk, a special thank you for your guidance in the lab especially in my first year of doing research.

- To the original Quantum Dots Group, Ms Lerato Machogo, Dr Mildred Airo, Dr Siziwe Gqoba, Dr Stefan Govindraju and Dr Pierre Kalenga, you guys made research to be so much fun. In times when undesirable nanoparticles were synthesized we always found ways of laughing about it and get ready to start the next reaction. The group discussions were very enlightening and I cherish the times when we would get so engrossed in critiquing each other’s presentations to the extent of forgetting that we were hungry. Much

appreciation is also given to other members who joined the group over the years to eventually form the now present Lab 330B Quantum Dots group.

- I would also like to thank Prof. Neil Coville and Dr Izaak Kotze and their CATMAT and Inorganic Groups respectively, for the immense contribution that they made during my presentations. Your inputs were greatly valued.

- Much appreciation goes to Prof. Alexandra Zieglar and his magnificent team at the microscopy unit at Wits University for assistance and training on the TEM, SEM, PMA and AFM microscopes. And to Dr Rudolph Erasmus, many thanks for patiently assisting with the acquisition of the Raman spectra. From the single crystal XRD unit, special thanks go to Prof Manuel Fernandes and Prof Andreas Lemmerer for assisting with solving crystal structures. Mr Eric Morifi and Mr Thapelo Mbhele, thank you for setting the right experiments to run the HPLC. I would also like to thank other researchers from other departments and institutions, namely Dr Francis Otieno, Dr Poslet Shumbula and Dr D. Oluwole Oluyinka for their advice, encouragement and contributions in my research.

- I would like to thank the National Research Fund for the immense funding during the course of my Masters through to PhD studies. I would like to express my gratitude to the University of the Witwatersrand for affording me an opportunity to advance my education and for taking care of my financial needs during the course of my Honors to PhD studies.

- And most importantly to my family, I would like to acknowledge the great contribution that my late father, Mr Daniel Kadzutu made in my life; for going against traditional beliefs that the girl-child should not be educated but be groomed for marriage. Instead, he worked tirelessly to educate all his six daughters without any limitations. Mom, you have been the greatest support in my life and thank you for always being there for me. Those days of forcing me to do my homework under the big table whilst you were sewing have finally paid off. Gladys, I cannot thank you enough for standing with me always from our infancy. Many thanks for taking care of my daughter whilst I was chasing research. A big thanks goes to all my siblings; Rebecca, Memory, Charity, Abigail, Dunmore & Douglas Kadzutu and also my friends Norah & Shepard Machekano, Samson & Siphilile Moyo and Nomsa Dube Dumane who were with me in my happy and painful moments. Lastly, to my daughter Osli, for the greater part of your life, you have known your mom as a student. Thank you for your patience and understanding.

Publications

1. S. Gqoba, M. Airo, N. Ntholeng, L. Machogo, R. Sithole, M.J. Moloto, J. van Wyk, N. Moloto. *Evolution of In_2S_3 Nanoplates with Time,* Materials Today: Proceedings, 7 (2015) 3901-3908.
   - I contributed in collecting the TEM data and in discussing some results as well as contributed in correcting the manuscript.

2. R.K. Sithole, L.F. Machogo, M.A. Airo, S.S. Gqoba, M.J. Moloto, P. Shumbula, J. Van Wyk, N. Moloto, *Synthesis and characterization of Cu_3N nanoparticles using pyrrole-2-carbaldpropyliminato Cu (ii) complex and Cu $(NO_3)_2$ as single-source precursors: the search for an ideal precursor*, New Journal of Chemistry, 42 (2018) 3042-3049.
   - The advisors conceptualized the project and I did; all the experimental work, manuscript writing and most characterization. Others contributed in discussing some results.

3. L.F. Machogo, P. Tetyana, R. Sithole, S.S. Gqoba, N. Phao, M. Airo, P.M. Shumbula, M.J. Moloto, N. Moloto, *Unravelling the structural properties of mixed-valence α-and β-AuSe nanostructures using XRD, TEM and XPS,* Journal of Applied Surface Science, (2018), 456, 973-979.
   - I contributed in discussing XRD results.

4. L.F. Machogo, M. Mthimunye, R. K. Sithole, P. Tetyana, N. Phao, G. N. Ngubeni, M. Mlambo, P. S. Mdluli, P.M. Shumbula, N. Moloto, *Elucidating the structural properties of gold selenide nanostructures*, New Journal of Chemistry, (2019), 43, 5773-5782.
   - I contributed in the collection and discussion of the TEM results.

5. R.K. Sithole, L.F. Machogo, P. M. Kalenga, M.J. Moloto, P. Shumbula, J. Van Wyk, N. Moloto. *Elucidating the effect of time on the structural and optical properties of copper (I) nitride nanocubes.* Submitted to Journal of Royal Society of Chemistry (2019). Under review (RA-ART-11-2019-009546).
   - I did; all the experimental work, manuscript writing and most characterization. Others contributed in discussing some results and the supervisors conceptualized the project.

6. R.K. Sithole, L.F. Machogo, Tswharela Kolokoto, Grace N Ngubeni, M.J. Moloto, J. Van Wyk, N. Moloto, *Substitution of hard nitrogen ions of Cu3N nanocrystals with soft sulfur ions of DDT via the HSAB theory to form chalcocite and digenite nanocrystals*. Journal: Materials Chemistry and Physics (2020). Just accepted.
   - The supervisors conceptualized the project and I did; all the experimental work, manuscript writing and most characterization. Others contributed in discussing some results.

7. Lerato F Machogo; Rudo K Sithole; Neo Phao; Tswharela Kolokoto; Siziwe S Gqoba; Mbuso Mlambo; Phumlane S Mdluli; Makwena J Moloto; Poslet Shumbula, *Probing the*

structure and functionalized surface of colloidal AuSe. Journal of Materials Science, (2019). Under review (JMSC-D-19-05229)

- I contributed in the collection and discussion of the data.

8. Lerato F.E. Machogo, Rudo K. Sithole, Neo Phao, Zakhele B. Ndala, Kalenga P Mubiayi, Poslet M. Shumbula and Nosipho Moloto, *Electrocatalytic activity of novel AuSe for potential use as a counter electrode in dye-sensitized solar cells*, Journal of RSC Advances, (2019). Under review (NA-COM-07-2019-000465)
   - I contributed in the collection and discussion of the TEM results.

9. Rudo Sithole, Lerato F.E. Machogo, Makwena J. Moloto, Siziwe S. Gqoba, Kalenga P. Mubiayi, Juanita Van Wyk and Nosipho Moloto. *One-step synthesis of Cu_3N, Cu_2S and Cu_9S_5 and their photocatalytic degradation of methyl orange and methylene blue*, Journal of Photochemistry and Photobiology A: Chemistry (2020). Just accepted.

Orcid Number: 0000-0003-0490-6283

Presentations

1. International Conference on Surfaces, Coatings and Nanostructured Materials (NANOSMAT-Africa): Held on the 19th to 23rd of November 2018, The Lord Charles Hotel, Cape Town, South Africa; *Colloidal Sulfidation of Copper Nitride to Copper Sulfides Nanoparticles using Dodecanethiol Ligand* – Oral presentation

2. The 16th Frontiers of Electron Microscopy in Materials Science International Conference (FEMMS): Held on 10th to 15 September 2017, Indaba Hotel and Conference Centre Fourways, Johannesburg; *Transitioning of Cu_3N to Cu_2S nanoparticles through the addition of small amounts of dodecanethiol* – Poster Presentation

3. Asia-Pacific Solar Research Conference (APSRC): Held on 29 Nov to 01 Dec 2016, 3rd Annual Asia-Pacific Solar Pacific Solar Research Conference: Australia National University, Canberra; *Effects of time on the growth of copper nitride nanocubes using copper nitrate as a single-source precursor for use in optoelectronics* – Poster presentation

4. International School of Solid State Physics, 69th Course, Materials for Energy and Sustainability-V;3rd EPS-SIF International School on Energy: Held on July 13th – 19th 2016, Ettore Majorana Foundation and Centre for Scientific Culture, Erice, Italy; *Colloidal Copper Nitride Nanoparticles: Application in Optoelectronics* – Poster presentation

5. 6th International Conference on Nanoscience & Nanotechnology in Africa (NanoAfrica): Held on 03-06 April 2016, University of South Africa (UNISA), Johannesburg;

Semiconducting copper nitride nanoparticles for use in optoelectronic devices –Oral presentation

6. International Conference on Nanoscience and Nanotechnology (ICONN): Held on 07-11 February 2016, National Convention Centre, Canberra, Australia: Australian National Fabrication Facility (ANFF) Short Course; *Introduction to Nanofabrication Technologies* – Attended

7. Asia-Pacific Solar Research Conference (APSRC): Held on 08-10 December 2015, Brisbane Convention and Exhibition Centre, Brisbane, Australia; *Semiconducting copper nitride nanoparticles for use in optoelectronic devices* – Poster presentation

8. The 17th South African Chemical Institute *Inorganic* Chemistry *Conference* (SACI *Inorg2015*): Held on 28 June to 2 July 2015: Rhodes University, Grahamstown; *Synthesis of copper (I) nitride nanoparticles using complexes as single-source precursors* – Flash talk & Poster presentation

9. International Symposium on macro-and supramolecular architecture and materials (MAM-14): Held on 23rd to 27th November 2014, Emperors Palace, Johannesburg; *Synthesis of copper nitride nanoparticles using single-source precursors* – Poster presentation

10. 6th Cross-Faculty Graduate Symposium: Held on 27-28 October 2014: University of the Witwatersrand, Johannesburg, South Africa, Effects of temperature on the synthesis of

copper nitride nanoparticles using a Schiff base complex as a single-source precursor – Poster presentation

11. Southern Africa Research in Science, Mathematics and Technology Education (SAARMSTE) 22nd Annual Conference: Held on 13th to 16th January 2014, Nelson Mandela Metropolitan University, Port Elizabeth; *Determination of quality of Topic Specific Pedagogical Content Knowledge in relation to Content Knowledge of experienced Physical Science teachers in ex-model C schools* – Oral presentation

Table of Contents

List of Figures

Chapter 1

Chapter 2

Chapter 3

Chapter 5

Chapter 6

Chapter 7

List of Tables

List of Schemes

Chapter 2

Chapter 3

Chapter 4

Chapter 7

Lists of Symbols and Abbreviations

^{1}H NMR	=	Proton Nuclear Magnetic Resonance
^{13}C NMR	=	Carbon-13 nuclear magnetic resonance
a.u	=	Arbitrary Unit
Bg	=	Band Gap
$CDCl_3$	=	Deuterated Chloroform
$CHCl_3$	=	Chloroform
C_2H_5OH	=	Ethanol
Cu_3N	=	Copper (I) Nitride
Cu_2O	=	Copper (I) Oxide
CuO	=	Copper (II) Oxide
Cu_2S	=	Copper (I) Sulfide/Chalcocite
Cu_9S_5	=	Digenite
DDT	=	Dodecanethiol
CVD	=	Chemical Vapour Deposition
DCM	=	Dichloromethane
DMF	=	Dimethylformamide
DMSO	=	Dimethyl Sulfoxide
DMSO-d_6	=	Deuterated Dimethylsulfoxide
EtOH	=	Ethanol
FTIR	=	Fourier Transform Infrared
FWHM	=	Full Width at Half–Maximum
HDA	=	Hexadecylamine

HOMO	=	Highest Occupied Molecular Orbital
HRTEM	=	High Resolution Transmission Electron Microscopy
LUMO	=	Lowest Unoccupied Molecular Orbital
MS	=	Mass Spectrometer
NCs	=	Nanocrystals
NPs	=	Nanoparticles
ODA	=	Octadecylamine
OD	=	1–Octadecene
OLA	=	Oleylamine
PL	=	Photoluminescence
PP	=	2-pyrrolecarbaldpropylimine
PPC	=	Bis(pyrrole-2-carbaldpropyliminato) Copper(II)
PPZ	=	Bis(pyrrole-2-carbaldpropyliminato) Zinc(II)
PXRD	=	Powder X-ray Diffractometer
QDs	=	Quantum Dots
SCXRD	=	Single Crystal X-ray Diffractometer
THF	=	Tetrahydrofuran
TEM	=	Transmission Electron Microscope
TiO_2	=	Titanium Dioxide
TOPO	=	Trioctylphosphine Oxide
UV–Vis	=	Ultraviolet–Visible Spectroscopy
XPS	=	X–ray Photoelectron Spectroscopy
XRD	=	X–ray Diffractometer

Zn_3N_2	=	Zinc Nitride
ZnO	=	Zinc Oxide

Thesis Synopsis

Colloidal copper and zinc nitride nanoparticles are some of the least studied materials therefore their synthetic procedures and properties are not well understood. Further probing into their synthesis, characterization and properties will better inform scientists on a whole range of possible applications in growing fields such as energy generation, gas sensing, photocatalysis, photothermal and photodynamic therapies. In this thesis, we aimed to synthesize colloidal Cu_3N and Zn_3N_2 nanoparticles using single-source precursor molecules. The photocatalytic activities of these chalcogenides were then to be tested in the photodegradation of azo dyes. The thesis consists of eight chapters and herein each chapter will be briefly outlined. All the results chapters have been sent for publication and as such have been written have been written in a publication format.

Chapter 1 provides a brief background to the study particularly the need to find new solutions for water purification and how nanotechnology can be a possible solution. The problem statement is given and the chapter concludes by detailing the aims and objectives of the study.

Chapter 2 gives a detailed account on the preparation of nanocrystals with emphasis on colloidal synthesis. A brief account is given on the factors that affect the synthesis and properties of colloidal nanoparticles (NPs). Different synthetic techniques are discussed prioritizing the single-source precursor method in the synthesis of colloidal NPs. Included is a background on the application of NPs in photocatalysis. Special attention is drawn to the use of copper-based chalcogenides in water treatment.

Chapter 3, embarks on the preparation and characterization of Schiff-base complexes, bis(pyrrole-2-carbaldpropyliminato) copper(II) (PPC) and bis(pyrrole-2-carbaldpropyliminato) zinc(II) (PPZ) as single-source precursors in the synthesis of copper (I) nitride and zinc nitride NPs respectively. In the synthesis of the Schiff-base complex, one synthetic procedure was investigated which involved the formation of a ligand first before metallization to form the complexes. Finally, the chapter informs on the use of the as-synthesized Schiff-base complexes in the synthesis of copper and zinc nitride NPs using different synthetic methods.

A comparative study of the synthesis of Cu_3N NPs using PPC and copper (II) nitrate as single-source precursors is reported in Chapter 4. Herein, a direct method of obtaining PPC from the starting materials was employed. Both the precursors were thermolyzed in hexadecylamine (HDA) in an inert atmosphere and resulted in crystalline Cu_3N NPs with anti-ReO_3 cubic structure. Although both precursors gave rise to Cu_3N NPs, Chapter 4 significantly demonstrates the impact that a change in the precursor has on the morphology and optical properties of the NPs obtained. This work has already been published by New Journal of Chemistry (2018). A detailed account on the effect of time on the synthesis of copper (I) nitride NPs is reported in Chapter 5. The reported work in this chapter graphically shows the progression in the formation of the nitride NPs and how the NPs eventually decompose resulting in Cu NPs. Ultimately, the chapter goes on to illustrate how HNMR can be employed in order to establish the role that the amine ligands plays in the formation of Cu_3N nanocrystals. A compilation of the findings from this investigation has already been submitted to the Journal of Royal Society of Chemistry and is under review.

Chapter 6 probes the conversion of Cu_3N NPs to other copper chalcogenides by the addition of a relatively small quantity of dodecanethiol. This chapter on the colloidal sulfidation of Cu_3N NPs to sulfides has been submitted to the Journal of Materials Chemistry and Physics and is under review. The application of the nitride and sulfide NPs in photocatalysis is explored in Chapter 7. The NPs are used as photocatalysts to degrade methyl orange and methylene blue dyes and the work is under review with the Journal of Photochemistry and Photobiology A. Finally, Chapter 8 entails a general overview of the work that was covered in this project. Together with the conclusions, achievements obtained in this work are pointed out and recommendations for further investigations are given.

Chapter 1

Introduction

1. General Background

The earth is facing quite a number of global problems that require the participation of every stackholder in order to obtain lasting solutions. These problems revolve around energy, pollution, climate changes, poverty and diseases, with Africa being the most affected. Water pollution is of great concern as water is of paramount importance to sustain life. 71% of earth is covered by water[1] and it supports both aquatic and terrestrial life. The human body is made up of 65% to 75% water [2] and that is the reason why adults are recommended to take in at least 1.8 litres of water per day [1]. According to the current data released by the United Nations [3], the world population is about 7.7 billion. Hence, according to the recommended daily intake of water, 13.86 billion litres of water is required daily, only for drinking purposes. Other human activities like cooking, bathing, laundry, and sewage disposal demand more water usage. Therefore, clean water must be available to sustain human life and any activities that pollute water sources cannot be condoned. Fig. 1(a) shows polluted water being disposed into a main stream. Such irresponsible actions have dire consequences as can be seen in Fig. 1(b) that shows hundreds of dead fish caused by pollution.

Fig. 1: Polluted water (a) flowing into a river and causing (b) dead fish.

There are many reports showing that textile industries are major contributors to water pollution (20%) [4-6]. Textile dye pollutes [7, 8] many water sources that are directly or indirectly linked to daily human activities. Some azo dyes or their derivatives have been reported to be carcinogenic and cause dermatological and mutagenic problems [9-11]. Considering the gravity of the adverse effects of textile dyes, polluted water must be treated before it is disposed of from the industries.

Solar radiation plays a role in photodegradation of some pollutants in water sources that are exposed to sunlight but this natural process is extremely slow [12]. Technology has played a crucial role in identifying photocatalysts that significantly speed up the rate of degradation of pollutants. Solar energy is highly abundant in most regions of Africa, hence regulations should be enforced to ensure that polluted water is not released from companies before it is adequately treated. Nanotechnology has designed and continues to design photosensitized nanomaterials that catalyze the degradation of pollutants. Titanium dioxide [12-15] is amongst the most efficient photocatalysts and a lot of work has been put in optimizing its efficiency. These phenomenal efforts, led to the now commercially available photocatalyst, HombiKat U 100 which is primarily

made up of 5 nm Ti_2O anatase nanoparticle [16]. Many specialists have highlighted the important role of semiconductor nanocrystals in photocatalysis hence, the need for further research.

2. Problem Statement

Pollutants from industries continue to contaminate water especially streams, ponds, rivers and lakes that are within or close to residential areas. Current treatment methods such as air stripping and adsorption by activated carbon do not result in the destruction of pollutant molecules but merely transfer the pollutants from water to another region. Investigations set to develop efficient photocatalysts have demonstrated that TiO_2 nanoparticles have good photocatalytic properties. However, the greatest setback for titanium dioxide is its wide band gap that lies around 3.2 eV [17]. Such a wide band gap does not allow pure phases [18] of TiO_2 to work efficiently under sunlight unless doping or other modifications are done. The fast recombination of charge carriers, poor absorption of organic molecules in water and agglomeration impact negatively on titanium dioxide's efficiency. As such, there is need for further research to discover semiconducting nanomaterials that can absorb within the visible range without requiring further treatment, hence making water treatment cheap, efficient and less cumbersome.

3. Rationale

Copper-based nanoparticles are semiconductors that can be used as photo sensitizers in photocatalysis. The band gaps of the nanoparticles can be engineered such that their optical properties are adjusted in order to give the desired photocatalytic activity. Colloidal synthesis offers a platform for surface modifications that enables solubility of the nanoparticles in medium where their bulk counterparts do not dissolve. Due to quantum confinement, nanoparticles have a

high surface area to volume ratio compared to their bulk counterparts and this facilitates the oxidation and reduction processes that take place on the surface of the semiconductor during photocatalysis. Recent technology has shown that the synthesis of nanoparticles can be facilitated by employing single-source precursors. This method is quite desirable because, the single-source precursor, usually an organometallic molecule, contains all elements that are required in the nanosynthesis. This method has been used quite successfully mostly in the synthesis of oxide and sulfide nanoparticles. Unlike the sulfides and the oxides, colloidal copper (I) nitride nanoparticles have not been explored much and their photocatalytic activity still remains unknown and that needs to be investigated. Cu and N are highly abundant on earth and their use in colloidal synthesis of copper nitride is cheap, non-toxic and can be achieved at relatively low temperatures.

4. Aim

The main aim of this research project was to use single-source precursors to synthesize and characterize colloidal copper nitride and zinc nitride nanoparticles for application in photocatalysis using efficient and environmentally friendly methods of synthesis.

5. Objectives

In order to achieve the above aim, the following objectives were set in place;

i. Prepare and characterize a Schiff base ligand from a carboxaldehyde and an amine.

ii. Complexation of prepared ligand to form copper and zinc Schiff-base complexes.

iii. Synthesize and characterize copper nitride and zinc nitride nanoparticles using the prepared complexes as single-source precursors.

iv. Comparative study of the effect of varying the single-source precursor in the synthesis of Cu_3N nanocrystals.

v. Study the effect of time on the colloidal synthesis of Cu_3N nanoparticles.

vi. Investigate the effect of adding dodecanethiol ligand on the colloidal synthesis of Cu_3N nanocrystals.

vii. Test the photocatalytic activity of Cu_3N against the products of sulfidation.

References

[1] H. Genda, *Geochemical Journal*, 50 (2016) 27-42.

[2] S. Nicolaidis, Hydration throughout Life, (1998).

[3] U. Nations, World Population Prospects 2019. Data Booklet, (2019).

[4] T.O. Durotoye, A.A. Adeyemi, D.O. Omole, O. Onakunle, *Cogent Engineering*, 5 (2018) 1531687.

[5] D. Paraschiv, C. Tudor, R. Petrariu, *Sustainability*, 7 (2015) 1280-1291.

[6] M. Sakamoto, T. Ahmed, S. Begum, H. Huq, *Sustainability*, 11 (2019) 1951.

[7] A. Altaf, S. Noor, Q.M. Sharif, M. Najeebullah, *Journal of the Chemical Society of Pakistan*, 32 (2010) 115-116.

[8] D. Yaseen, M. Scholz, *International Journal of Environmental Science and Technology*, 16 (2019) 1193-1226.

[9] B. Padhi, *International Journal of Environmental Sciences*, 3 (2012) 940.

[10] Z.W. Myslak, H.M. Bolt, W. Brockmann, *American Journal of Industrial Medicine*, 19 (1991) 705-713.

[11] J. Esancy, H. Freeman, L. Claxton, *Mutation Research/Reviews in Genetic Toxicology*, 238 (1990) 1-22.

[12] D. Ljubas, *Energy*, 30 (2005) 1699-1710.

[13] Y. Li, X. Li, J. Li, J. Yin, *Water research*, 40 (2006) 1119-1126.

[14] D. Yang, H. Liu, Z. Zheng, Y. Yuan, J.-C. Zhao, E.R. Waclawik, X. Ke, H. Zhu, *Journal of the American Chemical Society*, 131 (2009) 17885-17893.

[15] G. Colon, M. Maicu, M.s. Hidalgo, J. Navio, *Applied Catalysis B: Environmental*, 67 (2006) 41-51.

[16] M. Lindner, D.W. Bahnemann, B. Hirthe, W.-D. Griebler, *Journal of Solar Energy Engineering*, 119 (1997) 120-125.

[17] Z. Wang, U. Helmersson, P.-O. Käll, *Thin Solid Films*, 405 (2002) 50-54.

[18] L. Jing, S. Li, S. Song, L. Xue, H. Fu, *Solar Energy Materials and Solar Cells*, 92 (2008) 1030-1036.

Chapter 2

Literature Review

1. Introduction

The discovery of the semiconductor effect in 1833 by Michael Faraday and the invention of a rectifier in 1874 by Karl Fernand Braun, gave rise to progressive technological advancement in almost all spheres ranging from energy, photocatalysis, communication, vacuum tube, transistor, integrated circuit, computer, microprocessor to electronic circuit and control technologies amongst others [1, 2]. Nanotechnology has demonstrated that miniaturization has a strong positive correlation to efficiency. One notable example is the size and speed of the computer. The first built computer, ENIAC, at the University of Pennsylvania, weighed 30 000 Kg [3] and had a speed of about 100 cycles per millisecond. A home computer today weighs less than 5 Kg with speed exceeding 1 000 000 cycles per millisecond. Sizes of materials have been reduced to almost infinitesimal hence cannot be visualized with the naked eye. Dimensions of nanoparticles (NPs) range from 1 to 100 nanometers (nm) [1] and their properties tend to differ from bulk. Whilst properties of bulk material remain constant irrespective of size, physical and chemical properties [2] of NPs vary due to quantum confinement. As a result of quantization, nanosized particles have presented fascinating features hence their application in fields such as chemical sensing [3], drug delivery [4], optoelectronics [5], nonlinear optics [6], photocatalysis [7], bio-imaging [8], photothermic and photodynamic therapy [9].

1.1 Semiconductors

Semiconductors are materials whose conductivity increase with temperature [10]. Their structure is a result of overlapping of atomic orbitals (AO) to form bonding and antibonding molecular orbitals. The bonding molecular orbitals (BMO) make the valence band whilst the anti-bonding molecular orbitals (ABMO) constitute the conduction band. The valence and conduction bands are separated by an energy gap, referred to as the band gap (Bg) [10] as shown in Fig. 1. Semiconductors generally have band gaps that range between 0.3 and 3.8 eV [5]. This Bg is characteristic of each semiconductor and it has been shown that even for the same material, for example pure silicon, the Bg for the bulk material is different from that of its nanoparticles. Pure semiconductors like Si are referred to as intrinsic semiconductors. The introduction of impurities (dopants) in the matrix of a pure semiconductor gives rise to extrinsic semiconductors. The effect of adding a dopant like As atom, [Ar] $4s^2 4p^3$ into the matrix of pure Si, [Ne] $3s^2 p^2$ introduces an extra electron which can migrate through the conduction band. Since the charge carriers (electrons) are negatively charged, the semiconductor experiences an n-type conductivity [11]. A dopant with fewer electrons like Ga, [Ar]$4s^2 4p^1$ increases the overall number of holes in the semiconductor hence giving rise to p-type conductivity [12]. The presence of dopants in a semiconductor leads to an alteration of the band gap of the material.

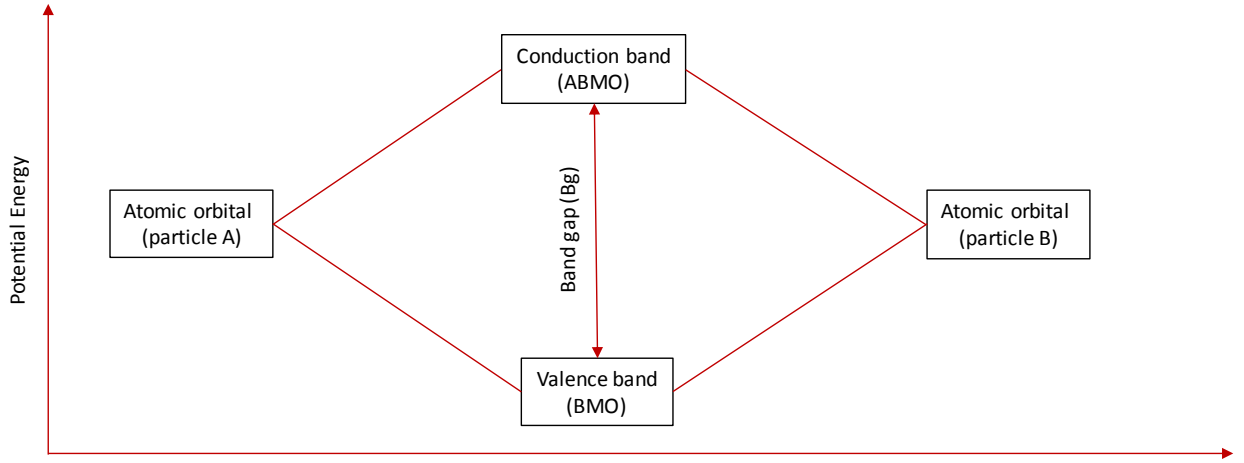

Fig. 1: Valence band from bonding molecular orbitals and conduction band from antibonding molecular orbitals. The band gap is indicated as the potential difference between the two bands.

The transition of electrons between the valence and conduction bands can either be direct or indirect. Semiconductors that permit electrons to use the direct path with the least energy difference between the valence and conductions bands without changing momentum are said to have direct band gaps. Indirect band gaps are obtained when electrons are forbidden to follow the route of least energy difference between the two bands without a change in momentum. Fig. 2 shows that momentum is conserved in direct transitions that occurred in gallium nitride but in silicon carbide, there was a change in the momentum hence indicating indirect transition of electrons between the valence and conduction bands [16].

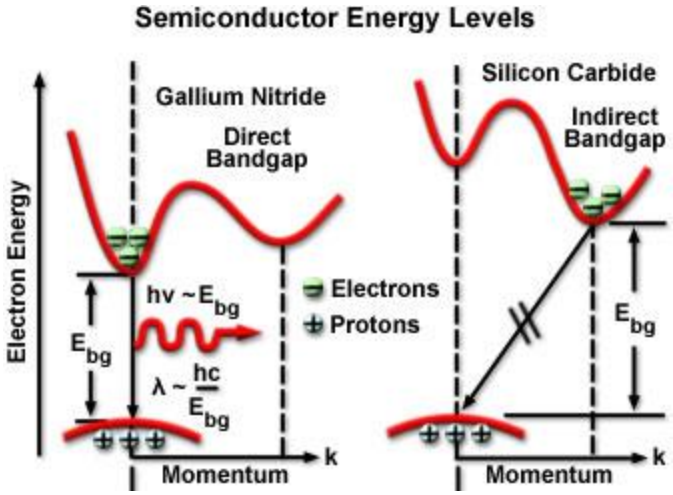

Fig. 2: Shows direct band gap in gallium nitride NPs and indirect band gap in silicon carbide NPs [13].

At low temperatures, the majority of the electrons in a semiconductor occupy the valence band and very few or none are found in the conduction band. In bulk materials, light absorption excites valence electrons to high density states in the conduction band [14] and this only happens if incident photons transfer enough energy for electrons to overcome the energy barrier (Bg). The excited electrons exit the highest occupied molecular orbital (HOMO) in the valence band, overcome the Bg and occupy the lowest unoccupied molecular orbital (LUMO) in the conduction band. The migration of electrons to the conduction band, leave holes in the valence band. When the size of a semiconductor is greatly reduced to the extent of quantization, charge carriers are limited within a potential well, which can be viewed as a 'particle in a box' [15-17] resulting in quantum effects. This means that, bands split into quantized levels [18-20] as can be seen in the quantum dot in Fig. 3, which depicts size quantization in a semiconductor and shows that confinement occurs when the size diameter of a semiconductor is reduced below a critical size.

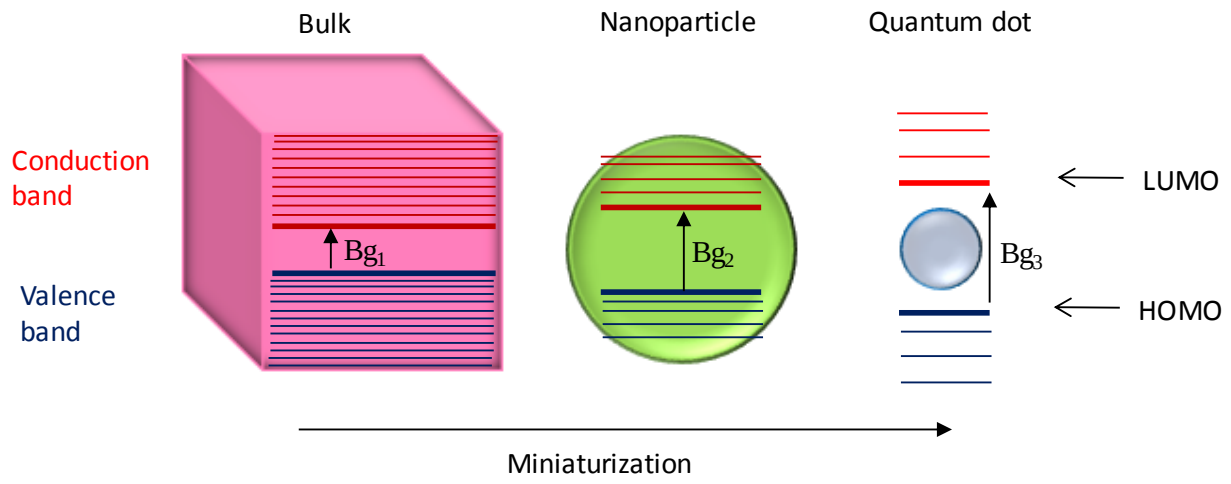

Fig. 3: Size quantization from bulk to quantum dot in a semiconductor. (Bg represent 'band gap').

The size of the quantum dot (QD) has become so small to the extent that it is smaller than the first excited state hence, the electron-hole pair (exciton) generated by incident photon cannot fit within the particle unless higher kinetic energy is assumed [18] . Size confinement in a semiconductor leads to band gap widening hence, $Bg_1 < Bg_2 < Bg_3$. The diameter of the QD is now smaller than the Bohr radius and it is this quantization effect that is responsible for the size-dependent optical and electronic properties of QDs. This has been demonstrated in PbS quantum dots [21] where size quantization resulted in the tuning of the band gap from infrared (0.41 eV in bulk) up to near ultraviolet region (5.2 eV in QDs) [22].

QDs are semiconducting nanoparticles with size diameter that are less than 10 nm [23] and confinement is dimensionless hence they are zero dimensional (0D). However, in semiconducting NPs, free motion of charge carries can be limited to one (quantum wires), two (quantum wells) or three (bulk) dimensions [24, 25] as illustrated in Fig. 4.

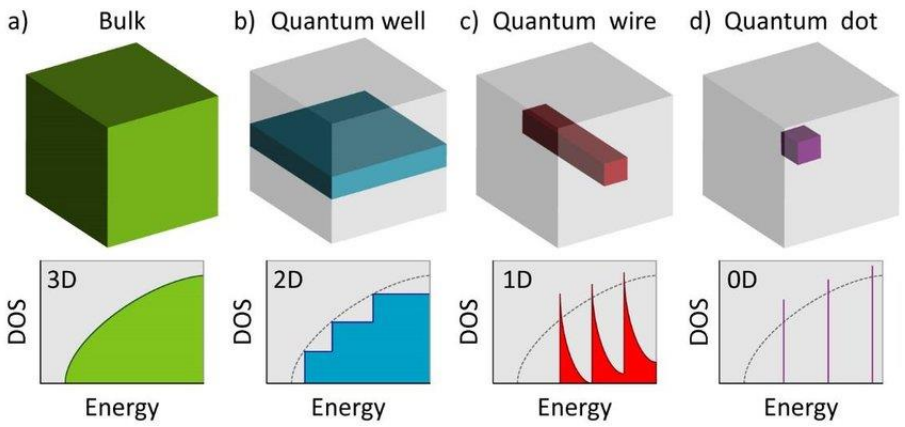

Fig. 4: Schematic representation of dimensionality in bulk (3D), quantum well (2D), quantum wire (1D) and quantum dot (0D). Corresponding densities of states versus energy are given below each diagram [26].

The density of states(DOS) refers to the average number of energy levels in a given energy range and this is not uniform in a band due to variations in the packing of energy levels within a band as observed in Fig. 3. The energy levels can be predicted by considering the quantum mechanics of a particle in a linear box [10, 27], Schrödinger's equation for a particle moving in one dimension can be presented as;

$$\hat{\mathrm{H}}\psi = E\psi \qquad (1)$$

$$E = -\frac{\hbar^2}{2m}\frac{\partial^2}{dx^2} + V(x) \qquad (2)$$

where; ψ represents the wavefunction, $\hat{H}$ the Hamiltonian and E represents possible energy levels, $\hbar$ stands for the Planck's constant ($\frac{\mathrm{h}}{2\pi}$), m is the mass of the particle, x stands for the spatial dimension and $V(x)$ represents the potential energy. If L is taken as the length of the box containing

the particle, with the following set boundary conditions; V(0) = +∞ , V(L) = +∞ and V(x) = 0 for 0 < x < L, then using these boundary conditions yields the energy levels given by Equation 3;

$$E = n^2 \frac{h^2}{8mL^2} \quad n = 1, 2, 3 \ldots \qquad (3)$$

where *n* stands for quantum numbers and ($n \in Z$). Hence, where $V = 0$, the particle inside a one-dimensional box only has kinetic energy and the permitted energies are shown in Equation 3 above. The particle in a box can be extended in other dimensions, like 2D and 3D. Resolution for the energy of an exciton, E_{ex} is the same as that for a spherical particle in a box;

$$E_{ex} = \frac{h^2}{8R^2}\left(\frac{1}{m_e} + \frac{1}{m_h}\right) - \frac{1.8e^2}{4\pi\varepsilon R} \qquad (4)$$

where: m_e and m_h represent the masses of the electron and hole respectively, *e* is the charge of an electron, the radius of the spherical particle is R and ε is the permittivity of the semiconductor. The boundary conditions for an exciton are the same as for the spherical particle in a box and are given as; V(r) = 0 for $0 \leq r < R$ and V(r) = +∞ for $r \geq R$. The energy levels of a spherical particle in a box are given by Equation 3.

Hence, the energy gap E_g is; $$E_g = -\frac{1.8e^2}{4\pi\varepsilon R} \qquad (5)$$

$$E_g = \frac{E'}{R} \qquad (6)$$

Where; $$E' = -\frac{1.8e^2}{4\pi\varepsilon} \qquad (7)$$

Hence; $$E_{ex} = \frac{h^2}{8R^2}\left(\frac{1}{m_e} + \frac{1}{m_h}\right) - \frac{E'}{R} \qquad (8)$$

An exciton is generated upon absorption of a photon with energy that is equal or above E_g. The charge carriers separate and the electron get promoted to the conduction band leaving behind a hole in the valence band. The electron recombines radiatively with the hole when it loses energy in form of a photon which is the main ingredient for photoluminescence. The rate of recombination is highly affected by factors such as defects or imperfections that act as recombination centers [28]. Defects play an important role in all solids as they affect major properties such as mechanical strength, chemical reactivity and electrical conductivity [29] of the solids. There are two major classifications of these defects, namely intrinsic and extrinsic defects. Occurrence of imperfections in pure solids give rise to intrinsic defects whilst extrinsic defects originate from the presence of dopants in the matrix of solids. As mentioned earlier, the presence of defects affects the rates of recombination and consequently the photoluminescence in semiconductors. The absorbance and emission reflect on the energy levels in NPs hence there is a need for monodispersity in samples. The absorbance of the NPs has been measured using the UV-Vis spectrometer and the emission using the photoluminescence spectrometer. Most reports, show that NPs absorb at wavelengths that are blue shifted compared to their corresponding bulk counterparts and that serves as evidence of size quantization [22, 30, 31]. The shape and surface chemistry play a role in the photoluminescence emission of NPs [32]. Emission spectra tend to be red shifted compared to the absorbance spectra [30] indicating that during relaxation, electrons emit less energy compared to absorbed energy as indicated in Fig. 5.

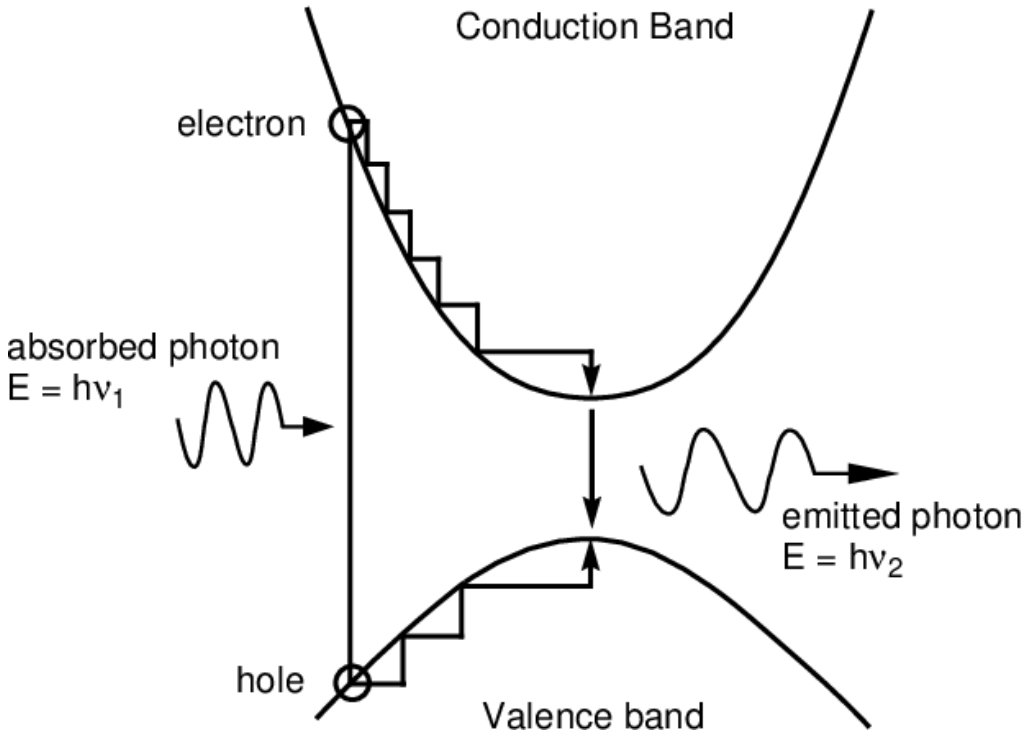

Fig. 5: Relaxation of carrier in a semiconductor. Frequency (v_1) of absorbed photon and (v_2) of emitted photon where h v_1 > h v_2 [33].

Quantum effects were observed in β-In_2S_3 NPs that were synthesized by Kumar and Muralidharan [34]. The size of the NPs of 8.08 ± 3.76 nm was less than the Bohr radius (~34 nm) of β-In_2S_3 [35] and due to quantum confinement, the band gap of the NPs of 2.45 eV was blue shifted to the bulk band gap of 2.0 eV [36, 37]. Further probing revealed a Stokes shift of 135 nm upon comparing the emission maxima to the excitation. The observed hypsochromic shift of the emission maxima with respect to absorbance describes photoluminescence Stokes (blue)-shift. Contrary to the law of conservation of energy [38, 39], bathochromic or anti-Stokes shifts [40-43] have been reported where the emitted photon has more energy (short wavelength) compared to the excitation one (long wavelength).

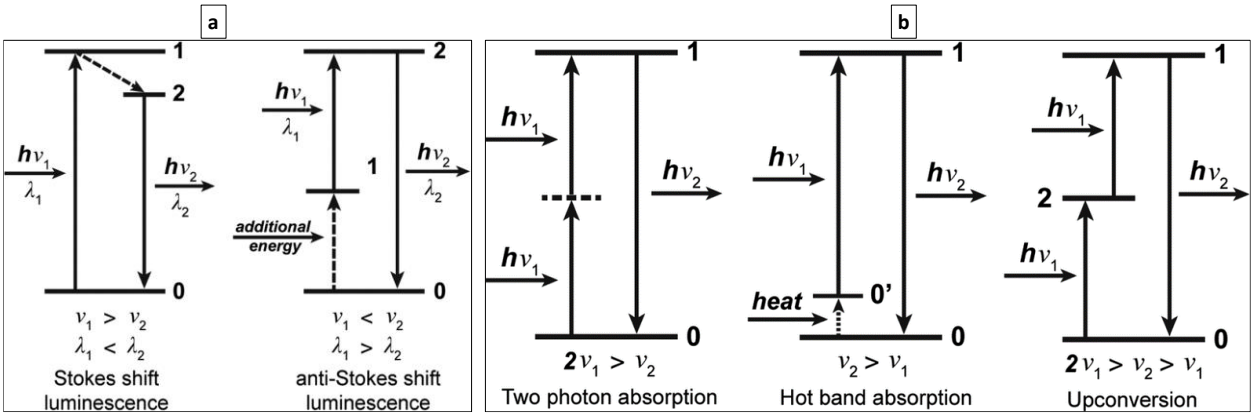

Fig. 6: Schematic representation of photoluminescence (a) Stokes and anti-Stokes shifts and (b) typical anti-stokes shift processes [44].

This special capacity to capture long wavelength excitation photons and emit short wavelength ones has been applied in bio-imaging [45] as the long wavelength light can penetrate deep into samples and avoid background interference [44]. Anti-stokes photoluminescence can be explained in terms of; two photon absorption, thermal activation by Auger transitions and absorption of phonons. The left part of Fig. 6(b) shows that in the two photon absorption (TPA), two photons are absorbed in sequence [42, 46] with a frequency of v_1 resulting in one higher energy photon of frequency v_2 hence the molecule is excited from ground state (0) to a higher level (1) then goes back to ground state by emitting a higher energy photon. In thermal or hot band activation, the electron and hole recombine non-radiatively and the emitted energy adds on to the excitation of other charge carriers to higher states [47]. The right side of Fig. 6(b) can be explained by the up-conversion process where the luminescence centers are able to absorb energies from two or more photons to generate one emission photon with higher energy than each individual excitation photon. In this process, a real excited intermediate state (2) exists which facilitates the process of photon absorption to act like a second-order elementary reaction, which has a higher degree of

probability than the case of absorption of two photons simultaneously [48]. Another interesting feature that suffices as a result of quantization is the high surface area to volume ratio. The number of atoms on the surface compared to the internal ones is much greater in NPs compared to bulk material. This effectively increases the surface area to volume ratio hence nanomaterials have been used to support the targeting ligand in the delivery of anticancer drugs [49].

2. General synthetic routes

Fig. 7 shows the two principal approaches in the synthesis of nanoparticles.

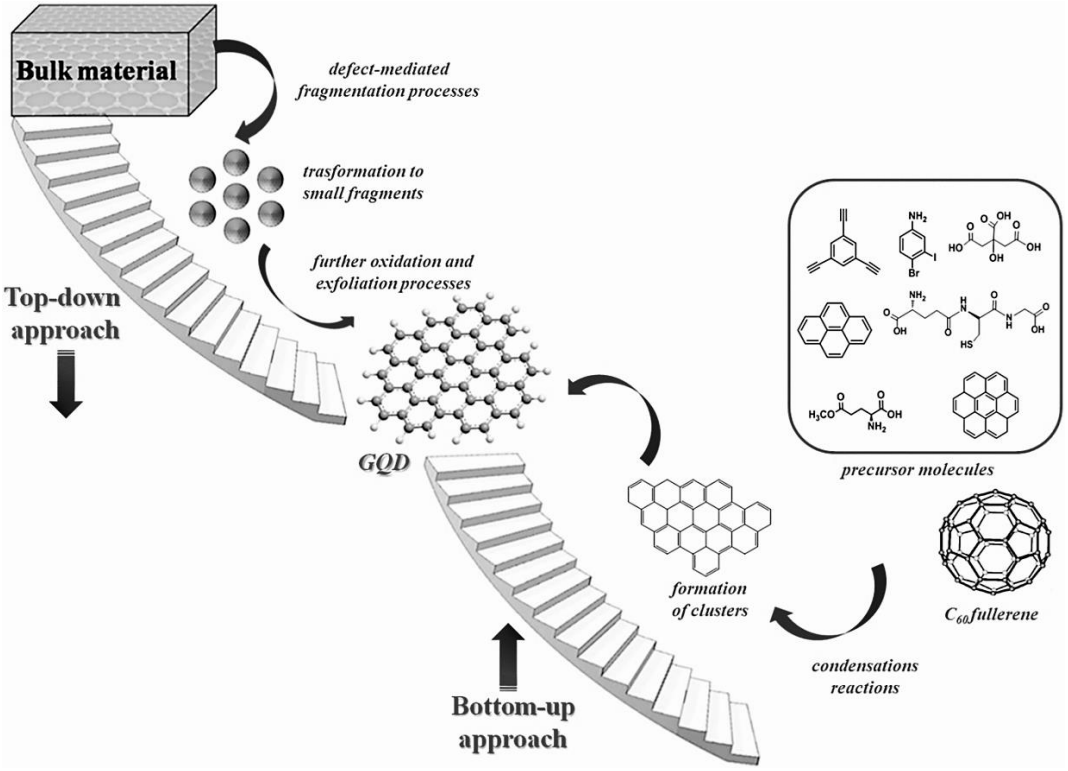

Fig. 7: Top-down and bottom-up approaches in the fabrication of graphene quantum dots (GQD) [49].

In the top-down approach (TDA), usually physical methods are employed to carve the bulk material to smaller parts until nanoparticles are obtained as depicted in Fig. 7. The direct

combination methods used tend to set conditions that are not favourable for the formation of monodispersed QDs or NPs. The reactants are larger in size compared to the NPs hence it takes a long time to reach equilibrium. Additionally, high temperatures tend to be used and this promotes growth and coarsening of nanoparticle, hence results in large crystals. The common methods that are used in this approach include; lithography, sputtering, chemical etching, thermal or laser ablation, mechanical or ball milling, electrochemical exfoliation, arc discharge and plasma treatment. On the other hand, in the bottom-up approach (BUA), particles at atomic or molecular levels combine in an orderly manner resulting in the formation of nanoparticles. In Fig. 7, Iannazzo *et al.* [49] went on to illustrate that small organic molecules react to form graphene QDs. Synthesis of nanoparticles in solution has become popular for generating monodispersed and uniformly shaped nanoparticles. Atoms and molecules are less than 0.1 nm in size and as they interact and combine, small nuclei of the desired material are formed and they grow to form NPs or QDs with sizes that fall within 1-100 nm.

Silicon is a well-known semiconductor with a band gap of 1.1 eV in its crystalline form [29] and has found sundry use in optoelectronic devices such as solar cells [50] and transistors [51]. Although Si-based semiconductors are efficient, relatively cheaper and easier to synthesize than most semiconductors, continued research has unveiled other semiconducting materials that can perform better than silicon. In semiconducting devices, binary semiconductors like GaAs have shown much faster response to electrical signals than silicon. Consequently, GaAs is preferred over silicon-based semiconductors in amplifying high frequency signals of satellite television [52]. In recent decades, there is been a spike in the synthesis and application of binary [53], ternary [54] and even quaternary [55] semiconductors.

Not much success has been achieved in the synthesis of metal nitrides as compared to metal chalcogenides like oxides mainly due to the fact that the enthalpy of formation of N^{3-} is much greater than that of O^{2-} [29]. Another set-back to nitride synthesis is its susceptibility to oxidation when exposed to water and air. It is for these reasons that there are numerous literature on the direct methods of synthesis of metal nitrides compared to solution-based methods of synthesis. Popular direct techniques such as magnetron sputtering [56-58] and chemical vapor deposition [59, 60] have been used successfully in the fabrication of thin films of metal chalcogenides. Sputtering techniques have been the most popular techniques in the synthesis of metal nitrides like Cu and Zn nitride films [56-58, 61-65] and, not much is known on the solution-based synthesis of these nitrides. The method of synthesis significantly influences the outcome of the reaction. Using physical methods to decompose $Cu(NO_3)_2$ yields Cu-oxides but thermolysis of the nitrate in organic solvents like octadecylamine gives rise to Cu_3N [66]. Recently, researchers are increasingly turning to solution-based synthetic methods which facilitate the engineering of desired morphology and properties of the NPs. In solution, the reagents have high mobility and interact at an atomic level leading to the formation of NPs that can be stabilized by surfactants or organic molecules. Hence, in this project, much focus was given to solution-based techniques but, a brief account of the popular physical methods in the synthesis of Cu_3N will be given first.

2.1 Sputtering Techniques

Juza and Hahn first reported the successful synthesis of Cu and Zn nitride films in 1938 [67] and 1940 [68] respectively. They employed the top-down method in reactive magnetron sputtering of Cu and Zn targets using pure nitrogen as working gas resulting in the deposition of Cu_3N and Zn_3N_2 films respectively. All sputtering techniques are plasma-based and mainly involve the use

of a target that is subjected to accelerated energetic ions of an inert gas resulting in the ejection of atoms or tiny clusters from the surface of the target material. The ejected particles traverse through a vacuum and are deposited on a substrate where they grow into a film. An overview of the sputtering process reveals that there are basically two electrodes that are involved and Figure 2.8 shows the substrate as the anode and the target as the cathode.

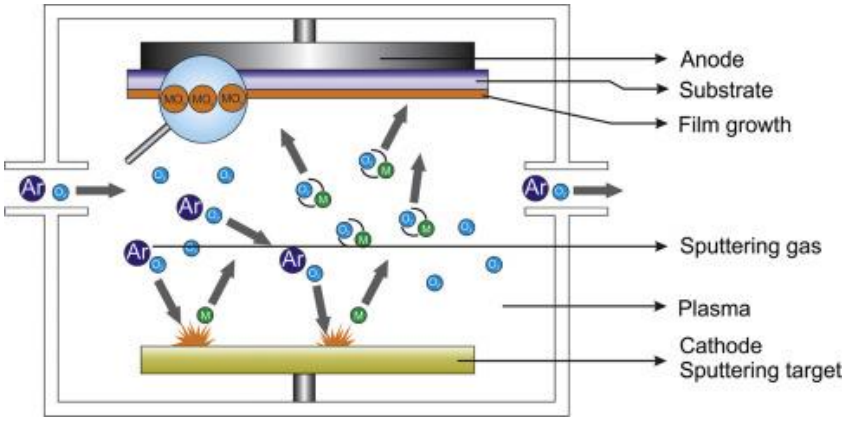

Fig. 8: Sputter deposition of a metal oxide film on the substrate using a metal as the target, oxygen as the reactive gas and argon as an inert gas [69].

In order to make a metal oxide film, Kumar *et al.* [69] first evacuated the chamber in order to get rid of undesired particles. A mixture of argon and oxygen gas was then introduced and a negative charge was applied on the metal target generating free electrons into the surrounding plasma. The free electrons collide with Ar and oxygen atoms and knock off electrons hence forming positively charged ions which are attracted to the cathode (target) at high speed. Due to the great momentum of collision, atomic or small cluster sized particles are sputtered off the surface of the target into the plasma, react with oxygen and eventually get deposited on the surface of the substrate. The efficiency of the sputtering process is measured by the sputter yield (S) of atoms or ions. This is

given by the number of target atoms or ions that are ejected with respect to the momentum transfer of a single incident atom or ion. Usually, sputtering yields range between 0.01 - 4 and bear a positive correlation to the energy of the sputtering gas and the mass of the metal [70]. Hence, the greater the energy of the gas particles and mass of metal, the greater the sputtering yield.

The sputtering process principally depends on the process of ion formation and ion focusing resulting in mainly three types; direct current (dc) [71], radio frequency (r. f.) [72] and magnetron [73] sputtering. Additionally, reactive sputtering [71] is brought about by the presence of a reactive gas. In the fabrication of Cu_3N thin films, just like other metal chalcogenide films, the processes are combined and result in the formation of good films. The most popular technique that has been used to make Cu_3N [57, 64, 72] and Zn_3N [58, 65, 74] is reactive r. f. magnetron sputtering. Reactive in that in the chamber, there is a gas, for example N_2 or O_2, which react to form a molecular compound before deposition is achieved. The r. f. indicates that radio frequencies are employed. Here, alternating electrical current reverses charge build up in cases when current is continuously flowing in one direction. Magnetron sputtering involves the use of magnets to increase the velocity and action of charges ions. The magnets are placed behind the negative electrode to facilitate electron trapping by the negatively charged target. As such, free electrons are no longer available to bombard the substrate resulting in a faster rate of deposition. Using the reactive radio-frequency magnetron sputtering technique, Toshikazu *et al.* [75] managed to deposit Cu_3N films on fused quartz substrate. The deposition was initially set at a pressure of less than $1x10^{-4}$ Pa, temperature of 100 °C, r. f. power of 100 W and N_2 gas pressure of 0.4 Pa. This resulted in a maximum thickness of 500 nm Cu_3N film with grain sizes ranging from 15 to 30 nm.

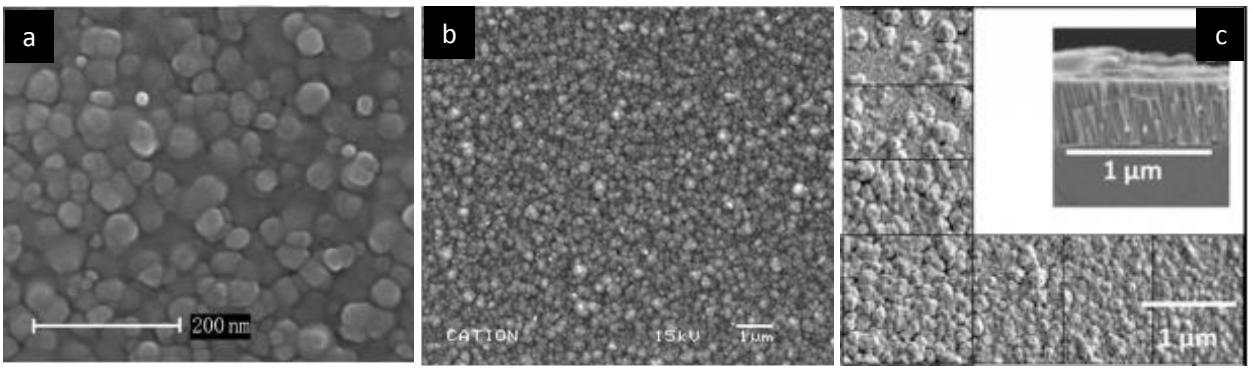

Fig. 9: SEM images of Cu_3N films grown using reactive magnetron sputtering technique to yield average grain sizes of (a) 40 nm [76] (b) 15 nm [77] and (c) 40 nm (includes insert of image of film cross section) [78] respectively.

The SEM images above show different films that were obtained by different researchers by sputtering Cu in the presence of nitrogen gas. Despite the great success in the film making of Cu_3N that dates as far back as 1938, acquiring the equipment and its maintenance are both expensive. The targets are usually expensive and the heat that is generated from most of the incident energy on the target has to be removed. Appropriate vacuum conditions have to be reached in order for foreign particles to be removed to avoid contamination and this contributes to low sputtering rates compared to thermal deposition. The main challenge in the sputtering techniques is lack of control in engineering NPs in order to get the desired morphologies and properties. Once a reaction starts, it becomes impossible to obtain samples of films at different time intervals showing different atomic layer depositions. The reaction has to run till the end of the set time in order to obtain the films.

2.2 Chemical vapor deposition

In this method, a solid deposit is made on the surface of a substrate by subjecting it to volatile precursors which react or decompose on its surface under certain conditions. This technique is popularly used in thin and thick film fabrication and has found various applications in protective coatings, optoelectronic semiconductor devices, magnetic recording media, photocatalysis, energy generation, gas sensing, drug delivery and light emitting diodes amongst others. There are various types of chemical vapor deposition techniques (CVD) such as atomic layer deposition, plasma assisted CVD, combustion CVD (pyrolysis) and ultrahigh vacuum CVD. The underlying principle in all types of CVD techniques is that some form of reaction occurs resulting in the deposition of solid products. The differences between them are brought about by the source of energy that is used to induce and maintain the deposition reaction. Figure 2.10 shows a typical set up in a hot wall CVD.

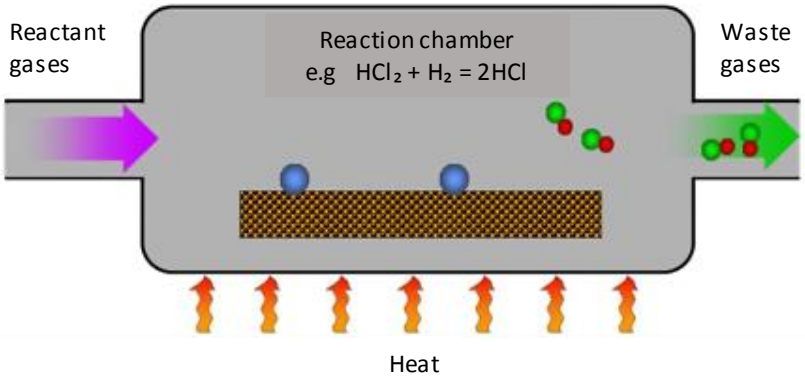

Fig. 10: A typical thermal CVD set-up for film deposition [79].

From the gas inlet, reactant gases are introduced into the reaction chamber that contains a clean substrate. Depending on the type of CVD, heat may be applied under a specified pressure and

reaction time. The reactants get adsorbed onto the surface of the substrate and react giving off a solid deposit and the by-products that are formed desorb from the surface and are evacuated through the gas outlet. Like any other chemical reaction, CVD reaction is only feasible if Gibbs free energy is negative at the set conditions [80]. Usually, the precursors used are organometallics or metal halides and although the organometallics are more volatile hence less energy consuming than the halides, they tend to introduce a higher level of contaminants compared to the halides due to fragmentation of associated ligands. Hence, care has to be taken in choosing the precursors as they influence the purity of the products, deposition temperature, growth rate and the structure of the film. The deposited products in CVD tend to be highly pure and deposition is achieved at relatively fast rates resulting in highly conformal films [81]. In a novel synthesis, Jammy *et al.* deposited highly conformal films in the CVD of TiN by passing titanium tetrachloride and ammonia over a silicon substrate at temperatures ranging from 350 to 800 °C [82]. CVD has also been manipulated in order to synthesize solids in powder form or as single crystals [83, 84]. The disadvantage with this technique is that very high decomposition temperatures of up to 2000 °C may be required and precursors and products of CVD can be highly toxic, corrosive or explosive. Fallberg [85] *et al.* [86] employed CVD in making Cu_3N films using copper(II) hexafluoroacetylacetonate ($C_{10}H_4CuF_{12}O_4$), NH_3 gas and water as precursors. The deposition was performed in a hot-wall reactor at temperatures ranging between 250 and 550 °C. The Cu source, H_2O and NH_3 were all introduced into the reactor in gaseous form (mixed with Ar) through separate tubes and were allowed to react for a period of 1 hr. Films were deposited on clean SiO_2 substrates and characterization using XRD revealed that single phase Cu_3N was synthesized up to 400 °C. At 425 °C, a mixture of Cu_3N and Cu were obtained but at 550 °C, single phase Cu was synthesized.

2.3 Solution-based Techniques

The NPs obtained from the liquid phase approach are usually dispersed in appropriate solvents and are referred to as colloidal semiconductor nanocrystals. These can be obtained in high yield and can be used in spin coating, inkjet printing and device fabrication [87] due to their high throughput at a relatively low cost. Researchers have established that solution-based nanofabrication offers better control of the morphology and properties of the desired NPs and a much higher yield is obtained within a relatively short period of time compared to physical methods of synthesis. Furthermore, apart from being reliable, wet synthetic routes are more cost effective than physical methods like magnetron sputtering which require expensive equipment. As mentioned earlier on, solution-based synthesis [88] facilitate the engineering of desired morphology resulting in NPs with enhanced properties [2]. In solution, precursor atoms or molecules get solvated and mingle hence the diffusion distance is generally small resulting in fast diffusion and hence the fast rate of reaction. The atoms or molecules become the building blocks that react forming tiny particles that self-assemble resulting in the formation of the desired monodispersed nanoparticles at relatively low temperatures. This nano-synthesis follows the bottom-up method of synthesis illustrated in Figure 2.7 and, can take place in inorganic, organic or organic-inorganic environments [19].

Chemical precipitation [20, 89] and hydrothermal [88, 90] approaches are examples of aqueous methods that have proved to be environmentally friendly. Normally, very mild temperatures are used in chemical precipitation and that is detrimental to the process of shape evolution resulting in poorly shaped NPs. The hydrothermal chemical synthesis of NPs is a water-based heterogeneous process that is usually performed under high pressure in a sealed container at temperatures ranging from the boiling point to the supercritical point of water [91]. This process is referred to as

solvothermal synthesis if the water is replaced by other solvents which usually are organic solvents. In the hydrothermal/solvothermal chemical synthesis, a temperature gradient is maintained whereby the hot end facilitates the solubility of the precursors and as products are formed, they self-assemble and crystallize at the cold end [92]. These synthetic processes are greatly governed by the chemical nature of the solvents and additives and also by the chemical composition, structure and properties of the precursors. On the other hand, the reaction temperature and pressure employed control the thermodynamics of the reaction. The hydrothermal method of synthesis is very popular in the fabrication of metal oxide NPs [93-95] and a number of other semiconducting materials such as metal sulfides, phosphides, selenides and nitrides.

Solvothermal synthesis is extensively used for colloidal synthesis of hybrid metal chalcogenides that incorporates organic and inorganic components. Relatively low temperatures are employed in the synthesis of organic-inorganic hybrid NPs to facilitate the integration of low molecular weight organic ligands into the inorganic nanoparticles formed without destroying the organic molecules. For this reason, researchers use functionalized capping agents that facilitate the chemical and physical design of the nanohybrids and alleviate agglomeration that occurs due to high surface energy. Depriving the colloidal system of surfactants can result in a continuous phase instead of discrete nano-units. Coordination of surfactant free NPs is incomplete making them to be highly reactive and hence leading to agglomeration. In the presence of coordinating ligands, the resultant nanoparticle-ligand entity is thermodynamically stable and its size is influenced by variations in type and concentration of capping agent. The surfactants or capping agents immensely contribute in regulating the growth and size of the NPs. The length of the surfactant has been shown to influence the size of the obtained NPs [96]. The length of the solvent molecules used also affects

the path of a reaction. Ammonolysis of copper (II) acetate monohydrate [$Cu(C_2H_3O_2)_2{\cdot}H_2O$] in short chain alcohols like $CH_3(CH_2)_4OH$ produced CuO NPs but under the same conditions, longer chain alcohols yielded Cu_3N nanoparticles [97].

Some of the most widely used capping agents include oleylamine (OLA), octadecylamine (ODA), hexadecylamine (HDA), dodecanethiol (DDT), triethanolamine, quinolone and oleic acid [98]. The functionality of capping agents depends on their amphiphilic nature that is brought about by the existence of a polar head and a non-polar hydrocarbon tail. The head interacts with the metal atom or ion whilst the tail interacts with the solvent. O-terminated ligands like linolinic and oleic acids have been widely used in the synthesis of NPs. Bala *et al.* [99] prepared Ag NPs by reducing Ag_2SO_4 in $NaBH_4$ in the presence of oleic acid and referred to the product as Ag hydrosol which precipitated out Ag NPs upon adding NaCl. The authors went on to prove that vigorous shaking of H_3PO_4 and a mixture of Ag hydrosols and cyclohexane results in a phase transfer in the oleic-acid capped Ag NPs giving rise to Ag-organosols as shown in *Scheme 1*.

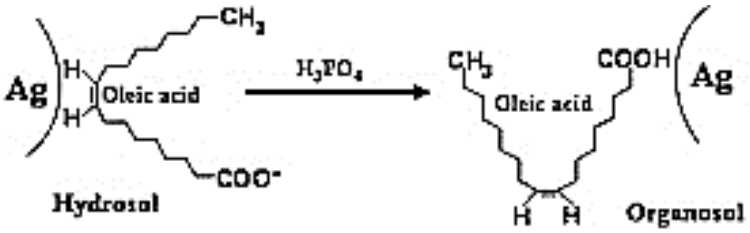

Scheme 1: Diagramatic representation of phase transfer due to changes on the surface binding of oleic acid on the surface of Ag NPs [99].

This study shows that depending on the orientation of oleic acid, chemisorption to the metal can occur through the double bond resulting in Ag hydrosols that easily disperse in aqueous media.

Alternatively, the oxygen atom on the carboxyl end of oleic acid can coordinate to the metal surface giving rise to Ag organosols that easily disperse in organic solvents. In order to obtain the desired morphology, scientists take advantage of the selective adsorption of capping agents in order to control the direction of growth of the NPs [100]. Tri-n-octylphosphine (TOP) and tri-n-octylphosphine oxide (TOPO) are typical examples of p-terminated ligands that are famous in the synthesis of NPs. Kruszynska *et al.* used TOPO to study the effect of temperature on the size of the Cu_2S NPs produced [101]. Colloidal synthesis of nanoparticles mainly involves the following stages; solvation, nucleation, growth and termination. Solvated precursor atoms or molecules react to form nuclei which can be allowed to grow till the growth is terminated by a reduction in temperature. The principal goal in a controlled solution-based nanocrystal synthesis revolves around simultaneous formation of a huge quantity of stable nuclei with extremely limited further growth. The nucleation and growth rates greatly affect the shape and size of the resultant nanoparticles. The more the growth stage is independent of the nucleation stage, the greater the probability of obtaining monodispersed NPs. For nucleation and growth to proceed appropriately, certain parameters such as pH, reaction temperature, time and capping agents need to be controlled.

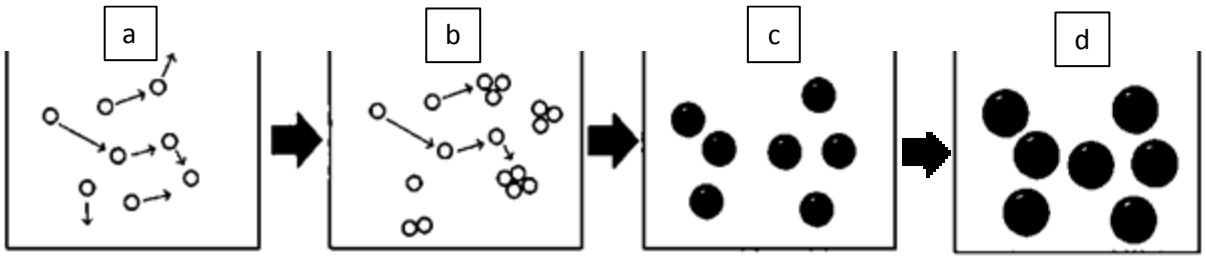

Scheme 2: Diagrammatic representation of (a) solvated atoms or molecules, (b) formation of clusters, (c) nucleation and (d) growth of nanoparticles in solution-based nanoparticle synthesis.

According to thermodynamics, nanocrystals grow towards a shape of minimum energy at equilibrium. Therefore, before the reaction has established the equilibrium stage, metastable nanocrystals of various shapes can be arrested from the reaction by varying the reaction conditions [102]. High temperatures promote nucleation whilst lower temperatures facilitate the growth process. It has been established that the process of nanocrystal formation is kinetically driven and this is based on relative growth rate [102]. The resultant shape in nanosynthesis plays a major role in surface chemistry. For example, if cubes are obtained, they offer a higher surface area to volume ratio compared to a sphere of the same volume [103]. The exposed 'active' surface area plays an important role in areas such as catalysis, chemical and biological sensing,

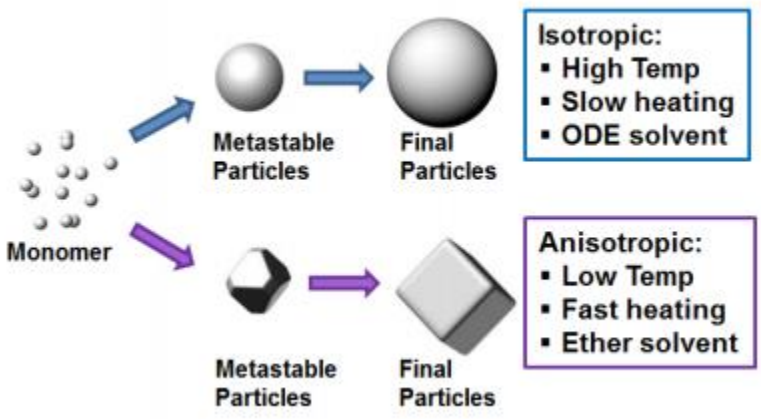

Scheme 3: Shape evolution of nanospheres and nanocubes due to different reaction conditions [103].

A major setback in solution-based synthesis is Ostwald ripening. Here, smaller nanoparticles re-dissolve and their solvated species recrystallize onto the larger particles resulting in polydispersed NPs with a relatively low nanoparticle count. This undesirable Ostwald ripening can be prevented by including surfactants or capping agents that assist in stabilizing the formed nanoparticles. Stable

nanoparticles will undergo very little or no further growth and re-dissolution is minimized due to formation of stable clusters hence monodispersed NPs are obtained. In order to obtain a high yield, the solubility of the NPs must be low and this is achieved by setting the correct temperature, solvent, pH and surfactant. Colloidal synthesis of the NPs was best described in the model that was proposed by Lamer and Dinegar as illustrated in Fig. 11.

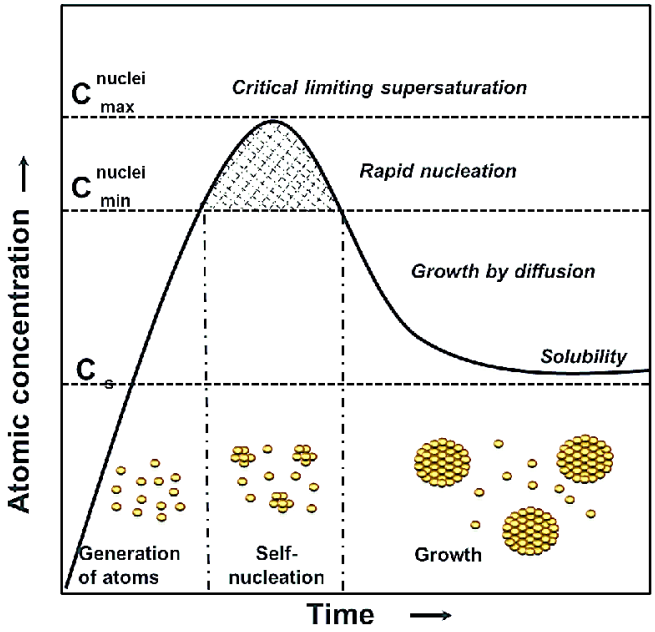

Fig. 11: Lamer and Dinegar diagram representing the mechanisms in colloidal synthesis [104].

Different approaches have been used in the colloidal synthesis of nanoparticles which include hot injection, seed-assisted growth and direct heating methods. In hot injection, usually a solvated ionic precursor is quickly injected into a solvated precursor at a high temperature resulting in a flood of nuclei (as a result of supersaturation) which grow spontaneously to give NPs of almost the same shape and size [105]. The temperature of the injected precursor is usually lower than the temperature of the solvent in the reaction vessel hence upon injection, the overall temperature of

the mixture decreases and is subsequently increased in order to facilitate growth of the nuclei to mature NPs. High quality nanoparticles have been obtained using the hot-injection method [105, 106] however, the drawback of this method is that it cannot be readily scaled up. As mentioned earlier, rapid nucleation at a high temperature is a requirement in the hot-injection method and as greater volumes are injected, the reagents mixing time is increased and will vary between users and between batches hence affecting the initial reaction kinetics. As such, as greater precursor volumes are used, it becomes more difficult to reproduce the high-quality NPs obtained in small batches.

The seed-mediated growth is a heterogeneous process that involves the synthesis of seed nanoparticles and their growth. Nucleation is distinctly separated from growth as seeds are pre-formed before they are introduced into a growth solution. Growth of the seeds [107] is accomplished in the presence of solvated metal precursors, reducing agents and shape directing agents. Seed-mediated growth is popular in the controlled synthesis of well-designed metal NPs like Au NPs [108-111]. Its greatest advantage is that specific highly crystalline seeds can be chosen and subjected to growth conditions that allow a specific design and size of NPs to be obtained. As this method involves a period of growing seeds, selecting the desired design and growing the seed, it tends to be cumbersome, time-consuming and results in a relatively low yield that is directly correlated to the seeds that were introduced in the growth solution.

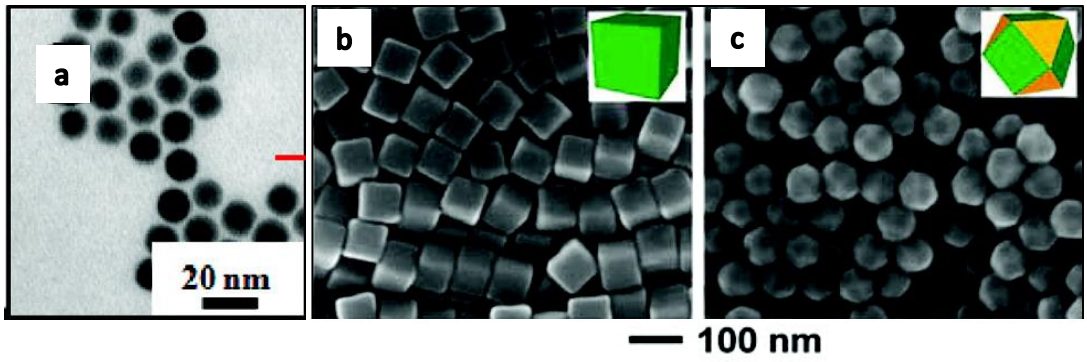

Fig. 12: Shows (a) TEM image of Cu_2S nanoparticles synthesized using the hot injection method [101] and SEM images of Ag (b) nanocubes and (c) cuboctahedrons formed after 10 min in 0.1 mM PVP55 respectively using the seed mediated approach [112].

The direct heating up approach offers an environmentally friendly, less cumbersome, highly controllable and scalable route in the synthesis of high quality NPs. This is a one-pot approach where all the precursors are mixed and heated in a controlled manner to prompt nucleation and growth of NPs. As heat increases, the precursor molecules are thermodynamically driven to decompose and generate monomers which at the right temperature are triggered to form nuclei that will subsequently grow into NPs as heating continues [113]. Conditions have to be carefully controlled such that at the right temperature, burst nucleation is accomplished in a short period of time and the growth phase has to occur independently of the nucleation stage in order to promote monodispersity of the formed NPs. Nanoparticles formation is usually achieved at elevated temperatures and this involves a heating period prior to nucleation. If precursors are very reactive, they start to nucleate at low temperatures before reaching the desired temperature hence promoting polydispersity and, if very stable precursors are used, then a low nuclei count is attained and growth rate becomes too fast to control [114]. Hence, careful consideration of the chemistry of precursors and coordinating ligands has to be done in order to ascertain a smooth sailing in the burst

nucleation process and in the composition of the resultant NPs. Through years of research, suitable conditions have been established to suit scalable industrial synthesis of high quality semiconducting NPs like $CuInS_2$ [115, 116], CdSe [117], MnS [118], GaP [119] and InAs [120]. One of the challenges that are faced in the synthesis of Cu_3N nanoparticles is the oxidation due to the presence of oxygen and water during the synthesis process, especially at elevated temperatures. As such, all precautions have to be taken in order to avoid every possible introduction of air and moisture into the reaction vessel. It is for this reason that reports that involve the hot injection method are rare in the synthesis of Cu_3N NPs but direct heat up methods have proved to be very successful.

2.4 Single-source precursor method

The synthesis of NPs using single-source precursors has been reported as far back as 1996 by Trindade and O'Brien [121]. This method has been well established in the preparation of II-VI, III-V and II-V semiconducting NPs. This method involves the use of single-source precursor molecule that contains all the elements that are required for the synthesis of the desired NPs. The aim is to synthesize high quality, defect free and monodispersed NPs from carefully designed precursors that ensure reproducibility and facile decomposition at relatively low temperatures. The single-source precursor method poses quite a number of benefits over the conventional methods of synthesis. Since the precursor contains all the chemical ingredients that are required to form the nanoparticles, the route avoids introduction of precursors once the reaction has started. This way, introduction of air is avoided hence promoting the reaction to proceed under anaerobic conditions. This is a necessary requirement especially in cases where air sensitive precursors would have been used. Single-source precursors are usually organometallic molecules that are air stable and non-

toxic [122] hence eliminate the use of toxic salts such as $PtCl_2$. Since the molecules are organometallic in nature, decomposition can occur at relatively low temperatures [123]. Another positive aspect about the use of a single precursor is the reduction in impurities hence facilitating the cleaning process of the acquired nanoparticles [124]. This method is an efficient route to producing high quality, crystalline semiconducting nanomaterials that are monodispersed [122]. In the synthesis of CdSe nanoparticles, the researchers used only one source that provided both the required Cd and Se elemental species.

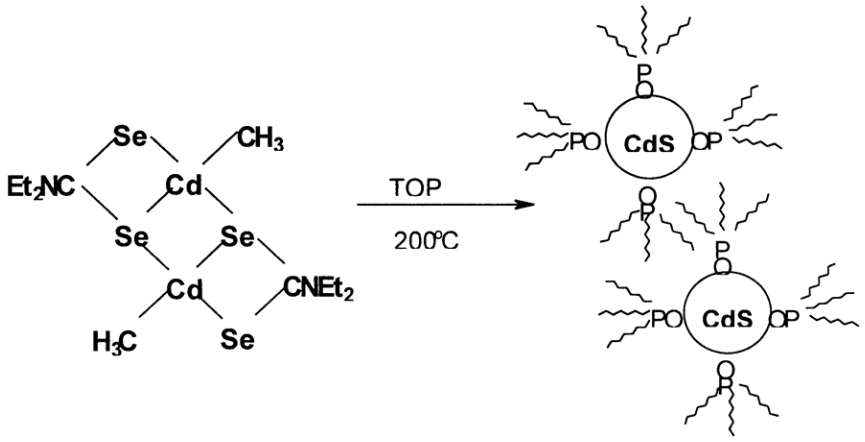

Scheme 4: The synthesis of CdSe nanoparticles from a single-source precursor [121].

Scheme 4 shows that in the molecule of the complex methyl-diethyldiselenocarbamato ($C_6H_{13}NOS_2$), the Cd already bonded to selenium hence facilitating the formation of the CdSe nanoparticles. This technique is best suited for large scale production [125] and offers an alternative route from the use of hazardous compounds like $Cd(CH_3)_2$ [126] and H_2Se [127]. The synthesized CdSe nanoparticles showed blue shifting with a band gap of 2.70 eV which is greater than that of the bulk material of 1.73 eV. In another synthesis, Costa [128] initially synthesized

two tin complexes (*Scheme 5*) and after characterization, used them as single-source precursors in the synthesis of SnS nanometric particles.

$$3SnR_2Cl_2 + 3Na_2S \longrightarrow Sn_3R_6S_3 + 6NaCl \quad (9)$$

$$4SnRCl_3 + 6Na_2S \longrightarrow Sn_4R_4S_6 + 12NaCl \quad (10)$$

where R =Me, Bu or Ph

Infrared spectroscopy, nuclear magnetic resonance spectroscopy and elemental analysis were used to characterize the complexes and the collected data matched that of known structures that are represented in *Scheme 5* below.

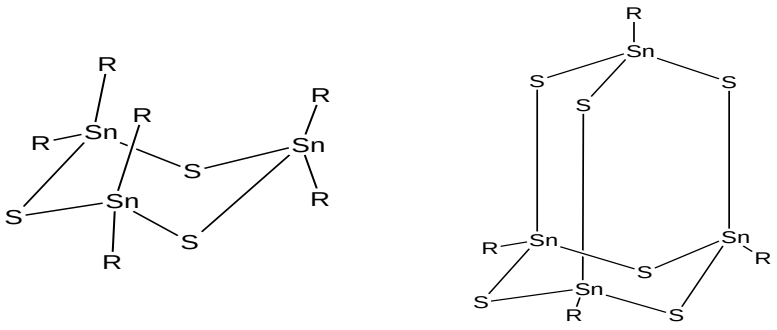

Scheme 5: Ring and cage structures of $R_6Sn_3S_3$ and $R_4Sn_4S_6$ complexes for use as single-source precursors in SnS NPs synthesis [128].

The complexes were then subjected to thermal decomposition and SnS NPs were formed as illustrated in the equation below;

$$Bu_4Sn_4S_6 \longrightarrow 4SnS + \text{volatile products} \quad (11)$$

Powder XRD analysis showed the presence of polycrystalline SnS nanoparticles of an average calculated crystal size of 45 nm. In the synthesis of colloidal Bi_2S_3 nanocrystals, Koh [129] separately performed thermolysis of bismuth (III) tris(N,N-diethyl dithiocarbamate $[Bi(S_2CNEt_2)_3]$ and chlorobismuth (III) bis(pyrroline dithiocarbamate) $[Bi(S_2CN(CH_2)_4)_2Cl]$ complexes in ethylene glycol $[(CH_2OH)_2]$ at 197 °C to obtain nanorods of an average diameter of 20 nm and 70 nm respectively. Onwudiwe and Ajibade [130] reported the synthesis of ZnS, CdS and HgS from single-source precursors, ML^1L^2 (where M = Zn, Cd, or Hg; L^1 = N-ethyl-N-phenyl dithiocarbamate and L^2 = *N*-butyl-*N*-phenyl dithiocarbamate). The thermal decomposition of the complexes in HDA at 180 °C produced nanoparticles of sizes ranging from 10 to 30 nm. The use of thiourea metal complexes as single-source precursors in the synthesis of nanoparticles is increasingly becoming popular. Sb(III)-thiourea [131] complex was synthesized, dissolved in CH_3OH and then thermally decomposed at temperatures ranging from 120-150 °C to give stibnite (Sb_2S_3) nanorods which grew in size upon increasing reaction time. In another study [132] near spherical HDA capped CdS nanoparticles by thermolysis of cadmium dithiocarbamates, $[Cd(S_2CNC_5H_{10})_2]$ and $[Cd(S_2CNC_9H_{10})_2]$ at 140-180 °C were obtained. Moloto *et al.* [133] reported on the synthesis of HDA-capped ZnS nanoparticles at 180 °C using Zn(II) complexes of N,N-diisopropylthiourea and N,N-dicyclohexylthiourea as precursors. Also reported are the Cd(II) thiourea complexes, $[Cd(CH_3COO)_2(SC(NHC_6H_{11})_2)_2]$ and $[Cd(CH_3COO)_2(SC(NHC_3H_7)_2)_2]$ used as sources of Cd and S in CdS NPs synthesis [134]. Thermal decomposition of the complexes in HDA at 180 °C produced NPs with sizes ranging from 2-5 nm. Malik and co-workers [135] compiled some work on single-source precursors that have been used to obtain semiconducting materials of the main group elements. Of interest to the current study is the synthesis of group (III) nitrides. Azide complexes like $MeGa(N_3)_3$ [136] are nitrogen-rich but pose a threat of exploding

upon hydrolysis of the Ga-N_3 bond. Recommended in the study is the use of Lewis base-stabilized compounds like [$(N_3)_2Ga(CH_2)_3NMe_2$] [137] to synthesis GaN. In the current study, Cu_3N nanoparticles were synthesized from Schiff base complexes for example, [((C_3H_7)-N=CH-$C_4H_3N)_2M$]. The complexes provide both the metal and the nitrogen required in the synthesis hence greatly reducing the chances of formation of other metal compounds.

The first report on Schiff-bases by the Italian chemist, Hugo Schiff in 1864 opened up an interesting area of research. Research has shown that these compounds can be used in homogeneous and heterogeneous catalysis [138], nitrification inhibitor activities [139] and antimicrobial activities amongst others. Schiff bases are organic or organometallic compounds that contain the azomethine group (HC=N) and can be formed easily through a reversible condensation reaction between primary amines and ketones or aldehydes upon heating or under the catalytic influence of acids or bases. Schiff-base ligands have made a huge contribution in coordination chemistry due to their ability to stabilize metals in different oxidation states during complexation. Amongst the known types of Schiff-base ligands are the closely related salicylaldimines and pyrrolylaldimines that mainly differ in their chelating groups as shown in the diagram below.

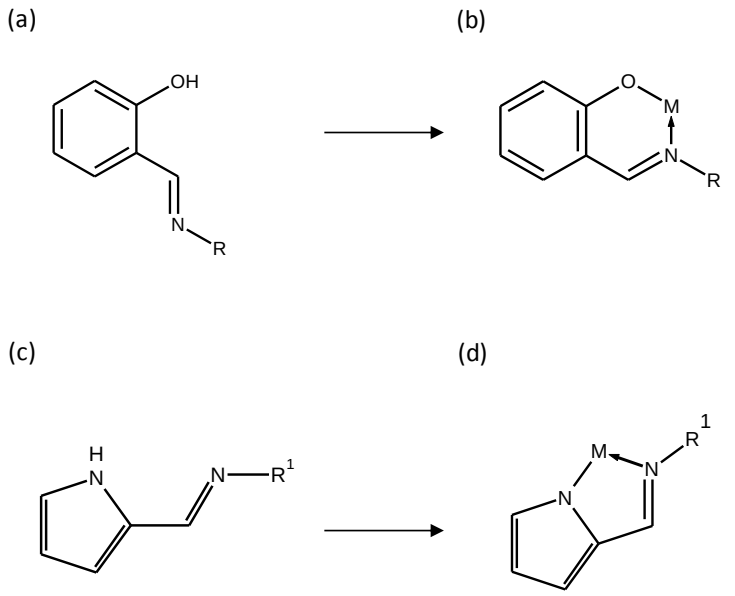

Scheme 6: Structures of Schiff-bases; salicylaldimine (a) ligand and (b) complex and, pyrrolylaldimine (c) ligand & (d) complex. [M = metal and R, R^1 = alkyl groups].

The salicylaldimine chelates through N, O to metals but chelation is achieved through N,N in pyrrolylaldimine. Intense studies have been done on the chemistry of salicylaldimines but pyrrolylaldimines still need to be explored. As such, this study focused on the synthesis and characterization of pyrrolylaldimines and used them as precursors in the synthesis of metal nitride NPs. Of great interest is their ability to form both mono and bis- pyrrolylaldimines and this depends mainly on the steric properties of the associated ligand or ligands and the nature of metal salt. In Figure 2.15, only the mono Schiff-base complexes are given but Scheme 7 shows the structure of a bis- pyrrolylaldimine complex.

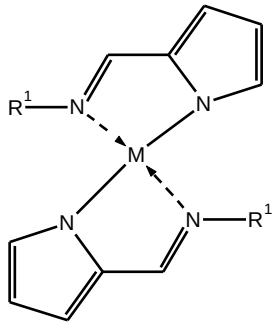

Scheme 7: Structure of bis-pyrrolylaldimine Schiff-base complex. [M = metal and R^1 = alkyl groups].

Generally, Schiff-base ligands are synthesized from a condensation reaction between an aldehyde and an amine. The ligands are then exposed to a metal salt in the presence of a catalyst or elevated temperatures to yield Schiff-base complexes. Perez-Puente successfully synthesized a bis-pyrrolylaldiminato Ni(II) complex from a salt of a ligand and $NiBr_2$(1,2-dimethoxyethane) [140].

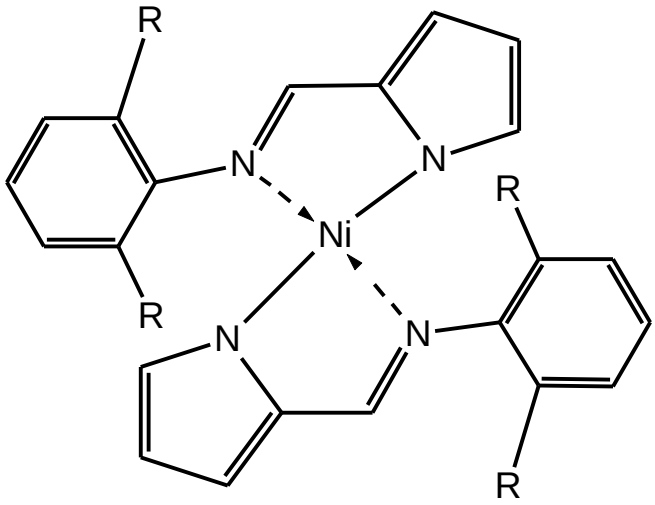

Scheme 8: Structure of a bis-pyrrolylaldiminato nickel (II) complex [140].

An interesting neutral pyrrolylaldimine complex was synthesized by van Stein *et al.* [141] when a 1:1 ratio of $ZnSO_4$ and $H_2N_2N_2$ methanolic mixture was reacted with two equivalents of KOH. The resultant product is shown below.

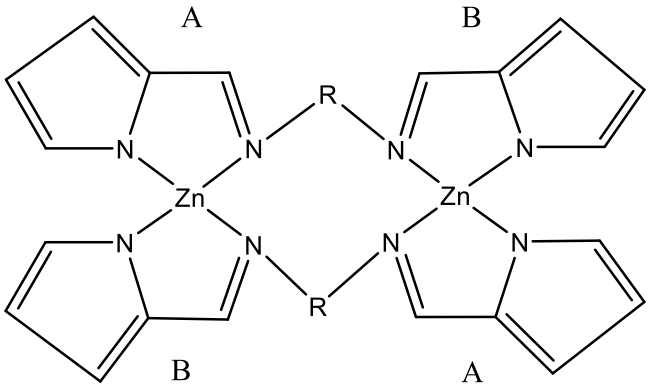

Scheme 9: Structure of a $Zn_2(N'_2\ N_2)_2$ pyrrolylaldimine Schiff-base complex. For $Zn_2(1)_2$, R = *(R)(S)*- 1,2-cyclohexane and for $Zn_2(2)_2$, R = 1,2-ethane [141].

If the metal is replaced by Cu, then the pyrrolylaldimine Cu(II) complexes become candidates for the synthesis of Cu_3N nanoparticles using the single-source precursor method as they possess both Cu and N. However, to become good candidates, complexes should not be too stable as very high decomposition temperatures will be required and at high temperatures, the nitride decomposes to copper. Furthermore, the toxicity and any hazardous effects of the by-products have to be carefully analyzed. Schiff-base complexes have been used successfully in the synthesis of nanoparticles. In their investigation, Aazam and El-Said [142] initially synthesized 2,3-bis-[(3-ethoxy-2-hydroxybenzylidene)amino]but2-enedinitrile ligand from a condensation reaction between 2,3-Diaminobut-2-ene-dinitrile and 3-ethoxy-2- hydroxybenzaldehyde. Complexation was achieved by separately reacting the obtained ligand with Cu and Ni acetate solutions in CH_3OH resulting in

the formation of 2,3-bis-[(3-ethoxy-2-hydroxybenzylidene)amino] but-2-enedinitrile copper and nickel complexes as shown in *Scheme 10*.

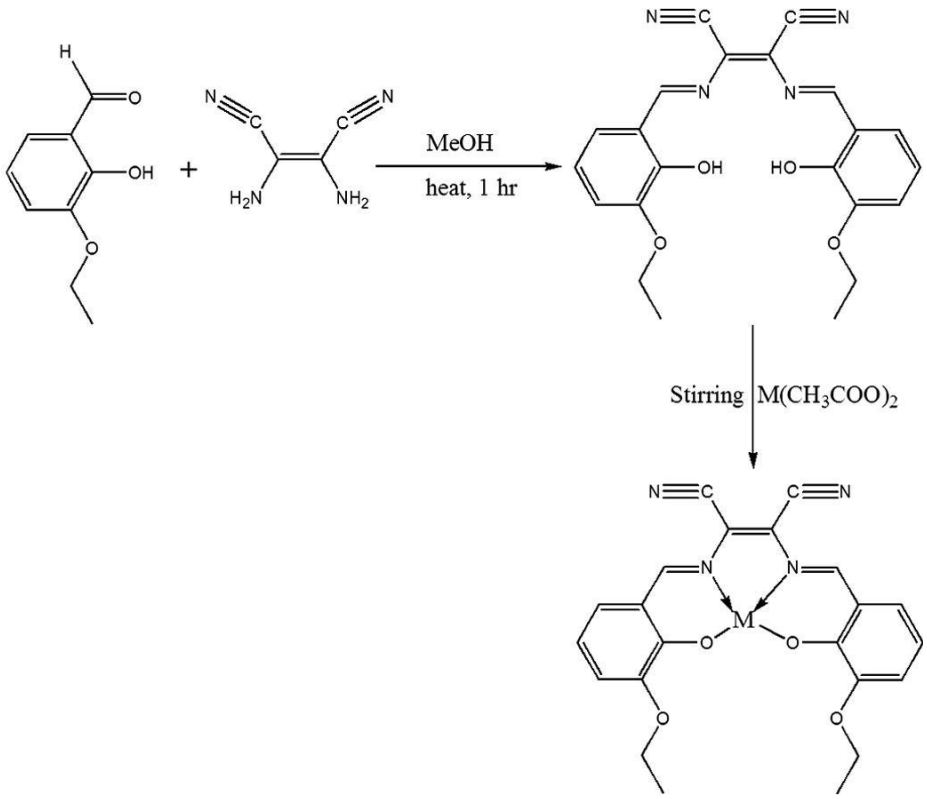

Scheme 10: Ligand formation and complexation to form 2,3-bis-[(3-ethoxy-2 hydroxybenzylidene)amino]but-2-enedinitrile metal complex (M= Cu or Ni) [142].

The authors then went on to use the Cu(II) and Ni(II) Schiff-base complexes as single-source precursors in the synthesis of Ni and Cu NPs. The NPs were obtained after thermal decomposition of the complexes for 1 hour using triton X-100 as a surfactant and triphenylphosphine as a reducing agent. TEM images showed that irregular shaped Cu and Ni NPs were obtained with size diameters of 25 and 28 nm respectively.

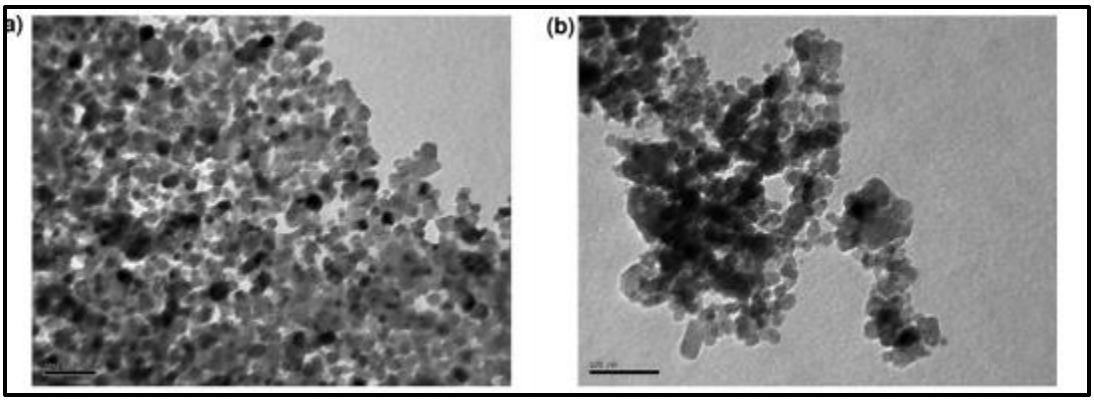

Fig. 13: TEM images of (a) Ni and (b) Cu NPs obtained using thermal decomposition of Ni and Cu Schiff-base complexes [137].

In another study, $[Co(C_{16}H_{11}N_3O_4)].12H_2O$ and $[Fe(C_{32}H_{22}N_4O_2)]\cdot 2H_2O$ Schiff-base complexes were thermally decomposed to give Co_3O_4 and γ-Fe_2O_3 NPs with average sizes of about 30 and 9 nm respectively [143]. ZnO NPs have been obtained by thermal decomposition of Zn(II) N4-tetradentate Schiff-base complex at 400 °C.

3. Metal nitrides

Although metal nitrides are not as abundant and not as well studied as other compounds like metal oxides, they have very important applications [144]. Due to their stability and high melting points, AlN, TaN and TiN are used in refractory ceramics. TiN, ZrN and CrN are used as wear resistant coatings for they remain stable even when exposed for a long time to humid conditions and temperatures of about 60 °C. In optoelectronics, the most used nitrides are GaN and InN that have shown remarkable semiconducting properties. Al, Ga and In are group III elements and their nitrides [145] exhibit direct band gaps of 6.2 eV, 3.4 eV and 1.9 eV respectively. Doping has resulted in InGaN and AlGaN systems where variations of quantities of Al and In have resulted in tunable band gaps where absorption occurs from the ultraviolet, the whole of the visible region

right into the infrared spectra. Nevertheless, the problem is the relatively low earth's crust abundances [146] of Ga and In approximated to be 0.00190% and 0.000025% respectively. It is important to consider the abundance and availability of raw materials required to synthesize the semiconducting materials. As shown above, elements like In and Ga are scarce; hence there is a need to seek alternative elements that are more abundant and environmentally friendly. More abundant elements like Cu, Zn and N with crust abundances [146] of 0.0047%, 0.0083% and 0.0019% respectively make good candidates for use in applications such as photocatalysis and photovoltaics.

Different synthetic methods have been used in the synthesis of Cu and Zn nitrides. Chemical methods have been used to directly react Zn with NH_3 [148-150] on quartz substrates to obtain Zn_2N_3 thin films with a wide band gap of 3.2 eV [149] and this is thought to be caused by the high ionicity of the Zn-N bond. Zn_3N_2 empty balls with an average size diameter of about 3-5 μm were obtained by nitridation of zinc powders at 600 °C for 120 min under ammonia gas [149, 150]. Zn_2N_3 thin films have been synthesized by reactive radio frequency (rf) magnetron sputtering [65, 151, 152] with indirect band gaps of 1.23 eV [65], 2.12 eV [151] and 1.01 eV (direct) [152]. A mixture of N-Ar gas was introduced as the sputtering gas with varying concentrations of N_2 from 5-100% targeting Zn discs. Borosilicate glass was used as the substrate and the temperature was kept at 423 °C with rf power at 25 W [65]. On the other hand, thermally stable Cu_3N thin films [153, 154] with band gaps of 1.85 eV [153] were grown by reactive rf magnetron sputtering at variable concentrations of nitrogen gas. These synthetic methods employ relatively high temperatures or high power resulting in high production costs. Colloidal synthetic techniques offer cheaper synthetic routes which can greatly cut down on the costs.

In another research, Futsuhara [65] reported a band gap of 1.23 eV for Zn_3N_2 thin films. Nanoneedles [155] with tips of 30-70 nm and stem ranging between 200-300 nm were synthesized by nitridation of ball-milled zinc powders for two hours at 600 ^oC under ammonia gas. Zn_3N_2 thin films have been synthesized but reported work on its nanoparticle synthesis and characterization has not been well explored. Cu_3N nanoparticles are considered to be semiconducting materials and are used as conductive ink [97] that are stable to oxidation. According to Du [153] Cu_3N may show excellent semiconductor behavior depending on the percentage of Cu in the sample. Samples with 76.9 % Cu gave a band gap of 1.85 eV. Cu_3N has been reported to be metastable with an enthalpy of formation of +71 KJ/mol [156] and decomposes at temperatures above 280 °C. Although not much research has been done on synthesis and characterization of colloidal Cu_3N nanoparticles [153, 154, 157] and Zn_3N_2 nanoparticles [158, 159], there is no evidence of researchers who have used Schiff base complexes as single-source precursors in the synthesis of Cu_3N nanoparticles.

Over the years, solution-based synthesis of Cu_3N has been achieved in different media and until recently, synthesis of Zn_3N_2 NPs had been confined to solid-state based methods of synthesis. Wu and Chen [157] demonstrated that size control can be accomplished by varying capping agents. In this study, the authors used primary amines, namely hexadecylamine ($C_{16}H_{35}N$), octadecylamine ($C_{18}H_{39}N$) and oleylamine ($C_{18}H_{37}N$) which acted as both solvents and capping agents. The hexadecylamine (HDA) and octadecylamine (ODA) are both saturated but only differ in chain length. On the other hand, octadecylamine and oleylamine (OLA) both have an 18 C chain but OLA unlike ODA is unsaturated. $Cu(NO_3)_2.3H_2O$ was thermolyzed in these amine in the presence of octadecene (OD). In each case, the temperature was set at 150 °C for 3 hours and then raised to 250 °C for 30 min. OD was required in order to slow down the nucleation that occurred during the

3 hours at 150 °C and this was evidenced by the change of color from blue, to green and finally yellow. After the nucleation, growth was then prompted by slowly increasing the temperature to 250 °C and maintained for 30 min yielding cubic Cu_3N nanocubes and this shows that a ripening process was required. The growth process was terminated by reducing the temperature after which the nanocubes were washed in alcohol. Cu_3N nanocubes with average sizes of 26.0 ± 5.6, 18.6 ± 2.3 and 10.8 ± 2.7 nm were obtained in the presence of ODA, HDA and OLA respectively. The longer chained amine (ODA) resulted in bigger NPs compared to the shorter chained HDA that resulted in smaller sized NPs. Although the unsaturated OLA has an 18 C chain, it resulted in the smallest sized nanocubes. The success of the formation of the nanocubes was due to the slow growth that was facilitated by the presence of octadecene and the preferential binding of the primary amines to the 100 facets of Cu_3N. Nanocubes were not obtained when synthesis was realized separately in the amine ligands alone or in octadecene but rather, ill-defined Cu_3N nanoparticles were obtained.

It has been noted that till now, that only two studies have reported the successful colloidal synthesis of Zn_3N_2 nanoparticles [158, 159]. Both studies were performed under highly inert conditions where a series of injections of diethylzinc [$(C_2H_5)_2Zn$] into a mixture of 1-octadecene:oleylamine in a ratio of 30:1 mL were performed in an NH_3-rich environment at 225 °C. Analysis of TEM images revealed that the sizes of the obtained nanoparticles increased as the number of injections increased. Ahumada-Lazo *et al.* [159] obtained well-defined quantum dots with the largest particles measuring ~8.9 nm but, the shapes of NPs (average size of ~8 nm) that were obtained by Taylor *et al.* [158] were not well-defined and the particles were not stable under the electron beam. Optical studies revealed that, as the size diameter of the Zn_3N_2 quantum dots increased from 2.7

to 8.9 nm, the band gap decreased from 3.2 to 1.5 eV [159]. A lot of controversy still exists over the optical properties Zn_3N_2 as band gaps ranging from 0.9 [160] to 3.36 [161] eV have been reported. Zn_3N_2 has not yet been well-studied hence its properties are not yet well-established meaning that many gaps still need to be filled to facilitate its application in the growing field of Nanotechnology.

Most of the colloidal synthesis of Cu_3N has been based on the thermal decomposition of $Cu(NO_3)_2$ in octadecylamine [66, 157, 162-164] only or mixed with OLA, HDA or with a solvent like OD [164]. Nearly perfect nanocubes were obtained in cases where ODA was used as a capping agent. Barman *et al.* [165] and Wu and Chen [157] obtained ill-defined nanocubes when OLA was used as a capping agent. For applications such as electrocatalysis, Mondal and Raj [166] proposed the use of shorter chained and lower boiling point coordinating ligands like hexamethylenetetramine (HTA) as a solvent and a reducing agent in order to avoid passivating the surfaces and hence hindering the catalytic activity of the NPs. $CuCl_2$ and an unstable azide (NaN_3) were reacted in toluene and tetrahydrofuran (THF) at temperatures not exceeding 185 °C in stainless steel high-pressure reactors and the total period was about 3-5 days [167]. The Cu_3N obtained was highly agglomerated but isolated cases of nearly cubic NPs were seen from the SEM images provided. In another study, quasi-spherical NPs of about 80 nm were obtained when HTA was added to $Cu(NO_3)_2.5H_2O$ in n-hexanol in a quartz pressure tube and heated for 60 min at 200 °C [166]. The agglomeration that is observed in the obtained Cu_3N is explained by the poor coordinating nature of the alcohols, toluene and THF and this was observed also when nitridation of CuO was realized in CH_3OH and NH_3 [168]. An interesting synthesis of Cu_3N and other nitrides (CoN and Ni_3N) was performed in pyridine at a very low temperature of 130 °C [169]. Initially, liquid NH_3 and

KNH_2 were added to CuI in pyridine at -35 °C and the mixture was warmed to room temperature resulting in the formation of a colorless solution of $Cu(NH_2)$ complex. The solution was then quickly warmed and refluxed for 30 min at 130 °C resulting in a brown suspension. Purification using acetonitrile resulted in a brown powder with a high yield of 90-95%. TEM image analysis revealed well dispersed spherically-shaped NPs with a size diameter of 4.2 ± 0.7 nm. This was facilitated using moderately coordinating and weak alkaline nature of pyridine which allowed the control of particle nucleation and promoted ammonolysis at low temperatures. Ultra-small, well-dispersed spherically-shaped Cu_3N NPs of about 2 nm were obtained in a study where Cu (II) methoxide was reacted with benzylamine ($C_6H_5CH_2NH_2$) at a low temperature of 140 °C for 15 min [170].

Synthesis of Cu_3N has also been achieved in long chain alcohols [97, 171, 172]. Cu_3N nanorods were obtained by bubbling ammonia gas for 40 min through a mixture of 1-nonanol containing CuC_{10} and CuC_2 separately [172]. The study that was performed by Nakamura *et al.* [97] revealed that nitridation of copper (II) acetate in relatively short-chained alcohols like 1-pentanol resulted in the formation of CuO but long chain alcohols like 1-heptanol or longer gave rise to Cu_3N NPs. It is worth noting that the NPs obtained in alcohol solutions did not have well-defined shapes like the nanocubes that were obtained in ODA.

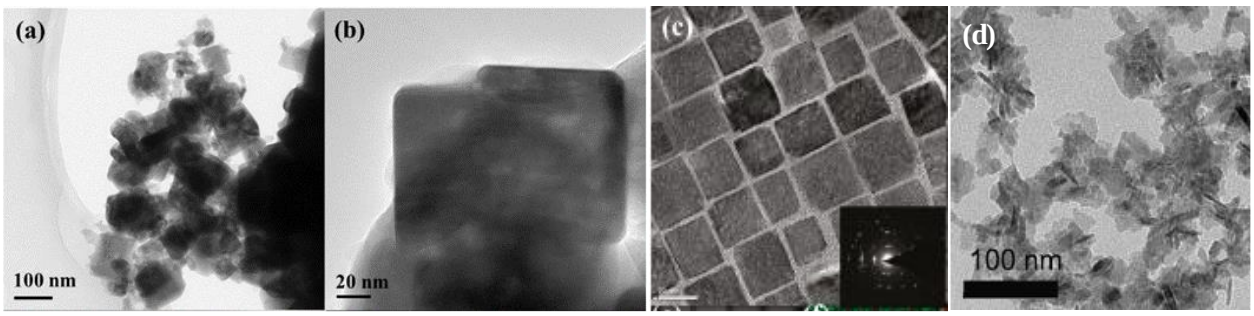

Fig. 14: Cu_3N NPs obtained through, (a and b) calcination of copper (II) acetate and urea [173], (c) thermolysis of $Cu(NO_3)_2$ in ODA [157] and (d) nitridation of a Cu complex (CuC_{10}) in 1-nonanol [172].

Lately, there have been a few reports on the synthesis of Cu_3N using urea as a nitrogen source [171, 173]. Cu3N was obtained by calcining copper (II) acetate ($Cu(OAc)_2$) and urea [173] at 300 °C. The authors indicated that, well-defined nanocubes of about 100 nm were formed but this could not be verified from the provided TEM images due to agglomeration (Fig. 14 (a) and (b)). Overall, from the micrographs, it has been observed that Cu_3N NPs that were obtained through solvothermal synthesis are well dispersed and well defined when amine coordinating ligands, especially ODA were used as capping agents. The well dispersed and nearly monodispersed nanocubes have been reported to be optically active and hence are good candidates in the optoelectronics, photocatalysis and energy generation amongst other applications.

4. Application in Photocatalysis

The robust research in nanotechnology is gradually increasing the answers to human problems especially in sectors like energy generation, gas sensing, wastewater management and water treatment. An increase in the world population has an adverse effect on environmental pollution and if not properly managed, water pollution can get out of hand to the extent that it becomes a

health hazard to human, animal and aquatic life. Nanotechnology is playing a major role in coming up with solutions in water treatment by unveiling, through research, various nanomaterials that have remarkable photocatalytic properties. If cost effective means of water purifications are put in place, it will alleviate problems like drought, water shortage and water borne diseases that arise as a result of pollution.

Research has shown that some materials can act as photocatalysts by absorbing visible light and catalyzing degradation of pollutants such as organic dyes in water. TiO_2 NPs, with a band gap of ~3.2 eV [174] have exhibited high photocatalytic activities specially when doped as this widens the absorption region in the visible spectra. The efficiency of a photocatalyst is measured by its ability to transform solar energy into chemical energy and this energy will then be used for applications such as hydrogen or energy production, water treatment and carbon dioxide cleavage amongst others. Various nanoparticles are still being investigated for their photocatalytic activities including Cu_3N, Cu_2S and Cu_9S_5. Intense use of nanoparticles has taken precedence over bulk materials due to the high surface area to volume ratio as a result of quantum confinement. In heterogeneous catalysis, the photocatalytic reactions occur on the surface of the nanomaterials in a solution-based environment.

4.1 Mechanism of photocatalysis

Commercially important dyes like azo dyes make up more than 60% of dyes that are used in mostly textiles and leather industries and about 10-15% of these dyes are not used up hence end up polluting the environment [175]. Azo dyes are water soluble organic compounds with an azo

chromophoric group (–N=N-) that is usually found bonded to aromatic rings. The color of these dyes is quite intense and it can be visible to the naked eye even at very low concentrations [176].

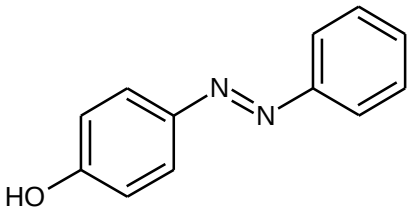

Scheme 11: Representation of the general structure of an azo dye.

The presence of dyes in aquatic systems compromises the quality of water and it reduces the intensity of sunlight reaching aquatic plants hence negatively affecting the concentration of dissolved oxygen that is required for aerobic respiration. Amongst the most commonly used azo dyes are basic red 18, methylene orange, methyl blue, direct blue 1, dinitroaniline orange, and pigment orange dyes. Benzidine derived azo dyes have been reported to be carcinogenic [177, 178]. Several methods have been employed to treat dye in polluted water and these include adsorption, oxidation and reduction, reverse osmosis, precipitation and biological methods and some of these are indicted in Table 1 below.

Table 1: Advantages and Disadvantages of current methods of dye removal from industrial effluents [179]

Physical/Chemical methods	Advantages	Disadvantages
Fenton's reagents	Effective decolorization of both soluble and insoluble dyes	Sludge generation
Ozonation	Applied in gaseous state: no alteration of volume	Short-half-life (20 min)

Photochemical	No sludge production	Formation of by-products
Cucurbituril	Good sorption capacity for various dyes	High cost
Electrochemical destruction	Breakdown compounds are non-hazardous	High cost of electricity
Activated carbon	Good removal of a wide variety of dyes	Very expensive
Peat	Good adsorbent due to cellular structure	Specific surface areas for adsorption are lower than activated carbon
Wood chips	Good sorption capacity for acid dyes	Requires long retention times
Silica gel	Effective for basic dye removal	Side reactions prevent commercial application
Membrane filtration	Removes all dye types	Concentrated sludge production
Ion exchange	Regeneration: no adsorbent loss	Not effective for all dyes
Irradiation	Effective oxidation at lab scale	Requires a lot of dissolved oxygen
Electrokinetic coagulation	Economically feasible	High sludge production

Sludge is mainly made up of organic and inorganic materials that contain fungi and protozoa. The organic matter, just like organic dyes, is degraded by photocatalysts leaving the inorganic waste which can be removed using analytical methods. Photocatalytic activities of various nanomaterials have been explored in degrading azo dyes [7, 180-182]. Materials such as TiO_2 and ZnO are popular photocatalysts that have been used to degrade dyes [181-184]. Other nanomaterials that have been used successfully to degrade azo dyes include PbO [185], ZnO-Eu [186], CuS [7] and SnS [187]. In particular, photocatalytic activities of NPs has been investigated in degrading dyes like methyl orange [188, 189], methylene blue [190, 191] and other azo dyes [192].

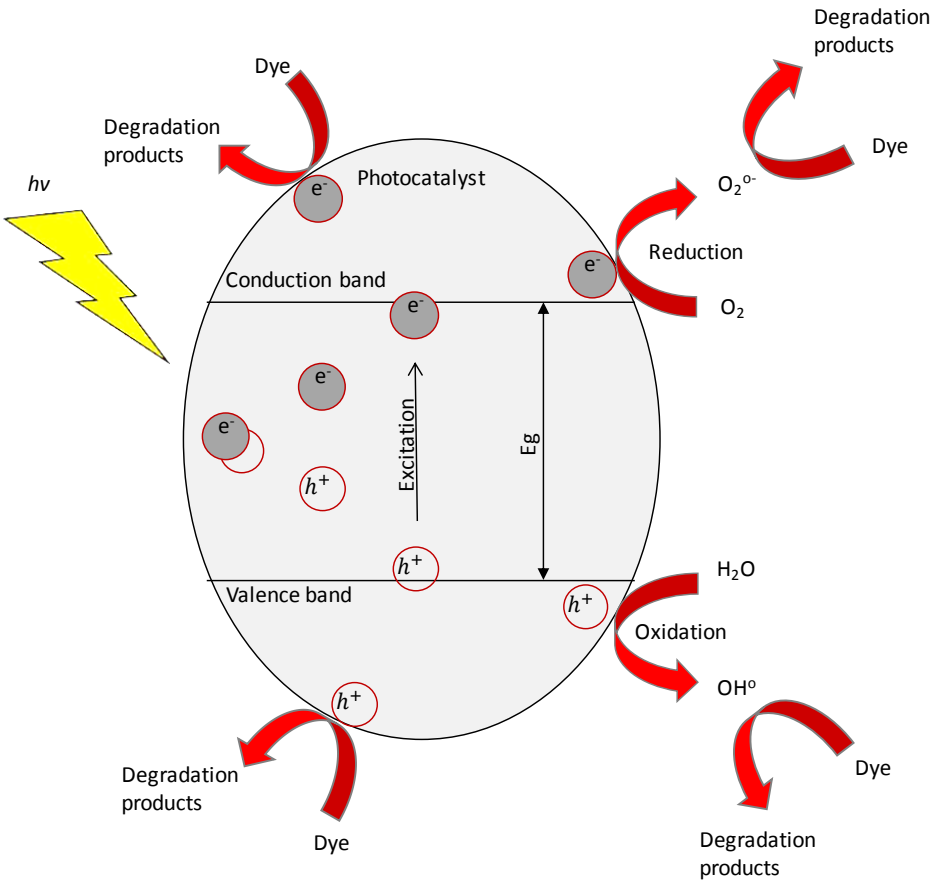

Fig. 15: Degradation of a dye using nanoparticles as photocatalysts in the presence of light.

The photocatalytic degradation of the dyes can be presented using the steps that have been suggested below;

1. Photons from visible light strike the nanoparticles and light energy is converted to chemical energy
2. Excitons absorb the energy and result in charge separation
3. Electrons in the valence band are excited and migrate to the conduction band leaving behind holes

$$CuS + hv \rightarrow h^+ + e^- \quad (11)$$

4. The holes and electrons can directly attack the dye

$$Dye + h^+ \rightarrow degradation\ products \quad (12)$$

$$Dye + e^- \rightarrow degradation\ products \quad (13)$$

5. Oxygen molecules in the reaction mixture adsorb onto the surface of the photocatalyst and take up electrons in the conduction band generating highly reactive superoxide radicals, ($O_2^{\cdot -}$) which can react with the dye and at the same time lead to the generation of $OH^{\cdot}$ radicals.

$$O_2 + e^- \rightarrow O_2^{\cdot -} \quad (14)$$

$$O_2^{\cdot -} + Dye \rightarrow degradation\ products \quad (15)$$

6. A series of steps can lead to the generation of $OH^{\cdot}$ radicals

$$O_2^{\cdot -} + e^- + 2H^+ \rightarrow H_2O_2 \quad (16)$$

$$2O_2^{\cdot -} + 2H^+ \rightarrow O_2 + H_2O_2 \quad (17)$$

$$H_2O_2 + e^- \rightarrow OH^- + OH^{\cdot} \quad (18)$$

7. In the valence band, holes (h^+) oxidize water and OH^- ions forming OH° radicals

$$H_2O + h^+ \rightarrow OH^{\cdot} + H^+ \quad (19)$$

$$OH^- + h^+ \rightarrow OH^{\cdot} \quad (20)$$

8. The $OH^{\cdot}$ radicals oxidize the dye molecules through a series of steps to form intermediates which usually are turned into harmless products like CO_2, H_2O and other products.

$$Dye + OH^{\cdot} \rightarrow degradation\ products \quad (21)$$

The photocatalytic process reveals that dye molecules can be attacked by electrons (e^-), holes (h^+), superoxide ($O_2^{\cdot -}$) and hydroxyl ($OH^{\cdot}$) radicals but basing on the Langmuir-Hinshelwood

kinetic theory, Aarthi *et al.* [193] carried out a study that showed that the main pathway that was involved in degrading the dye was the indirect route of electrons producing $OH^{\cdot}$ radicals. The contribution that was made from the direct oxidation of the dye by holes and the indirect oxidation by holes via $OH^{\cdot}$ radicals was negligible. However, it is interesting to note that photodegradation of MB in water was thought to be mainly due to $O_2^{\cdot -}$ radicals and photoexcited holes [194] whilst in MO, the $O_2^{\cdot -}$ and the generated $OH^{\cdot}$ radicals are thought to play a pivotal role [195-197]. One of the greatest challenges in photocatalysis when using semiconducting nanomaterials as photocatalysts is the recombination of electrons and holes. To circumvent this, Saranya *et al.* [198] added hydrogen peroxide (H_2O_2) to the reaction mixture in the degradation of methylene blue using copper sulfide/reduced graphene oxide (CuS/rGO) composite. Excited electrons are passed over from the CuS to the graphene sheets that further excite the electrons hence promoting the formation of $OH^{\cdot}$ radicals. Additionally, electrons are transferred to H_2O_2, a good electron acceptor, hence reducing the chances of electron/hole recombination and increasing the concentration of $OH^{\cdot}$ radicals. The overall effect was the high efficiency of the CuS/rGO in degrading the MB dye due to the high presence of $OH^{\cdot}$ and $O_2^{\cdot -}$ radical species in the reaction mixture. An investigation that was performed using TiO_2 in water showed rapid decolorization of methyl orange to form CO_2, NH_4^+, NO_3^- and SO_4^{2-} [190].

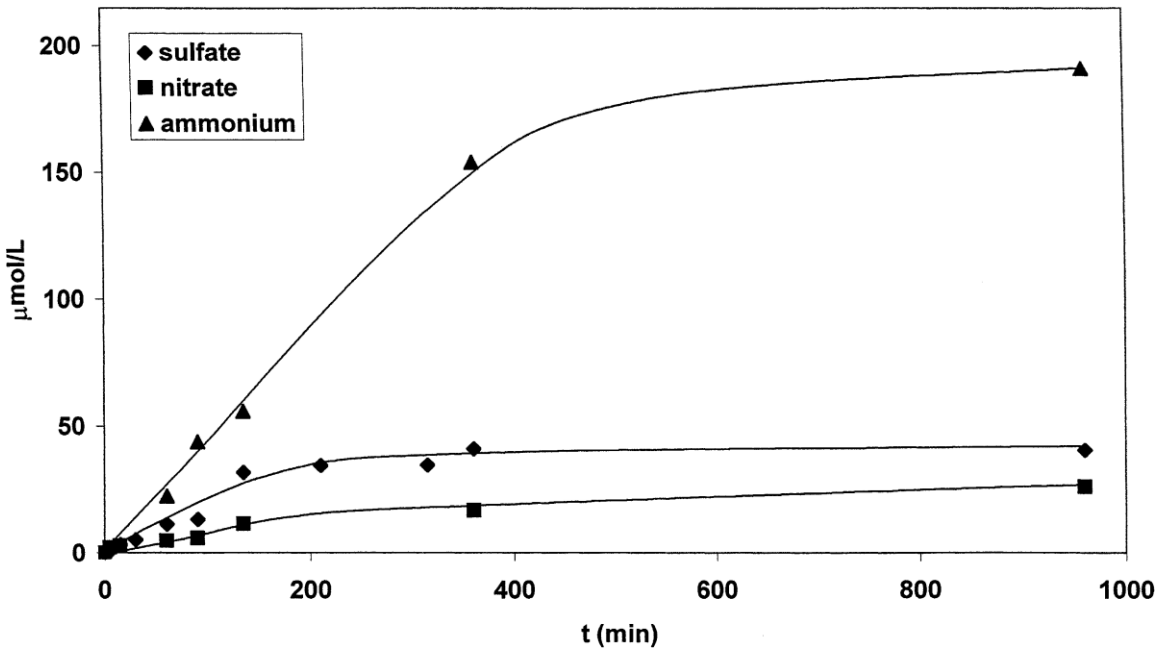

Fig. 16: Concentrations of NH_4^+, NO_3^- and SO_4^{2-} ions in the reaction mixture during the photocatalytic degradation of MB [190].

UV-irradiation was performed at 290 and 340 nm and decolorization was almost complete after 60 min and 120 min respectively. Fig. 16 shows that with time the concentrations of ammonium nitrate and sulfate ions and eventually level off between 200 and 400 min of irradiation. The authors then attempted to identify the intermediate products using GC/MS and LC/MS and proposed the following pathway for the degradation of MB;

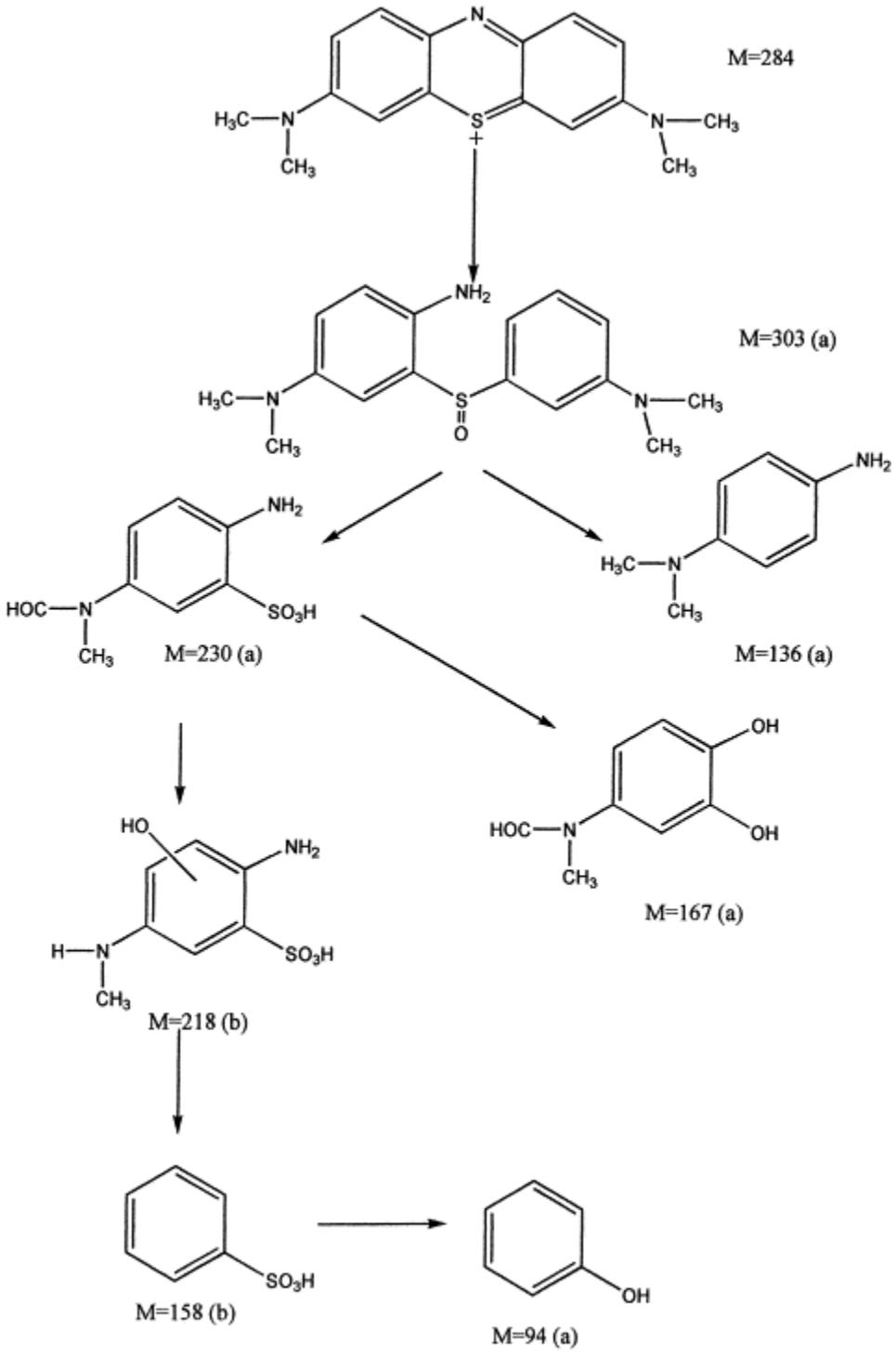

Scheme 12: Degradation pathway of methylene blue using TiO_2 as a photocatalyst [190].

Methyl orange was degraded using as-synthesized BiOBr nanoflakes that were obtained after 6 hours reaction time at 120 °C [199]. These NPs had an indirect band gap of 2.85 - 2.92 eV and they performed better than other NPs that were obtained at longer and shorter reaction times and at higher temperatures. Nearly all the dye had been degraded by 240 min and the nanoparticles did not show a significant change in their photocatalytic activity after 15 runs. In the photodegradation of methyl orange using Zn_4O organic-metal frameworks (UTSA-38), Wang *et al.* [200] proposed a mechanism showing the main path that is followed in the degradation. The final products were non-toxic and were identified as CO_2 and H_2O.

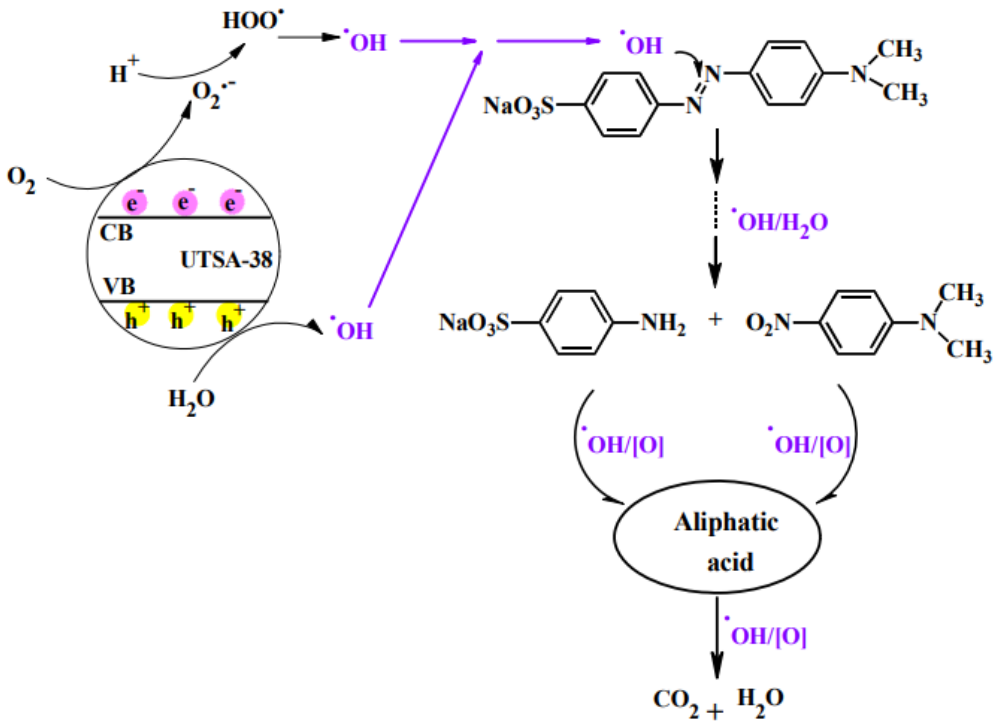

Scheme 13: Photodegradation pathway of MO showing in intermediate products and final naturalization products using Zn_4O MOF as photocatalyst [200].

To date, only one report has been published on the photocatalytic degradation properties of Cu_3N and its composite [201]. In a recently published report, copper nitride NPs were obtained by thermally decomposing $Cu(NO_3).3H_2O$ in a mixture of OLA and ODE at 210 °C for 15 min. After cleaning the Cu_3N NPs, they were then decorated with gold using chloroauric acid in OLA and ODE at 50 and 40 °C yielding ACN1 and ACN2 respectively and these were identified as Cu_3N/Au composites from the XRD diffractograms. The TEM images show ill-defined NPs that were well-dispersed in Cu_3N but showed a bit of agglomeration in the composites. For the photocatalytic experiments, 15 mg each of Cu_3N, ACTN1 and ACTN2 were mixed separately with methyl orange and methylene blue and the mixtures were homogenized by stirring in the dark for 5 min. The mixtures were then exposed to different light sources and aliquots were extracted at regular time intervals, centrifuged and the absorbance of the solutions were measured using a UV-Vis spectrophotometer that operated under green light emitting diode. The study showed negligible degradation of the dyes in the dark and in absence of photocatalysts. Upon irradiation, the concentrations of the dyes started to decrease in all samples with the ACN2 being the most efficient of the three catalysts. The authors report a pseudo first order kinetics with time for all the samples hence obtaining linear fits of graphs of;

$$In\left(\frac{C}{C_o}\right) = -kt$$

where, t is time, k is the rate constant and C & C_o are equilibrium and initial concentrations respectively.

Table 2: Best and worst percentage degradation of MO & MB after 25 min irradiation time [201]

Catalyst	Dye	
	MB (% degradation)	MO (% degradation)
Cu_3N **(worst catalyst)**	32	38
ACN2 **(best catalyst)**	93	84

The relative concentrations per given time interval were then displayed as shown in Fig. 17 below.

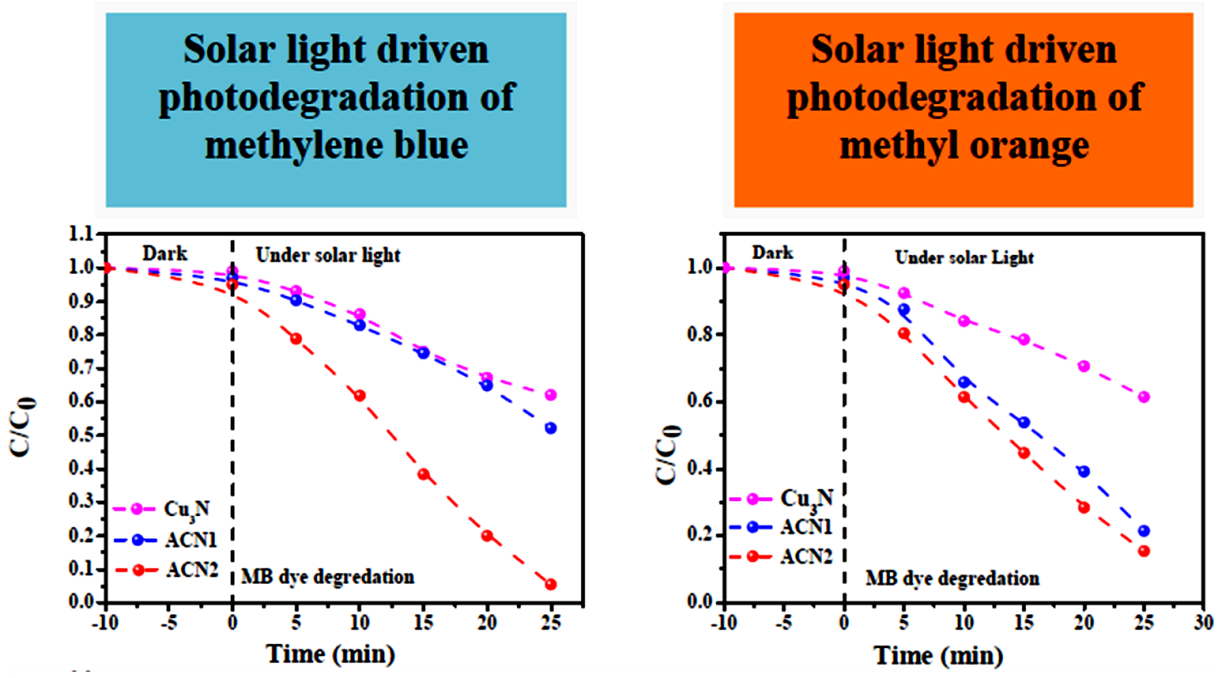

Fig. 17: Degradation of MO and MB dyes using Cu_3N, ACTN1 and ACTN2 photocatalysts under solar light [195].

The poor and good performances of pure Cu_3N and Cu_3/Au heterostructures respectively, can be explained by analyzing the proposed electron transfer illustrated in Fig. 18. In Cu_3N (Fig. 18(a)), the photon energy might not be high enough to give rise to significantly high numbers of reactive charge carriers and radicals. The dye molecule gets excited and produces an abundance of excited electrons in its excited state (LUMO level) which is energetically higher than the conduction band of the Cu_3N. This results in the transference of photoexcited electrons from the dye species to the Cu_3N NPs. The injection of the photoexcited electrons onto the surface of the catalyst leads to the generation of reactive species that will initiate the process of photocatalysis. This phenomenon is referred to as photosensitization [197] and it explains how photocatalysis can occur in cases where the photocatalyst does not receive enough photon energy for effective charge separation that should lead to generation of active species.

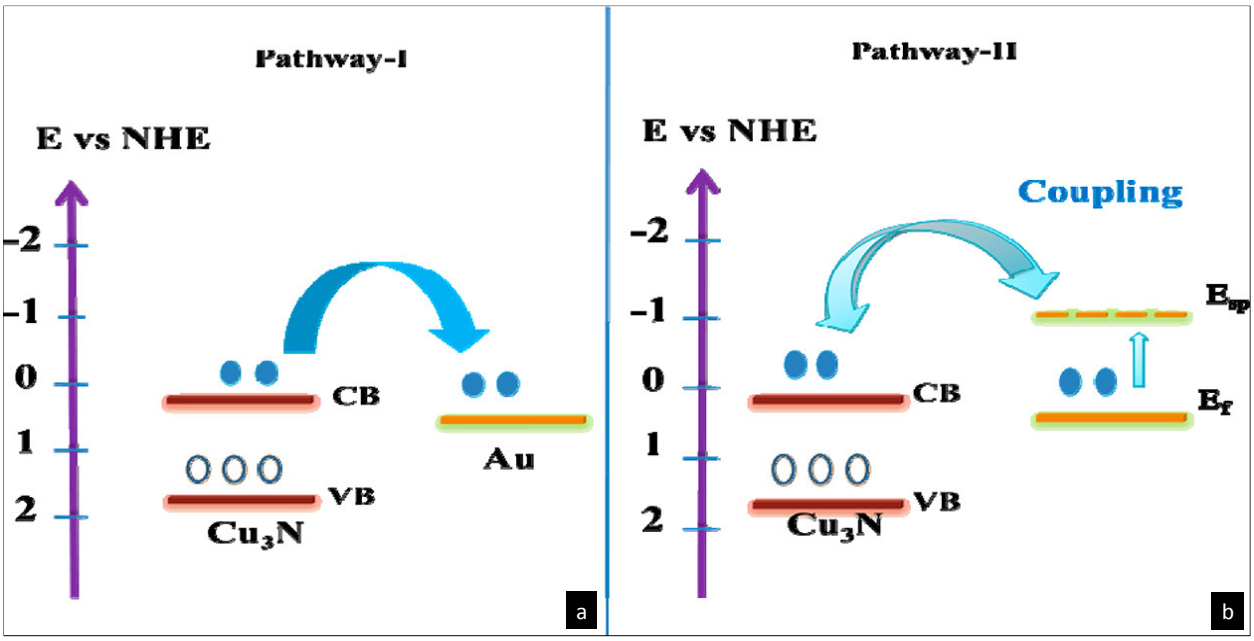

Fig. 18: Electron transfer mechanism in (a) Cu_3N and (b) Au decorated Cu_3N [195].

The high photocatalytic performance of ACN2 composite is explained by the two pathways that are shown in Fig. 18 (b). In Pathway I, the band levels in the ACN2 heterostructure facilitate the charge separation of charge carriers. Upon illumination, charge separation occurs and photoexcited electrons in the conduction band (CB) of Cu_3N are easily transferred to the Au particles whose fermi level is at a lower energy level than the CB of the nitride. The photoexcited electrons then reduce dissolved O_2 whilst the holes in the VB oxidize OH^- ion to highly reactive $O_2^{\cdot -}$ and $OH^{\cdot}$ radicals respectively. Using Pathway II, the high photocatalytic activity of ACN2 under green light was explained by the plasmonic absorption of Au around the 540 nm wavelength. The Au NPs act as the concentrator of the local electric field and this is best achieved when the light source is resonant with the Au NPs LSPR. This ascertains the highest near-field enhancement leading to an increase in light absorption efficiency of the composite hence propelling photocatalysis [202, 203].

The study of Cu_3N-Au NPs yielded better results than the copper nitride alone. It could be interesting to investigate the photocatalytic effect of integrating copper(I) nitride into widely used catalysts such as TiO_2 and ZnO.

References

[1] E. ASTM, 2456-06 Terminology for Nanotechnology, ASTM International, 2 (2006).

[2] S. Suresh, *Journal of Nanoscience and Nanotechnology*, 3 (2013) 62-74.

[3] M.A. Airo, R. Rodrigues, S. Gqoba, N. Ntholeng, F. Otieno, M.J. Moloto, M.W. Greenshields, I.A. Hümmelgen, N. Moloto, *Sensors and Actuators B: Chemical*, 236 (2016) 116-125.

[4] C. Fasciani, M.J. Silvero, M.A. Anghel, G.A. Arguello, M.C. Becerra, J.C. Scaiano, *Journal of the American Chemical Society*, 136 (2014) 17394-17397.

[5] M.P. Kalenga, S. Govindraju, M. Airo, M.J. Moloto, L.M. Sikhwivhilu, N. Moloto, *Journal of Nanoscience and Nanotechnology*, 15 (2015) 4480-4486.

[6] N. Venkatram, D.N. Rao, M. Akundi, *Optics Express*, 13 (2005) 867-872.

[7] M. Saranya, R. Ramachandran, E.J.J. Samuel, S.K. Jeong, A.N. Grace, *Powder Technology*, 279 (2015) 209-220.

[8] P. Sharma, S. Brown, G. Walter, S. Santra, B. Moudgil, *Nanoparticles for Bioimaging, Advances in Colloid and Interface Science*, 123 (2006) 471-485.

[9] N. Gamaleia, E. Shishko, G. Dolinsky, A. Shcherbakov, A. Usatenko, V. Kholin, *Experimental Oncology*, (2010).32, 44-47

[10] P. Atkins, J. De Paula, Physical Chemistry: Thermodynamics, Structure, and Change 8th Ed, in, Oxford: Oxford University Press, 2006.

[11] W.S. Liu, Q. Zhang, Y. Lan, S. Chen, X. Yan, Q. Zhang, H. Wang, D. Wang, G. Chen, Z. Ren, *Advanced Energy Materials*, 1 (2011) 577-587.

[12] N. Zhang, J. Sun, H. Gong, *Coatings*, 9 (2019) 137.

[13] R.K Spring, T. J. Fellersnand M. W. Davidson, *Olympus Life Science*, (2019).

[14] D.W. Bahnemann, *Israel Journal of Chemistry*, 33 (1993) 115-136.

[15] A. Hagfeldt, M. Graetzel, *Chemical Reviews*, 95 (1995) 49-68.

[16] S.V. Gaponenko, Optical Properties of Semiconductor Nanocrystals, Cambridge University Press, 1998.

[17] T. Kippeny, L.A. Swafford, S.J. Rosenthal, *Journal of Chemical Education*, 79 (2002) 1094.

[18] H. Weller, A. Eychmüller, *Advances in Photochemistry*, 20 (1995) 165-216.

[19] J. Chang, E.R. Waclawik, *RSC Advances*, 4 (2014) 23505-23527.

[20] M.L. Steigerwald, L.E., *Accounts of Chemical Research*, 23 (1990) 183-188.

[21] N.O. Dantas, F. Qu, R. Silva, P.C. Morais, A., *The Journal of Physical Chemistry B*, 106 (2002) 7453-7457.

[22] R. Thielsch, T. Böhme, R. Reiche, D. Schläfer, H.-D. Bauer, H. Böttcher, *Nanostructured Materials*, 10 (1998) 131-149.

[23] M.S. Silberberg, *Chemistry: The Molecular Nature of Matter and Change*, (2012).

[24] D. Dorfs, A. Eychmüller, Semiconductor Nanocrystal Quantum Dots: Synthesis, Assembly, Spectroscopy and Applications ed AL Rogach, in, Vienna: Springer, 2008.

[25] E. Pomerantseva, F. Bonaccorso, X. Feng, Y. Cui, Y. Gogotsi, *Science*, 366 (2019).

[26] F.T. Rabouw, C. de Mello Donega, *Springer*, 2017, pp. 1-30.

[27] R. Chang, Physical Chemistry for the Biosciences, University Science Books, 2005.

[28] M. De Laurentis, A. Irace, *Journal of Solid State Physics*, 2014 (2014).

[29] P. Atkins, T. Overton, Shriver and Atkins' Inorganic Chemistry, Oxford University Press, USA, 2010.

[30] K. Schmidt, G. Medeiros-Ribeiro, J. Garcia, P.M. Petroff, *Applied Physics Letters*, 70 (1997) 1727-1729.

[31] H. Zeng, Z. Li, W. Cai, B. Cao, P. Liu, S. Yang, *The Journal of Physical Chemistry B*, 111 (2007) 14311-14317.

[32] V.K. Sreenivasan, A.V. Zvyagin, E.M. Goldys, *Journal of Physics: Condensed Matter*, 25 (2013) 194101.

[33] K. Cumblidge, Using Time-Resolved Photoluminescence to Measure the Excitation and Temperature Dependence of Carrier Relaxation in Mid-Wave Infrared Semiconductors, Air Force Institute Of Technology, 2004.

[34] B.G. Kumar, K. Muralidharan, *Journal of Materials Chemistry*, 21 (2011) 11271-11275.

[35] W. Chen, J.-O. Bovin, A.G. Joly, S. Wang, F. Su, G. Li, *The Journal of Physical Chemistry B*, 108 (2004) 11927-11934.

[36] P. Herrasti, E. Fatas, J. Herrero, J. Ortega, *Electrochimica Acta*, 35 (1990) 345-349.

[37] W.T. Kim, C.D. Kim, *Journal of Applied Physics*, 60 (1986) 2631-2633.

[38] J.R. Lakowicz, *Springer Science & Business Media*, 2013.

[39] J. Zhou, Q. Liu, W. Feng, Y. Sun, F. Li, *Chemical Reviews*, 115 (2014) 395-465.

[40] E. Poles, D.C. Selmarten, O.I. Mićić, A.J. Nozik, *Applied Physics Letters*, 75 (1999) 971-973.

[41] P. Vagos, P. Boucaud, F. Julien, J.-M. Lourtioz, R. Planel, *Physical Review Letters*, 70 (1993) 1018.

[42] Z. Su, K. Teo, P. Yu, K. Uchida, *Solid State Communications*, 99 (1996) 933-936.

[43] V. Alex, T. Iino, *MRS Online Proceedings Library Archive*, 442 (1996).

[44] X. Zhu, Q. Su, W. Feng, F. Li, *Chemical Society Reviews*, 46 (2017) 1025-1039.

[45] S.A. Hilderbrand, F. Shao, C. Salthouse, U. Mahmood, R. Weissleder, *Chemical Communications*, (2009) 4188-4190.

[46] M. Junnarkar, E. Yamaguchi, *Solid-State Electronics*, 40 (1996) 665-671.

[47] H.M. Cheong, B. Fluegel, M.C. Hanna, A. Mascarenhas, *Physical Review B*, 58 (1998) R4254.

[48] F. Auzel, *Chemical Reviews*, 104 (2004) 139-174.

[49] D. Iannazzo, I. Ziccarelli, A. Pistone, *Journal of Materials Chemistry B*, 5 (2017) 6471-6489.

[50] T. Saga, *NPG Asia Materials*, 2 (2010) 96.

[51] G.K. Teal, *IEEE Transactions on Electron Devices*, 23 (1976) 621-639.

[52] L.E. Larson, *IEEE Journal of Solid-State Circuits*, 33 (1998) 387-399.

[53] A.I. Persson, M.W. Larsson, S. Stenström, B.J. Ohlsson, L. Samuelson, L.R. Wallenberg, *Nature Materials*, 3 (2004) 677.

[54] V. Gurin, *Colloids and Surfaces A: Physicochemical and Engineering Aspects*, 142 (1998) 35-40.

[55] I. Repins, M.A. Contreras, B. Egaas, C. DeHart, J. Scharf, C.L. Perkins, B. To, R. Noufi, *Photovoltaics: Research and Applications*, 16 (2008) 235-239.

[56] L. Maya, *Journal of Vacuum Science & Technology A: Vacuum*, Surfaces, and Films, 11 (1993) 604-608.

[57] Z. Liu, W. Wang, T. Wang, S. Chao, S. Zheng, *Thin Solid Films*, 325 (1998) 55-59.

[58] G. Xing, D. Wang, B. Yao, L.A. Qune, T. Yang, Q. He, J. Yang, L. Yang, *Journal of Applied Physics*, 108 (2010) 083710.

[59] J.J. Wu, S.C. Liu, *Advanced Materials*, 14 (2002) 215-218.

[60] D. Wang, Y. Liu, R. Mu, J. Zhang, Y. Lu, D. Shen, X. Fan, *Journal of Physics: Condensed Matter*, 16 (2004) 4635.

[61] A. Hojabri, N. Haghighian, K. Yasserian, M. Ghoranneviss, *IOP Conference Series: Materials Science and Engineering*, IOP Publishing, 2010, pp. 012004.

[62] M. Mikula, D. Búc, E. Pincik, *Acta Physica Slovaca*, 51 (2000) 35-43.

[63] A. Majumdar, S. Drache, H. Wulff, A.K. Mukhopadhyay, S. Bhattacharyya, C.A. Helm, R. Hippler, Coatings, 7 (2017) 64.

[64] D. Dorranian, L. Dejam, A. Sari, A. Hojabri, *The European Physical Journal Applied Physics*, 50 (2010) 20503.

[65] M. Futsuhara, K. Yoshioka, O. Takai, *Thin Solid Films*, 322 (1998) 274-281.

[66] D. Wang, Y. Li, *Chemical Communications*, 47 (2011) 3604-3606.

[67] R. Juza, H. Hahn, *Zeitschrift Für Anorganische Und Allgemeine Chemie*, 239 (1938) 282-287.

[68] R. Juza, H. Hahn, *Zeitschrift Für Anorganische Und Allgemeine Chemie*, 244 (1940) 125-132.

[69] D.S. Kumar, B.J. Kumar, H. Mahesh, *Nanomaterials*, Elsevier, 2018, pp. 59-88.

[70] C. Steinbrüchel, D. Gruen, Journal of Vacuum Science and Technology, 18 (1981) 235-237.

[71] M. Mikula, D. Buc, E. Pincik, *Acta Physica Slovaca*, 51 (2000) 35-43.

[72] S. Ghosh, F. Singh, D. Choudhary, D. Avasthi, V. Ganesan, P. Shah, A. Gupta, *Surface and Coatings Technology*, 142 (2001) 1034-1039.

[73] T. Maruyama, T. Morishita, *Applied Physics Letters*, 69 (1996) 890-891.

[74] M. Futsuhara, K. Yoshioka, O. Takai, *Thin Solid Films*, 322 (1998) 274-281.

[75] T. Nosaka, M. Yoshitake, A. Okamoto, S. Ogawa, Y. Nakayama, *Thin Solid Films*, 348 (1999) 8-13.

[76] A. Ji, R. Huang, Y. Du, C. Li, Y. Wang, Z. Cao, *Journal of Crystal Growth*, 295 (2006) 79-83.

[77] J. Pierson, *Vacuum*, 66 (2002) 59-64.

[78] C.M. Caskey, R.M. Richards, D.S. Ginley, A. Zakutayev, *Materials Horizons*, 1 (2014) 424-430.

[79] A.C.E.C. Solutions, What is CVD?, (2017).

[80] X.-T. Yan, Y. Xu, Chemical vapour deposition: an integrated engineering design for advanced materials, Springer Science & Business Media, 2010.

[81] A. Yanguas-Gil, Y. Yang, N. Kumar, J.R. Abelson, *Journal of Vacuum Science & Technology A: Vacuum, Surfaces, and Films*, 27 (2009) 1235-1243.

[82] R. Jammy, C.G. Faltermeier, U. Schroeder, K.H. Wong, Highly conformal titanium nitride deposition process for high aspect ratio structures, in, Google Patents, 2002.

[83] S. Hartner, M. Ali, C. Schulz, M. Winterer, H. Wiggers, *Nanotechnology*, 20 (2009) 445701.

[84] M.T. Swihart, *Current Opinion in Colloid & Interface Science*, 8 (2003) 127-133.

[85] A. Fallberg, Chemical Vapour Deposition of Undoped and Oxygen Doped Copper (I) Nitride, in, Acta Universitatis Upsaliensis, 2010.

[86] A. Fallberg, M. Ottosson, J.O. Carlsson, *Chemical Vapor Deposition*, 15 (2009) 300-305.

[87] J.Y. Kim, O. Voznyy, D. Zhitomirsky, E.H. Sargent, *Advanced Materials*, 25 (2013) 4986-5010.

[88] G. Demazeau, *Research on Chemical Intermediates*, 37 (2011) 107-123.

[89] L. Spanhel, M. Haase, H. Weller, A. Henglein, *Journal of the American Chemical Society*, 109 (1987) 5649-5655.

[90] D.L. Morgan, H.-Y. Zhu, R.L. Frost, E.R. Waclawik, *Chemistry of Materials*, 20 (2008) 3800-3802.

[91] S. Feng, L. Guanghua, *Modern Inorganic Synthetic Chemistry*, Elsevier, 2011, pp. 63-95.

[92] P. Horcajada, C. Serre, M. Vallet-Regí, M. Sebban, F. Taulelle, G. Férey, *Angewandte Chemie International Edition*, 45 (2006) 5974-5978.

[93] B. Baruwati, D.K. Kumar, S.V. Manorama, *Sensors and Actuators B: Chemical*, 119 (2006) 676-682.

[94] G. Wang, X. Shen, J. Horvat, B. Wang, H. Liu, D. Wexler, J. Yao, *The Journal of Physical Chemistry C*, 113 (2009) 4357-4361.

[95] S. Ge, X. Shi, K. Sun, C. Li, C. Uher, J.R. Baker Jr, M.M. Banaszak Holl, B.G. Orr, *The Journal of Physical Chemistry C*, 113 (2009) 13593-13599.

[96] A. Memar, C.M. Phan, M.O. Tade, *Applied Surface Science*, 305 (2014) 760-767.

[97] T. Nakamura, H. Hayashi, T.-a. Hanaoka, T. Ebina, *Inorganic Chemistry*, 53 (2013) 710-715.

[98] S. Gulati, M. Sachdeva, K. Bhasin, *AIP Conference Proceedings, AIP Publishing*, 2018, pp. 030214.

[99] T. Bala, A. Swami, B. Prasad, M. Sastry, *Journal of Colloid and Interface Science*, 283 (2005) 422-431.

[100] Y. Yin, A.P. Alivisatos, *Nature*, 437 (2004) 664.

[101] M. Kruszynska, H. Borchert, A. Bachmatiuk, M.H. Rümmeli, B. Büchner, J.r. Parisi, J. Kolny-Olesiak, *ACS Nano*, 6 (2012) 5889-5896.

[102] Y. Wang, J. He, C. Liu, W.H. Chong, H. Chen, *Angewandte Chemie International Edition*, 54 (2015) 2022-2051.

[103] C. Jiang, Synthesis, assembly, and integration of magnetic nanoparticles for nanoparticle-based spintronic devices, HKU Theses Online (HKUTO), (2017).

[104] V.K. LaMer, R.H. Dinegar, *Journal of the American Chemical Society*, 72 (1950) 4847-4854.

[105] J. Lim, W.K. Bae, J. Kwak, S. Lee, C. Lee, K. Char, *Optical Materials Express*, 2 (2012) 594-628.

[106] K. De Nolf, R.K. Capek, S. Abe, M. Sluydts, Y. Jang, J.C. Martins, S. Cottenier, E. Lifshitz, Z. Hens, *Journal of the American Chemical Society*, 137 (2015) 2495-2505.

[107] C.J. Murphy, T.K. Sau, A.M. Gole, C.J. Orendorff, J. Gao, L. Gou, S.E. Hunyadi, T. Li, *ACS Publications*, 2005.

[108] W. Niu, S. Zheng, D. Wang, X. Liu, H. Li, S. Han, J. Chen, Z. Tang, G. Xu, *Journal of the American Chemical Society*, 131 (2008) 697-703.

[109] W. Niu, L. Zhang, G. Xu, *Nanoscale*, 5 (2013) 3172-3181.

[110] C.J. Murphy, L.B. Thompson, D.J. Chernak, J.A. Yang, S.T. Sivapalan, S.P. Boulos, J. Huang, A.M. Alkilany, P.N. Sisco, *Current Opinion in Colloid & Interface Science*, 16 (2011) 128-134.

[111] L. An, Y. Wang, Q. Tian, S. Yang, *Materials*, 10 (2017) 1372.

[112] X. Xia, J. Zeng, L.K. Oetjen, Q. Li, Y. Xia, *Journal of the American Chemical Society*, 134 (2012) 1793-1801.

[113] O. Chen, X. Chen, Y. Yang, J. Lynch, H. Wu, J. Zhuang, Y.C. Cao, *Angewandte Chemie International Edition*, 47 (2008) 8638-8641.

[114] Y.C. Cao, J. Wang, *Journal of the American Chemical Society*, 126 (2004) 14336-14337.

[115] H. Zhong, Y. Zhou, M. Ye, Y. He, J. Ye, C. He, C. Yang, Y. Li, *Chemistry of Materials*, 20 (2008) 6434-6443.

[116] H. Zhong, S.S. Lo, T. Mirkovic, Y. Li, Y. Ding, Y. Li, G.D. Scholes, *ACS Nano*, 4 (2010) 5253-5262.

[117] Y.A. Yang, H. Wu, K.R. Williams, Y.C. Cao, *Angewandte Chemie International Edition*, 44 (2005) 6712-6715.

[118] L. Peng, S. Shen, Y. Zhang, H. Xu, Q. Wang, *Journal of Colloid and Interface Science*, 377 (2012) 13-17.

[119] M. Green, P. O'Brien, *Journal of Materials Chemistry*, 14 (2004) 629-636.

[120] M.A. Malik, P. O'Brien, M. Helliwell, *Journal of Materials Chemistry*, 15 (2005) 1463-1467.

[121] T. Trindade, P. O'Brien, *Advanced Materials*, 8 (1996) 161-163.

[122] M.A. Malik, N. Revaprasadu, P. O'Brien, *Chemistry of Materials*, 13 (2001) 913-920.

[123] N.O. Boadi, M.A. Malik, P. O'Brien, J.A. Awudza, *Dalton transactions*, 41 (2012) 10497-10506.

[124] N.L. Pickett, P. O'Brien, *The Chemical Record*, 1 (2001) 467-479.

[125] H. Weller, *Advanced Materials*, 5 (1993) 88-95.

[126] C. Murray, D.J. Norris, M.G. Bawendi, *Journal of the American Chemical Society*, 115 (1993) 8706-8715.

[127] R.S. Urquhart, D.N. Furlong, T. Gengenbach, N.J. Geddes, F. Grieser, *Langmuir-Blodgett films, Langmuir*, 11 (1995) 1127-1133.

[128] G.A. Costa, M.C. Silva, A.C. Silva, G.M. de Lima, R.M. Lago, M.T. Sansiviero, *Physical Chemistry Chemical Physics*, 2 (2000) 5708-5711.

[129] Y.W. Koh, C.S. Lai, A.Y. Du, E.R. Tiekink, K.P. Loh, *Chemistry of Materials*, 15 (2003) 4544-4554.

[130] D.C. Onwudiwe, P.A. Ajibade, ZnS, *International Journal of Molecular Sciences*, 12 (2011) 5538-5551.

[131] J. Yang, J.-h. Zeng, S.-H. Yu, L. Yang, Y.-H. Zhang, Y.-T. Qian, *Chemistry of Materials*, 12 (2000) 2924-2929.

[132] T. Mthethwa, V.R. Pullabhotla, P.S. Mdluli, J. Wesley-Smith, N. Revaprasadu, *Polyhedron*, 28 (2009) 2977-2982.

[133] N. Moloto, N. Revaprasadu, M. Moloto, P. O'Brien, J. Raftery, *South African Journal of Science*, 105 (2009) 258-263.

[134] N. Moloto, N. Revaprasadu, M. Moloto, P. O'Brien, M. Helliwell, *Polyhedron*, 26 (2007) 3947-3955.

[135] M.A. Malik, M. Afzaal, P. O'Brien, *Chemical Reviews*, 110 (2010) 4417-4446.

[136] A.C. Frank, F. Stowasser, O. Stark, H.T. Kwak, H. Sussek, A. Rupp, H. Pritzkow, O. Ambacher, M. Giersig, R.A. Fischer, *Advanced Materials for Optics and Electronics*, 8 (1998) 135-146.

[137] A. Devi, W. Rogge, A. Wohlfart, F. Hipler, H.W. Becker, R.A. Fischer, *Chemical Vapor Deposition*, 6 (2000) 245-252.

[138] P. Das, W. Linert, *Coordination Chemistry Reviews*, 311 (2016) 1-23.

[139] A. Datta, S. Walia, B.S. Parmar, *Journal of Agricultural and Food Chemistry*, 49 (2001) 4726-4731.

[140] P. Pérez-Puente, E. de Jesús, J.C. Flores, P. Gómez-Sal, *Journal of Organometallic Chemistry*, 693 (2008) 3902-3906.

[141] G.C. Van Stein, G. Van Koten, H. Passenier, O. Steinebach, K. Vrieze, *Inorganica Chimica Acta*, 89 (1984) 79-87.

[142] E.S. Aazam, W.A. El-Said, *Bioorganic Chemistry*, 57 (2014) 5-12.

[143] E. Ibrahim, L.H. Abdel-Rahman, A.M. Abu-Dief, A. Elshafaie, S.K. Hamdan, A. Ahmed, *Materials Research Bulletin*, 99 (2018) 103-108.

[144] J. Buha, I. Djerdj, M. Antonietti, M. Niederberger, *Chemistry of Materials*, 19 (2007) 3499-3505.

[145] J. Orton, C. Foxon, *Reports on Progress in Physics*, 61 (1998) 1.

[146] A. Yaroshevsky, *Geochemistry International*, 44 (2006) 48-55.

[147] R. Long, Y. Dai, L. Yu, M. Guo, B. Huang, *The Journal of Physical Chemistry B*, 111 (2007) 3379-3383.

[148] K. Kuriyama, Y. Takahashi, F. Sunohara, *Physical Review B*, 48 (1993) 2781.

[149] F. Zong, H. Ma, C. Xue, W. Du, X. Zhang, H. Xiao, J. Ma, F. Ji, *Materials Letters*, 60 (2006) 905-908.

[150] W.S. Khan, C. Cao, *Journal of Crystal Growth*, 312 (2010) 1838-1843.

[151] F. Zong, H. Ma, W. Du, J. Ma, X. Zhang, H. Xiao, F. Ji, C. Xue, *Applied Surface Science*, 252 (2006) 7983-7986.

[152] T. Yang, Z. Zhang, Y. Li, M. Lv, S. Song, Z. Wu, J. Yan, S. Han, *Applied Surface Science*, 255 (2009) 3544-3547.

[153] Y. Du, A. Ji, L. Ma, Y. Wang, Z. Cao, *Journal of Crystal Growth*, 280 (2005) 490-494.

[154] G. Yue, P. Yan, J. Liu, M. Wang, M. Li, X. Yuan, *Journal of Applied Physics*, 98 (2005) 103506.

[155] W.S. Khan, C. Cao, D.Y. Ping, G. Nabi, S. Hussain, F.K. Butt, T. Cao, *Materials Letters*, 65 (2011) 1264-1267.

[156] R.C. Weast, CRC Handbook of Chemistry and Physics, The Chemical Rubber Company, Cleveland, Ohio, 1971.

[157] H. Wu, W. Chen, *Journal of the American Chemical Society*, 133 (2011) 15236-15239.

[158] P.N. Taylor, M.A. Schreuder, T.M. Smeeton, A.J. Grundy, J.A. Dimmock, S.E. Hooper, J. Heffernan, M. Kauer, *Journal of Materials Chemistry C*, 2 (2014) 4379-4382.

[159] R. Ahumada-Lazo, S.M. Fairclough, S.J. Hardman, P.N. Taylor, M.A. Green, S.J. Haigh, R. Saran, R. Curry, D.J. Binks, *ACS Applied Nano Materials*, (2019).

[160] G. Paniconi, Z. Stoeva, R.I. Smith, P.C. Dippo, B.L. Gallagher, D.H. Gregory, *Journal of Solid State Chemistry*, 181 (2008) 158-165.

[161] V. Kambilafka, P. Voulgaropoulou, S. Dounis, E. Iliopoulos, M. Androulidaki, V. Šály, M. Ružinský, E. Aperathitis, *Superlattices and Microstructures*, 42 (2007) 55-61.

[162] P. Xi, Z. Xu, D. Gao, F. Chen, D. Xue, C.-L. Tao, Z.-N. Chen, *RSC Advances*, 4 (2014) 14206-14209.

[163] R. Sithole, L. Machogo, M. Airo, S. Gqoba, M.J. Moloto, P. Shumbula, J. van Wyk, N. Moloto, *New Journal of Chemistry*, (2018).

[164] Z.-Q. Liang, T.-T. Zhuang, A. Seifitokaldani, J. Li, C.-W. Huang, C.-S. Tan, Y. Li, P. De Luna, C.T. Dinh, Y. Hu, *Nature Communications*, 9 (2018).

[165] D. Barman, S. Paul, S. Ghosh, S.K. De, *ACS Applied Nano Materials*, (2019).

[166] S. Mondal, C.R. Raj, *The Journal of Physical Chemistry C*, 122 (2018) 18468-18475.

[167] J. Choi, E.G. Gillan, *Inorganic Chemistry*, 44 (2005) 7385-7393.

[168] S. Li, W. Cheng, L. Yan, C. Xu, N. Zhu, Z. Zhang, W. Li, S. Yu, *Inorganic and Nano-Metal Chemistry*, 49 (2019) 51-55.

[169] A. Egeberg, L. Warmuth, S. Riegsinger, D. Gerthsen, C. Feldmann, Chemical Communications, 54 (2018) 9957-9960.

[170] R. Deshmukh, G. Zeng, E. Tervoort, M. Staniuk, D. Wood, M. Niederberger, *Chemistry of Materials*, 27 (2015) 8282-8288.

[171] T. Nakamura, H. Hayashi, T. Ebina, *Journal of Nanoparticle Research*, 16 (2014) 2699.

[172] T. Nakamura, N. Hiyoshi, H. Hayashi, T. Ebina, *Materials Letters*, 139 (2015) 271-274.

[173] C. Panda, P.W. Menezes, M. Zheng, S. Orthmann, M. Driess, *ACS Energy Letters*, 4 (2019) 747-754.

[174] G.R. Bamwenda, S. Tsubota, T. Nakamura, M. Haruta, *Journal of Photochemistry and Photobiology A: Chemistry*, 89 (1995) 177-189.

[175] J. Shaikh, N. Patil, V. Shinde, V. Gaikwad, *Journal of Microbiology and Biochemistry Technology*, 8 (2016) 428-432.

[176] A. Pandey, P. Singh, L. Iyengar, *International Biodeterioration & Biodegradation*, 59 (2007) 73-84.

[177] E. Engel, H. Ulrich, R. Vasold, B. König, M. Landthaler, R. Süttinger, W. Bäumler, *Dermatology*, 216 (2008) 76-80.

[178] T. Yahagi, M. Degawa, Y. Seino, T. Matsushima, M. Nagao, T. Sugimura, Y. Hashimoto, *Cancer Letters*, 1 (1975) 91-96.

[179] T. Robinson, G. McMullan, R. Marchant, P. Nigam, *Bioresource Technology*, 77 (2001) 247-255.

[180] G. Ghadimkhani, N.R. de Tacconi, W. Chanmanee, C. Janaky, K. Rajeshwar, *Chemical Communications*, 49 (2013) 1297-1299.

[181] M. Janczarek, E. Kowalska, *Catalysts*, 7 (2017) 317.

[182] X. Lan, L. Wang, B. Zhang, B. Tian, J. Zhang, *Catalysis Today*, 224 (2014) 163-170.

[183] K. Nohara, H. Hidaka, E. Pelizzetti, N. Serpone, *Journal of Photochemistry and Photobiology A: Chemistry*, 102 (1997) 265-272.

[184] J. Trawiński, R. Skibiński, *Environmental Science and Pollution Research*, 24 (2017) 1152-1199.

[185] A.V. Borhade, D.R. Tope, B.K. Uphade, *Journal of Chemistry*, 9 (2012) 705-715.

[186] L.V. Trandafilović, D.J. Jovanović, X. Zhang, S. Ptasińska, M. Dramićanin, *Applied Catalysis B: Environmental*, 203 (2017) 740-752.

[187] F. Jamali-Sheini, R. Yousefi, N.A. Bakr, M. Cheraghizade, M. Sookhakian, N.M. Huang, *Materials Science in Semiconductor Processing*, 32 (2015) 172-178.

[188] Y. Li, X. Li, J. Li, J. Yin, *Water research*, 40 (2006) 1119-1126.

[189] R. Kumar, G. Kumar, A. Umar, *Materials Letters*, 97 (2013) 100-103.

[190] A. Houas, H. Lachheb, M. Ksibi, E. Elaloui, C. Guillard, J.-M. Herrmann, *Applied Catalysis B: Environmental*, 31 (2001) 145-157.

[191] M.A. Rauf, M.A. Meetani, A. Khaleel, A. Ahmed, *Chemical Engineering Journal*, 157 (2010) 373-378.

[192] H. Lachheb, E. Puzenat, A. Houas, M. Ksibi, E. Elaloui, C. Guillard, J.-M. Herrmann, *Applied Catalysis B: Environmental*, 39 (2002) 75-90.

[193] T. Aarthi, P. Narahari, G. Madras, *Journal of Hazardous Materials*, 149 (2007) 725-734.

[194] R. Cao, H. Yang, X. Deng, S. Zhang, X. Xu, *Scientific Reports*, 7 (2017) 15001.

[195] F. Chen, Z. Deng, X. Li, J. Zhang, J. Zhao, *Chemical Physics Letters*, 415 (2005) 85-88.

[196] S. Yan, Z. Li, Z. Zou, *Langmuir*, 26 (2010) 3894-3901.

[197] Y.-H. Chiu, T.-F.M. Chang, C.-Y. Chen, M. Sone, Y.-J. Hsu, *Catalysts*, 9 (2019) 430.

[198] M. Saranya, R. Ramachandran, P. Kollu, S.K. Jeong, A.N. Grace, *RSC Advances*, 5 (2015) 15831-15840.

[199] Z. Jiang, F. Yang, G. Yang, L. Kong, M.O. Jones, T. Xiao, P.P. Edwards, *Journal of Photochemistry and Photobiology A: Chemistry*, 212 (2010) 8-13.

[200] M.C. Das, H. Xu, Z. Wang, G. Srinivas, W. Zhou, Y.-F. Yue, V.N. Nesterov, G. Qian, B. Chen, *Chemical Communications*, 47 (2011) 11715-11717.

[201] D. Barman, S. Paul, S. Ghosh, S.K. De, *ACS Applied Nano Materials*, 2 (2019) 5009-5019.

[202] K. Li, N.J. Hogan, M.J. Kale, N.J. Halas, P. Nordlander, P. Christopher, *Nano Letters*, 17 (2017) 3710-3717.

[203] J. Yang, Y. Guo, W. Lu, R. Jiang, J. Wang, *Advanced Materials*, 30 (2018) 1802227.

Chapter 3

Synthesis and Characterization of Cu_3N and Zn_3N_2 Nanoparticles: The Search for an Ideal Precursor

Abstract

Pyrrolylaldiminato Schiff-base complexes are potentially good single-source precursors in the synthesis of metal nitride nanoparticles as both the metal and nitrogen atoms are found in one molecule. As-synthesized pyrrole-imine ligand was used to synthesize bis-2-pyrrolylaldiminato Cu and Zn complexes, $[(C_4H_3N)CH=N-(C_3H_7)]_2Cu$ (PPC) and $[(C_4H_3N)CH=N-(C_3H_7)]_2Zn$ (PPZ) respectively. Thermolysis of the Cu complex using colloidal, microwave and chemical vapor deposition (CVD) methods resulted in the formation of Cu_3N nanoparticles (NPs), a mixture of Cu_3N-Cu_2O NPs and Cu NPs respectively. In the case of the Zn complex, only ZnO was obtained using the three methods of synthesis hence further studies had to done using $Zn(NO_3)_2.H_2O$ and zinc powder as other sources of Zn. The outcomes revealed that the zinc powder was the best precursor in the synthesis of Zn_3N_2 nanomaterials using CVD as a method of synthesis.

Keywords: Cu_3N nanoparticles; Zn_3N_2 nanoparticles; single-source precursor synthesis

1. Introduction

Nanosynthesis using single-source precursors is fast gaining momentum due to the relative ease of obtaining fine nanoparticles (NPs) with diverse applicability [1-4]. This method of synthesis is desirable as only one precursor offers all the required elemental components to form the NPs. In this manner, addition of precursors to the reaction flask is avoided hence limiting chances of introducing undesirable species such as oxygen from the atmosphere. In the synthesis of metal nitride NPs such as Cu_3N and Zn_3N, oxidation easily occurs in the presence of oxygen yielding oxides instead of the desired nitrides [5, 6]. After Juza and Hahn pioneered the synthesis of Cu_3N and Zn_3N_2 in 1938 and 1940 respectively [7, 8], the study of these nitrides remained dormant for about half a century. However, due to their interesting properties, they have attracted much attention in recent years. The chemical composition of both nitrides is made up of inexpensive earth-abundant elements that are non-toxic. The crystal structures of both Cu_3N and Zn_3N are depicted in Fig. 1 below.

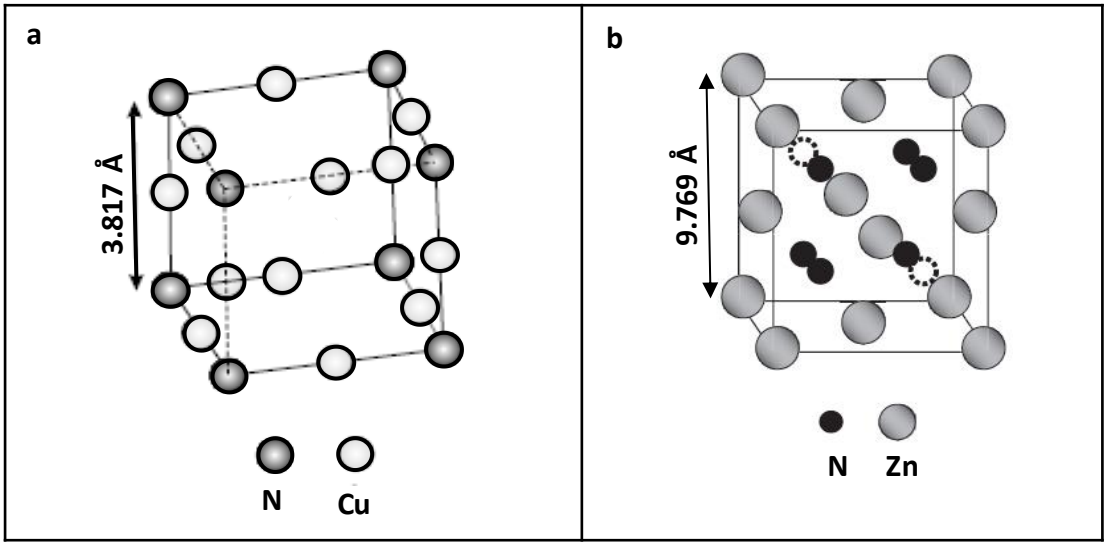

Fig. 1: Adapted crystal lattice structures of (a) Cu_3N [9] and (b) Zn_3N_2 [10]

Powder Zn_3N_2 is black in color and manifests an anti-scandium oxide (Sc_2O_3) cubic structure [11] whilst Cu_3N powder is deep red and of anti-rhenium trioxide (ReO_3) cubic structure [12, 13]. Copper (I) nitride is a promising material in catalysis [14], integrated high speed circuits [15], solar energy [16] and optical storage devices [17]. Zn_3N_2 has been explored in Li-ion batteries [18] and optoelectronics [19] due to its high electrical conductivity and high electron mobility. The properties of these metal nitrides are not well established. Literature has reported band gaps of Zn_3N_2 NPs from 0.9 [20] to 3.36 [20] eV and of Cu_3N ranging from 0.13 [21] to 2.06 eV [22]. Although Cu_3N has been reported as stable [23], Yue et al. [24] described Cu_3N films as unstable and upon decomposition at 200 °C in an inert atmosphere, nitrogen was reemitted leaving behind copper. On the other hand, Zn_3N_2 has been reported to be generally unstable with decreasing stability as temperature increases [25] and Zong *et al.* [26] demonstrated that zinc nitride is stable in air at temperatures that are below 500 °C. Furthermore, another study [25] revealed that Zn_3N_2 is highly reactive, hence it easily oxidizes when exposed to air resulting in the formation of ZnO. Cu (I) compounds are known to disproportionate when exposed to air and water to form copper oxide and Cu. Therefore, in order to minimize or eliminate oxidation, this study focused on the use of single-source precursors in synthesizing copper and zinc nitride nanoparticles. This was achieved by thermal decomposition of single-source precursors using colloidal, microwave-assisted and chemical vapour deposition synthetic methods.

These methods of synthesis have proven to be highly efficient in synthesizing various nanoparticles. Colloidal synthetic routes tend to offer a better way of controlling properties. The desired morphology, electrical and optical properties can be obtained by carefully varying time, temperature and organic ligands (which may act as solvents, capping agents or reducing agents).

A very successful colloidal synthesis was reported in 2011 [14] where Cu_3N nanocubes were synthesized in organic solvents using copper (II) nitrate as a precursor [27]. The synthesized nanocubes had edges of about 26 nm with a direct band gap of 1.5 eV. Variation in the organic solvent resulted in production of nanoparticles with different sizes. Nakamura et al. [28], used copper (II) acetate in different alcohols at temperatures between 130 and 200 °C to obtain Cu_3N. A few accounts of the colloidal synthesis of Zn_3N_2 have been reported using alkyl metal and ammonia as precursors [29, 30].

The success of using the microwave-assisted method depends on the ability of absorption of microwave energy by the reagents and converting it to heat. This method poses a number of advantages in that instant contactless, direct and even dielectric heating of reagents is achieved without heating the reaction vessel [31]. Other positive aspects of this method include the incredible decrease in reaction times and good yields with minimal impurities compared to other methods of synthesis. Microwave synthesis of nanoparticles using single-source precursors has been reported [32] and this method has proven to be very successful in the production of metal oxide [33] and chalcogenide [34] nanoparticles. Very few reports have been published on the microwave assisted synthesis of metal nitride nanoparticles [35] and to the best of our knowledge, no literature has reported on the microwave synthesis of Cu_3N NPs.

Chemical vapor deposition (CVD) usually involves one or more volatile precursors that react or decompose resulting in the deposition of a solid product [36]. This procedure generally involves a reactive gas that is transported and adsorbs onto a hot surface resulting in decomposition and subsequent reaction that leads to the formation of desired products. Undesirable products desorb

and are transported out of the reaction chamber. As such, high purity samples are usually obtained using this method at high deposition rates without employing high vacuum conditions. Although, it is popularly used in fabrication of thin films, this method can be used to obtain solid products in powder form [37]. Chemical vapor deposition of nitride NPs has been demonstrated in previous reports. Fallberg *et al.* [38] showed the application of this method in synthesizing Cu_3N and the synthesis of Zn_3N_2 was demonstrated by Wei *et al.* [39]. Herein, the evaluation of the as-synthesized Schiff-base Cu and Zn complexes as single-source precursors in the synthesis of Cu_3N and Zn_3N_2 were studied. Furthermore, the study also embarked on investigating the use of $Zn(NO_3)_2$ and Zn powder as alternative sources of zinc.

2. Experimental Section

2.1. Materials

Cu (II) acetate monohydrate ($Cu(CH_3COO)_2{\cdot}H_2O$) (puriss p.a., 99.0%), diethylzinc ($Zn(C_2H_5)_2$) (1.0 M in hexanes), pyrrole-2-carboxaldehyde (98%), n-propylamine (99.0%), acetic acid (g;acial, ReagentPlus 99%), octadecylamine (ODA) (99%), tetrahydrofuran (THF, spectroscopic grade), zinc (II) acetate dihydrate ($Zn(CH_3COO)_2.2H_2O$) (puriss p.a. 99.0%), zinc nitrate hexahydrate ($Zn(NO_3)_2.6H_2O$) (purum, p.a. 99%), $MgSO_4$ (puriss p.a. drying agent, anhydrous 98.0%), NaH (dry, 98%), C, tetramethylsilane (TMS) (analytical standard) and $CDCl_3$ (100%, 99.96 atom % D) were purchased from Sigma-Aldrich. Dichloromethane (anhydrous, 99.8%), n-hexane (puriss, p.a., ACS reagent, 99%), heptane (anhydrous, 99%) and ethanol (absolute, ≥99.8% (GC)) were obtained from SAARCHEM®. Purification of THF and diethyl ether was performed by distillation in sodium-benzophenone and were immediately used.

2.1 Synthesis of ligand

2.1.1 Synthesis of 2-pyrrolylaldpropylimine ligand (PP)

In a two-necked round bottom flask, 2-pyrrolecarboxaldehyde (2.13 g, 22.37 mmol) was dissolved in dry diethyl ether (30 mL). Propylamine (1.85 ml, 22.38 mmol) was injected into the reaction mixture, followed by addition of glacial acetic acid (0.01 mL). The reaction mixture was stirred at room temperature and maintained under nitrogen gas flow for 8 h. The solvent was removed using a rotary evaporator and the product was dissolved in dichloromethane (30 mL) and successively purified with water (5 x 30 mL) in a separatory funnel. The water was decanted off and the remaining organic layer was dried using anhydrous $MgSO_4$. Finally, the product was dried *in vacuo* yielding a yellow liquid and stored for characterization.

Yield 2.77 g (91%), FTIR-ATR (cm^{-1}) *ν*(C=N) = 1635, ^{1}H NMR (300 MHz, $CDCl_3$): δ (in ppm) = 0.96 (t, 3H, *J* = 7.4 Hz), 1.69 (q, 2H, *J* = 7.2 Hz), 3.56 (t, 2H, *J* = 6.9, 1.3 Hz), 6.27 (dd, 1H, *J* = 3.6, 2.5 Hz); 6.55 (dd, 1H, *J* = 3.7, 1.5 Hz); 6.85-6.97 (m, 1H), 8.11 (s, 1H,) and 10.82 (s, 1H). ^{13}C NMR (75 MHz, $CDCl_3$) δ (in ppm) = 11.88 (C_9, aliphatic CH_3), 24.36 (C_8, CH_3CH_2), 62.12 (C_7, NCH_2) and (CH_2), 110.11 (C_5); 115.28 (C_4); 122.85 (C_3), (pyrrole CH) and 151.68 (C_6, HC-N) and HRMS (ESI) m/z $[M+H]^+$ = 137.11 calculated for $C_8H_{12}N_2$.

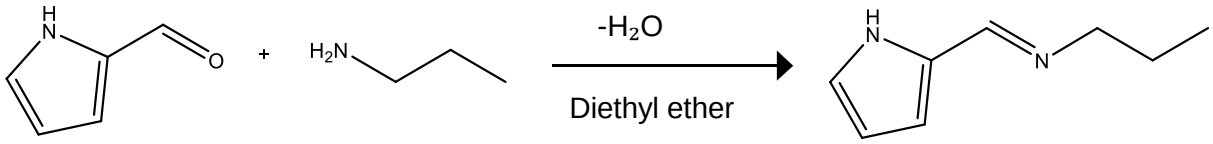

Scheme 1: Reaction scheme for the synthesis of 2-pyrrolylaldpropylimine ligand (PP).

2.2. Synthesis of Schiff-base Complexes

2.2.1 Synthesis of bis(2-pyrrolylaldpropyliminato) Cu (II) complex

In a Schlenk flask, an excess amount of NaH (0.50 g, 20.84 mmol) was washed three times using dry hexane (10 mL) and dried under vacuum. Dry THF (35 mL) was injected to dissolve the NaH, followed by addition of 2-pyrrolylaldpropylimine (2.36 g, 17.33 mmol) dissolved in dry THF (15 mL) giving a pinkish-red coloration with effervescence. The mixture was stirred for 30 min under nitrogen gas flow and filtered under vacuum with the filtrate being transferred into a flask containing dry ($Cu(CH_3COO)_2$) (1.57 g, 8.67 mmol) resulting in a greyish-black mixture, which was stirred under nitrogen for 12 h at room temperature. The solvent was removed using a rotary vapor resulting in a deep green solid which was dissolved in CH_2Cl_2 and filtered under vacuum to afford a dark green residue and a black filtrate. The black filtrate was concentrated by evaporation to obtain a black solid with a yield of 2.59 g. Recrystallization was performed using two different procedures. 1.0 g of the black solid was dissolved in hot heptane and cooled to 5 °C for 1 h forming small black crystals. Three portions of cold hexane (3 mL each) were used to quickly wash the crystals, which were then dried under vacuum to obtain relatively small shiny black crystals of bis(2-pyrrolylaldpropyliminato) copper(II) (PPC). In the second procedure, 1.0 g of the black solid was recrystallized using a mixture of CH_2Cl_2:C_2H_5OH in a ratio of 1:3 at -20 °C for 21 days and shiny black crystals of PPC were obtained.

The yield of analytically pure complex was 1.71 g (59%). Microanalysis for $C_{16}H_{22}N_4Cu$: Calculated (%), C 57.55, H 6.69, N 16.78, found C 57.36, H 6.91, N 16.58; FT-IR (cm^{-1}), ν(C=N) = 1584; ESI-MS m/z$[M+H]^+$ found 335.10 and calculated 334.92.

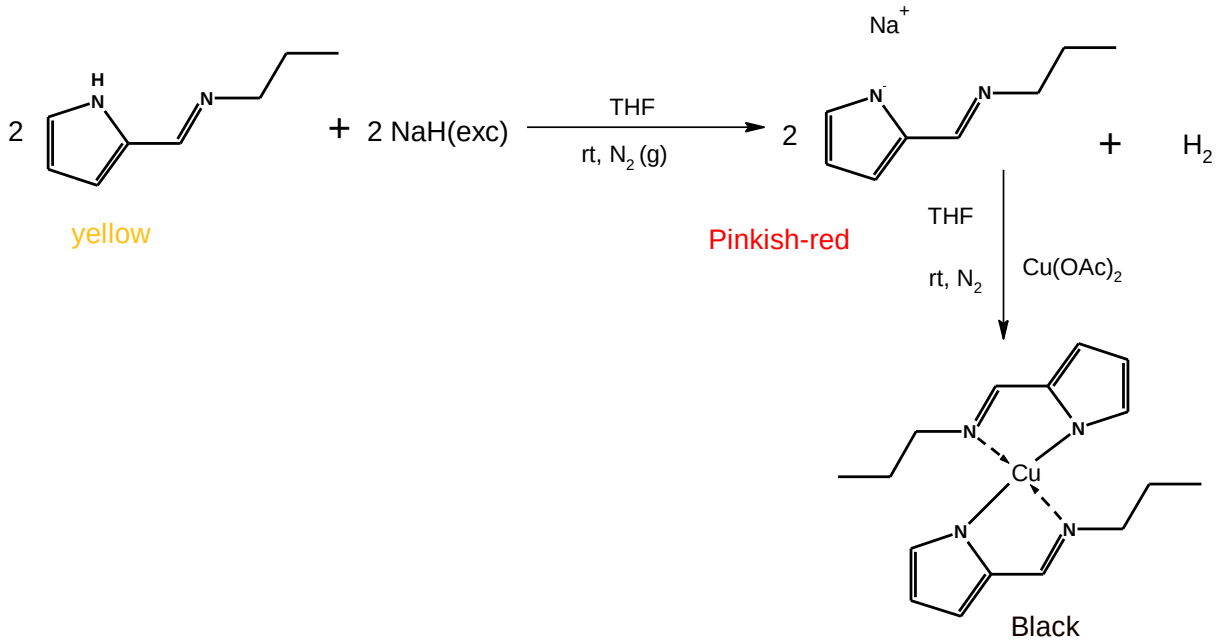

Scheme 2: Schematic representation of the synthesis of bis(2-pyrrolylaldpropyliminato) copper(II) complex (PPC) from PP Schiff-base ligand.

2.2.2 Synthesis of bis(2-pyrrolylaldpropyliminato) Zn complex (PPZ)

2-pyrrolylaldpropylimine ligand (1.00 g, 7.3 mmol) was added to dry n-hexane (20 ml) at -78 °C and stabilized before adding diethyl zinc (0.45 g, 3.7 mmol) dissolved in dry n-hexane (20 mL). The mixture was slowly warmed to room temperature and stirred for 2 h under continuous N_2 gas flow. The product was dried under vacuum to give an orange liquid.

Yield 1.08 g, 88%, FTIR-ATR (cm^{-1}) ν(C=N) = 1635, ^{1}H NMR (300 MHz, $CDCl_3$) δ (in ppm) 0.72-0.96 (t, 6H), 1.49 (q, 4H, J = 7.2 Hz), 3.33-3.55 (t, 4H), 6.33-6.42 (dd, 2H); 6.70-6.84 (dd, 2H); 7.04 (m, 2H) and 7.93-8.13 (s, 2H). ESI-MS m/z $[M+H]^+$ = 335.10 found and 336.78 calculated for $C_{16}H_{22}N_4Zn$.

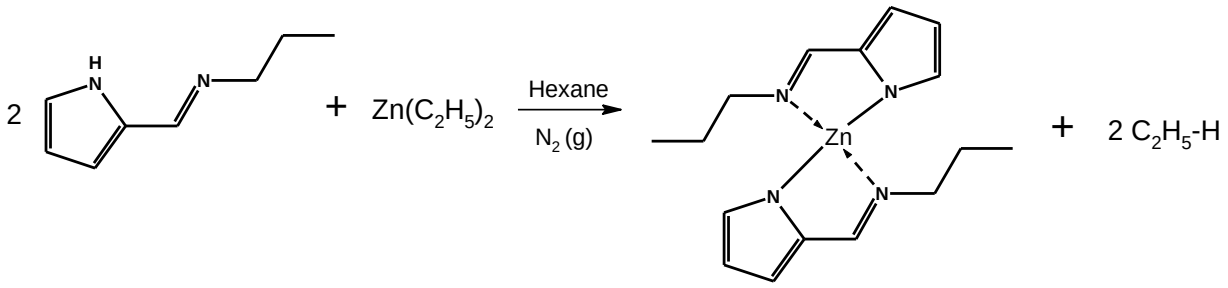

Scheme 3: Schematic representation of the synthesis of bis(2-pyrrolylaldpropyliminato) zinc(II) complex (PPC) from PP Schiff-base ligand.

2.3. Characterization techniques of Schiff-base ligand and complexes

Fourier transform infrared spectroscopy was performed on a Bruker Tensor 27 attenuated total reflectance (ATR) cell spectrophotometer. ^{1}H NMR (300MHz) and ^{13}C NMR (300 MHz) spectra were obtained on a Bruker Ultra Shield superconducting magnet spectrometer, using tetramethylsilane (TMS) as the internal standard. The NMR data was processed using MNOVA software. High resolution mass spectra were recorded on a Bruker Compact Q-TOF mass spectrometer (Bruker Daltonics, Bremen, Germany) with ESI in positive ionization mode using formic acid as matrix and a detection range of 0 – 1300 m/z. The elemental compositions (C, H and N) were measured using a Vario Elementar III microcube CHN.

2.4. Synthesis of copper nitride and zinc nitride nanoparticles

2.4.1. Colloidal Synthesis

The colloidal synthesis of Cu_3N using PPC and $Cu(NO_3)_2.3H_2O$ was reported in our previous study [1]. Following the same procedure, PPC and PPZ (0.50 mmol) were separately added to ODA (10 g) and degassed for 1 h at 115 °C. The temperature was raised to 240 °C and aliquots were

taken at predetermined time interval of 5, 10 and 20 min. The products were washed in dry ethanol under centrifugation.

2.4.2. Microwave Synthesis

PPC or PPZ (0.0625 mmol) were separately added to ODA (4.6375 mmol) in a quartz vessel in a nitrogen glovebox and left overnight to remove any traces of oxygen. The vessel was then closed tightly and was loaded into a Monowave 50 microwave. The temperature was set to 240 °C with ramping at 8 °C.min^{-1} and holding time of 5, 10 and 20 min. The temperature of the reaction mixture was adjusted to 70 °C and dry ethanol was added to flocculate the nanoparticles (NPs). The NPs were successively cleaned using ethanol under centrifugation.

2.4.3. Chemical Vapor Deposition

PPC and PPZ complexes (50 mg each) were separately placed in a quartz boat positioned at the center of a horizontal tube furnace and purged using nitrogen gas for 15 min. The reaction temperature was varied from 100 to 600 °C. The N_2 gas flow was maintained at 300 mL/min in all the reactions. In each case, the temperature was ramped up at a rate of 10 °C/min to the pre-set temperature, which was held for 4 h. At the end of each reaction, the system was allowed to cool to room temperature. To further probe the nitridation of zinc, other zinc precursors were tested. About 1 g each of $Zn(NO_3)_2$ and Zn powder were reacted with NH_3 (100 cm^3/min) at 600 °C for 4 h.

2.3. Characterization of nanoparticles

2.3.1 X-Ray Diffraction

Powder X-ray diffractograms were recorded on a Bruker D2 phaser D2-205530 diffractometer using CuKα radiation (λ=1.5418 Å) at 30 kV and 10 mA but earlier samples were analyzed using $CoK\alpha_1/K\alpha_2$ radiation (λ = 1.78897/1.79285 Å) operated at 30 kV and 10 mA. The XRD data was acquired using a Bruker Lynxeye PSD detector set to measure at 5^o 2θ and all measurements were acquired at room temperature. The data was analyzed using Bruker AXS Evaluation package (EVA, 2008) equipped with ICDD PDF 4+.

2.3.2 Raman Spectroscopy

The Raman spectra were acquired using the 514.5 nm line of a Lexel Model 95-SHG argon ion laser as the excitation source. The Raman spectrometer used was a Horiba LabRAM HR equipped with an Ar ion laser (514.5 nm/785 nm) and an Olympus BX41 microscope attachment. The incident beam was focused onto the sample using a 100x objective (N.A. = 0.90) and the backscattered light was dispersed via a 600 lines/mm grating onto a liquid nitrogen cooled CCD detector. The software used for acquisitions was LabSpec v.5. The incident beam power was fixed at ~ 0.04 mW) to minimize any possible localized heating for all the spectra, except for zinc nitride where the power was 0.4 mW. The higher power gave a better spectrum.

2.3.3 Microscopy

As-synthesized particles were dispersed in chloroform and drop-cast onto a lacey carbon grid then were studied using a FEI Spirit 120 kV transmission electron microscope (TEM) equipped with an EDX detector operated at an acceleration voltage of 200 kV with a beam spot size of 20 - 100 nm in TEM mode. The Bruker AXS Evaluation package (EVA, 2008) software was used to process the data.

3. Results and discussion

3.1 Synthesis and characterization of 2-pyrrolylaldpropylimine and its copper and zinc complexes

The 2-pyrrolylaldpropylimine (PP) ligand was synthesized via a simple condensation reaction as reported in the literature [40]. The ligand was obtained as a clear yellow liquid in a yield of 91%. The elemental analysis data agrees with the calculated value. In the IR spectrum of the ligand, the ν(N-H) of the pyrrole moiety is observed as a broad vibrational band in the region 3100- 3300 cm^{-1} as a result of intermolecular hydrogen bonding and the ν(C=N) band of the imine is observed at 1635 cm^{-1} The full assigned ^{1}H –NMR spectrum of the ligand is shown in Fig. 4 and this result is consistent with published data for this ligand [40]. In the HRMS (ESI) spectrum (Fig. S1), the molecular ion of the ligand is observed as the $[M+H]^{+}$ species at a m/z value of 137.11. The bis(2-pyrrolylaldpropyliminato) Cu (II) complex (PPC) was prepared by reacting the sodium salt of the PP ligand with copper acetate monohydrate. The complex was obtained as a black powder in a yield of 59%. Comparison of the FTIR spectra of the ligand and complex (Fig. 2) confirmed coordination via the azomethine nitrogen since a significant shift of the ν(C=N) stretching frequency from 1635 to 1586 cm^{-1} was observed. In addition, the disappearance of the ν(N-H) band confirms coordination via the nitrogen of the pyrrole ring. The molecular ion of the complex is observed as the [M+1] specie at m/z value of 334.10 (Fig. S2) and the elemental analysis data (Table S1) obtained is consistent with formation of the expected tetrahedral coordinate bis(2-pyrrolylaldpropyliminato) Cu(II) complex.

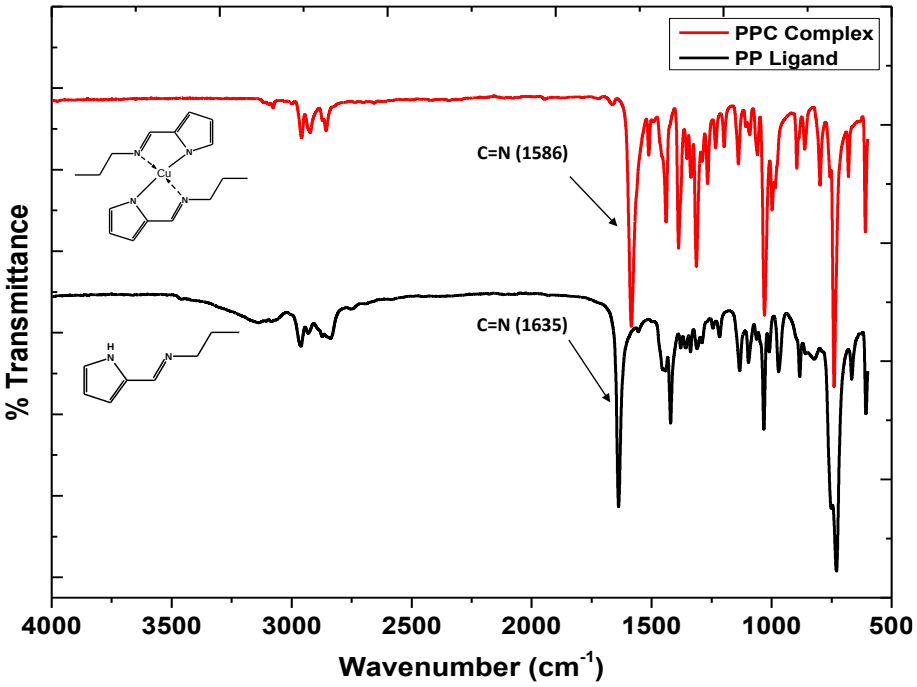

Fig. 2: FTIR spectra of the PP ligand and PPC complex.

Complexation of the PP ligand was also performed using 1 M solution of diethylzinc to yield 88% of a thick orange liquid, bis(2-pyrrolylaldpropyliminato) Zn(II) complex (PPZ). Complexation was evidenced by the chemical shift of the ν(C=N) stretching mode from 1636 cm^{-1} in the PP ligand to 1584 cm^{-1} in the formed PPZ complex as observed in Fig. 3. Also, as seen with the PPC complex, the broad ν(N-H) band in the region 1635-1586 cm^{-1} in the ligand was not detected in the PPZ complex.

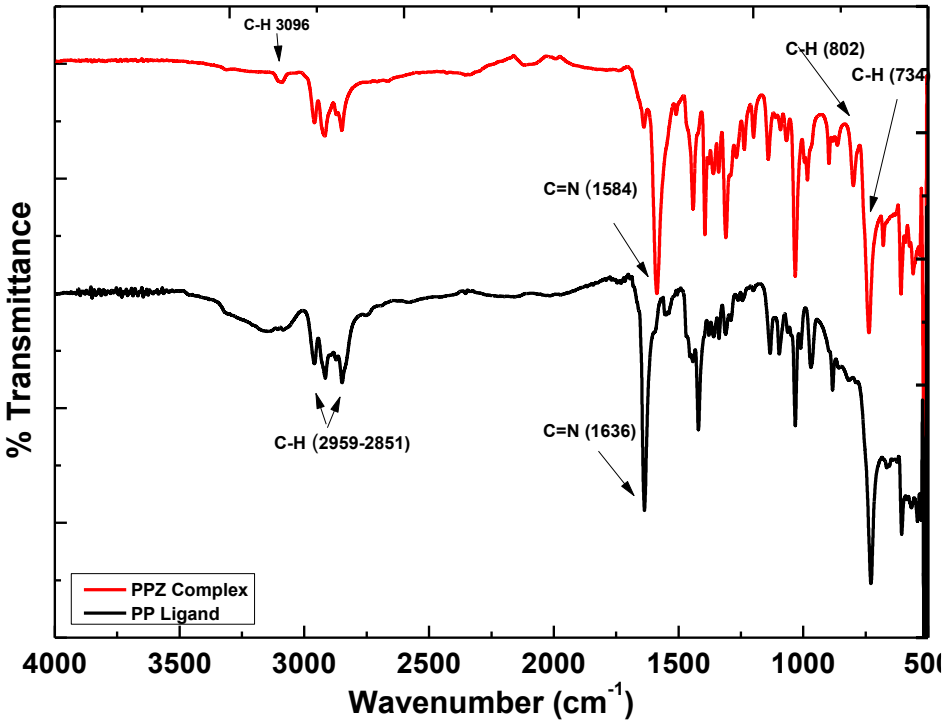

Fig. 3: FTIR spectra of the PP ligand and PPZ complex.

The HRMS spectrum of the PPZ molecular ion $[M+H]^+$ showed [M+1] m/z from 335.10 to 339.10 due to the variety of naturally occurring Zn isotopes [41] whose atomic mass numbers range from 64 to 70 . For PPZ complex bearing the ^{64}Zn isotope, the expected PPZ m/z [M] = 334.37 and hence the observed m/z $[M+H]^+$ of 335.10 in Fig. S3. The full spectra for both PPC and PPZ show a dominant peak at m/z 137.09 that corresponds to the PP ligand as a result of fragmentation [42] that occurs during ionization. Furthermore, the formation of the PPZ was confirmed using ^1H NMR, Fig. 4. As a result of coordination, the resonance signal of the proton on the imine group on C_6 showed an up-field shift from 8.11 in the ligand to 8.06 ppm in the complex. Most importantly, the PP ligand exhibits a broad H-N proton peak at δ 10.82 but due to deprotonation that occurred during complexation, this peak was not detected in the spectra of the PPZ complex.

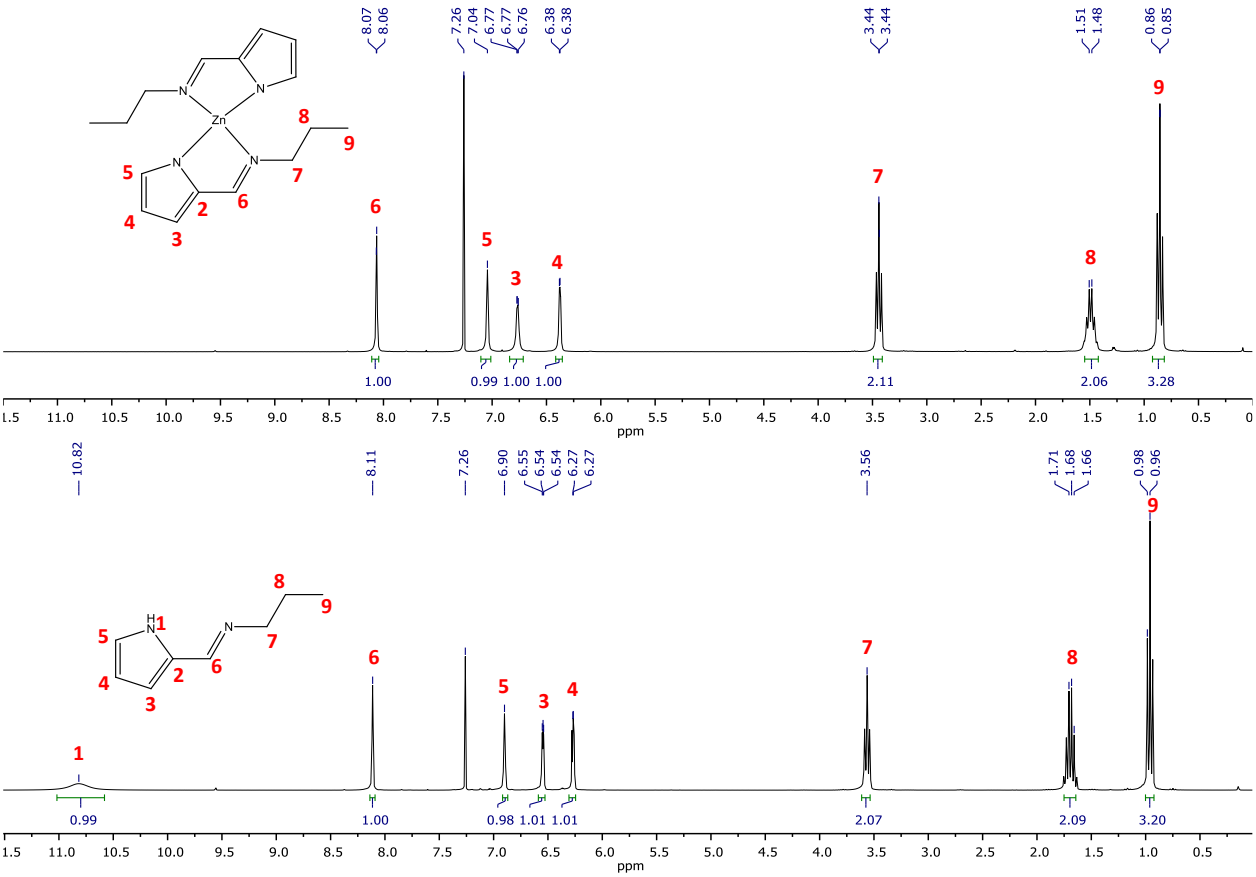

Fig. 4: ^{1}HNMR of the PP ligand and PPZ complex.

3.2 Colloidal synthesis of the nanoparticles

The colloidal method involves the decomposition of precursors (single-source or multiple sources) in a high boiling organic solvent which also acts as a capping ligand. The reactions are usually carried out under an inert atmosphere at elevated temperatures (± 300 °C). The reaction times are typically short and the method is scalable and usually produces high yields of NPs [43]. The use of capping ligands means that the surface chemistry of the NPs is modified and they in turn can be dispersed in various media for specific applications [44]. The capping ligands also stabilize the NPs, preventing agglomeration. One of the biggest advantages of colloidal synthesis is in its flexibility. The ability to change different reaction parameters in order to tune the size and shape

of the NPs obtained hence their properties. This is what makes colloidal synthesis one of the most studied synthetic procedures for NPs [45] and why it is the method of choice in this study. In the colloidal synthesis, the formation of the NPs occurs in two stages, namely the nucleation step and the growth step. The nature of the precursor, time and temperature are some of the factors that affect the formation of the NPs. Herein, both the PPC and the PPZ complexes were thermolyzed in ODA in a nitrogen atmosphere to produce Cu_3N and Zn_3N_2 NPs. The reaction temperature was set at 240 °C and aliquots were extracted after 5, 10 and 20 min. Shown in Fig. 5 are the XRD patterns of colloidal synthesized NPs. The diffraction peaks that were obtained from the thermolysis of PPC in ODA were indexed to the cubic structure of Cu_3N (PDF 00-055-0308). The Cu_3N peaks intensified with time from 5 to 20 min and the peak due to impurities at $2\theta = 24.77°$ relatively reduced in intensity. The impurity peak is associated with the degradation product of ODA and this has been reported previously [1]. Fig. 5(b) displays reflections that were obtained from thermolysis of the PPZ complex. The three diffraction patterns obtained were in agreement with hexagonal ZnO (card number PDF 01-089-1397) and no peaks corresponding to Zn_3N_2 were detected. As observed with the PPC complex, the peak intensities increased with time and they became sharper. This suggests that the crystallite sizes were becoming bigger. The peaks due to impurities that were detected around $20° < 2\theta < 30°$ in the 5 min sample were not detected in the 10 and 20 min samples of thermolysis of the PPZ complex.

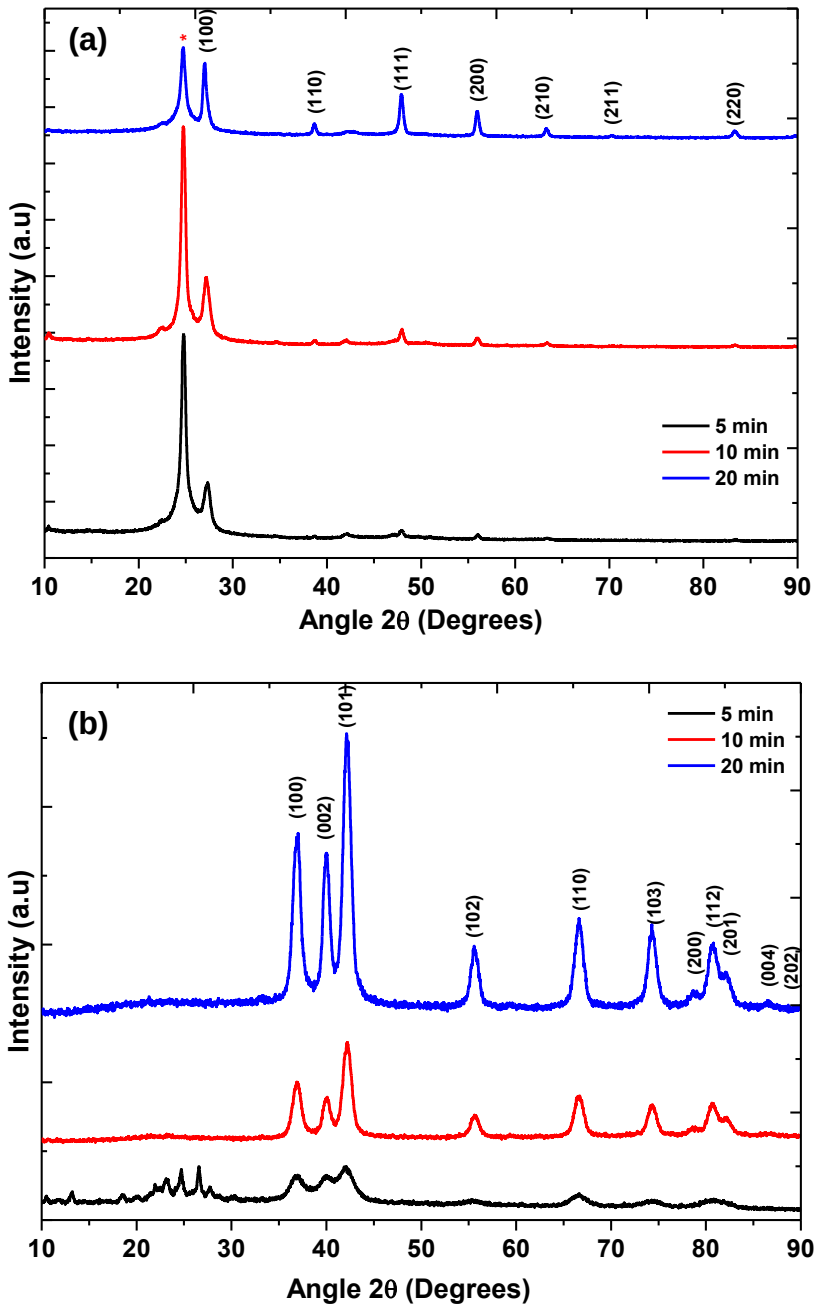

Fig. 5: X-ray diffraction patterns of the colloidal synthesis of (a) PPC derived NPs and (b) PPZ derived NPs.

To further probe the structural properties of Cu_3N, Raman spectroscopy was undertaken. The Raman spectra of Cu_3N and that of ODA are shown in Fig. 6. The crystal structure of Cu_3N belongs

to the space group O_h^1 (Pm3) where 12 phonon modes at Γ point have been predicted. Of the predicted 12 modes, nine optic modes have symmetry representations; $2F_{1u} + F_{2u}$ where the $2F_{1u}$ modes are infrared active whilst the F_{2u} modes are optically inactive [46]. This gives an overall theoretical prediction that perfect cubic Cu_3N does not manifest any first order Raman active modes. Despite these predictions, several studies have reported two peaks at 220 and 634 cm^{-1} [47] and at 275 and 610 cm^{-1} [48]. In the current study, of great importance is the broad peak at 634 cm^{-1} resembling the Raman Cu_3N signal that was obtained in previous studies [49]. This can be attributed to defects or presence of impurities in the crystals. The additional peaks are attributed to sp^2 and sp^3 hybridized carbon emanating from ODA [50]. These were confirmed by running the product of thermolyzed ODA as shown in Fig. 6(b). Two peaks were observed corresponding sp^2 and sp^3 hybridized carbon.

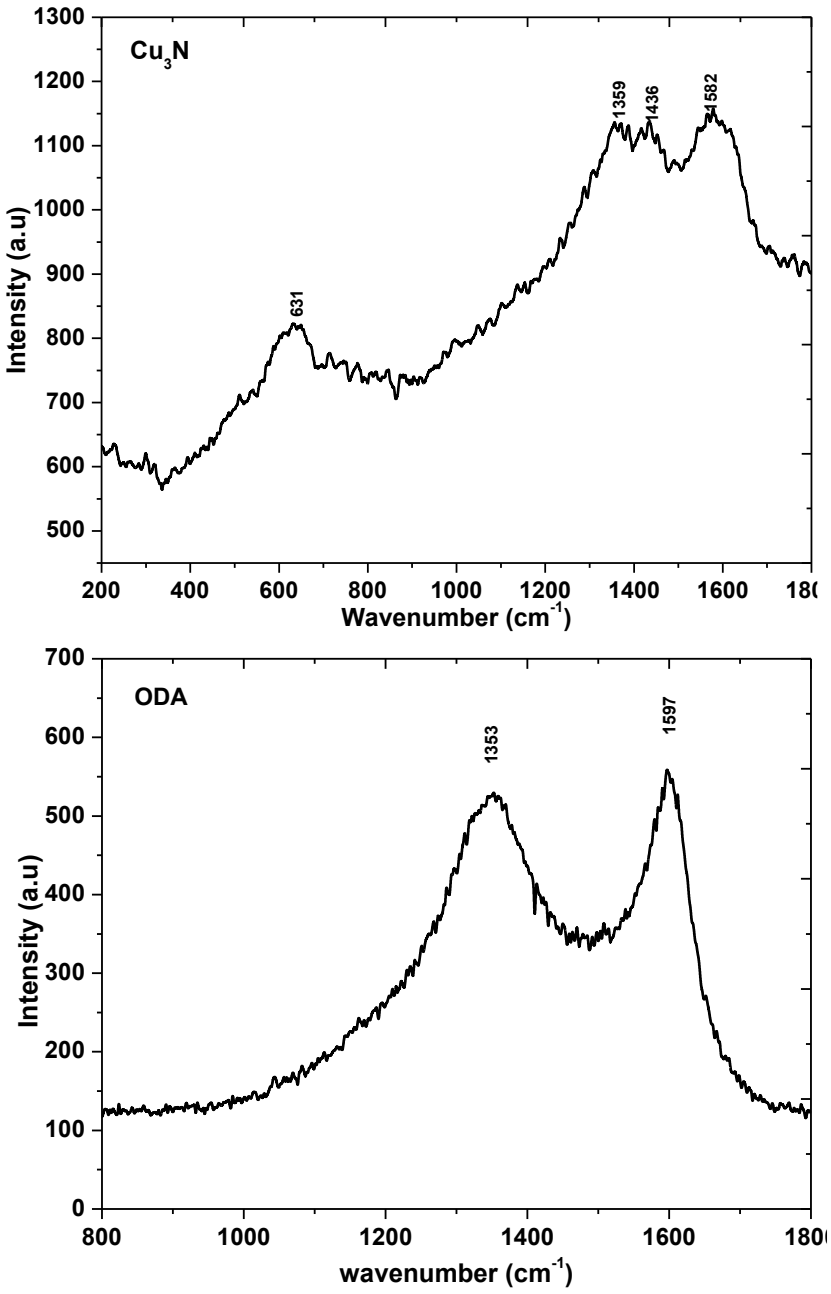

Fig. 6: Raman spectra of Cu_3N NPs and thermolyzed ODA.

Elucidation of the morphological properties of the synthesized NPs was facilitated by acquiring TEM images. The images of colloidal Cu_3N NPs show a cloud of small dot-like NPs at 5 min.

After 10 and 20 min, the dots grew bigger with time and are well-dispersed as shown in Fig. 7(a). The ZnO NPs synthesized from PPZ are shown in Fig. 7(b). The particles are agglomerated spheres and they also increase in size with time due to Ostwald ripening.

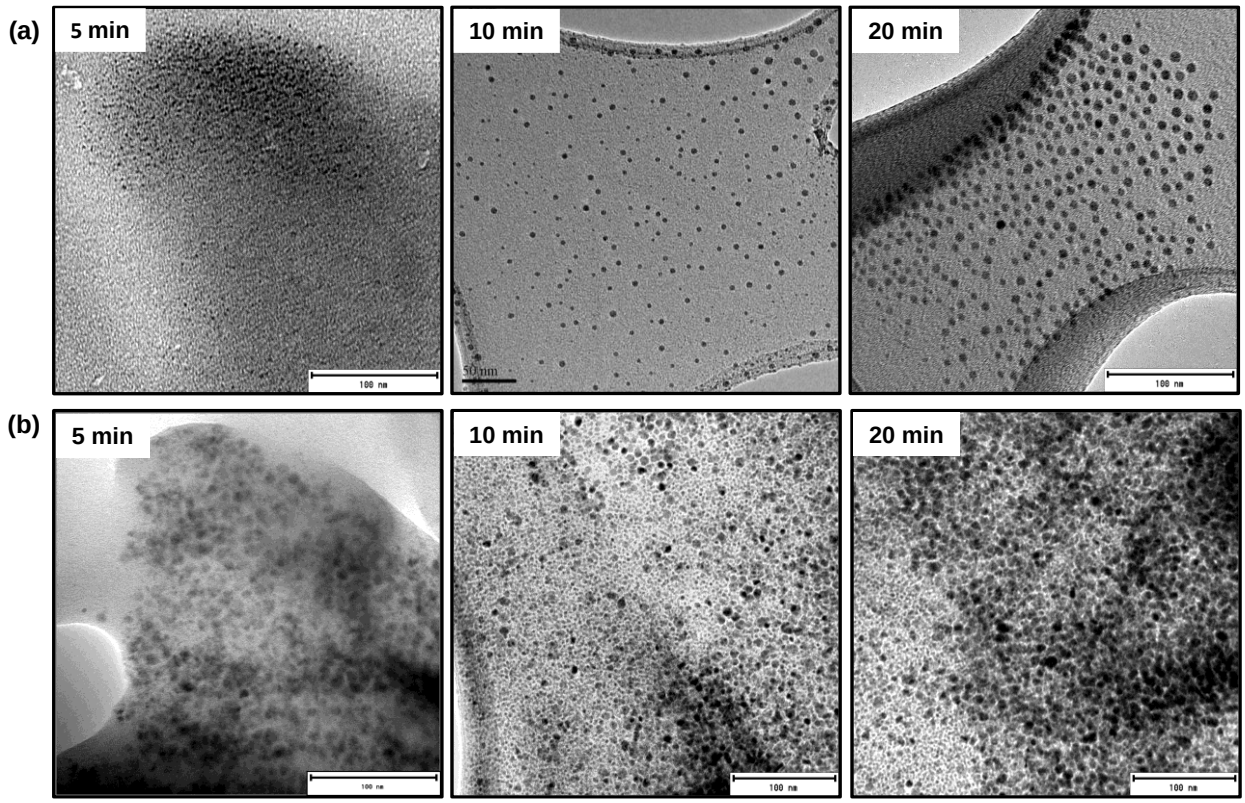

Fig. 7: TEM images of the colloidal synthesis of (a) PPC derived NPs and (b) PPZ derived NPs. (The scales are 100 nm except for 10 min which is 50 nm).

The size distribution of Cu_3N NPs synthesized in 10 min is shown in Fig. 8(a). The average size of the nanoparticles are 3.2 ± 1.3 nm. On the other hand the size distribution for ZnO NPs synthesized in 10 min is 6.8 ± 1.2 nm. The use of PPC and PPZ in the colloidal synthesis resulted in the formation of Cu_3N and ZnO NPs respectively. The decomposition of PPC resulted in Cu at +1 oxidation state. This therefore being a moderate Lewis acid, reacts readily with a moderate N^{-3}

Lewis base. On the other hand, at the set conditions, the PPZ decomposes to Zn^{+2} which is the most stable oxidation state of Zn and being a softer metal, tends to bind and react more readily with soft donor ligands such as O^{-2}. The presence of oxygen in colloidal synthesis is unavoidable even though the reaction occurs under the flow of inert gas such as N_2 or Ar due to the type of apparatus used.

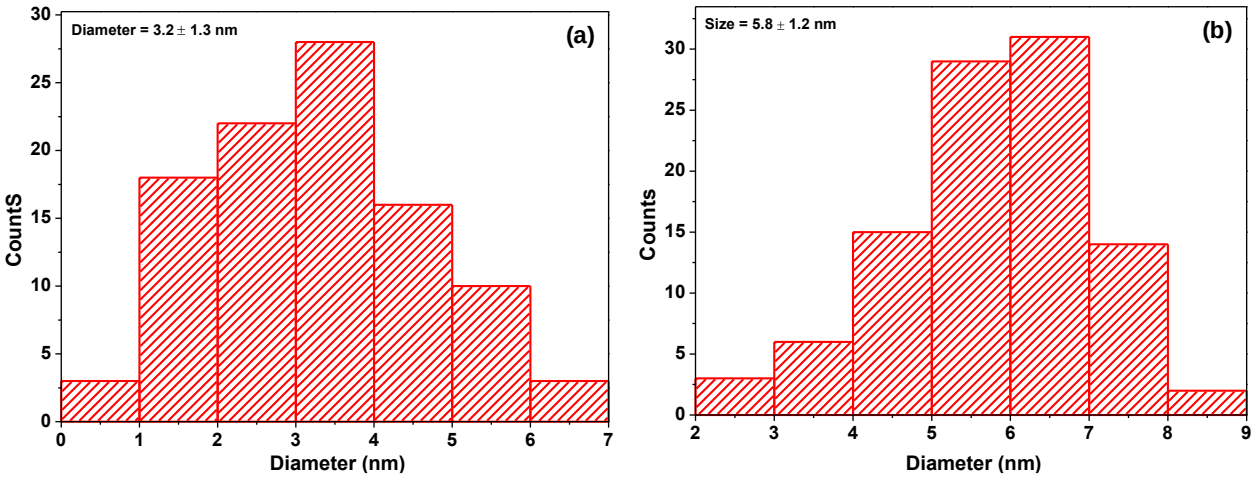

Fig. 8: Size distribution of the 10 min colloidal samples of (a) Cu_3N NPs and (b) ZnO NPs.

3.3 Microwave-assisted synthesis

In microwave-assisted synthesis, electromagnetic energy of microwaves (1 to 1000 mm) is converted to thermal energy that interacts directly with molecules without heating the reaction vessel. The synthesis of nanomaterials using microwave irradiation as an energy source to drive chemical reactions is increasingly becoming popular in nanosynthesis [45]. It has been reported to have short reaction times but with high product yields [44]. The success of this technique depends on how efficient the reaction mixture is in absorbing the microwave energy. Unlike the conventional colloidal method of synthesis, microwave synthesis allows direct, speedy and non-contact heating of reactants to temperatures that are far above the boiling point of the solvent under

atmospheric conditions. Rapid in-core volumetric heating is attained by direct interaction of electromagnetic irradiation with molecular species that are in the reaction mixture [51]. This heating phenomenon is often referred to as dielectric heating and it is effected by two main mechanisms namely; dipolar polarization and ionic conduction. In dipolar polarization, dipoles are sensitized by an external electrical field and will rotate to try and align with the field. High frequency electrical fields do not give the dipoles enough time to respond to the oscillating field hence as they try to align, the dipoles collide with each other dissipating power that generates heat in the particles. This mechanism allows electrically insulating substances to be heated through dielectric loss [52]. In the conduction mechanism, introduction of a microwave electric field induces mobile charge carriers to make forward and backward movements through the material creating an electric current. The charged particles then collide with neighboring molecules or atoms causing the material to heat up. The greater the induced current, the greater the collisions leading to greater heat being generated in the material. It is worth noting that the energy of a microwave photon is too small to break a bond, making it impossible to induce a chemical reaction [53] hence microwave based synthesis is powered by the heat that is generated. In cases where an electrolyte is distributed in a non-conducting material, polarization and conduction mechanisms of heating can occur concurrently as dipoles and mobile charge carriers in the reaction mixture oscillate in a bid to align with the electric field.

In the current study, the PPC and PPZ complexes were dissolved in ODA and the mixtures were heated in a microwave. Shown in Fig. 9 are the XRD patterns of microwave synthesized nanoparticles using PPC and PPZ as precursors. The analysis of the XRD diffraction pattern of the PPC derived NPs that was obtained after 5 min shows peaks that can be indexed to the cubic phase

of Cu_3N (PDF-1088). Additionally, a small peak was detected at $2\theta = 42.41°$ and it intensified as time progressed to 20 min. This peak and other peaks that emerged (indicated with (*) in Fig. 9(a) matched the peaks of Cu_2O (JCPDS no. 05-0667). The intensity of Cu_3N peaks decreased with time whilst the Cu_2O intensified and this can be explained by the replacement of N_2 (g) by O_2 (g) as time progresses in the reaction vessels. This is due to the fact that no constant nitrogen flow is provided in the microwave synthesis. The reaction vessel is purged with nitrogen prior to synthesis and sealed however, as time proceeds; it is possible that there is a change in the reaction atmosphere. Although pure phase Cu_3N was not obtained, we have demonstrated that the microwave method of synthesis can be employed to synthesize Cu_3N NPs if inert conditions are maintained. To the best of our knowledge, there is no report that has demonstrated the microwave synthesis of Cu_3N NPs. The microwave synthesis of PPZ derived NPs yielded ZnO NPs (card number, PDF 01-089-1397) as was the case with the colloidal synthesis and no peaks could be matched to Zn_3N_2 (Fig, 9(b)).

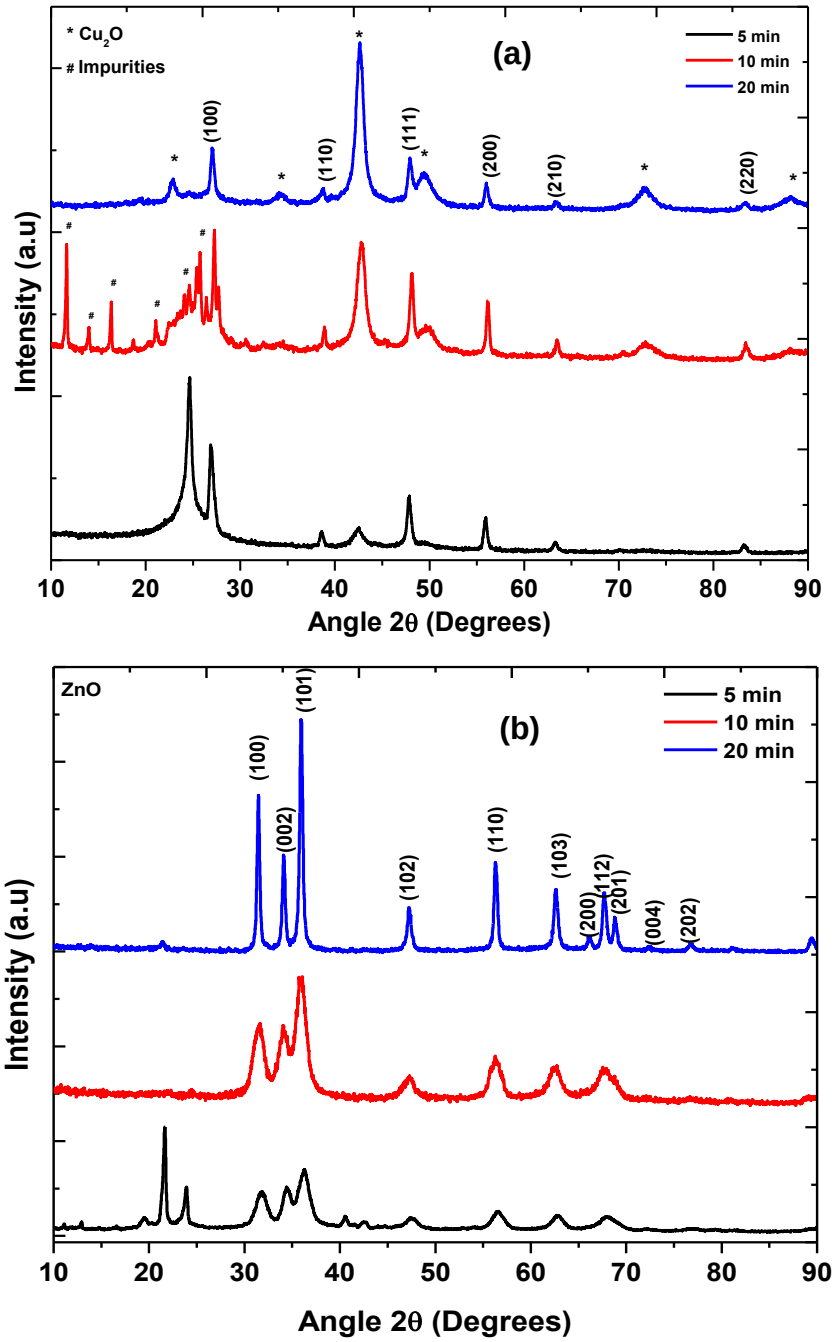

Fig. 9: X-ray diffraction of the microwave synthesis of (a) PPC derived NPs and (b) PPZ derived NPs.

The morphologies of the particles are shown in Fig. 10. Well-dispersed near spherical NPs were obtained after 5 min of microwave irradiation for the PPC derived NPs as depicted in Fig. 10(a). From XRD analysis, this sample consisted mainly of Cu_3N with a bit of Cu_2O impurities. The particles grew in size and showed polydispersity at 10 min with the majority of the particles having a near-spherical shape whilst others had a shape that is undefined. A mixed morphology of small spherical and relatively big nanocubes was obtained for the 20 min sample. A cluster of agglomerated ZnO particles was observed after 5 min. This developed into a network of particles after 10 min and clustered rod-like NPs after 20 min as depicted in Fig. 10(b).

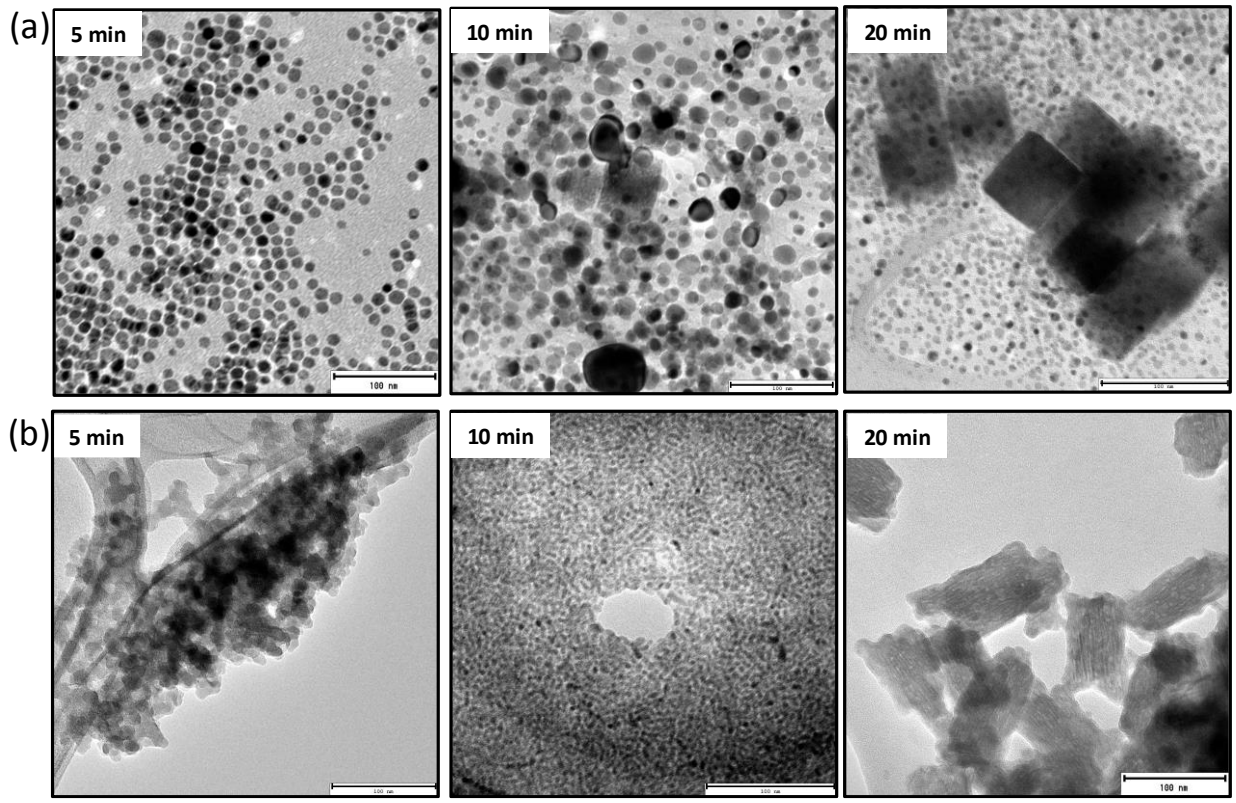

Fig. 10: TEM images of the microwave synthesis of (a) PPC derived NPs and (b) PPZ derived NPs. (All scale bars were set at 100 nm).

3.4 CVD Synthesis

The CVD process involves the dissociation and/or chemical reaction of gaseous reactants in an activated environment (e.g. heat, plasma, light etc.) to produce high-purity materials [54]. The process first involves the generation and transport of an active gaseous reactant species to a reaction chamber by an inert carrier gas where the substrate is located. These gaseous species react in the gas phase and produce intermediates [55]. At temperatures below dissociation, diffusion across the boundary layer (the hot zone above the substrate) occurs. The intermediates are absorbed on the surface of the substrate where they subsequently diffuse to growth sites, react and nucleate to produce epitaxial thin-films [56]. The volatile by-products are transported to the exhaust. Herein, PPC and PPZ were initially used as the single-source precursors. Fig. 11 (a) shows the XRD patterns for particles emanating from the PPC complex. The diffraction pattern obtained for the 100 °C sample showed resemblance of the PPC complex hence no decomposition was observed. When the PPC complex was heated at 150 °C, very broad peaks at 11.32° and 24.79° were observed in the diffraction pattern which suggests the formation of an amorphous material. Increasing the temperature to 300 °C brought about the emergence of new peaks at 50.57° and 59.24° which intensified at 600 °C and could be indexed to the (111) and (210) peaks of Cu (JCP2.2CA:00-085–1326). In the CVD synthesis, no diffraction peaks could be associated with the Cu_3N crystal structure. Powder XRD analysis of the products of heating PPZ using the CVD method showed reflections that correspond to pure ZnO (PDF 01-089-1397) in all samples as shown in Fig. 11(b).

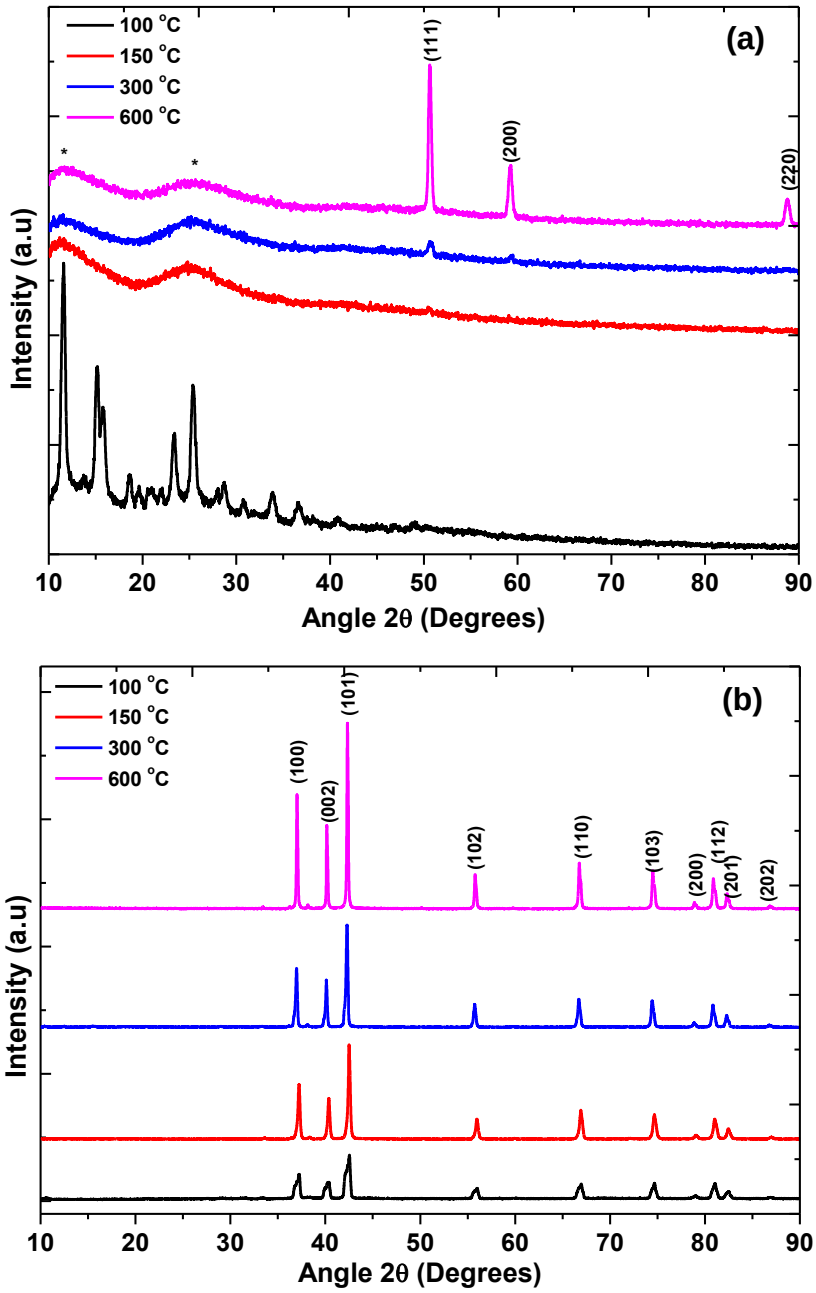

Fig. 11: X-ray diffraction of the CVD synthesis of (a) PPC derived NPs and (b) PPZ derived NPs.

The TEM images of the PPC derived NPs are shown in Fig. 12(a). The particles synthesized at 100 °C are small crystallites. As the temperature is increased the particles agglomerate and

ultimately at 600 °C, large particles with cube and rod-like morphology were formed. The morphologies of the PPZ derived particles are small agglomerates at 100 °C. These become larger and denser as the temperature is increased (Fig. 12(b)).

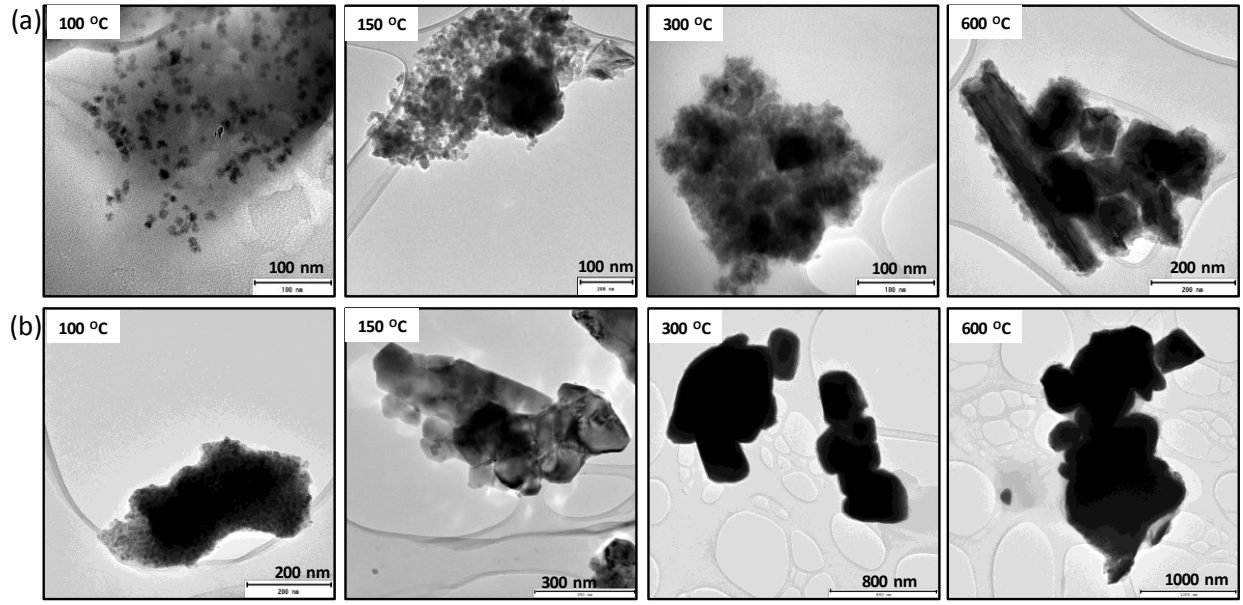

Fig. 12: TEM images of the CVD synthesis of (a) PPC derived NPs and (b) PPZ derived NPs.

All efforts to make Zn_3N_2 NPs using PPZ as a precursor failed; be it changing the reaction parameters or changing the synthetic methods. A few studies have reported the use of metal nitrates and elemental metals in the presence of ammonia in the CVD synthesis of metal nitrides [57]. Herein $Zn(NO_3)_2$ and Zn powder were reacted with 300 cm^3/min NH_3 at 600 °C for 4 h. The PXRD patterns of the decomposition of $Zn(NO_3)_2$ shown in Fig. 13(a) exhibited diffraction peaks that were in good agreement with zincite crystal structure of ZnO (PDF 01-089-1397). In the case of the zinc metal powder, the acquired diffraction lines were indexed to the cubic phase of Zn_3N_2 (PDF 00-035-0762) as shown in Fig. 13(b). Employing the colloidal, microwave and CVD

methods of synthesis using PPZ and CVD using zinc nitrate all resulted in the formation of ZnO but CVD using zinc powder and NH_3 yielded the desired Zn_3N_2.

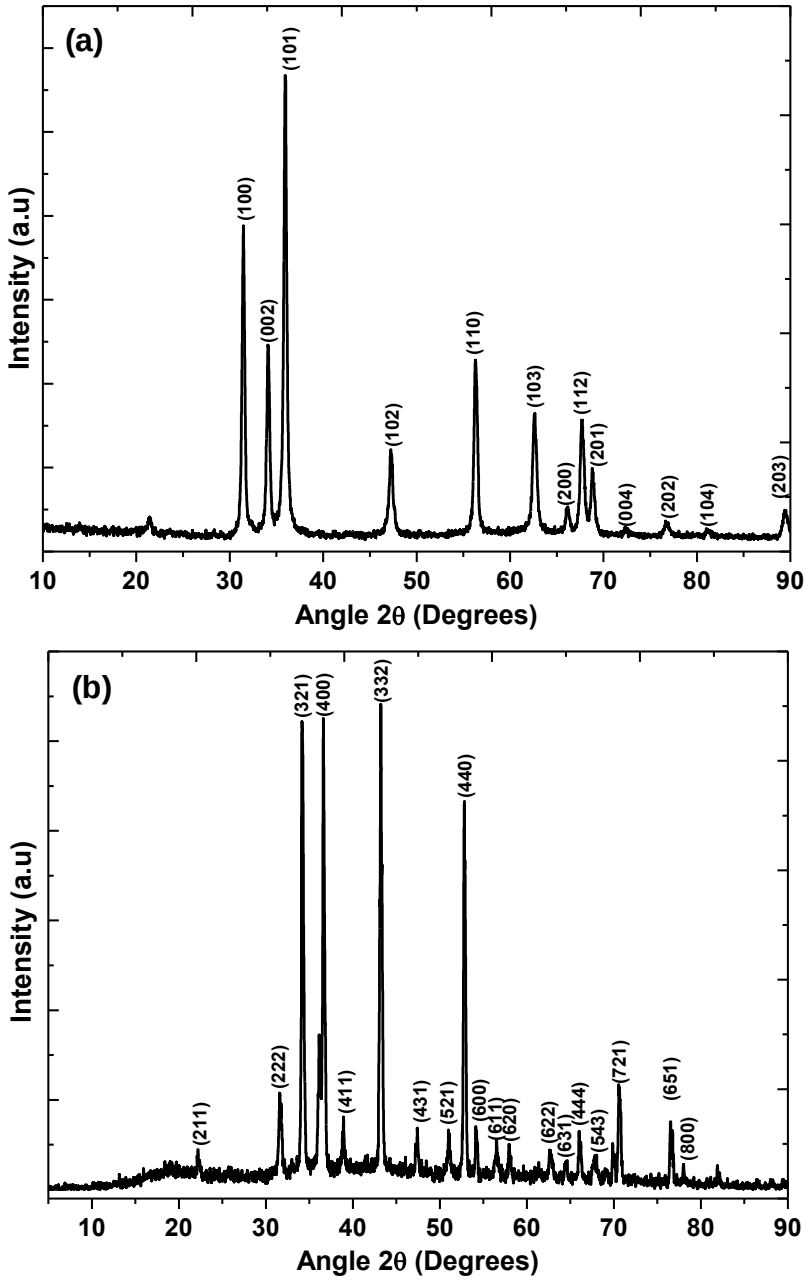

Fig. 13: X-ray diffraction patterns of products of CVD synthesis using (a) $Zn(NO_3)_2$ and (b) Zn powder at 600 ºC.

In Fig. 14, the Raman spectral analysis of Zn_3N_2 shows signals at 273, 327, 435 and 572 cm^{-1} consistent with most Raman vibrational modes that were detected from other reports of Zn_3N_2 [5, 39, 58-60] as shown in Table 1. In the Raman analysis of O-doped zinc nitride films, Lin *et al.* attributed the vibrational modes at 275.1, 579.5 and 641.5 cm^{-1} to the presence of N in the films [5]. The slight variation in the tabulated results may be caused by defects and/or impurities that are found in the different samples.

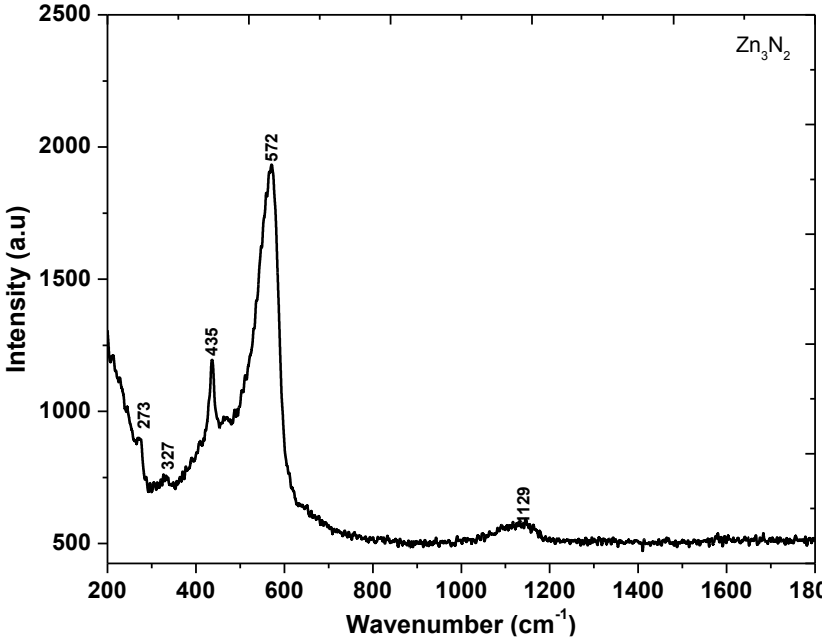

Fig. 14: Raman spectrum of Zn_3N_2 NPs.

Table 1: Raman activity of Zn_3N_2

Peak	Zn_3N_2 in current Study	Zn_3N_2 microtips [39]	Tb-doped Zn_3N_2 film [58]	Zn_3N_2 in Ar-N_2 [59]	High quality Zn_3N_2 [60]	O-doped Zn_3N_2 [5]
1	273	267-270	258	270.81	257	275.1
2	327	325.4	-	-	-	-

3	-	371.7	-	-	-	-
4	435	433	-	-	-	-
5	-	503.5	520	520.04	-	-
6	572	570.5	565	569.80	565	579.5
7	-	610	-	-	-	641.5
8	1129	-	-	-	-	-

The TEM images of the ZnO and Zn_3N_2 NPs are shown in Fig. 15. The TEM image of the ZnO is consistent with the morphology observed in Fig. 11, large dense irregular shaped NPs. The morphology of the Zn_3N_2 NPs is agglomerated spheres with a few larger particles.

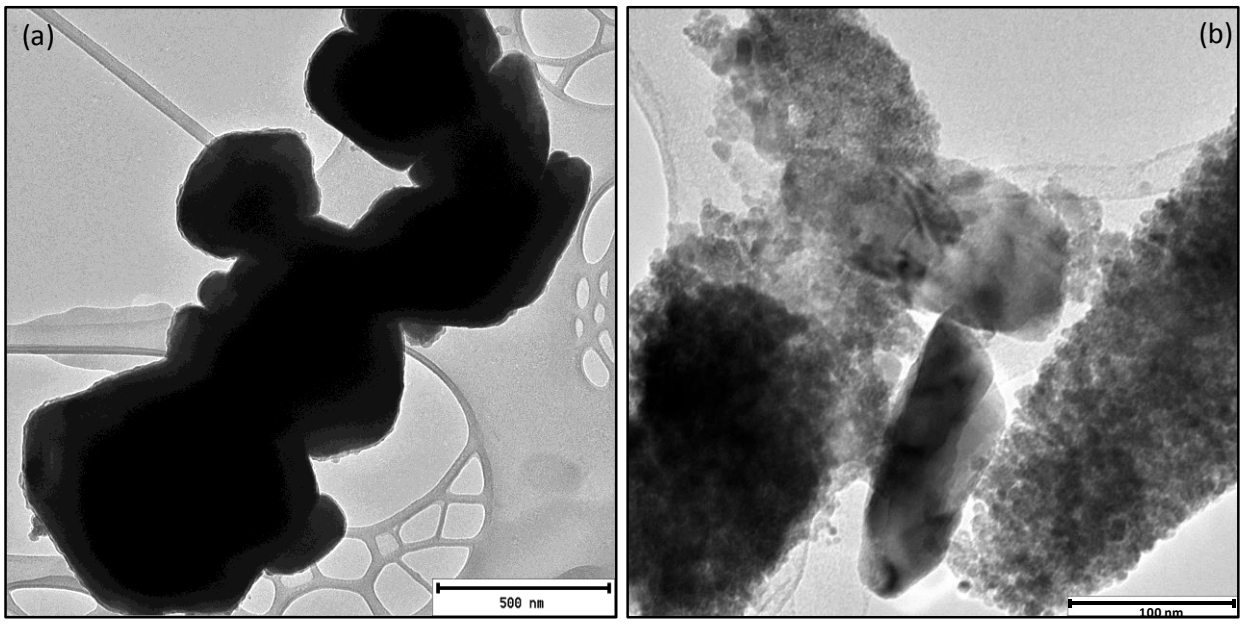

Fig. 15: TEM images of (a) $Zn(NO_3)_2$ derived NPs and (b) Zn_3N_2 NPs.

4. Conclusions

The complexes bis-2-pyrrolylaldiminato Cu and Zn (PPC and PPZ) were synthesized successfully and used as single-source precursors to synthesize Cu_3N and Zn_3N_2 nanoparticles using three methods namely the colloidal method, microwave synthesis and CVD. Thermolysis of the Cu complex using colloidal, microwave and CVD methods resulted in the formation of Cu_3N NPs, a mixture of Cu_3N-Cu_2O NPs and Cu NPs respectively. In the case of the Zn complex, only ZnO was obtained using the three methods of synthesis hence further studies were done using zinc nitrate and zinc powder as other sources of Zn in the presence of ammonia by CVD. The zinc nitrate precursor resulted in the formation of ZnO NPs and the zinc powder was the best precursor in the synthesis of Zn_3N_2 nanomaterials.

References

[1] R.K. Sithole, L.F. Machogo, M.A. Airo, S.S. Gqoba, M.J. Moloto, P. Shumbula, J. Van Wyk, N. Moloto, *New Journal of Chemistry, 42 (2018) 3042-3049.*

[2] T. Trindade, P. O'Brien, *Advanced Materials*, 8 (1996) 161-163.

[3] N. Moloto, N. Revaprasadu, M. Moloto, P. O'Brien, M. Helliwell, *Polyhedron*, 26 (2007) 3947-3955.

[4] N. Moloto, N. Revaprasadu, M. Moloto, P. O'Brien, J. Raftery, *South African Journal of Science*, 105 (2009) 258-263.

[5] C.-W. Lin, Y.-P. Song, S.-C. Chang, *Journal of Applied Physics*, 54 (2015) 04DH06.

[6] M.D. Reichert, M.A. White, M.J. Thompson, G.J. Miller, J. Vela, *Inorganic Chemistry*, 54 (2015) 6356-6362.

[7] R. Juza, H. Hahn, *Zeitschrift Für Anorganische Und Allgemeine Chemie*, 239 (1938) 282-287.

[8] R. Juza, H. Hahn, *Zeitschrift für anorganische und allgemeine Chemie*, 244 (1940) 125-132.

[9] D.M. Borsa, *University Library Groningen][Host]*, 2004.

[10] K. Toyoura, H. Tsujimura, T. Goto, K. Hachiya, R. Hagiwara, Y. Ito, *Thin Solid Films*, 492 (2005) 88-92.

[11] R. Long, Y. Dai, L. Yu, M. Guo, B. Huang, *The Journal of Physical Chemistry B*, 111 (2007) 3379-3383.

[12] R. Juza, J. Hahn, *Zeitschr Anorgan Allgem Chem*, 239 (1938) 282-287.

[13] D. Wang, Y. Li, *Chemical Communications*, 47 (2011) 3604-3606.

[14] H. Wu, W. Chen, *Journal of the American Chemical Society*, 133 (2011) 15236-15239.

[15] D. Borsa, S. Grachev, C. Presura, D. Boerma, *Applied Physics Letters*, 80 (2002) 1823-1825.

[16] A. Zakutayev, C.M. Caskey, A.N. Fioretti, D.S. Ginley, J. Vidal, V. Stevanovic, E. Tea, S. Lany, *The Journal of Physical Chemistry Letters*, 5 (2014) 1117-1125.

[17] T. Nosaka, M. Yoshitake, A. Okamoto, S. Ogawa, Y. Nakayama, *Applied Surface Science*, 169 (2001) 358-361.

[18] J. Bates, N. Dudney, B. Neudecker, A. Ueda, C. Evans, *Solid State Ionics*, 135 (2000) 33-45.

[19] S.-H. Yoo, A. Walsh, D.O. Scanlon, A. Soon, *RSC Advances*, 4 (2014) 3306-3311.

[20] G. Paniconi, Z. Stoeva, R.I. Smith, P.C. Dippo, B.L. Gallagher, D.H. Gregory, *Journal of Solid State Chemistry*, 181 (2008) 158-165.

[21] W. Yu, J. Zhao, C. Jin, *Physical Review B*, 72 (2005) 214116.

[22] M. Mikula, D. Buc, E. Pincik, *Acta Physica Slovaca*, 51 (2000) 35-43.

[23] K.-i. Tanaka, Dynamic Chemical Processes on Solid Surfaces, (2017).

[24] G. Yue, P. Yan, J. Liu, M. Wang, M. Li, X. Yuan, *Journal of Applied Physics*, 98 (2005) 103506.

[25] Y. Kumagai, K. Harada, H. Akamatsu, K. Matsuzaki, F. Oba, *Physical Review Applied*, 8 (2017) 014015.

[26] F. Zong, H. Ma, C. Xue, W. Du, X. Zhang, H. Xiao, J. Ma, F. Ji, *Materials Letters*, 60 (2006) 905-908.

[27] P. Xi, Z. Xu, D. Gao, F. Chen, D. Xue, C.-L. Tao, Z.-N. Chen, *RSC Advances*, 4 (2014) 14206-14209.

[28] T. Nakamura, H. Hayashi, T.-a. Hanaoka, T. Ebina, *Inorganic Chemistry*, 53 (2013) 710-715.

[29] P.N. Taylor, M.A. Schreuder, T.M. Smeeton, A.J. Grundy, J.A. Dimmock, S.E. Hooper, J. Heffernan, M. Kauer, *Journal of Materials Chemistry C*, 2 (2014) 4379-4382.

[30] R. Ahumada-Lazo, S.M. Fairclough, S.J. Hardman, P.N. Taylor, M. Green, S.J. Haigh, R. Saran, R.J. Curry, D.J. Binks, *ACS Applied Nano Materials*, 2 (2019) 7214-7219.

[31] R. Das, D. Mehta, H. Bhardawaj, *International Journal of Research and Development in Pharmacy & Life Sciences*, 1 (2012) 32-39.

[32] J.-Q. Sun, X.-P. Shen, L.-J. Guo, K.-M. Chen, Q. Liu, *Low-dimensional Systems and Nanostructures*, 41 (2009) 1527-1532.

[33] R.C. Hoffmann, S. Sanctis, E. Erdem, S. Weber, J.J. Schneider, *Journal of Materials Chemistry C*, 4 (2016) 7345-7352.

[34] Y. Zhang, Z.-P. Qiao, X.-M. Chen, *Journal of Materials Chemistry*, 12 (2002) 2747-2748.

[35] J. Fitzmaurice, A. Hector, A. Rowley, I. Parkin, *Polyhedron*, 13 (1994) 235-240.

[36] M.L. Hitchman, K.F. Jensen, *Elsevier*, 1993.

[37] K. Nakaso, B. Han, K. Ahn, M. Choi, K. Okuyama, *Journal of Aerosol Science*, 34 (2003) 869-881.

[38] A. Fallberg, M. Ottosson, J.O. Carlsson, *Chemical Vapor Deposition*, 15 (2009) 300-305.

[39] P.-C. Wei, S.-C. Tong, C.-M. Tseng, C.-C. Chang, C.-H. Hsu, J.-L. Shen, *Journal of Applied Physics*, 116 (2014) 143507.

[40] J.N. Mugo, S.F. Mapolie, J.L. van Wyk, *Inorganica Chimica Acta*, 363 (2010) 2643-2651.

[41] N. Holden, R. Martin, I. Barnes, *Pure and Applied Chemistry*, 55 (1983) 1119-1136.

[42] H. Yu, W. Zhang, Q. Yu, F.-P. Huang, H.-D. Bian, H. Liang, *Molecules*, 22 (2017) 1772.

[43] Z. Lin, A. McCreary, N. Briggs, S. Subramanian, K. Zhang, Y. Sun, X. Li, N.J. Borys, H. Yuan, S.K. Fullerton-Shirey, *2D Materials*, 3 (2016) 042001.

[44] J. Polte, *Crystal Engineering Communication*, 17 (2015) 6809-6830.

[45] J.H. Han, S. Lee, J. Cheon, *Chemical Society Reviews*, 42 (2013) 2581-2591.

[46] C.S. Kumar, Raman Spectroscopy for Nanomaterials Characterization, Sptinger Science & Business Media, 2012

[47] A. Fallberg, M. Ottosson, J.-O. Carlsson, *Journal of Crystal Growth*, 312 (2010) 1779-1784.

[48] R. Szczęsny, E. Szłyk, M.A. Wiśniewski, T.K. Hoang, D.H. Gregory, *Journal of Materials Chemistry C*, 4 (2016) 5031-5037.

[49] Y. Zhang, L.F. Leung-Yuk, Z. Yan, X. Hu, *Science in China Series E: Technological Sciences*, 52 (2009) 352.

[50] F. Cataldo, S. Iglesias-Groth, Fulleranes: the hydrogenated fullerenes, Springer Science & Business Media, 2010.

[51] M.P. Kalenga, S. Govindraju, M. Airo, M.J. Moloto, L.M. Sikhwivhilu, N. Moloto, *Journal of Nanoscience and Nanotechnology*, 15 (2015) 4480-4486.

[52] A. Loupy, R.S. Varma, *Chimica Oggi• Chemistry Today*, 24 (2006) 36.

[53] C.O. Kappe, D. Dallinger, S.S. Murphree, Practical microwave synthesis for organic chemists, Strategies, Instruments, and Protocols (Wiley-VCH, Weinheim, Germany, 2009), (2009).

[54] J.R. Brent, N. Savjani, P. O'Brien, *Progress in Materials Science*, 89 (2017) 411-478.

[55] S. Bhattacharyya, R. Ayouchi, M. Pinnisch, R. Schwarz, *Physica Status Solidi C*, 9 (2012) 469-472.

[56] A.C. Newport, J.E. Bleau, C.J. Carmalt, I.P. Parkin, S.A. O'Neill, *Journal of Materials Chemistry*, 14 (2004) 3333-3336.

[57] A. Kafizas, C.J. Carmalt, I.P. Parkin, *Coordination Chemistry Reviews*, 257 (2013) 2073-2119.

[58] Z.-X. Zhang, X.-J. Pan, L.-X. Liu, Z.-W. Ma, H.-T. Zhao, L. Jia, E.-Q. Xie, Green photoluminescence from Zn 3 N 2: Tb films prepared by magnetron sputtering, in, AIP, 2009.

[59] J. Khoshman, N. Peica, C. Thomsen, J. Maultzsch, B. Bastek, C. Wan, M. Kordesch, *Thin Solid Films*, 520 (2012) 7230-7235.

[60] G. Xing, D. Wang, B. Yao, L.A. Qune, T. Yang, Q. He, J. Yang, L. Yang, *Journal of Applied Physics*, 108 (2010) 083710.

Chapter 4

Synthesis and characterization of Cu_3N nanoparticles using pyrrole-2-carbaldpropyliminato Cu(II) complex and $Cu(NO_3)_2$ as single-source precursors: the search for an ideal precursor

Abstract

Herein, we report on the synthesis and characterization of Cu_3N nanocrystals using two single-source precursors, bis (pyrrole-2-carbalpropyliminato) Cu(II) (PPC) and $Cu(NO_3)_2.3H_2O$. The optical and structural properties were investigated and the suitability of the two precursors was studied in terms of producing good quality Cu_3N nanocrystals without the detection of Cu or oxidation to CuO. Both precursors resulted in crystalline Cu_3N with anti-ReO_3 cubic structure with no presence of copper impurities, however, peaks due to the capping agent were detected by XRD and confirmed with XPS. The PPC complex resulted in spherical nanocrystals whilst the copper nitrate resulted in nanocubes. The band gaps were in the visible region with the copper nitrate nanocrystals slightly red shifted from the PPC derived particles due to larger crystal sizes. The emission spectra were blue-shifted from the absorption band edges hence indicating an up-conversion process.

Keywords: Copper nitride; single-source precursor; nanocrystals

1. Introduction

Since the first report on the synthesis of copper(I)nitride (Cu_3N) by Juza and Hahn in 1938 [1], researchers are still seeking clarity on the synthesis, morphology and properties of copper nitride. In a bid to explore the properties further, a variety of synthetic techniques which mainly include sputtering [2] and vapor deposition [3] amongst others have been employed. Cu_3N obtained from these different techniques have been reported to exhibit good optical, electrical and catalytic properties [4-6]. Copper nitride has a primitive open anti-rhenium trioxide cubic structure with nitrogen atoms occupying the corners of the cube and a copper atom found in between two consecutive nitrogen atoms. The face centers and the body of the cube are not occupied in pure copper nitride and this leaves void interstitial sites that can be occupied by either copper, nitrogen or other foreign atoms. As a result, copper nitride has been cited as a host candidate [7, 8]. The occupation of these sites results in the alteration of the optical and electrical properties. Calculations by Moreno-Armenta et al. [9] showed that the lattice parameters of the cell increase as the copper content at the center of the cube increases. Consequently, the band gap increases and eventually the copper nitride exhibits a metallic nature and this was further evidenced from experimental results [10]. Reports on calculated and experimental band gaps of Cu_3N vary from 0.13 eV [11] to 2.06 eV [12].

Different temperatures have been used to deposit Cu_3N films. Typically, deposition occurs at temperatures between 100 and 200 °C with metallization occurring at higher temperatures [13-14]. Nitrogen is thought to re-emit above 250 °C resulting in the formation of Cu^0. Fallberg *et. al.* [15] reported on the formation of a single phase Cu_3N up to 400 °C using chemical deposition, however, Liu *et. al*. [16] started obtaining films with extra interstitial Cu^0 atoms at temperatures just above

150 °C [17]. As such, Cu_3N is viewed as a metastable compound decomposing at temperatures below 300 °C and hence useful in the formation of metallic links and optical recording devices [18, 19]. It is therefore evident that other synthetic strategies are required in tailoring properties of copper nitride nanoparticles. Colloidal synthetic routes tend to offer a better way of controlling properties. The desired morphology, electrical and optical properties can be obtained by carefully varying time, temperature and organic ligands (which may act as solvents, capping agents or reducing agents). A very successful colloidal synthesis was reported in 2011 [20] where Cu_3N nanocubes were synthesized in organic solvents using copper(II) nitrate as a precursor [21]. The synthesized nanocubes had edges of about 26 nm with a direct band gap of 1.5 eV. Variation in the organic solvent resulted in a production of nanoparticles with different sizes. Nakamuri *et al.* [22], used copper (II) acetate in different alcohols at temperatures between 130 and 200 °C to obtain Cu_3N. In spite of a few reports of successful synthesis of Cu_3N, common to all is the presence of opportunistic CuO. The exposure of the synthesized Cu_3N to water and oxygen, either from the atmosphere or from the copper precursors as well as the solvents, results in the formation of CuO. In the presence of oxygen, Cu_3N easily disproportionates to give Cu^0 and Cu^{2+} as shown below [23, 24].

$$2Cu^{+}\,(aq) \rightarrow Cu^{0}\,(aq) + \,Cu^{2+}(aq) \qquad (1)$$

This poses a huge challenge for example, in the synthesis of metallic links where CuO will be formed instead of the desired metallic copper. Due to scanty synthetic methods for the synthesis of Cu_3N nanoparticles, we report on the synthesis of copper nitride using the colloidal single-source precursor method. An advantage of single-source precursors is that the molecules consist

of all the elements that are required to make the final product and can be designed in such a way that no additional oxygen is present. In addition, the decomposition of the precursor determines the reaction temperature. Herein, we report on the synthesis of Cu_3N nanocrystals using two single-source precursors, bis(pyrrole-2-carbalpropyliminato) Cu(II) (PPC) and $Cu(NO_3)_2.3H_2O$. $Cu(NO_3)_2.3H_2O$ as previously stated, has been successfully utilized to produce Cu_3N although with CuO as a minor impurity [21]. PPC though previously synthesized [25], has never been utilized in the synthesis of nanocrystals and given its electronic properties, it appears to be a good molecular precursor, hence our interest. In addition, we investigate the optical and structural properties of Cu_3N nanocrystals and by optimizing the conditions for the thermolysis of the two precursors; we ensure that no Cu or oxidation to CuO is observed.

2. Experimental section

Materials

Copper (II) acetate monohydrate ($Cu(CO_2CH_3)_2.H_2O$) (puriss p.a., 99.0%), pyrrole-2-carboxaldehyde (98%), n-propylamine (99%), dichloromethane (CH_2Cl_2) (anhydrous, 99.8%), octadecylamine (ODA) (99%) and ethanol (EtOH) (absolute, ≥99.8% (GC)) were purchased from Sigma-Aldrich.

Synthesis of pyrrole-2-carbaldpropyliminato Cu (II) (PPC)

The synthesis of pyrrole-2-carbaldpropyliminato Cu(II) precursor ($C_{16}H_{22}N_4Cu$) was done similar to reported work with some modifications [25]. Briefly, 2-pyrrolecarboxaldehyde (22.37 mmol) was dissolved in 20 mL of deionized and copper acetate monohydrate (12.07 mmol) was slowly added under vigorous stirring. Thereafter, 4 mL of propylamine was added dropwise and the

mixture was left at ambient temperature for 2 h, 100 mL of water was then added and the reaction was left to run for 4 h. The crystals were obtained through filtration, dried and recrystallized in 50% CH_2Cl_2: 50% EtOH mixture at -20 °C.

Yield: 89%, FT-IR (cm^{-1}):2968 (vw), 1583 (s), 1311 (m), 1033 (s), 742 (vs). ESI-MS m/z $[M+H]^+$: 334.05 (calculated), 334.9 (found). Microanalysis calculated, %: C 57.55; H 6.69; N 16.78; found, %: C 58.26; H 6.79; N, 16.88.

Characterization of the complex

The mass spectrometry of the complex was acquired on a Thermo-Finnigan LXQ with atmospheric pressure chemical ionization (APCI). The elemental compositions (%C, %H and %N) of PPC complex was measured using a Vario Elementar III microcube CH. The single crystal X-ray data of the complex was measured on a Bruker APEX II CCD with graphite monochromated Mo Kα radiation (50 kV, 30 mA) at a temperature of 25 °C. The structure was solved by direct methods using SHELXS97 [26]. Isotropic refinement was initially performed on the non-hydrogen atoms followed by anisotropic refinement by full matrix least-squares calculations based on F2 using SHELXTL. The H atoms were calculated geometrically and refined with a riding model. Thermogravimetric analysis (TGA) was done on a Pyris Stat 4000 analyzer using nitrogen as carrier gas at a flow rate of 20 mL/min. The FT-IR was measured on a Bruker Tensor 27 FT-IR.

Synthesis of Cu_3N nanocrystals using PPC and $Cu(NO_3)_2.3H_2O$ as the single-source precursor

Copper nitride nanocrystals were synthesized using the single-source precursor method as depicted in Scheme 2. Typically, 0.25 mmol of PPC or $Cu(NO_3)_2.3H_2O$/$Cu(CO_2CH_3).H_2O$ and 18.55 mmol of octadecylamine (ODA) were mixed and degassed under a continuous flow of nitrogen gas at

105 °C for 1 hr. The reaction mixture was then raised to 260 °C and maintained for 5 min. Thereafter, the reaction was stopped and cooled to 80 °C. Ethanol was added to flocculate the particles. The particles were then centrifuged at 7000 rpm and repeatedly washed using ethanol. After washing, the particles were left to dry in a desiccator.

Characterization of the nanocrystals

The structure and phase of the powdered nanocrystals were determined with the Bruker MeasSrv (D2-205530) diffractometer using CoKα radiation (λ 1.78897 Å) at 30 kV/30 mA. Measurements were taken using a glancing angle of incidence detector at an angle of 2°, for 2θ values over 10 - 90° in steps of 0.026° with a step time of 37 s and at a temperature of 25 °C. X-ray photoelectron spectroscopy measurements were performed with a PHI 5000 Versaprobe - Scanning ESCA Microprobe operating with a 100 µm 25 W 15 kV Al monochromatic X-ray beam. The particle sizes and morphology were studied using a FEI Spirit 120 kV transmission electron microscope operated at an acceleration voltage of 200 kV with a beam spot size of 20 - 100 nm in TEM mode. The particles were dispersed in chloroform and drop casted onto a lacey carbon copper grid. The solvent was then evaporated at room temperature. A Specord 50 AnalytikJena UV-Vis spectrophotometer was used to carry out the absorption measurements. An Agilent Cary Eclipse fluorescence spectrometer was used to measure the photoluminescence of the particles. The nanoparticles were dissolved in chloroform and placed in quartz cuvettes (1cm path length) for both UV-Vis absorption and photoluminescence spectral analyses.

3. Results and discussion

The pyrrole-2-carbaldpropyliminato Cu(II) complex was synthesized using a modified method similar to that reported by Grushin *et al.* [25]. The complex was formed by adding all the reactants in one pot and then refluxing contrary to forming the 2-pyrrolcarbaldpropylimine ligand first (*Scheme 1*) [25].

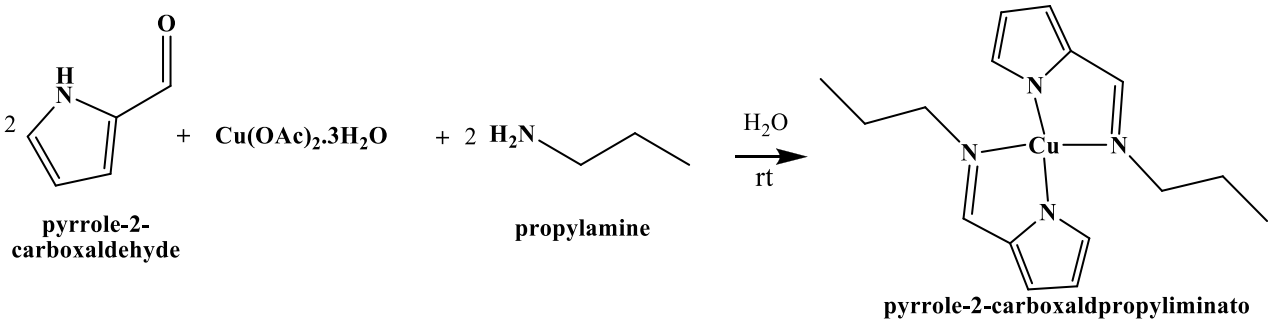

Scheme 1: Synthesis of pyrrole-2-carbaldpropyliminato Cu(II).

The resultant complex was in good yield (89%). The elemental composition, mass spectrometry (Fig. S1) and FTIR spectroscopy confirmed the formation of the complex. The FTIR spectra depicted in Fig. 1 showed a shift of the frequencies from the free 2-pyrrolcarbaldpropylimine ligand to the coordinated ligand hence suggesting the formation of the complex, in particular, the υ(N-H) showed the largest shift from 1635 cm^{-1} to 1592 cm^{-1} confirming the coordination through the imine (Table 1).

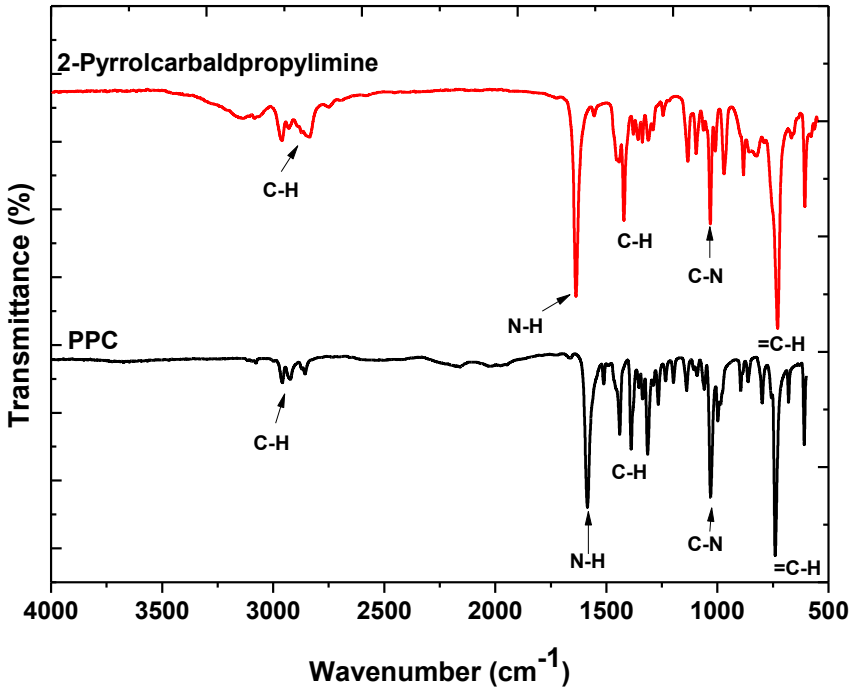

Fig. 1: FTIR spectra of the complex PPC and the ligand 2-pyrrolcarbaldpropylimine.

Table 1: Frequencies of selected functional groups

Assignment	Ligand frequencies (cm^{-1})	Complex frequencies (cm^{-1})
N-H bending	1635	1592
C-H bending	1422	1384
C-N stretch	1031	1031
=C-H bending	721	740

The shiny well-defined black crystals were then analyzed by X-ray crystallography (Fig. S2). The data collected showed that the crystal structure of the PPC complex belongs to the orthorhombic

crystal system with the centrosymmetric $P2_12_12_1$ space group similar to the published data [CCDC-241810] [25]. The crystal structure is shown in *Scheme 2*.

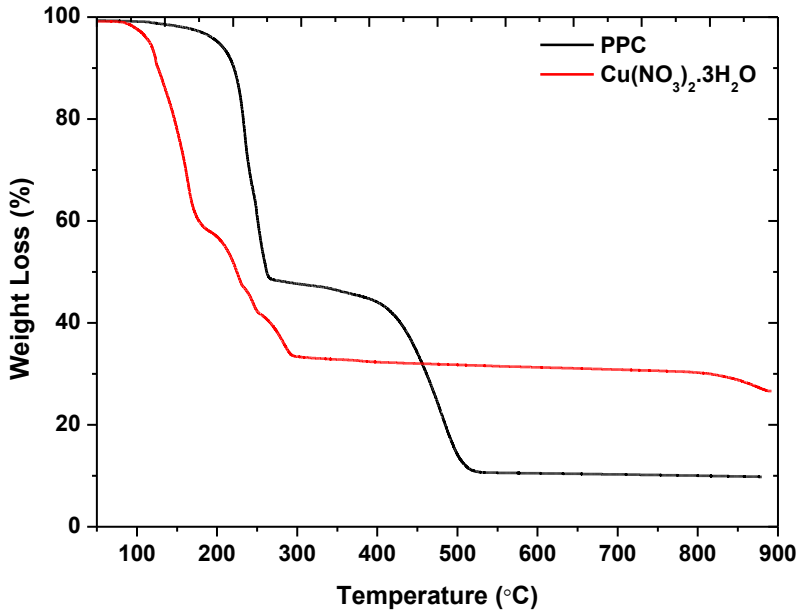

Fig. 2: TGA of the PPC complex and $Cu(NO_3)_2.3H_2O$ precursors.

The PPC complex together with $Cu(NO_3)_2.3H_2O$ was then used as single-source precursors for the synthesis of copper nitride nanocrystals, with the PPC complex acting as a molecular precursor whilst the copper nitrate is an ionic precursor with Cu^{+2} as a cation and NO_3^{-1}as the anion. Prior to the synthesis of the nanocrystals, the thermal decomposition of the precursors was evaluated using TGA. The TGA results are shown in Fig. 2. The PPC complex showed two degradation steps at 235 °C and 469 °C attributed to the decomposition of the organics and the residual assigned to metallic copper. On the other hand, copper nitrate, showed four degradations steps with the final residual associated with CuO. The degradation products suggest that for PPC, Cu is a thermodynamically favored product whilst CuO is favored for $Cu(NO_3)_2.3H_2O$. It is therefore not

surprising that a lot of work report on the presence of Cu and CuO as impurities [23, 24]. Therefore, it is essential that the synthetic parameters are well-controlled in order to produce the less favored Cu_3N.

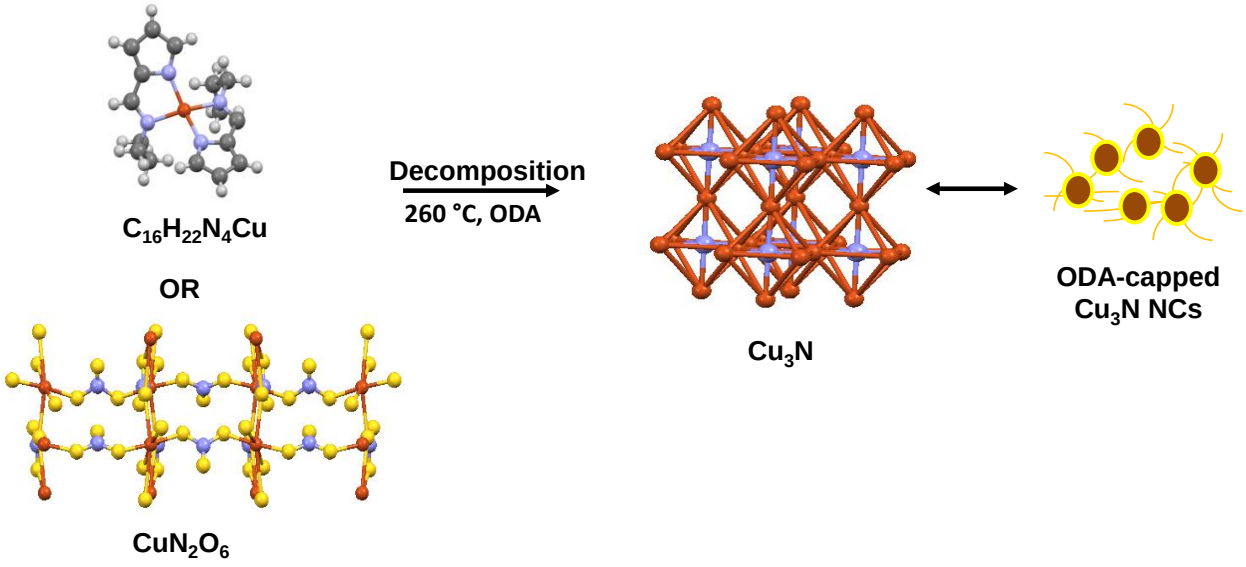

Scheme 2: Thermal decomposition of the precursors to form Cu_3N nanocrystals.

The precursors were then thermolyzed in ODA under mild conditions to prevent the formation of Cu and CuO and produce Cu_3N nanocrystals as depicted in *Scheme 2*. The resultant nanocrystals were then characterized by XRD. The powder diffraction patterns are shown in Fig. 3. Both the diffraction patterns were indexed to Cu_3N with an anti-ReO_3 cubic structure (JCP2.2CA:00-002-1156). However, the diffraction peaks for the particles synthesized with copper nitrate were sharper compared to those synthesized with PPC suggesting bigger particle sizes. In addition, peaks attributed to the ODA capping agent were also observed. It is worth noting that no peaks could be indexed to copper or its oxides. To check that the peaks indeed belonged to ODA, XRD patterns of ODA as it was purchased was done as well as when heated to 260 °C for prolonged

periods of time (Fig. S3). It is clear that ODA is crystalline in nature depicted by the observed sharp peaks and that upon heating it becomes more amorphous with most peaks disappearing except for the ones found in 10° - 30° 2θ, similar to the ones observed in XRD patterns of the nanocrystals.

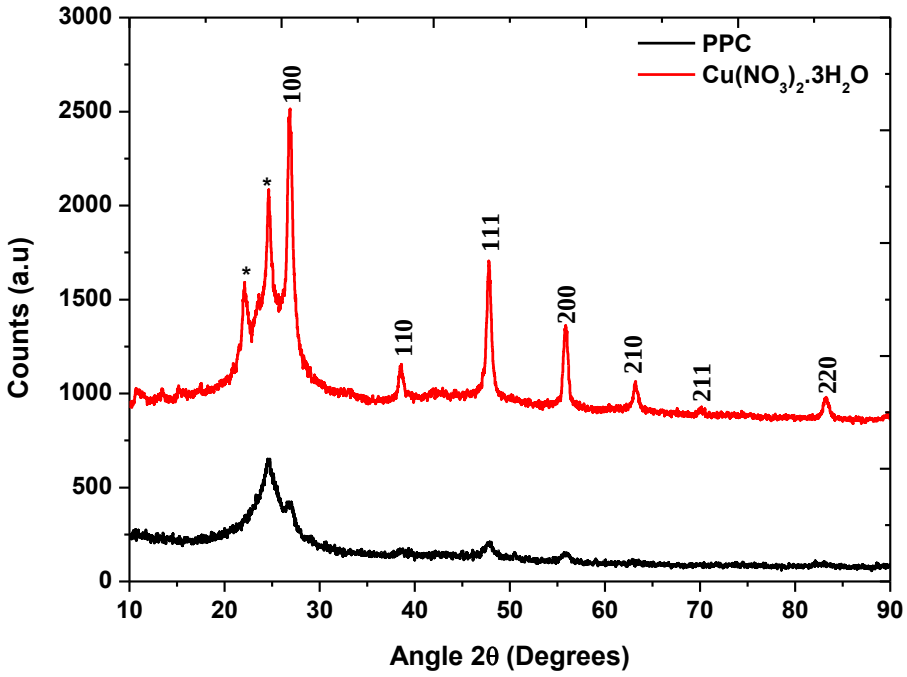

Fig. 3: X-ray diffractograms of nanocrystals synthesized from the PPC and $Cu(NO_3)_2.3H_2O$ precursors (* peaks due to the capping agent).

To further ascertain whether indeed ODA was present on the surface of the nanocrystals hence attributing for the peaks observed in the XRD, FTIR spectroscopy was done. The FTIR spectra of the pure ODA and ODA-capped Cu_3N nanocrystals synthesized from PPC and $Cu(NO_3)_2.3H_2O$ are shown in Fig. 4. The spectra from the Cu_3N nanocrystals synthesized from both precursors resembled that of pure ODA. However, small frequency shifts are observed as well as accentuations, but more importantly, a Cu-N peak at 592 cm^{-1} and 655 cm^{-1} for PPC synthesized

and $Cu(NO_3)_2.3H_2O$ synthesized nanocrystals is observed. This suggests that ODA is covalently bonded to the nanocrystals via the amine group.

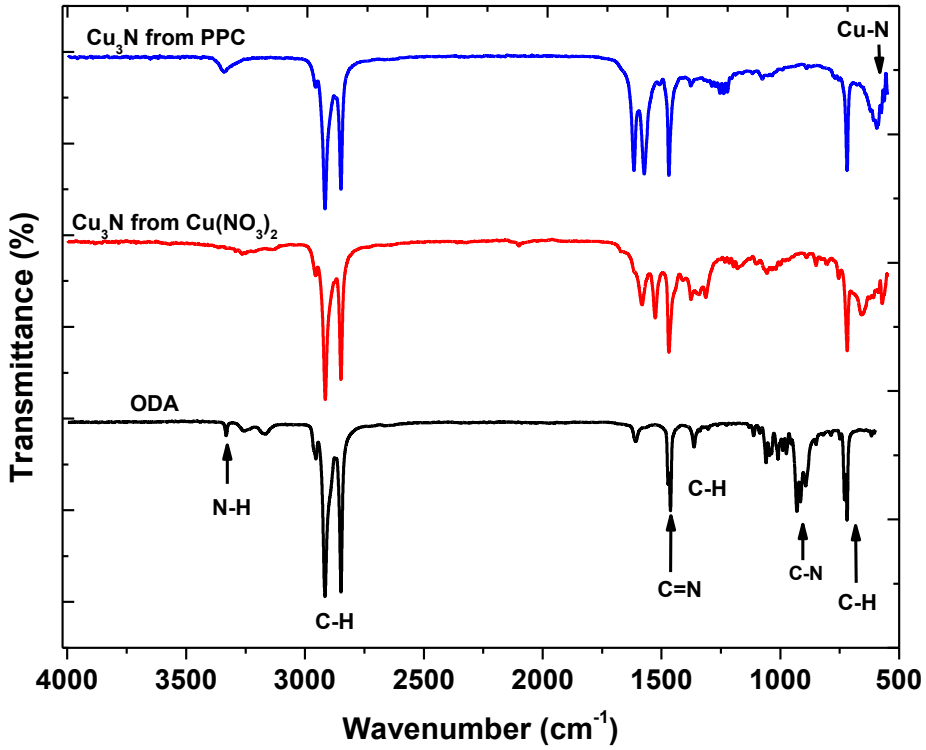

Fig. 4: FTIR spectra of ODA, ODA capped nanocrystals synthesized from PPC and $Cu(NO_3)_2.3H_2O$.

To confirm the composition of the nanocrystals and determine any present impurities, XPS was done. Shown in Fig. 5 is the XPS survey spectrum of the nanocrystals synthesized from the $Cu(NO_3)_2.3H_2O$ precursor. Similar results were obtained for the nanocrystals synthesized with PPC. The spectrum showed a strong C 1s peak confirming the presence of carbon due to the capping agent on the surface of the nanocrystals. The attribution of the carbon peak to the capping agent is consistent with other reported work on capped nanoparticles and XPS has in fact been

used to trace ligand exchange on the surface of the nanocrystals [27-28]. The O 1s peak was due to the adsorption of oxygen from the atmosphere. More importantly, Cu 2p (76, 125, 933, 952 eV), and N 1s (399 eV) were also observed confirming the formation of Cu_3N. The relative atomic abundance showed a presence of about 94% carbon which is consistent with many long-chain molecules on the surface of the nanocrystals as depicted in *Scheme 2*.

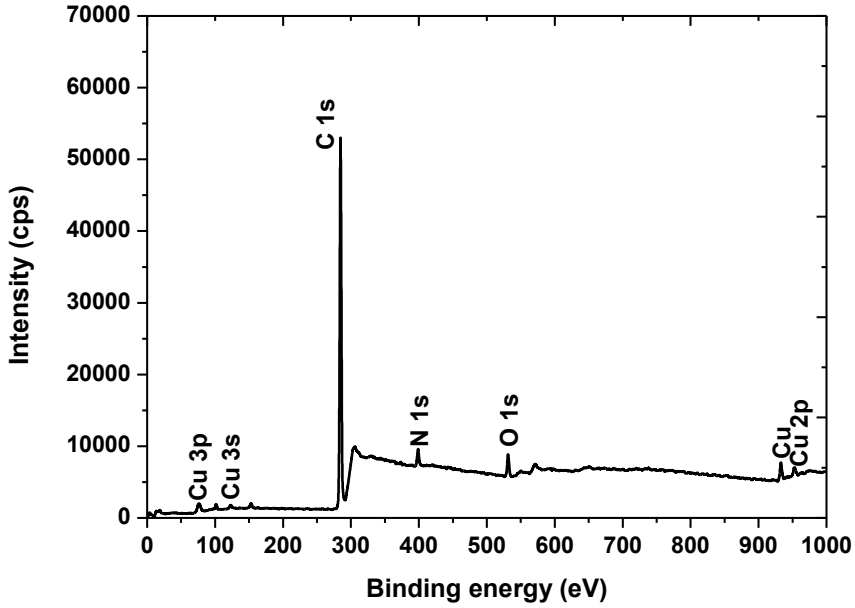

Fig. 5: XPS survey spectrum of Cu_3N nanocrystals synthesized from the $Cu(NO_3)_2.3H_2O$ precursor.

The high resolution XPS spectra of the nanocrystals were performed with the focus on O 1s, N 1s, and Cu 2p as shown in Fig. 6. The deconvoluted spectrum of C 1s showed sp^3 and sp^2 carbon peaks attributed to the capping agent. The O 1s showed two peaks at 531 eV and 532.5 eV corresponding the C-O and C=O respectively thought to be brought about by the interaction of the adsorbed oxygen from the atmosphere and the capping agent. N 1s accounted for one peak corresponding

to N–Cu (399.7 eV). Cu 2p was deconvoluted to three sub-peaks corresponding to Cu–N (932 eV), Cu $2p_{3/2}$ (933.2 eV), and Cu–C (933.8 eV).

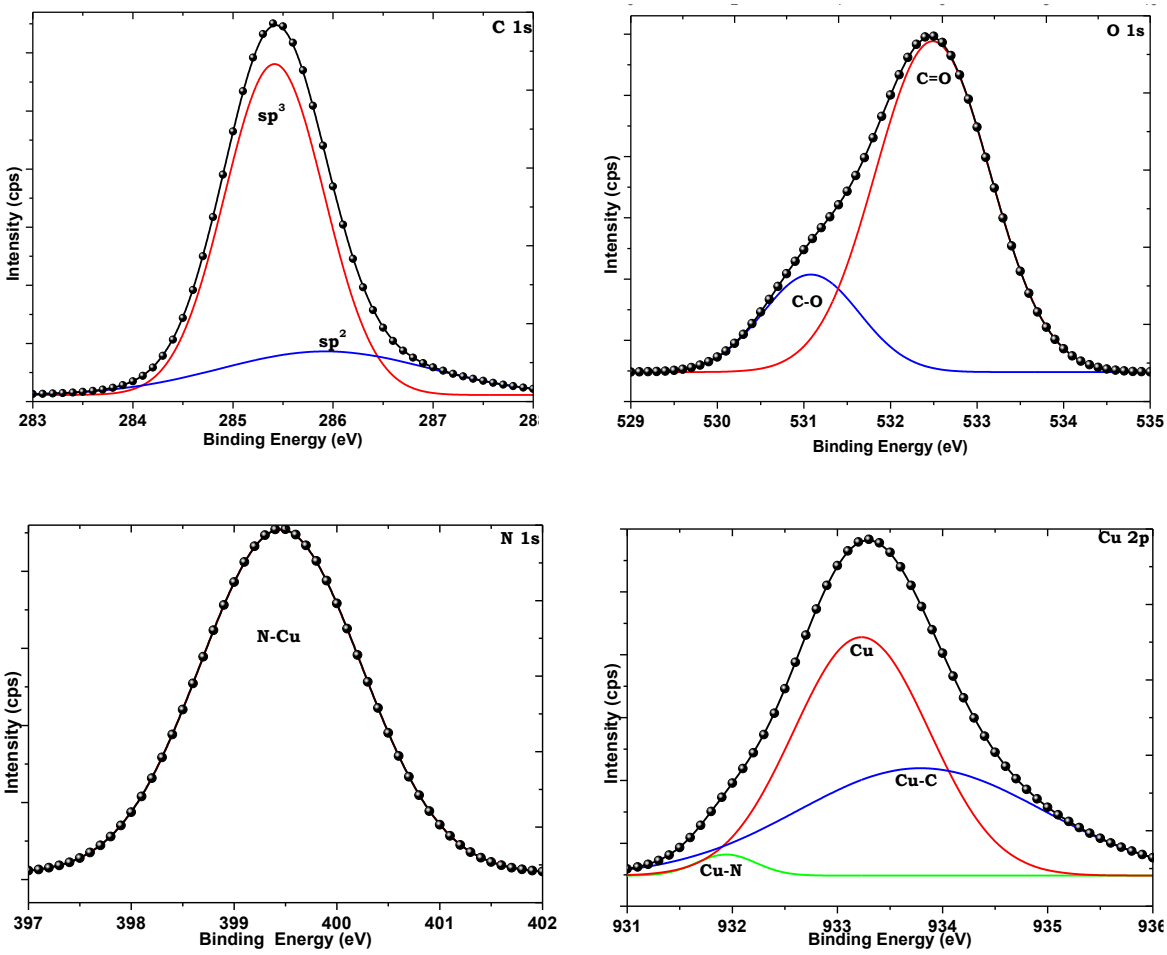

Fig. 6: XPS survey spectrum of Cu_3N nanocrystals synthesized from $Cu(NO_3)_2.3H_2O$ and high resolution core level spectra of Cu_3N nanoparticles with focus on C 1s, O 1s, N 1s, Cu 2p.

The sizes and shapes of the nanocrystals were determined using TEM. The TEM micrographs and size distribution histograms of PPC and $Cu(NO_3)_2.3H_2O$ synthesized nanocrystals are shown in Fig. 7 and Fig. 8 respectively. The PPC synthesized nanocrystals are spherical in shape; however, they are polydispersed with most of the population being 2.8±0.6 nm in size. The HRTEM in Fig.

7(c) shows lattice fringes with a d-spacing of 0.381 nm corresponding to the (100) plane of an anti-ReO_3 cubic structure of Cu_3N.

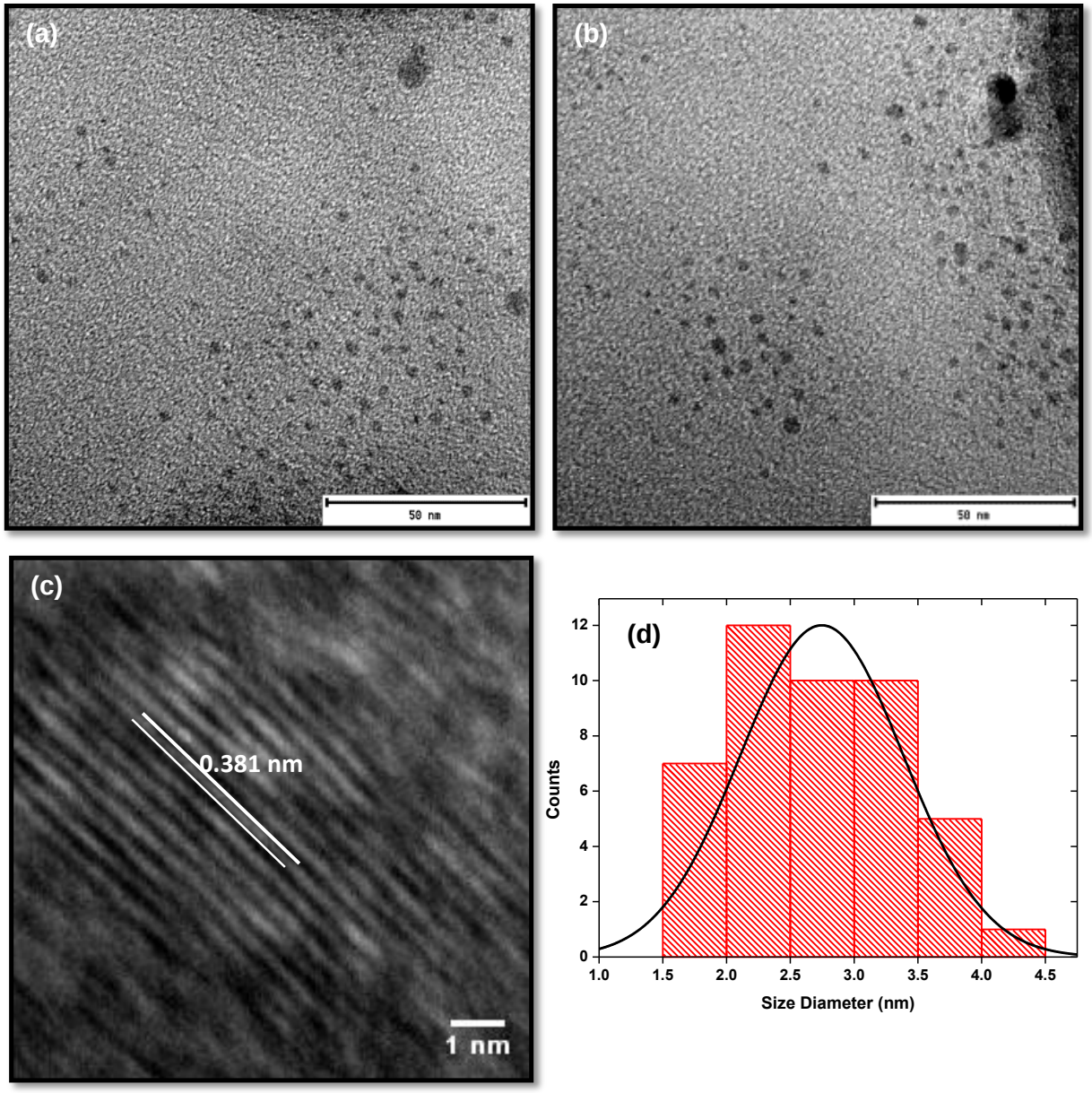

Fig. 7: TEM micrographs (a) and (b) of Cu_3N nanocrystals synthesized from PPC, (c) HRTEM depicting crystal fringes and (d) size distribution histogram. (Scales (a) 50 nm (b) 50 nm and (c) 1 nm.

The TEM and HRTEM micrographs as well as the size distribution of particles synthesized from $Cu(NO_3)_2.3H_2O$ are shown in Fig. 8. The nanocrystals show the characteristic crystalline cube-like nanocrystals similar to those that were obtained in previous studies at different reaction conditions [29]. The average length of the sides of the as-synthesized nanocubes is approximately 19±4 nm. The 0.377 nm d-spacing can also be indexed to a (100) plane of the cubic Cu_3N crystal structure.

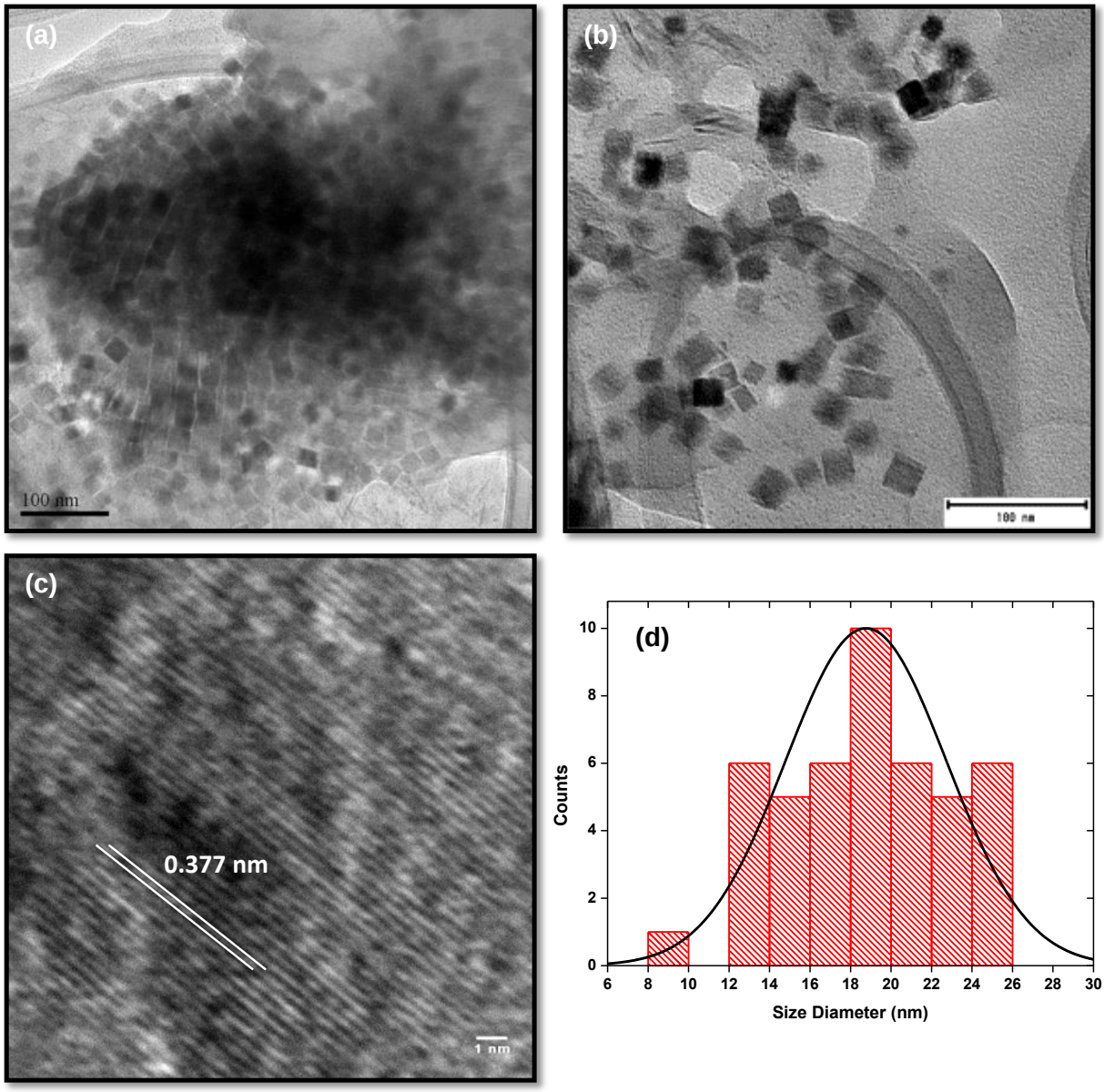

Fig. 8: TEM micrographs (a) and (b) of Cu_3N nanocrystals synthesized from $Cu(NO_3)_2.3H_2O$, (c) HRTEM depicting crystal fringes and (d) size distribution histogram. (Scales (a) 100 nm (b) 100 nm and (c) 1 nm.

It is evident that the type of precursor used influences the morphology of the resultant nanocrystals. The more stable PPC precursor attested by the clean two-step decomposition as shown on the TGA result in the more thermodynamically stable spherical morphology whereas $Cu(NO_3)_2.3H_2O$ which

is characterized by multi-decomposition steps and the formation of CuO results in less favorable cubes. The single-source precursor method and the synthetic conditions used herein result in Cu_3N nanocrystals with superior quality where smaller sizes are obtained, nearly monodispersed samples as well as no traces of CuO or Cu impurities as compared to other reported work on Cu_3N. In another solvothermal study, irregularly shaped nanocrystals with diameters ranging from 22 nm to 220 nm were obtained from the nitridation of CuO using urea or ammonia [21]. The synthesized nanocrystals were unstable and oxidized when left exposed to humid air. Nakamuri *et al.* decomposed copper acetate in long chain alcohols in the presence of ammonia and also obtained irregularly shaped copper nitride nanocrystals with sizes ranging between 100 to 200 nm [22].

To establish whether ODA, a nitrogen containing ligand does not act as a nitrogen source for the Cu_3N nanocrystals hence nullifying the contribution of the two precursors, a control experiment was done. Copper acetate was thermolyzed in ODA at the same conditions as the PPC and $Cu(NO_3).2H_2O$ precursors. The acetate contains oxygen similar to the nitrate. From the XRD pattern shown in Fig. S4, it is evident that ODA could not possibly act as the nitrogen source as only copper is formed. When comparing ODA with NH_3, a known source for nitridation, NH_3 decomposes to form N_2 and H_2. The nitrogen thereby acts as a nitridation source [30]. The direct nitridation using N_2 gas requires very high pressures and therefore does not work for this method [31]. Heating up of ODA also showed no signs of any gas evolving and resulted in amorphous ODA or formation of a new organic species as shown on the XRD pattern in Fig. S3. The mechanism for the synthesis of nanocrystals using molecular precursors is somewhat known and has been thought to follow the Lamer and Dinegar type of growth and with the metal and nitrogen bond already intact, the decomposition results in the formation of Cu-N nuclei which then grow

over time due to Ostwald ripening and then growth is terminated by stopping the reaction [32-34]. However, it is not quite clear as to what the mechanism of growth for the ionic precursors such as copper nitrate. Nevertheless, from the control experiment of copper acetate, it is clear that the type of salt used as well as the conditions, need to be perfect to result in the formation of Cu_3N as a lot of studies have previously shown that CuO and Cu are readily formed [23, 24].

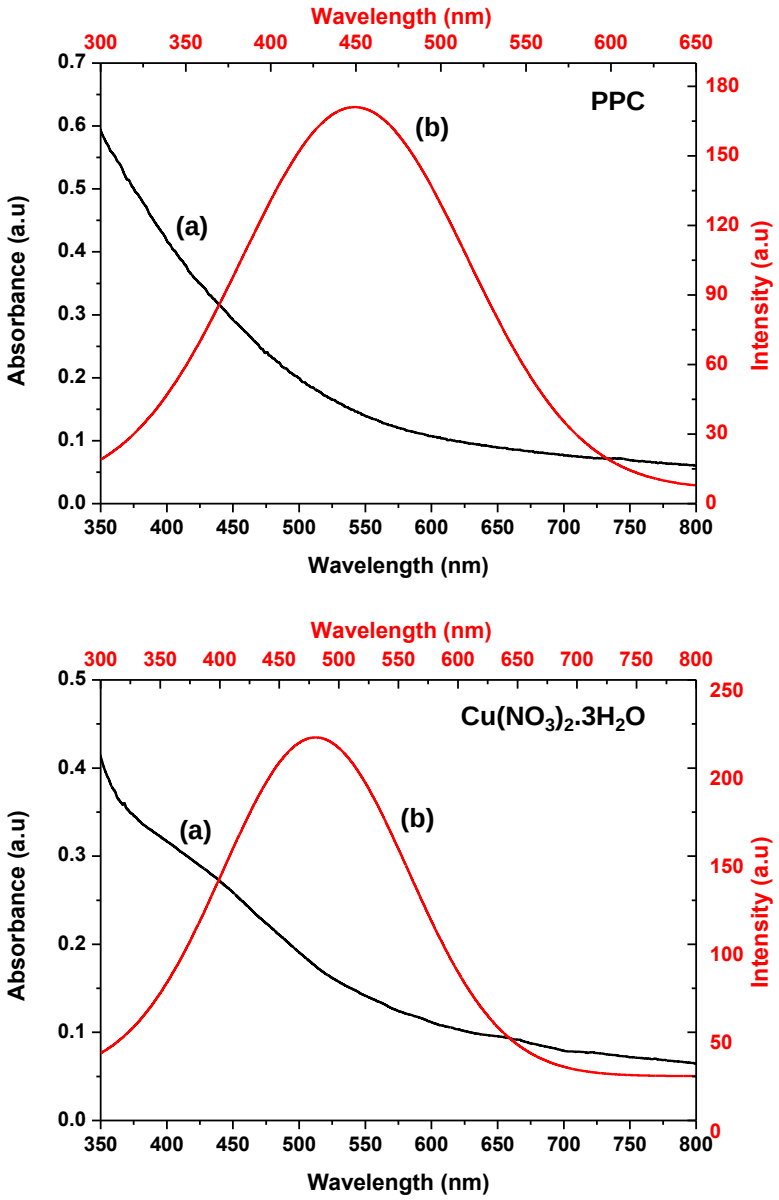

Fig. 9: (a) UV-Vis absorption and (b) photoluminescence spectra of nanocrystals synthesized from PPC and $Cu(NO_3)_2.3H_2O$.

The optical properties of the nanocrystals were then evaluated and are shown in Fig. 9. The band gap energies of Cu_3N obtained from different reports range from 0.23 to 2.06 eV for both bulk and nanocrystals [34]. According to Weber and Hahn, the calculated accurate energy gap for bulk

Cu_3N should be 0.23 eV [35]. The nanocrystals obtained from the PPC complex have a band gap of about 2.21 eV whilst $Cu(NO_3)_2.3H_2O$ synthesized nanocrystals show a band gap of 1.89 eV as extracted from the UV-Vis absorption spectra. The slight blue-shift of the band gap of the PPC compared to $Cu(NO_3)_2.3H_2O$ synthesized nanocrystals is consistent with the smaller sizes observed for the PPC nanocrystals. Nevertheless, both samples had blue-shifted band gaps from bulk due to quantum confinement effects. The emission spectra for both samples are blue-shifted from their corresponding band edges with the emission maxima at 450 nm and 480 nm respectively. The anti-Stokes shift of the emission spectra is indicative an up-conversion process as a result of phonon interactions.

4. Conclusions

In summary, we have demonstrated that single-source precursors can be used in the synthesis of Cu_3N nanocrystals. Furthermore, we have shown that having a pre-existing Cu-N bond prevents the formation of CuO and Cu as in the PPC complex and that the nitrate anion also acts as a source of nitrogen and also prevent the opportunistic formation of the oxides. The choice of precursor also determines the resultant morphology. Spherical morphology was obtained for PPC synthesized nanocrystals whilst cube-like morphology was obtained from $Cu(NO_3)_2.3H_2O$ synthesized nanocrystals. In addition, the synthesized nanocrystals had band gaps in the visible region with anti-Stoke shifted emission spectra. This therefore suggests that Cu_3N nanocrystals can be used in up-conversion optoelectronic devices.

References

[1] R. Juza, H. Hahn, *Zeitschrift für Anorganische und Allgemeine Chemie*, 239 (1938) 282-287.

[2] W. Tao, L. Rui-Shan, P. Xiao-Jun, Z. Pei-Zeng, Z. Ming, S. Xi, X. Er-Qing, *Chinese Physics Letters*, 26 (2009) 066801.

[3] I. Odeh, *Journal of Alloys and Compounds*, 454 (2008) 102-105.

[4] D. Dorranian, L. Dejam, A. Sari, A. Hojabri, *The European Physical Journal Applied Physics*, 50 (2010) 20503.

[5] D. Dorranian, L. Dejam, G. Mosayebian, *Journal of Theoretical and Applied Physics*, 6 (2012) 13.

[6] A. Hojabri, N. Haghighian, K. Yasserian, M. Ghoranneviss, *IOP Conference Series: Materials Science and Engineering*, IOP Publishing, (2010), pp. 012004.

[7] M.G. Moreno-Armenta, G. Soto, *Solid State Sciences*, 10 (2008) 573-579.

[8] Z. Hou, *Solid State Sciences*, 10 (2008) 1651-1657.

[9] M.G. Moreno-Armenta, A. Martínez-Ruiz, N. Takeuchi, *Solid State Sciences*, 6 (2004) 9-14.

[10] D.-y. Wang, N. Nakamine, Y. Hayashi, *Journal of Vacuum Science & Technology A: Vacuum, Surfaces, and Films*, 16 (1998) 2084-2092.

[11] W. Yu, J. Zhao, C. Jin, *Physical Review B*, 72 (2005) 214116.

[12] M. Mikula, D. Búc, E. Pincik, *Acta Physica Slovaca*, 51 (2000) 35-43

[13] Z. Li, R.G. Gordon, *Chemical Vapor Deposition*, 12 (2006) 435-441.

[14] S. Chwa, K. Kim, *Journal of Materials Science Letters*, 17 (1998) 1835-1838.

[15] A. Fallberg, M. Ottosson, J.O. Carlsson, *Chemical Vapor Deposition*, 15 (2009) 300-305.

[16] Z. Liu, W. Wang, T. Wang, S. Chao, S. Zheng, *Thin Solid Films*, 325 (1998) 55-59.

[17] C.M. Caskey, R.M. Richards, D.S. Ginley, A. Zakutayev, *Materials Horizons*, 1 (2014) 424-430.

[18] L. Maya, *Journal of Vacuum Science & Technology A: Vacuum, Surfaces, and Films*, 11 (1993) 604-608.

[19] M. Asano, K. Umeda, A. Tasaki, *Japanese Journal of Applied Physics*, 29 (1990) 1985.

[20] H. Wu, W. Chen, C, *Journal of the American Chemical Society*, 133 (2011) 15236-15239.

[21] P. Xi, Z. Xu, D. Gao, F. Chen, D. Xue, C.-L. Tao, Z.-N. Chen, *RSC Advances*, 4 (2014) 14206-14209.

[22] T. Nakamura, H. Hayashi, T.-a. Hanaoka, T. Ebina, *Inorganic Chemistry*, 53 (2013) 710-715.

[23] R. Salomon, J. Kochi, *Journal of the American Chemical Society*, 95 (1973) 1889-1897.

[24] Y. Du, B. Xu, T. Fu, M. Cai, F. Li, Y. Zhang, Q. Wang, *Journal of the American Chemical Society*, 132 (2010) 1470-1471.

[25] V.V. Grushin, W.J. Marshall, *Advanced Synthesis & Catalysis*, 346 (2004) 1457-1460.

[26] G. Sheldrick, SHELXS-97, *Program for Crystal Structure Solution*, University of Göttingen, Göttingen, Germany (1997);(b) GM Sheldrick, SHELXL-97, *Program for Crystal Structure Refinement*, University of Göttingen, Göttingen, Germany, (1997).

[27] A. Atewologun, W. Ge, A.D. Stiff-Roberts, *Journal of Electronic Materials*, 42 (2013) 809-814.

[28] I-S. Liu, H-H. Lo, C-T. Chien, Y-Y. Lin, C-W. Chen, Y-F. Chan, W-F. Sue, S-C. Liou, *Journal of Materials Chemistry*, 18 (2008) 675-682.

[29] D. Wang, Y. Li, *Chemical Communications*, 47 (2011) 3604-3606.

[30] R. Deshmukh, U. Schubert, *Journal of Materials Chemistry*, 21 (2011) 18534-18536.

[31] W. Lengauer, *Journal of Crystal Growth*, 87 (1988) 295-298.

[32] V.K. Lamer, R.H. Dinegar, *Journal of the American Chemical Society*, 72(11) (1950) 4847-4854.

[33] N. Moloto, M.J. Moloto, N.J. Coville, S.S. Ray, *Journal of Nanoscience and Nanotechnology*, 10(9) (2010) 5594-5601.

[34] T. Xaba, M.J. Moloto, N. Moloto, *Materials Letters*, 146 (2013) 91-95.

[35] U. Hahn, W. Weber, *Physical Review B*, 53 (1996) 12684.

Chapter 5

Elucidating the effect of time on the structural and optical properties of copper (I) nitride nanocubes

Abstract

To study the effect of time on the colloidal synthesis of Cu_3N nanoparticles, copper (II) nitrate was thermally decomposed at 260 °C for up to 60 min in octadecylamine as stabilizing ligand. Thermolysis of the nitrate followed four steps which include; nucleation, growth, ripening and decomposition. At 5 min, partially developed nanocubes were found in a dense population of Cu_3N nuclei. Well-defined Cu_3N nanocubes were obtained at 15 min with no presence of the nuclei. TEM images showed disintegration of the cubes at 20 min and as time progressed, all the Cu_3N decomposed to Cu by 60 min. The formation of the Cu_3N nanocubes was confirmed by XRD and XPS. FTIR suggested the formation of a nitrile (RCN) as a result of the thermal decomposition in octadecylamine (ODA) and this was confirmed using proton NMR and hence, a reaction mechanism was then proposed. The optical properties of the as-synthesized Cu_3N were studied using UV-Vis and photoluminescence spectroscopies. The absorption spectra for particles synthesized from 5 min to 15 min showed a singular exciton peak while from 20 min to 60 min two peaks were observed. The two peaks may both be associated with the two direct transition observed in Cu_3N or the more red-shifted peak could be as a result of localized surface plasmon resonance due to the Cu nanoparticles. Nevertheless, similar to other studies, it is clear that the optical properties of Cu_3N are complex.

Keywords: Copper nitride; structural properties; optical properties

1. Introduction

The industrial application of semiconducting nanomaterials cannot be overemphasized, more especially in photonics and medicine. Colloidal synthesis of Cu_3N continues to receive tremendous research focus marking a variation from the popular solid-state methods which involves the use of RF magnetron sputtering. In literature, there are many discrepancies in the data that has been reported for Cu_3N nanoparticles (NPs). For example, the band gap and thermal stability and this has been attributed to the unstable nature of Cu_3N acquired during the growth stage [1]. Researchers are slowly turning their focus to solution-based synthesis of Cu_3N NPs due to the ease with which the desired morphology and properties of the NPs can be engineered. Few reports have demonstrated that Cu_3N NPs can be synthesized by employing ammonolysis or use of N sources such as azide, hexamethylenetetramine and urea but the challenge with these methods is that the resultant NPs are ill-shaped [2, 5-8]. Special attention is recently being given to the synthesis of Cu_3N NPs using direct thermal decomposition of $Cu(NO_3)_2.3H_2O$ in octadecylamine (ODA) to obtain well defined nanocubes [9-13]. Thermal decomposition of other metal nitrates for example, $Mn(NO_3)_2$, $Ni(NO_3)_2.6H_2O$, $Zn(NO_3)_2.6H_2O$, $Ce(NO_3)_3.6H_2O$, $Co(NO_3)_2.6H_2O$ in ODA resulted in the formation of corresponding metal oxides and not metal nitrides [14]. Wang *et al.* [11] demonstrated that it is very crucial to control the concentration of $Cu(NO_3)_2$ in ODA in order to get Cu_3N and not Cu or its oxides. Xi *et al.* [13] reported on the formation of Cu_3N upon decomposing $Cu(NO_3)_2$ in a mixture of two reducing agents, ODA and oleylamine (OLA) at 240 °C for up to 10 min. The report revealed that very few cubes were observed amongst small nuclei of Cu_3N after 2 min but only cubes were present after 10 min. However, the authors did not report on the effect of time beyond 10 min. Herein, we probe the effect of precursor decomposition time on the formation of Cu_3N nanocubes through thermolysis of $Cu(NO_3)_2$ at 260 °C for up to 60 min

in ODA as the capping and reducing agent. Progression in the formation of the Cu_3N nanocubes could be summarized in four stages namely; nucleation, growth, ripening and decomposition. In order to verify our findings, the same synthetic procedure was followed using hexadecylamine (HDA) as the capping and reducing agent. In nanosynthesis, high temperatures are generally known to be conducive for nucleation whilst low temperatures are known to be conducive for growth of nanoparticles. In the colloidal synthesis of Cu_3N, 260 ^oC is generally high, hence the study seeks to investigate the synthesis under conditions that seek to promote nucleation and not necessarily nanoparticle growth.

2. Experimental section

Materials

Copper (II) nitrate trihydrate (puriss p.a., 99-104%), octadecylamine (ODA), octadecene, hexadecylamine (HDA) (technical grade, 90%), chloroform (anhydrous, ≥99%, contains 0.5-1.0% ethanol as stabilizer) and ethanol (absolute, ≥99.8% (GC)) were purchased from Sigma-Aldrich.

Synthesis of Cu_3N Nanoparticles

The controlled synthesis of Cu_3N nanocrystals was achieved by thermal decomposition of copper (II) nitrate in octadecylamine. $Cu(NO_3)_2.3H_2O$ (12.5 mmol) was dissolved in octadecene (1 ml), mixed with ODA (10 ml) and degassed under a continuous flow of N_2 gas at 110 °C. After an hour, the temperature was slowly raised to 260 °C. Aliquots were then extracted at 5, 10, 15, 20, 30 and 60 min. Powders were obtained after repeated washing in ethanol and were kept under inert conditions before characterization.

Characterization

A Varian Cary Eclipse (Cary 50) UV-Vis spectrophotometer was used to carry out the optical properties of the NPs. The photoluminescence spectra of the NPs were recorded on a Varian Cary Eclipse EL04103870 spectrofluorometer with a medium PMT voltage at an excitation wavelength of 200 nm. The absorption and emission spectra were obtained in chloroform and placed in quartz cuvettes (1cm path length). Powdered XRD patterns of the samples were measured on a Bruker MeasSrv D2-205530 diffractometer using Co Kα radiation ((λ 1.78897 Å) at 30 kV/10 mA. The XRD data was acquired using a Bruker Lynxeye PSD detector set to measure at 5^{o} 2θ and all measurements were acquired at room temperature. The data was analyzed using Bruker AXS Evaluation package (EVA, 2008) equipped with ICDD PDF 4+. X-ray photoelectron spectroscopy measurements were performed with a PHI 5000 Versaprobe - Scanning ESCA Microprobe operating with a 100 µm 25 W 15 kV Al monochromatic X-ray beam. The transmission electron microscopy (TEM) was carried out on a FEI Technai T12 operated at an acceleration voltage of 200 kV with a beam spot size of 20 - 100 nm in TEM mode. The vibrational modes were measured on a Bruker Tensor 27 FT-IR and the nuclear magnetic resonance (NMR) data was obtained using a 500 MHz Bruker AVANCE III, the samples were run using $CDCl_3$ as a solvent at 300K. The acquired NMR data was analyzed using MNOVA software.

3. Results and discussion

The powder X-ray diffraction was used to determine the crystal phases of the resultant NPs and for the detection of any impurities. Shown in Fig. 1 are the XRD patterns of the NPs synthesized from 5 min to 60 min in ODA. The series of Bragg reflections in the given patterns show peaks that correspond to planes (100), (110), (111), (200), (210), (211), (220) and (320) of the cubic

phase of Cu_3N (card number JCP2.2CA:00-002-1156). The sharp peaks that were obtained show that the Nps obtained were highly crystalline. An additional peak from the 20 min sample is observed at $2\theta = 50.61°$ showing the initial stage of Cu formation. More copper peaks emerge till all the Cu_3N had been converted to Cu (JCP2.2CA:00-085–1326) at 60 min. These sets of data show that thermal decomposition of $Cu(NO_3)_2$ in ODA at 260 °C result in the formation of Cu_3N after about 5 min. Cu_3N continues to be the only product present until about 20 min, then the Cu_3N NPs begin to decompose until only Cu is detected at 60 min. Understanding of the metallization of Cu_3N can come in handy in making microscopic Cu metallic links during the fabrication of optical recording media [15] and optical data storage [16].

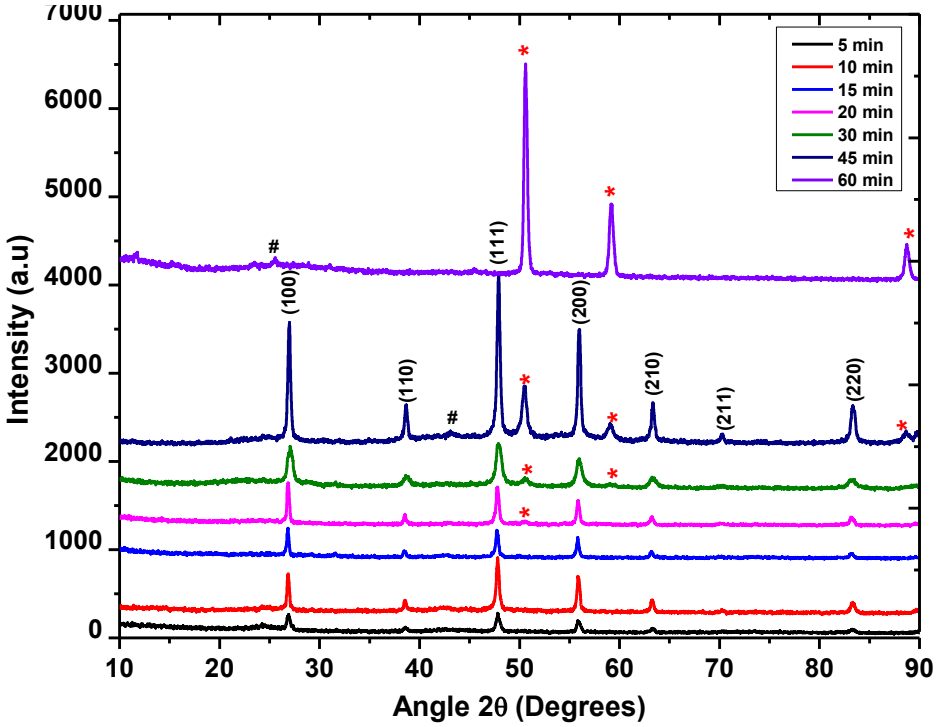

Fig. 1: Powder XRD diffractograms of Cu_3N NPs obtained after 5, 10, 15, 20, 30, 45 and 60 min at 260 °C in ODA. The symbol (*) shows peaks for Cu and (#) decomposition product of the capping agent.

The composition of the formed Cu_3N NPs and oxidation states of Cu and N was further confirmed by employing X-ray photoelectron spectroscopy (XPS) and the results are shown in Fig. 2 and Fig. 3. From the survey spectra, it can be deduced that the as-synthesized Cu_3N NPs contain C, O, N and Cu. Majumdar *et al.* [17] discovered that Cu_3N films that were synthesized by RF magnetron sputtering consisted of 20.4% C and 35.5% O after being exposed to air. As such, exposure of the as-synthesized Cu_3N NPs to air and the presence of the organic stabilizer could explain the observed pivotal amount of C in the sample as seen in Fig. 2. Two peaks centralized at 285.35 and 285.95 eV from the C 1s high-resolution spectrum confirm the presence of C in the sample. The presence of oxygen is inevitable because the NPs are exposed to air. The O 1s spectrum has a broad peak that is centered at 532.04 eV and deconvolution of the O 1s spectrum gives rise to two peaks at 531.87 and 533.36 eV that are ascribed to the presence of C-O and C=O respectively [12].

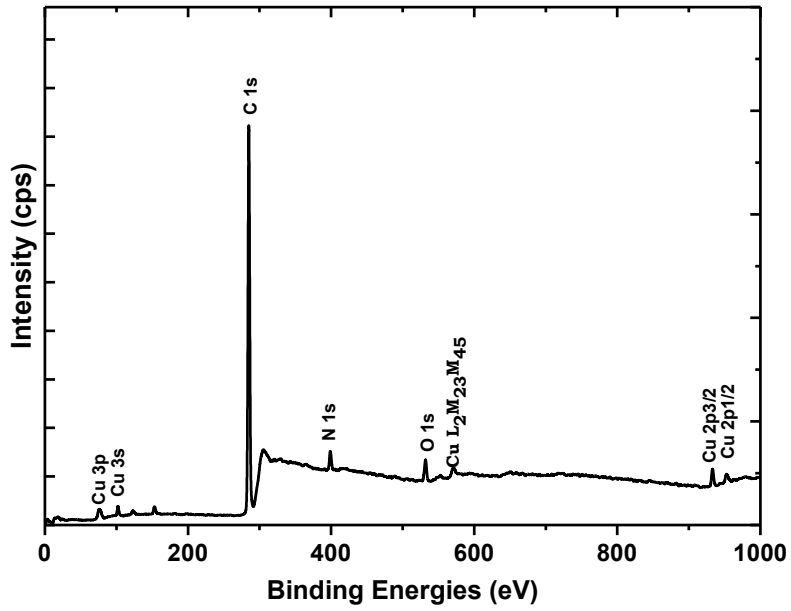

Fig. 2: XPS wide scan of Cu_3N NPs (15 min sample).

The NPs were synthesized in a nitrogen-rich atmosphere and N 1s high-resolution XPS depicts the main peak centered at 399.70 eV showing the main bonding of nitrogen in the Cu_3N nanocubes. This value is higher than the 397.7 eV that has been reported [18-21]. The peak at 403.01 eV is said to be a result of dissolved nitrogen in the Cu_3N [19] or N_2 that is adsorbed/loosely bound to the surface [22, 23]. Interestingly, Navio *et al.* and others were of the idea that the 397.7 eV peak is attributed to the presence of nitrogen that is adsorbed to the surface of the $Cu_3N(100)$ and the second peak that they obtained at 398.7 eV was attributed to the presence of N that is in the bulk of the Cu_3N [20, 24].

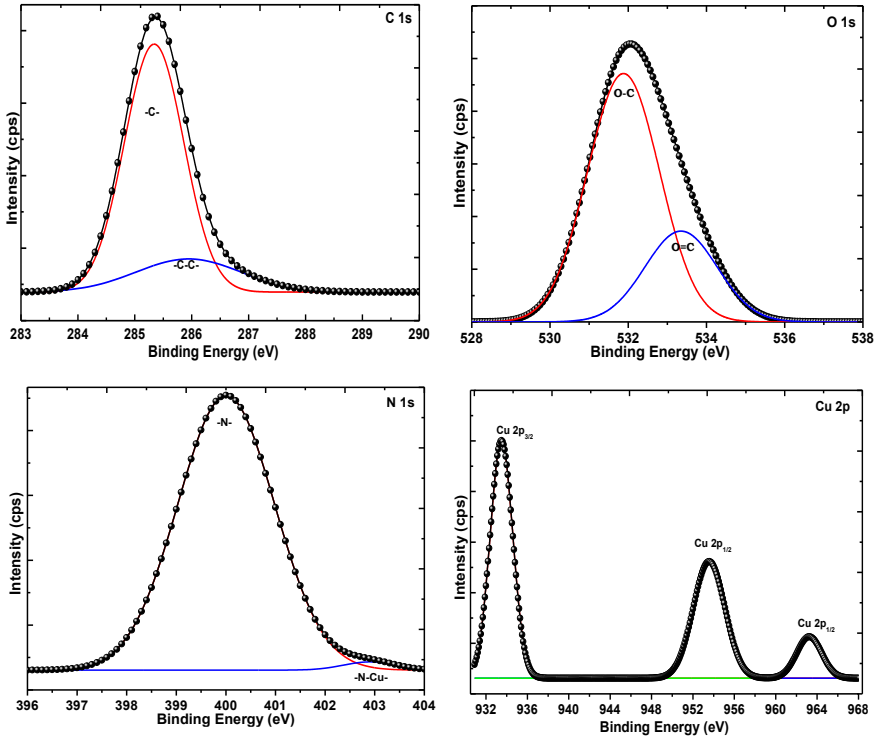

Fig. 3: High-resolution spectra of Cu_3N NPs with focus on C 1s, O 1s, N 1s, and Cu 2p.

In the Cu 2p spectrum, the expected Cu^+ peaks were obtained at 933.48 eV and 953.52 eV of the Cu $2p_{3/2}$ and Cu $2p_{1/2}$ states respectively, consistent with previous reports [25]. Corresponding

shakeup peaks at around 934.4 and 954.63 eV [25] were not obtained hence suggesting the lack of Cu^{2+} in the NPs. However, a peak of relatively lower intensity was obtained around 963.20 eV and reports [26-28] have associated this peak as a shakeup peak to Cu $2p_{1/2}$ suggesting the presence of CuO. In the XRD pattern, there were no evident peaks that could be ascribed to CuO hence, the detected oxide in the Cu_3N nanocubes could be a result of mild surface oxidation due to exposure to atmospheric oxygen.

To study the morphology of the as-synthesized NPs, powders were dispersed in chloroform and drop-casted onto Cu and Ni grids. After drying, they were then analyzed and imaged under the transmission electron microscope and the images are shown in Fig. 4. The images obtained show that the sample that was collected after 5 min at 260 °C consisted of mixed morphology. Relatively few nanocubes were found in between a cloud of very small dot-like NPs. A closer look revealed that some of the nanocubes were incompletely formed and in close contact with a number of the dot-like NPs. In another study, Xi *et al.* obtained a similar mixture of nuclei and cubes after 5 min of thermal decomposition of $Cu(NO_3)_2$ in a mixture of ODA and oleylamine at 240 °C [13].

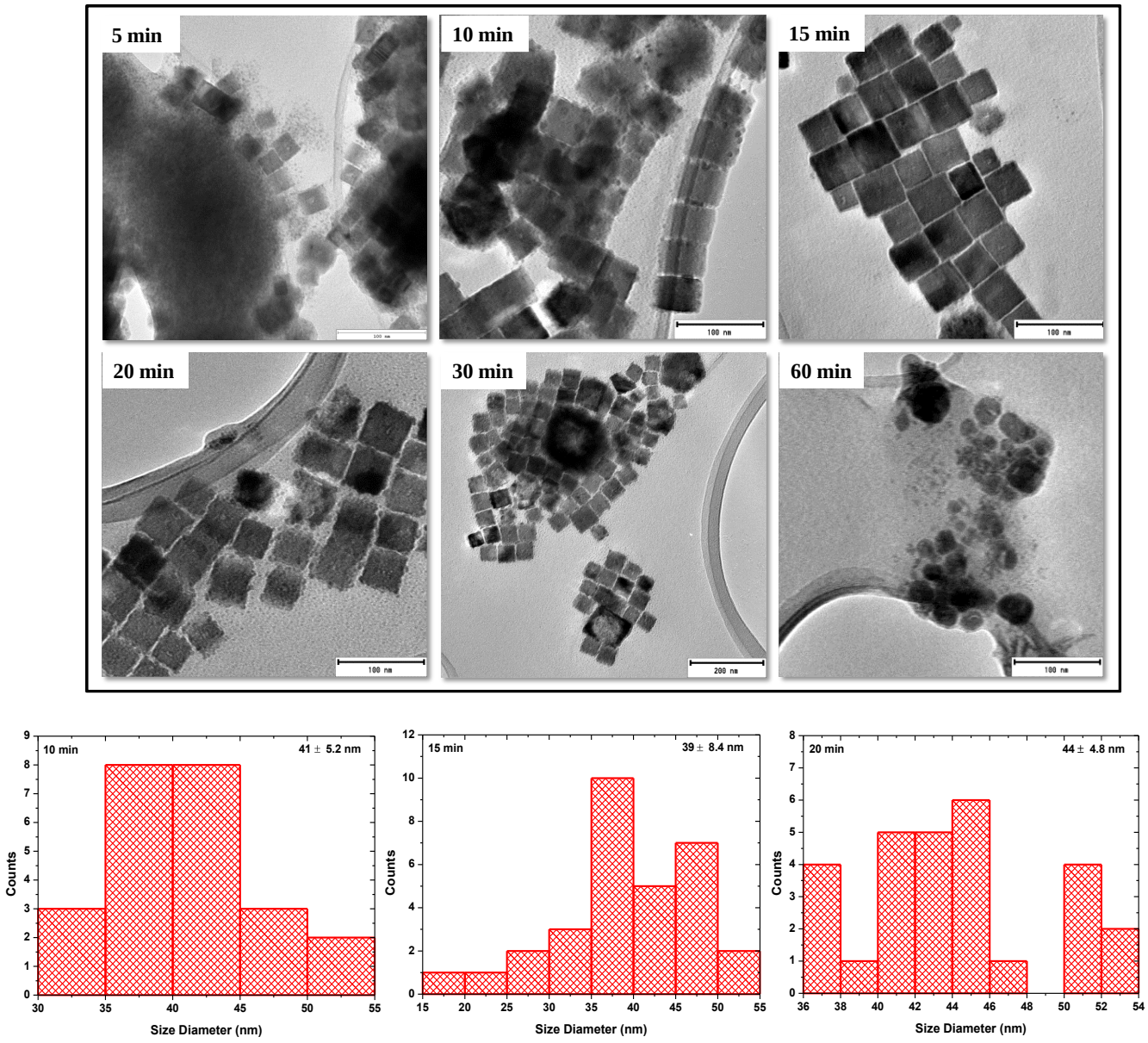

Fig. 4: TEM images of Cu_3N NPs obtained after 5, 10, 15, 20, 30 min and 60 min in ODA and size distribution for 10, 15 and 20 min samples. (All scales are 100 nm except 30 min that is 200 nm)

At 10 min, there was a much greater population of the nanocubes and much less of the dot-like NPs and the nanocubes were much more defined and showed some degree of self-assembly. The

‘dots’ could still be seen and some were found on and in between the cubes and on the edges of the cubes hence making it slightly difficult to measure the size of the cubes as some of them did not possess well-defined edges, nevertheless, the average size was estimated to be 41 ± 6.2 nm. The 15 min sample brought about a change in composition. The nanocubes were aligned next to each other resembling a pattern of layered bricks. The dot-like NPs were almost non-existent and the edges of the cubes were well-defined with no evidence of dots on them. These were then named ‘perfect nanocubes’ and measurement of their edges gave a 39 ± 8.4 nm. At 20 min of synthesis, the ‘perfect nanocubes’ were no longer perfect however, the sizes could still be estimated at 44 ± 4.8 nm. They looked like they were crumbling and the edges started having the dot-like NPs again. At this stage, XRD shows the emergence of a peak around $2\theta = 50.6\ °$ that was assigned to Cu. Attempted measurements of the edges gave a rough estimate of 44 nm and no further measurements were taken thereafter as the nanocubes had no well-defined shapes. The breakdown of the nanocubes continued and by 30 min, the brokendown cubes seemed to affect the neighbouring cubes resulting in the formation of giant cube-like structures with hollow interiors. At this stage, Cu related peaks could be seen on the XRD pattern although they were of very low intensity compared to the Cu_3N peaks. By 60 min, no cubes could be seen but polydispersed nanoparticles were obtained and the XRD showed peaks that were all ascribed to Cu and there was no evidence of peaks that could be associated with Cu_3N.

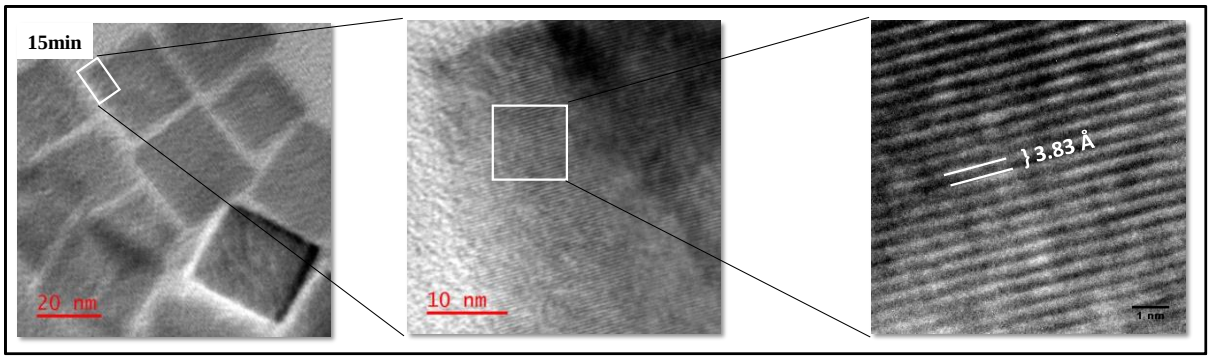

Fig. 5: HRTEM of Cu_3N NPs synthesized after 15 min in ODA.

Shown in Fig. 5 are the HRTEM images of the perfect nanocubes. The nanocubes have lattice fringes with the d-spacing of 3.83 Å corresponding to the (100) plane of the anti-ReO_3 cubic structure of Cu_3N. This is consistent with the results obtained in the X-ray diffraction in Fig. 1.

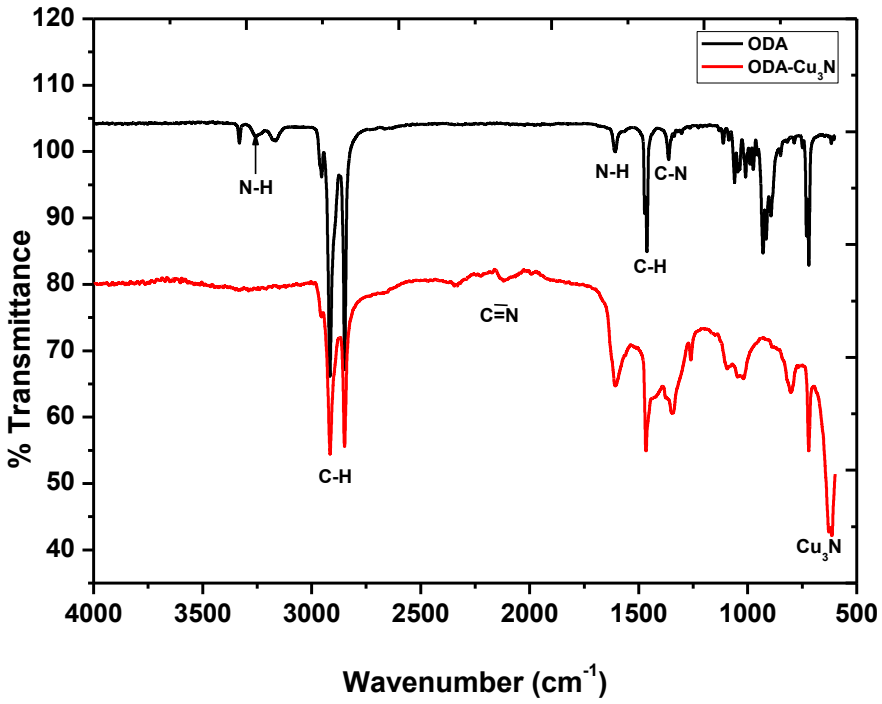

Fig. 6: FTIR spectra of the 15 min synthesized Cu_3N NPs and raw ODA.

To investigate the coordination of the ligand, Fourier transform infra-red (FTIR) spectroscopic analysis was performed and the spectrum that was obtained from the nanoparticles synthesized in 15 min was compared with that of raw ODA (Fig. 6). Generally, the results show that the Cu_3N NPs were capped by the organic ligand, as the corresponding vibrations in ODA were detected on the synthesized NPs. The characteristic C-H stretching vibrations were obtained from 2845 to 2959 cm^{-1} and the $–CH_2$ bending vibrations at 1460 cm^{-1} is slightly shifted from the 1465 in ODA showing that the chemical environment has slightly changed due to the coordination. A sharp peak was obtained at 624.6 cm^{-1} which is very close to the 639 [29], ~650 [6] and 653 cm^{-1} [5] cm^{-1} that were obtained in previous reports ascribed to Cu-N vibrations in copper (I) nitride [30].

Wang and Li [11] suggested that the ODA does not participate in the reaction but rather acts as a catalyst that facilitates the transfer of electrons from O^{2-} to Cu^{2+} and N^{5+} of the nitrate. However, we are of the notion that ODA is most likely a participant in the reaction. In the FTIR spectra, the symmetric and antisymmetric N-H vibration modes found at 3259.5 and 3333 cm^{-1} respectively on the ODA spectrum were not detected on the Cu_3N spectrum. Instead, a new peak was spotted at 2120 cm^{-1} and can be assigned to C≡N stretching vibration mode. In another stud, this peak was detected at about 2092 cm^{-1} and we agree with the authors who suggested the possibility of the existence of C≡N due to the high temperature breakdown of ODA [10].

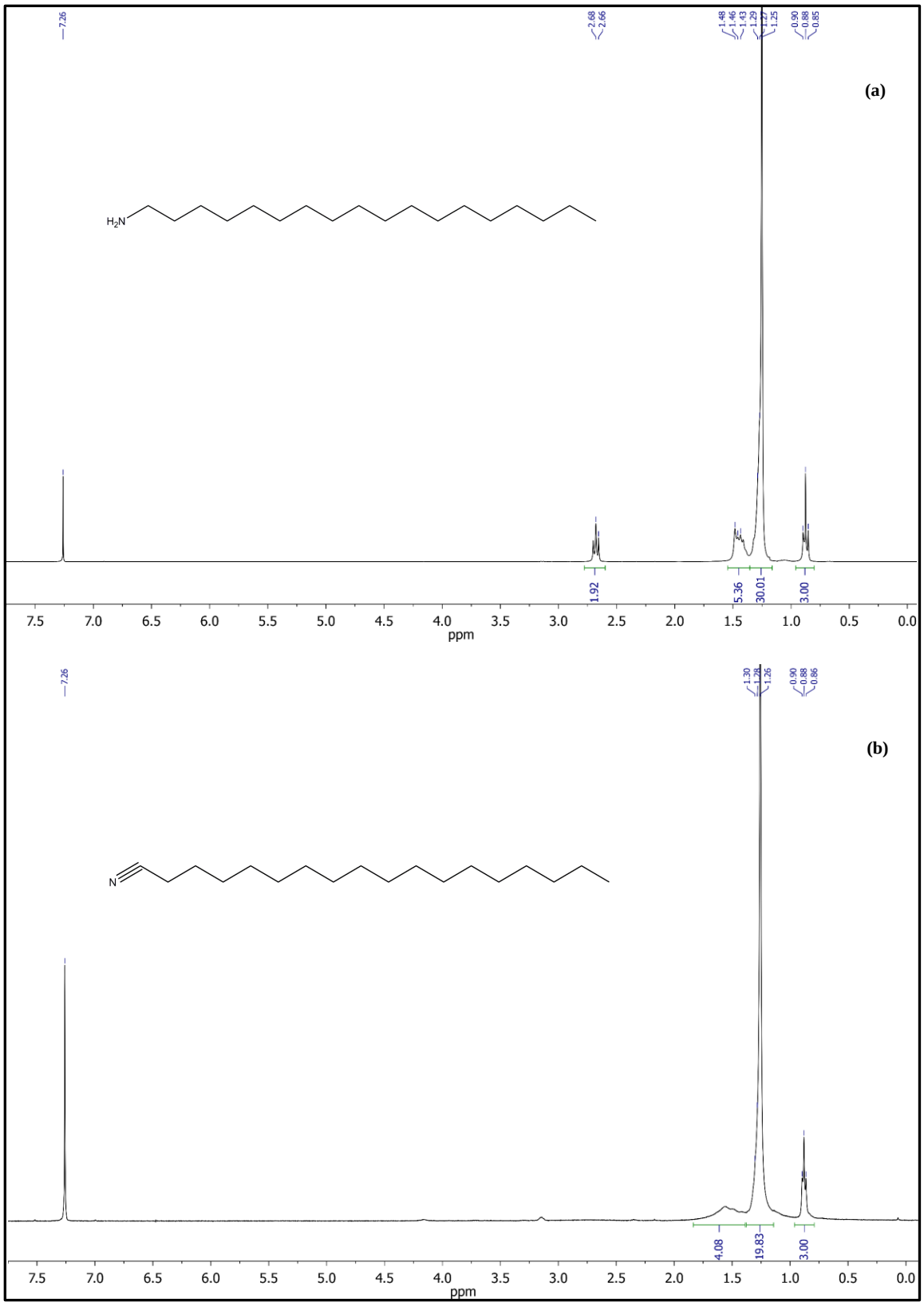

Fig. 7: ^{1}HNMR spectra of (a) ODA and (b) Cu_3N nanocubes in $CDCl_3$ (15 min sample).

To further probe this theory, the as-synthesized Cu_3N nanocubes and raw ODA were analyzed using proton nuclear magnetic resonance (^{1}H NMR). Analysis of the ^{1}H NMR clearly revealed the deprotonation of the ODA ($CH_3(CH_2)_{16}CH_2$-NH_2), resulting in the formation of stearonitrile ($CH_3(CH_2)_{16}C\equiv N$). From the ^{1}HNMR spectra in Fig. 7, the resonance for the H_3C- protons is centralized around δ0.88 ppm in both the spectra of raw ODA and the Cu_3N NPs. At δ1.25 and δ1.26 ppm, a singlet is observed in both spectra and it accounts for protons that are on the CH_2 chains respectively. Henceforth, notable differences were observed in the two spectra. In the raw ODA, a slightly broad triplet was observed centralized at δ1.46 ppm but on the other hand, the spectrum that was obtained from the NPs showed a very broad peak with a peak maximum at δ1.57 ppm. Thereafter, no further proton peaks were detected on the spectrum of the Cu_3N NPs but a triplet was obtained at δ2.68 ppm on raw ODA and this accounted for the missing 2 H in the -CH_2 that is directly bonded to the N on the amine end. These CH_2 protons are clearly non-existent in the spectrum of the Cu_3N NPs. This is most probably because the H on the H_2N-CH_2- are all involved in the reaction that leads to the formation of Cu_3N NPs and stearonitrile remains as a by-product as depicted in the proposed chemical equation below:

$$3Cu(NO_3)_2 + 3CH_3(CH_2)_{16}CH_2NH_2 \rightarrow Cu_3N + 5NO + \frac{7}{2}O_2 + 6H_2O + 3CH_3(CH_2)_{16}C \equiv N \qquad (1)$$

The formation of the stearonitrile is in agreement with the C≡N vibration modes that were detected at 2120 cm^{-1} on the FTIR spectra in Fig. 6. At temperatures above 21.2 °C, NO_2 is a reddish-brown gas with an pungent odor and it decomposes at about 160 °C [31] to give NO and O_2 which are both colorless gases. At the reaction temperature of 260 °C that was used in this investigation, it

is most likely that the colorless NO and O_2 gases were emitted as suggested in equation above because no pungent nor colored fumes were observed during the course of the reaction.

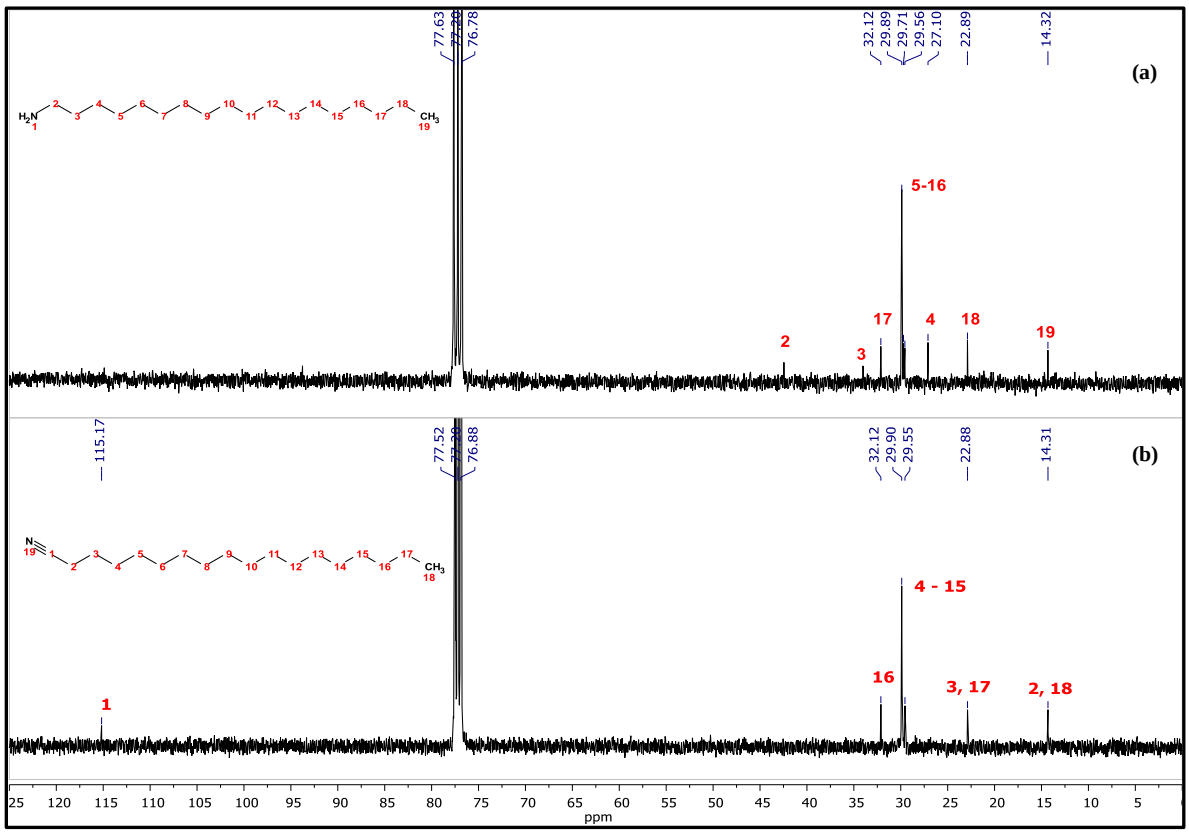

Fig. 8: ^{13}C NMR spectra of (a) ODA and (b) Cu_3N nanocubes in $CDCl_3$ (15 min sample).

The ^{13}C NMR spectra of raw ODA and ODA-capped Cu_3N NPs are shown in Fig. 8. In both spectra, the ^{13}C signals of the methyl and methylene groups were detected around δ 14.32 and 22.89 – 32.12 ppm respectively. Of great interest is the huge downfield shift of the carbon peak at δ 42.46 in raw ODA to δ 115.17 ppm in the NPs which can be used as a diagnostic signal. The obtained 115.17 ppm in this study is lower than the 119.77 ppm that was obtained by Gunstone [32] when he was working with oleyl compounds but fall within the shift ranges of nitriles. This huge downfield shift is due to the deprotonation of the carbon that is bonded to nitrogen, H_2C-NH_2

to form the nitrile (RCN). The appearance of the carbon peak at δ 115.17 ppm suggests the formation of a quaternary nitrile-bearing center hence, confirms the presence of octadecylnitrile in the Cu_3N NPs. Due to the strong influence of the nitrile group, the nearby carbon atoms, C3 and C4 are greatly affected owing to π-electron deshielding and the polar inductive effect [33] of the nitrile group. As suggested in the equation above, the synthesis of Cu_3N nanoparticles involves the process of deprotonation of octadecylamine to form octadecylnitrile. The nitrile group then forms sigma bonds with the Cu^+ ions resulting in end-on coordination hence accounting for the obtained down field shift at 115.17 ppm. If the coordination was side-on through the π system of the triple bond, a farther downfield resonance in the 180- 240 ppm range would have been detected [34].

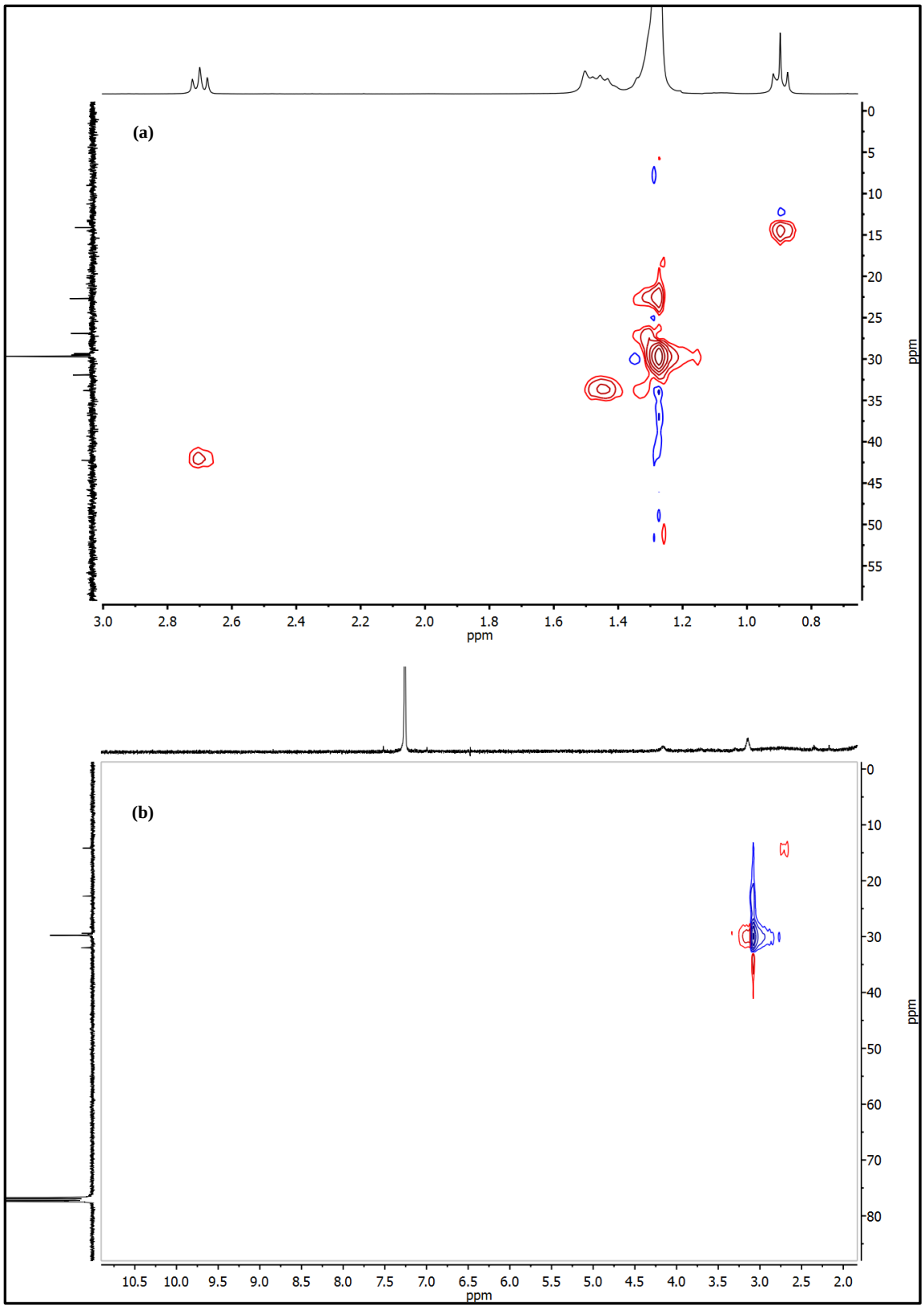

Fig. 9: ^{1}H ^{13}C HSQC NMR spectra of (a) ODA and (b) Cu_3N nanocubes (15 min) in $CDCl_3$.

The protons are matched to the carbon peaks as shown on the ^{1}H ^{13}C HSQC NMR spectra in Fig. 9(a) and 9(b) for both the ODA and Cu_3N nanocubes respectively and all the protons and carbons are accounted for. This confirms that copper is in the oxidation state of +1 since there are no unpaired electrons in the analyzed Cu_3N NPs. If copper existed as Cu^0 or Cu^{2+} in the analyzed Cu_3N 'perfect' nanocubes that were obtained after 15 min, then the spectrum would not have been clearly resolved due to the unpaired electrons that exist in the 4s and 3d orbitals respectively.

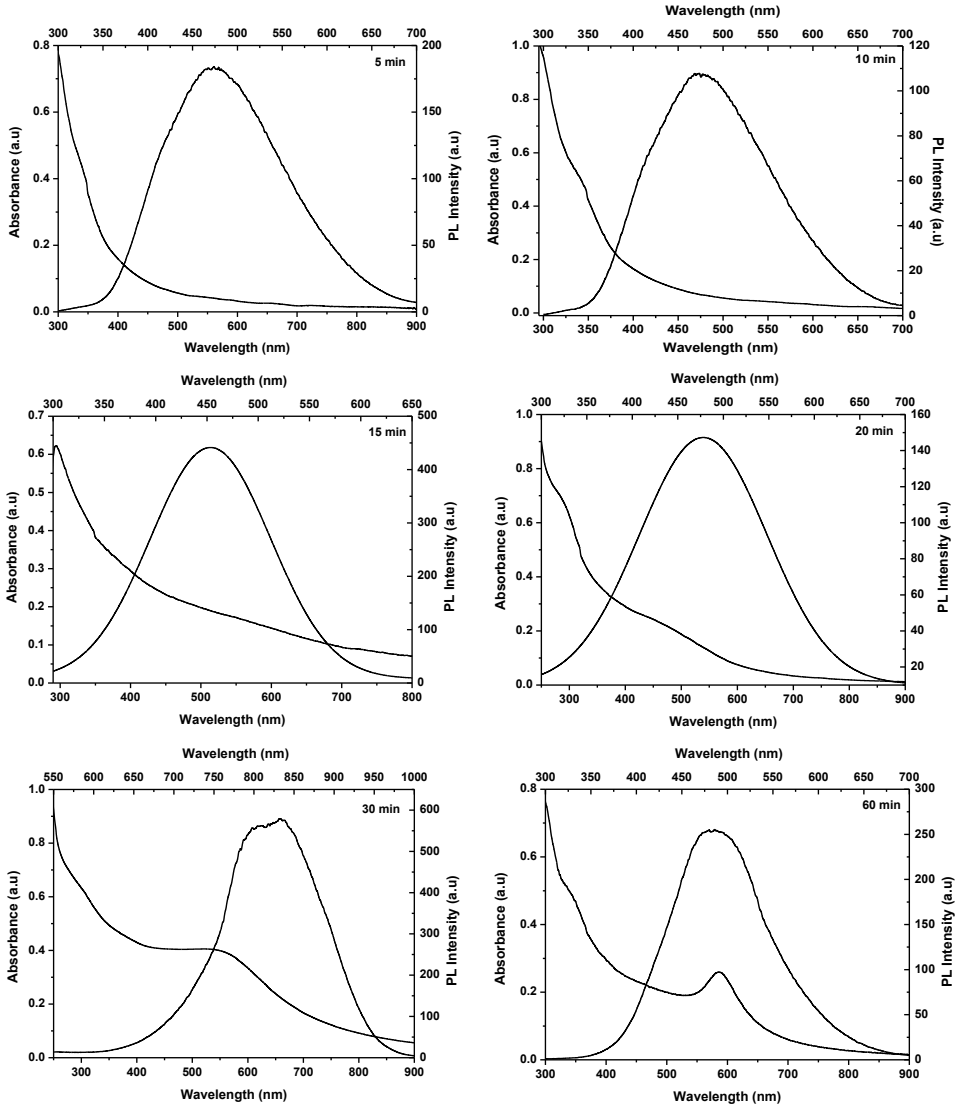

Fig. 10: UV-Vis and PL spectra of Cu_3N NPs obtained at 5, 10, 15, 20, 30 and 60 min.

Table 1: Summary of the optical properties of Cu_3N NPs

Time (min)	Exciton A (nm)	Exciton A (eV)	Exciton B (nm)	Exciton B (eV)	λmax (nm)	λmax (eV)
5	476	2.61	-	-	476	2.61
10	456	2.72	-	-	476	2.61
15	436	2.84	-	-	455	2.73
20	378	3.28	608	2.04	478	2.59
30	340	3.65	760	1.63	832	1.49
60	400	3.10	695	1.78	487	2.55

The optical properties of the resultant Cu_3N NPs were studied using UV-Vis absorption and photoluminescence spectroscopy and the results are depicted in Fig. 10. In literature, there has been controversy with regards to the optical properties of Cu_3N. From the varying band gap values obtained both theoretically and experimentally, they are said to vary between 0.23 eV and 2.06 eV, to the nature of the band gap transition whether it is direct or indirect [35, 36]. Presented in Table 1 is the summary of the optical properties. A single sharp excitonic peak is observed for 5 and 10 min samples whilst a tailing spectrum, also with a single excitonic peak is observed for the 15 min sample. Two peaks are observed for particles synthesized from 20 min to 60 min. From band structure calculations, three transitions have been reported, one indirect and two direct band gaps at the Γ and R points [36]. The exciton A is blue-shifted from the reported values and the transition is in the visible region of the electromagnetic spectrum whilst exciton B is consistent with the reported values with the band gap energies of 1.6 eV – 2.04 eV. The observed trends could be because of quantum confinement effects in the nanocrystals as most reported results are for

bulk Cu_3N [35-36]. Also possible, is the presence of the localized surface plasmon resonance (LSPR) due to the presence of copper nanoparticles. The LSPR for Cu nanoparticles is usually found around 570 nm and can be blue or red shifted due to the size and shape of the nanoparticles, the photoluminescence is usually weak hence the observed photoluminescence peaks are only associated with the semiconducting Cu_3N NPs [37].

The photoluminescence spectra are red-shifted with respect to the excitonic peak A for samples synthesized for 10 – 20 min as well as 60 min however for the 30 min sample the emission maximum correlates with the exciton B transition. The photoluminescence spectra confirm that the resultant nanoparticles are direct band gap semiconductors. Evident from the results is the complexity of the optical properties and the need to further probe these. Based on the obtained results, it is quite evident that Cu_3N is an interesting and rather complex semiconductor. Nevertheless, herein using TEM, a mechanism for the evolution of Cu_3N morphologies can be postulated and it is depicted in Fig. 11. The reaction was started by dissolution of $Cu(NO_3)_2.3H_2O$ in OD and mixed with ODA and then the temperature was raised from room temperature to 110 °C resulting in a deep blue mixture. After an hour, the temperature was slowly increased and at about 165 °C, a very pale yellow clear solution was obtained. This could be a result of the formation of a complex between the Cu(I) ions and octadecylamine as has been observed in a previous study [10]. The blue coloration that was caused by the unpaired electron in the Cu^{2+} suddenly disappeared due to the reduction of Cu^{+2} to Cu^{+} in the presence of ODA. Due to complete d orbital, Cu^{+} does not give off color hence the yellow color is brought about by the complexation that occurs between the Cu(I) ions and the amine. The solution then slowly turned to a clear brown around 200 °C and then to an opaque brown by the time the temperature reached 260 °C. It has

been shown that in direct heating methods, high quality crystals are generally obtained at high temperatures that are above 200 °C hence 260 °C was chosen as the reaction temperature in this study. Also, in nanosynthesis, high temperatures are generally known to be conducive for nucleation whilst low temperatures are known to be conducive for growth of nanoparticles. In the colloidal synthesis of Cu_3N, 260 ^oC is generally high, hence the study seeks to investigate the synthesis under conditions that seek to promote nucleation and not necessarily nanoparticle growth.

The introduction of the brown color indicates the initial stages of the formation of Cu_3N nuclei. An attempt to analyze the samples that were obtained after 30 sec at 260 °C proved futile as the aliquots turned greenish blue upon adding organic solvents like ethanol or chloroform to clean the NPs. This color change indicated the oxidation of the Cu^+ to Cu^{2+}. There was no marked difference between the NPs obtained after 1 min and those obtained at 5 min except that there were more defined nanocubes at 5 min as compared to 1 min as seen in Fig. 11. As such, below 1 min, the nuclei that had formed were not yet stable and reacted rapidly with air and the added solvent. ODA has been reported as having a tendency to bind to the 100 plane of Cu_3N NPs hence it slows down the growth process and facilitates the formation of cubes [10]. High population of 'dots' were detected in the 5 min sample while few cubes had already been formed although not fully developed. The less stable small nanocrystals undergo Oswald ripening [38] as they slowly dissolve and recrystallize on the larger particles giving rise to nanocubes. This was observed at 10 min where self-assembly of cubes was noted and fewer but bigger dots were seen on and in-between the cubes. Subsequent ripening or shaping led to the formation of the 'perfect' nanocubes with smooth edges and no apparent blemishes at 15 min. Continued heating resulted in further

reduction which led to the detected small peak of Cu in the XRD of the 20 min sample. The reduction of the copper ions on the surface of the cubes led to the influx of Cu^{+} ions from the core to the surface of the nanocubes [39]. As such, the smooth surface that had been observed on the 'perfect' nanocubes could no longer hold on the NPs that were obtained at 20 min. The cationic movement of Cu^{+} from the core of the cubes to the edges continued and voids can be seen in the interior of the distorted cubes, consequently resulting in the reemission of nitrogen. This phenomenon occurs when the barrier that prevents recombination of N atom to form N_2 gas has been overcome. As the cubes broke down, they joined together to form larger cubes with void interiors. That is why at this stage, pronounced Cu peaks could be detected at 30 min as Cu_3N decomposed and the Cu^{+} was reduced to Cu^{0} whilst the N^{3-} was oxidized to nitrogen gas. Finally, with time, 'all' Cu_3N had been reduced to Cu hence no copper nitride peaks could be detected after 60 min.

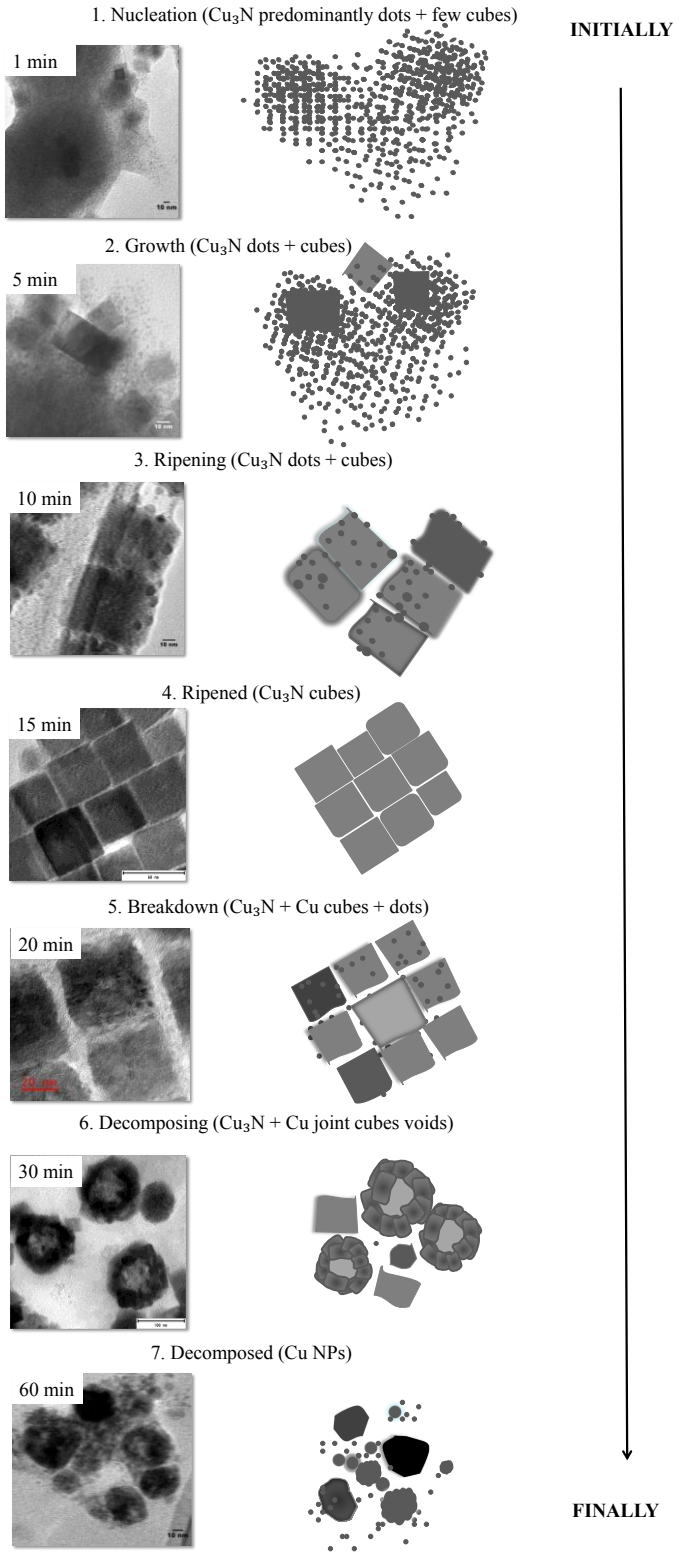

Fig. 11: Steps followed in the colloidal thermolysis of $Cu(NO_3)_2$ in ODA to form Cu_3N NPs and eventually Cu.

To determine if this is a unique feature to octadecylamine, the coordinating ligand was changed from ODA to hexadecylamine (HDA). The same synthetic procedure was followed and the resultant X-ray diffractograms are shown in Fig. 12.

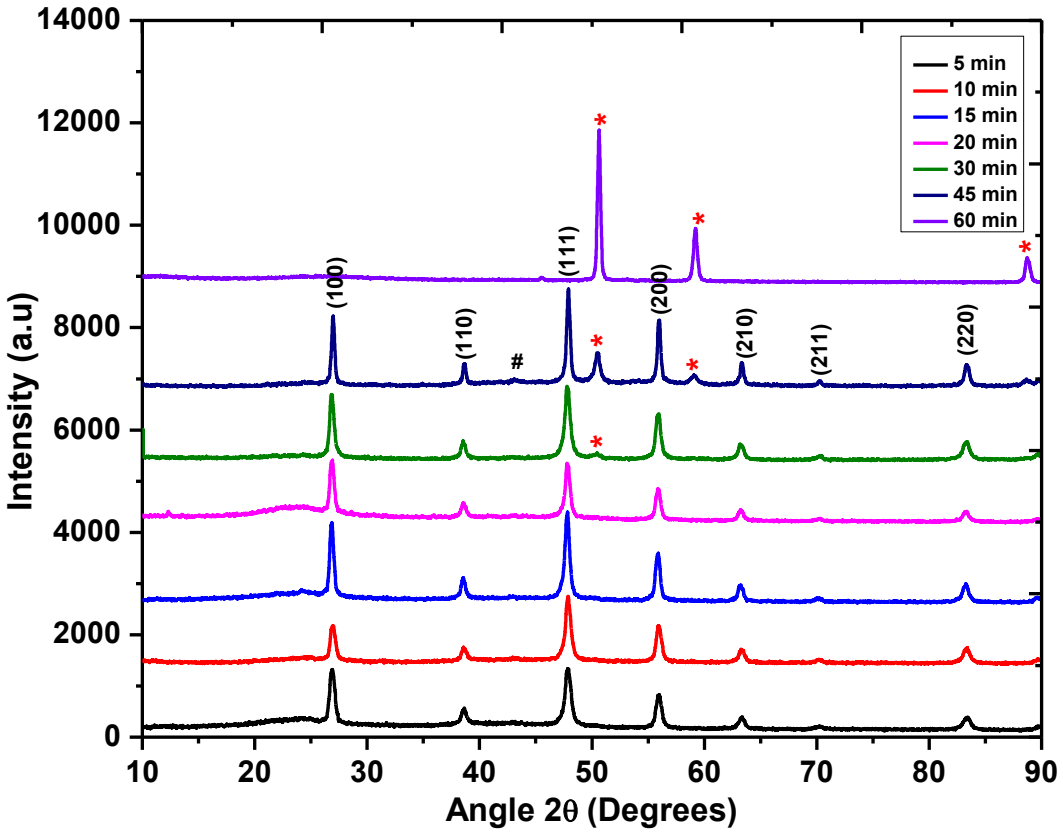

Fig. 12: Powder XRD of Cu_3N NPs obtained after (a) 5, 10, 15, 20, 30, 45 and 60 min at 260 °C in HDA. The symbol (*) shows peaks for Cu and (#) decomposition product of the capping agent.

The XRD diffractograms showed a similar pattern with the one obtained in ODA, the main difference being the initial detection of Cu occurring after 30 min whilst in ODA it was detected at 20 min. This difference was seen in the TEM images of the NPs that were obtained in HDA. 'Perfect' nanocubes could be seen at 15 min but not much variation was detected in the 20 min

sample. Mixed morphology of nanocubes and tiny dot-like NPs were clearly seen in the 5 and 10 min samples and breaking down of the nanocubes was only detected after 30 min. Just like in ODA, compact Cu NPs were obtained after 60 min and no nanocubes could be seen (Fig. 13). The ^{1}HNMR and ^{13}CNMR of HDA shown in Fig. 1S and 2S respectively were similar to the ODA NMR and therefore the mechanism was consistent with ODA.

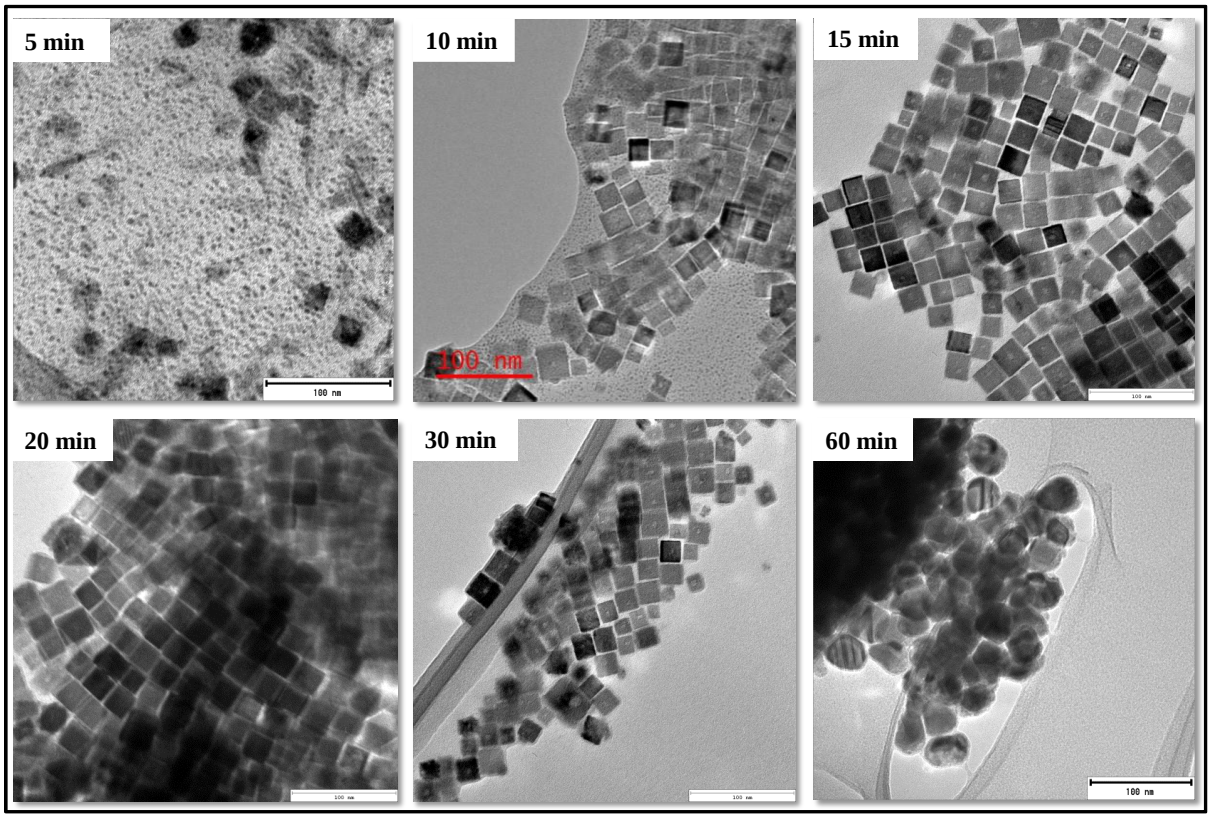

Fig. 13: TEM images of Cu_3N NPs obtained after 5, 10, 15, 20 and 30 min and Cu at 60 min in HDA at 260 °C. (All scales are 100 nm)

4. Conclusions

The thermal decomposition of $Cu(NO_3)_2$ at 260 °C in ODA leads to the formation of dot-like nuclei which resulted in the formation of Cu_3N nanocubes. A cloud of Cu_3N nuclei with developing

nanocubes was obtained after 5 min. Aligned nanocubes were seen at 10 min with the presence of bigger but fewer 'dots'. With time, well-defined Cu_3N nanocubes were obtained after 15 min and this was observed in both ODA and HDA. Further heating resulted in the breaking down of the nanocubes and XRD indicated the presence of both Cu_3N and Cu at 30 min. By 60 min, the Cu_3N had completely decomposed to Cu. Furthermore, results from the FTIR and NMR spectroscopy suggested the formation of a nitrile (RCN) as a byproduct in the synthesis of Cu_3N in ODA. As such, ODA, apart from capping the nanoparticles was involved in the reaction that led to the formation of Cu_3N NPs. The optical studies revealed that the as-synthesized nanoparticles were semiconducting with two transitions observed in the UV-Vis absorption spectra. The synthesized Cu_3N NPs can potentially be applied as microscopic metallic links due to its metallization at relatively low temperatures.

References

[1] Z. Cao, Thin Film Growth: Physics, Materials Science and Applications, Woodheal Publishing Limited, (2011).

[2] T. Nakamura, N. Hiyoshi, H. Hayashi, T. Ebina, *Materials Letters*, 139 (2015) 271-274.

[3] T. Nakamura, H. Hayashi, T.-A. Hanaoka, T. Ebina, *Inorganic Chemistry*, 53 (2013) 710-715.

[4] M.D. Reichert, M.A. White, M.J. Thompson, G.J. Miller, J. Vela, *Inorganic Chemistry*, 54 (2015) 6356-6362.

[5] R. Szczęsny, E. Szłyk, M.A. Wiśniewski, T.K. Hoang, D.H. Gregory, *Journal of Materials Chemistry C*, 4 (2016) 5031-5037.

[6] J. Choi, E. Gillan, *Inorganic Chemistry*, 44 (2005) 7385.

[7] S. Mondal, C.R. Raj, *The Journal of Physical Chemistry C*, 122 (2018) 18468-18475.

[8] T. Nakamura, H. Hayashi, T. Ebina, *Journal of Nanoparticle Research*, 16 (2014) 2699.

[9] Z.-Q. Liang, T.-T. Zhuang, A. Seifitokaldani, J. Li, C.-W. Huang, C.-S. Tan, Y. Li, P. De Luna, C.T. Dinh, Y. Hu, Nature Communications, 9 (2018) 1-8.

[10] H. Wu, W. Chen, Journal of the American Chemical Society, 133 (2011) 15236-15239.

[11] D. Wang, Y. Li, *Chemical Communications*, 47 (2011) 3604-3606.

[12] R.K. Sithole, L.F. Machogo, M.A. Airo, S.S. Gqoba, M.J. Moloto, P. Shumbula, J. Van Wyk, N. Moloto, *New Journal of Chemistry*, 42 (2018) 3042-3049.

[13] P. Xi, Z. Xu, D. Gao, F. Chen, D. Xue, C.-L. Tao, Z.-N. Chen, *RSC Advances*, 4 (2014) 14206-14209.

[14] D.S. Wang, T. Xie, Q. Peng, S.Y. Zhang, J. Chen, Y.D. Li, *D Chemistry–A European Journal*, 14 (2008) 2507-2513.

[15] T. Maruyama, T. Morishita, *Applied Physics Letters*, 69 (1996) 890-891.

[16] R. Cremer, M. Witthaut, D. Neuschütz, C. Trappe, M. Laurenzis, O. Winkler, H. Kurz, *Microchimica Acta*, 133 (2000) 299-302.

[17] A. Majumdar, S. Drache, H. Wulff, A.K. Mukhopadhyay, S. Bhattacharyya, C.A. Helm, R. Hippler, *Coatings*, 7 (2017) 64.

[18] X. Fan, Z. Wu, H. Li, B. Geng, C. Li, P. Yan, *Journal of Physics D: Applied Physics*, 40 (2007) 3430.

[19] A. Fallberg, M. Ottosson, J.O. Carlsson, *Chemical Vapor Deposition*, 15 (2009) 300-305.

[20] C. Navio, M. Capitan, J. Alvarez, F. Yndurain, R. Miranda, *Physical Review B*, 76 (2007) 085105.

[21] L.-C. Wang, B.-H. Liu, C.-Y. Su, W.-S. Liu, C.-C. Kei, K.-W. Wang, T.-P. Perng, *ACS Applied Nano Materials*, 1 (7) (2018) 3673-3681.

[22] M. Trivedi, G. Singh, A. Kumar, N.P. Rath, *RSC Advances*, 4 (2014) 34110-34116.

[23] H. Sanghera, J. Sullivan, *Surface and Interface Analysis*, 27 (1999) 678-690.

[24] A. Miura, T. Takei, N. Kumada, *Journal of Asian Ceramic Societies*, 2 (2014) 326-328.

[25] A.K. Mukhopadhyay, A. Roy, S.C. Das, H. Wulff, R. Hippler, A. Majumdar, *AIP Conference Proceedings*, AIP Publishing, 2018, 100078.

[26] O. Akhavan, R. Azimirad, S. Safa, E. Hasani, *Journal of Materials Chemistry*, 21 (2011) 9634-9640.

[27] M. Younas, J. Shen, M. He, R. Lortz, F. Azad, M. Akhtar, A. Maqsood, F.C. Ling, *RSC Advances*, 5 (2015) 55648-55657. Scientific Reports, 7 (2017) 8903.

[29] R. Deshmukh, G. Zeng, E. Tervoort, M. Staniuk, D. Wood, M. Niederberger, *Chemistry of Materials*, 27 (2015) 8282-8288.

[30] J. Choi, E.G. Gillan, *Inorganic Chemistry*, 48 (2009) 4470-4477.

[31] R.P. Pohanish, Sittig's Handbook of Toxic and Hazardous Chemicals and Carcinogens, William Andrew, 2008.

[32] F. Gunstone, *Chemistry and Physics of Lipids*, 66 (1993) 189-193.

[33] R.J. Abraham, *Magnetic Resonance in Chemistry*, 38 (2000) 570-579.

[34] A.B. Jackson, Nitrile reduction and carbon monoxide replacement in tungsten (II) bis (acetylacetonate) complexes, The University of North Carolina at Chapel Hill, 2008.

[35] U. Hahn, W. Weber, *Physical Review B*, 53 (1996) 12684.

[36] M. Mikula, D. Búc, E. Pincik, *Acta Physica Slovaca*, 51 (2000) 35-43.

[37] O.A. Yeshchenko, I.S. Bondarchuk, M.Yu. Losytskyy, *Journal of Applied Physics*, 116 (2014) 054309.

[38] M. Mlambo, M.J. Moloto, N. Moloto, P.S. Mdluli, *Materials Research Bulletin*, 48 (6) (2013) 2196-2200.

[39] A. Bruckman, G. Simkovich, *Corrosion Science*, 12 (1972) 595-601.

Chapter 6

Simultaneous capping and substitution of nitrogen ions of Cu_3N nanocrystals with sulfur ions using DDT as a co-surfactant to form chalcocite and digenite nanocrystals

Abstract

Uncapped nanocrystalline cuprous nitride (Cu_3N) decomposes spontaneously to CuO at room temperature due to the presence of water and oxygen in the atmosphere. Long-chain capping molecules have been successfully used to cap and protect the core nanocrystals from oxidation. Moreover, the use of co-surfactants has been shown to alter the morphologies and properties of nanocrystals due to preferential binding. In an attempt to cap Cu_3N nanocrystals and alter their morphology, hexadecylamine (HDA) and 1-dodecanethiol (DDT) were used as surfactant and co-surfactant respectively. Contrary to common belief, herein we show that DDT does not only act as a co-surfactant, it also results in the complete substitution of nitrogen ions in Cu_3N with sulfur ions thereby resulting in the formation of a mixture of Cu_3N and Cu_2S after 2.5 min of DDT addition. Longer reaction times result in the formation of pure Cu_2S (chalcocite) and ultimately Cu_9S_5 (digenite). The substitution is consistent with the HSAB theory. XRD, EDX, TEM, and XPS confirmed the transitioning of Cu_3N nanocrystals to chalcocite and digenite nanocrystals. The resultant morphologies were spherical particles for Cu_3N, hexagonal particles for Cu_2S and small spherical particles for Cu_9S_5 nanocrystals. ^{1}HNMR and FTIR spectroscopies elucidated the capping of the nanocrystals by HDA and DDT. The optical properties showed the transitioning of

the band-gap. The photoluminescence spectra of both Cu_2S and Cu_9S_5 showed an up-conversion process with the emission energy blue-shifted from the band gap energy.

Keywords: cuprous nitride; chalcocite; digenite

1. Introduction

Copper-based nanocrystals (NCs) are amongst the topmost synthesized semiconducting nanomaterials [1, 2]. Copper oxide [3-5] and copper sulfide [6-9] are the most studied whilst copper nitride has been less studied in spite of being synthesized as far back as in 1938 [10]. However, increasingly it is being studied due to its interesting physical properties and application in data storage, photovoltaics as well as in microelectronics to name a few. The chemistry of Cu_3N and particularly its stability is also quite interesting. Cu (I) is a soft metal ion and Cu (II) is borderline hence Cu (II) forms more stable complexes with borderline donors like nitrogen. As a result, the synthesis of Cu_3N NCs is quite complex and difficult as the copper is being forced to acquire the +1 oxidation state with nitrogen. It is for this reason that uncapped Cu_3N NCs can easily disproportionate in air due to the presence of oxygen to form the more stable Cu (0) and Cu (II) species [11]. To circumvent the oxidation, surfactant molecules have been used and these are often functionalized long-chain alkanes or alkenes. The surfactants play a critical role in nanocrystal syntheses as they control the growth of the nanocrystals in terms of the resultant size and morphology, they stabilize and protect the nanocrystals and they can act as reducing agents and solvents. However, overlooked, is their potential role as precursors and monomers in the reaction mixture. Herein, we report on the conversion of Cu_3N NCs to Cu_2S and Cu_9S_5 by the co-surfactant 1-dodecanethiol (DDT).

Several papers have been published where DDT has been used a co-surfactant and the role of DDT varies from stabilizing certain oxidation states [12] to preferentially promoting growth in certain crystallographic planes thereby resulting in a change of morphology [13]. It has also been used as a direct source of sulfur in the synthesis of $Cu_{2-x}S$ NCs when reacted with copper salts [14]. In

another study, $Cu_{2-x}Se$ NCs have been capped with DDT with no substitution of Se with S occurring (Senthilkumar, 2017) [15]. In a more related study, Wang *et al.* synthesized $Cu_{2-x}S$ NCs using Cu_3N NCs as the copper source and ammonium diethyldithiocarbamate as the sulfur source in a combination of octadecene/DDT surfactant mixture. Overlooked by Wang *et al.* is the possibility of DDT acting also as a sulfur source [16]. Herein, we show that based on the HSAB theory, a soft donor such as sulfur can easily replace an intermediate donor such as nitrogen to bind to Cu (I) ions (soft acid) in Cu_3N hence resulting in the formation of copper sulfide NCs and this can easily occur and can be caused by even small amounts of sulfur containing surfactants such as DDT. Therefore, by exploiting the HSAB principle one can selectively design materials with interesting properties.

Copper sulfides are semiconducting chalcogenides and have been used in solar devices, magnetic sensors, and catalysis. A wide range of copper sulfides have been reported from the Cu-rich chalcocite (Cu_2S) [17], to the less Cu-rich djurleite ($Cu_{1.97}S$), digenite (Cu_9S_5), geerite ($Cu_{1.6}S$) till the sulfur-rich covellite (CuS) [18] and villamaninite (CuS_2) [19]. There are many reports on the synthesis of copper sulfides, but the main challenge still lies on obtaining the stoichiometric sulfides especially the intermediates between Cu_2S and CuS. Different studies have shown that the oxidation state of Cu in chalcocite is +1 and the S carries a -2 charge [20-23]. On the other hand, it has been suggested that Cu^0, Cu^+ and Cu^{2+} species [24] are present in digenite together with S^{2-} ions. Liu *et al.* [25] are of the view that the formula for $Cu_{1.8}S$ can be expressed as $[(Cu^+)_8Cu^{2+}(S^{2-})_5]$. There are two crystal structures that are associated with digenite, namely the ordered hexagonal low-digenite and the less ordered cubic high digenite phases and these are interchangeable between 60 and 65 °C [26]. The main challenge in the synthesis of copper sulfide

NCs lies in the setting up of conditions that allow for the synthesis of one phase of sulfide especially the meta-stable ones that lie between the copper-rich chalcocite and the sulfur-rich covellite. Alkanethiols upon decomposition are known to form alkenes and H_2S [27]. Herein, we show that with time, there is gradual availability of the H_2S monomers thereby resulting in the early formation of chalcocite and later digenite.

2. Experimental Section

2.1 Materials

Copper (II) nitrate trihydrate (puriss p.a., 99-104%), hexadecylamine (HDA) (technical grade, 90%), dodecanethiol (DDT) (≥ 98%), ethanol (absolute, ≥99.8% (GC)), deuterated chloroform (CDCl3) (99.8 atom % D) and chloroform (anhydrous, ≥99%, contains 0.5-1.0% ethanol as stabilizer) were all purchased from Sigma-Aldrich and were used without further purification.

2.2 Synthesis of the nanoparticles

The first part of the reaction consisted of thermal decomposition of copper (II) nitrate in HDA to form copper (I) nitride NCs. This was followed by the addition of DDT that led to the sulfidation of the nitride NCs.

2.2.1 Synthesis of Cu_3N NCs

Cu_3N NCs were synthesized following a procedure that was reported in previously [11] with slight modifications. In a typical synthesis, a mixture of $Cu(NO_3)_2.3H_3O$ (1 mmol) and HDA (9.5 mL) were degassed using a continuous flow of nitrogen gas at 110 °C under magnetic stirring. After an

hour, the reaction temperature was raised to 230 °C and an aliquot (2 mL) was extracted after 5 min.

2.2.2. Synthesis of Cu_2S and Cu_9S_5 NCs

The second phase involved the addition of DDT (2 mL) to the reaction mixture above. This led to a drop of temperature which was subsequently raised and maintained at 230 °C for up to 20 min. Aliquots were extracted at 2.5, 5, 7.5, 10 and 20 min. The resultant NCs were washed several times in ethanol and centrifuged at 7000 rpm.

2.3 Characterization

The structure and phase of the powdered nanocrystals were determined with the Bruker MeasSrv (D2-205530)/D2-205530 diffractometer using CoKα radiation (λ 1.78897 Å) at 30 kV/10 mA. The XRD data was acquired using a Bruker Lynxeye PSD detector set to measure at 5º 2θ and all measurements were acquired at room temperature. The data was analyzed using Bruker AXS Evaluation package (EVA, 2008) equipped with ICDD PDF 4+. The particle sizes and morphology were studied using a FEI Spirit 120 kV transmission electron microscope (TEM) equipped with an EDX detector operated at an acceleration voltage of 200 kV with a beam spot size of 20 - 100 nm in TEM mode. The particles were dispersed in chloroform and drop-casted onto a lacey carbon nickel grid. The solvent was then evaporated at room temperature. Particle sizes were determined using ImageJ. Proton Nuclear Magnetic Resonance (^{1}H NMR) spectra were acquired using a Bruker AVANCE 111 300 spectrometer in deuterated chloroform ($CDCl_3$) using trimethylsilane (TMS) as the internal standard (δ = 0). Chemical shift units were recorded in δ (ppm) with reference to the signals of the deuterated chloroform. MNOVA software was used to process the

NMR data. Fourier transform infrared (FTIR) spectroscopic data was determined using a PerkinElmer Spectrum Two spectrometer equipped with a diamond attenuated total reflectance crystal. The FTIR spectra of the samples were recorded at 25 °C between the wavenumbers ranging from 550 to 4000 cm^{-1}. X-ray photoelectron spectroscopy measurements were performed with a PHI 5000 Versaprobe - Scanning ESCA Microprobe operating with a 100 µm 25 W 15 kV Al monochromatic X-ray beam. A Specord 50 AnalytikJena UV-Vis spectrophotometer was used to carry out the absorption measurements. An Agilent Cary Eclipse fluorescence spectrometer was used to measure the photoluminescence of the particles. The nanoparticles were dissolved in chloroform and placed in quartz cuvettes (1 cm path length) for both UV-Vis absorption and photoluminescence spectral analyses.

3. Results and discussion

Copper nitrate was thermolyzed in HDA at 230 °C in order to obtain Cu_3N NCs. After the removal of an aliquot of Cu_3N NCs for analysis, 2 mL of DDT was added. Further aliquots were taken to study the effect of the addition of DDT on the properties of the NCs. Shown in Fig. 1 are the X-ray diffractograms of the samples taken at different time intervals using Co Kα as the radiation source.

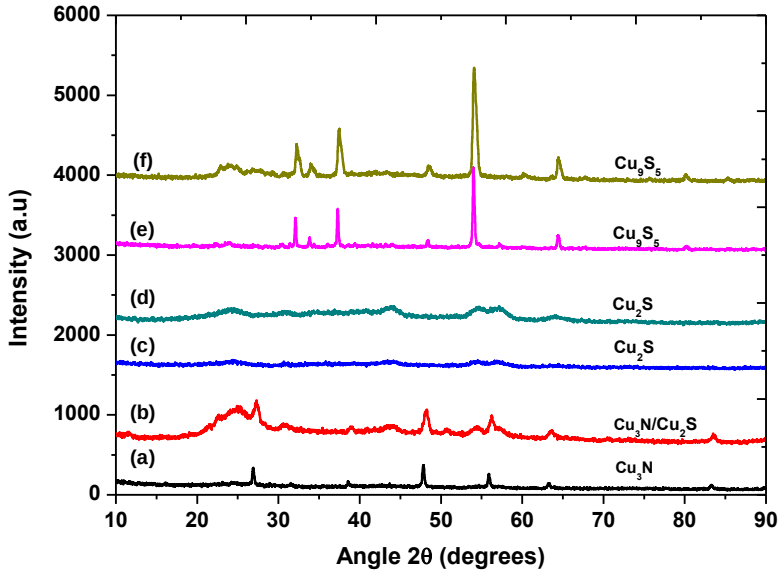

Fig. 1: X-ray diffractograms of (a) Cu_3N NCs and sulfidation products after (b) 2.5, (c) 5, (d) 7.5, (e) 10 and (f) 20 min in HDA/DDT mixture at 230 °C.

Prior to the addition of DDT, pure Cu_3N NCs were formed, indexed to an anti-ReO_3 cubic structure (JCP2.2CA: 00-002-1156). After the addition of DDT, the XRD pattern that was obtained after the first 2.5 min showed that there existed not only Cu_3N but also Cu_2S in the sample. After 5 min, there were no evident peaks for Cu_3N as all peaks were indexed to the cubic phase of Cu_2S. Diffraction peaks were obtained at 2θ values of 30.8°, 32.5°, 43.9°, 54.6°, 57.2° and 64.1° corresponding to the hkl values of (302), (104), (382), (600), (346), and (337) confirming the presence of low α-chalcocite Cu_2S (JCP2.2CA: 00-009-0328). A similar pattern was obtained at 7.5 min but a different scenario was observed after 10 min. Very sharp and well-defined peaks were obtained at 2θ values of 30.8°, 32.1°, 34.0°, 37.5°, 48.5°, 54.0°, 60.2°, 64.5°, 67.8°, 80.2° and 85.5° corresponding to hkl values, (101), (0015), (107), (1010), (0117), (0120), (0027), (1115), (0030), (2020) and (1127) of the rhombohedral phase of digenite (Cu_9S_5), (JCP2.2CA: 00-047-

1748). Further monitoring of the sample showed no change in the composition as seen in the 20 min sample. This was in agreement with the observed physical changes of the reaction mixture, where a brown solution (Cu_3N) turned to greyish-brown (mixture) to grey (Cu_2S) and ultimately greyish-black (Cu_9S_5). In the XRD diffractograms, peaks are observed in the range $20°<2\theta<25°$ owing to impurities that result from thermal decomposition of unbounded amine ligands (capping agent) as demonstrated in a previous study [11].

To study the morphological features of the resultant materials, TEM studies were undertaken. Shown in Fig. 2 are the TEM images and size distribution histograms of the resultant NCs. Spherical-like Cu_3N NCs of the size diameter of 4.2 ± 3.2 nm were obtained prior to the addition of DDT. Upon introducing DDT, Cu_2S begins to form as observed in the XRD pattern in Fig. 1(b) and the tuning of the size is observed as shown in Fig. 2(b) where the sample becomes nearly monodispersed (3.3 ± 0.9 nm). Well-defined hexagonal NCs were obtained at 5 min with an average diameter of 4.9 ± 0.6 nm. An increase in size is observed however the particles still maintain their monodispersity suggesting that the nuclei seeds formed in 2.5 min continue to grow through the Ostwald ripening process as the time proceeds. An aliquot taken 7.5 min after the addition of DDT shows continued growth of the particles with sizes averaging 5.8 nm. In addition to particle growth, an agglomeration of particles is observed as shown in Fig. 2(d). Following the agglomeration, a resizing of the particles occurs resulting in the formation of smaller particles that are nearly monodispersed. These particles are Cu_9S_5 evident from the XRD pattern in Fig. 1(e).

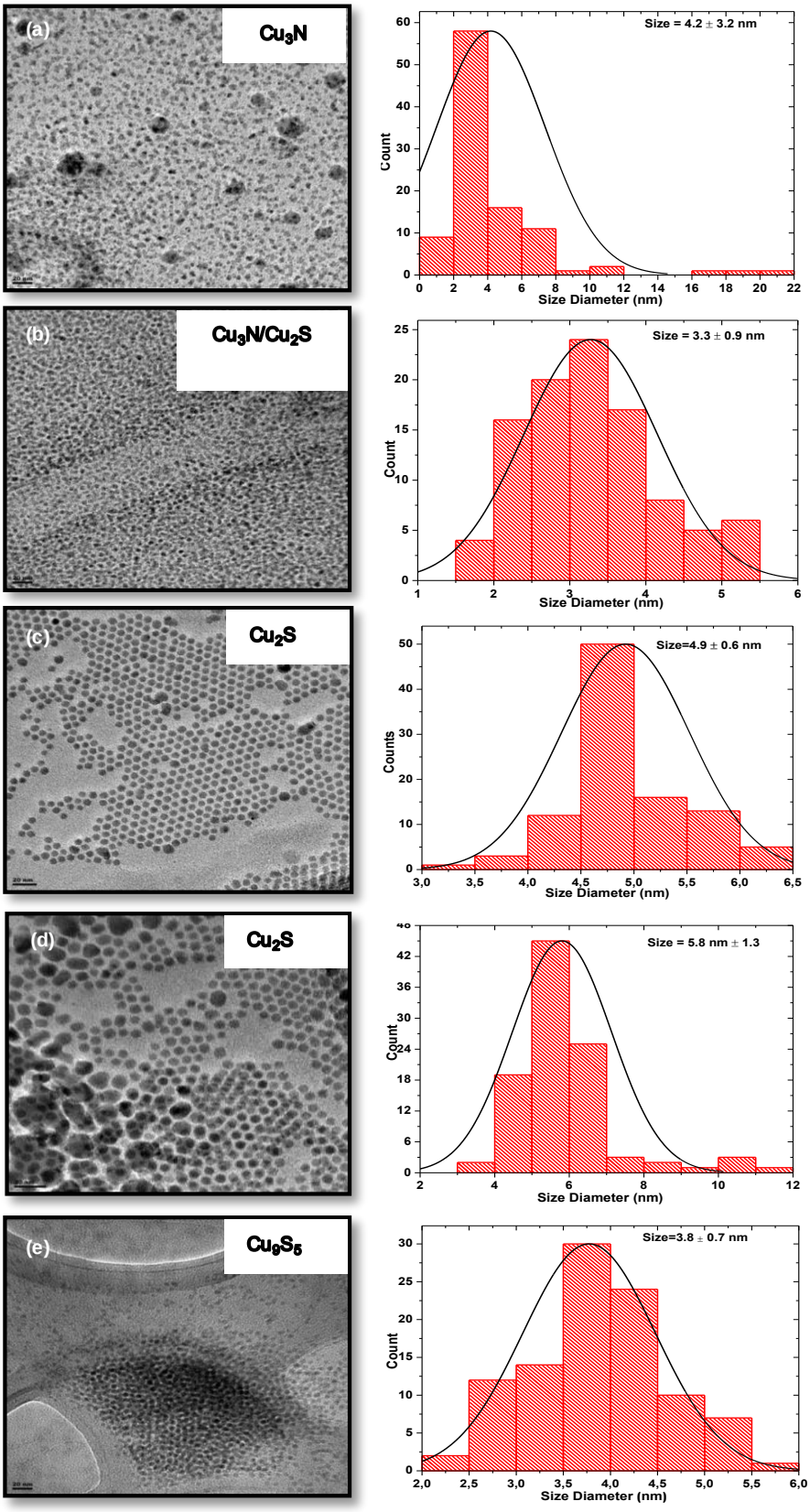
(a)
Cu3N
Size = 4.2 ± 3.2 nm
Count
Size Diameter (nm)
(b)
Cu3N/Cu2S
Size = 3.3 ± 0.9 nm
Count
Size Diameter (nm)
(c)
Cu2S
Size=4.9 ± 0.6 nm
Counts
Size Diameter (nm)
(d)
Cu2S
Size = 5.8 nm ± 1.3
Count
Size Diameter (nm)
(e)
Cu9S5
Size=3.8 ± 0.7 nm
Count
Size Diameter (nm)

Fig. 2: TEM images and size distribution histograms of (a) Cu_3N NCs and sulfidation products after (b) 2.5, (c) 5, (d) 7.5 and (e) 10 min in HDA/DDT mixture at 230 °C. (All scales are 20 nm)

As further evidence, EDX spectroscopy was done to ascertain the composition of the samples (Fig. 3). The EDX spectrum of Cu_3N showed only the presence of Cu and N. After the addition of DDT, a sulfur peak was observed approximately at 2.35 keV. As reaction time was prolonged, continued heating released S^{2-} ions from DDT hence resulting in the different stoichiometries of copper sulfide as evidenced in XRD analysis. The S peak is clearly seen in all samples that were collected after adding the DDT 'capping agent'. The nitrogen peak is attributed to both Cu_3N and HDA hence its presence in all four samples. The amount of the capping agent in relation to the core particle is much larger and this is the reason why the intensity of the nitrogen is generally constant.

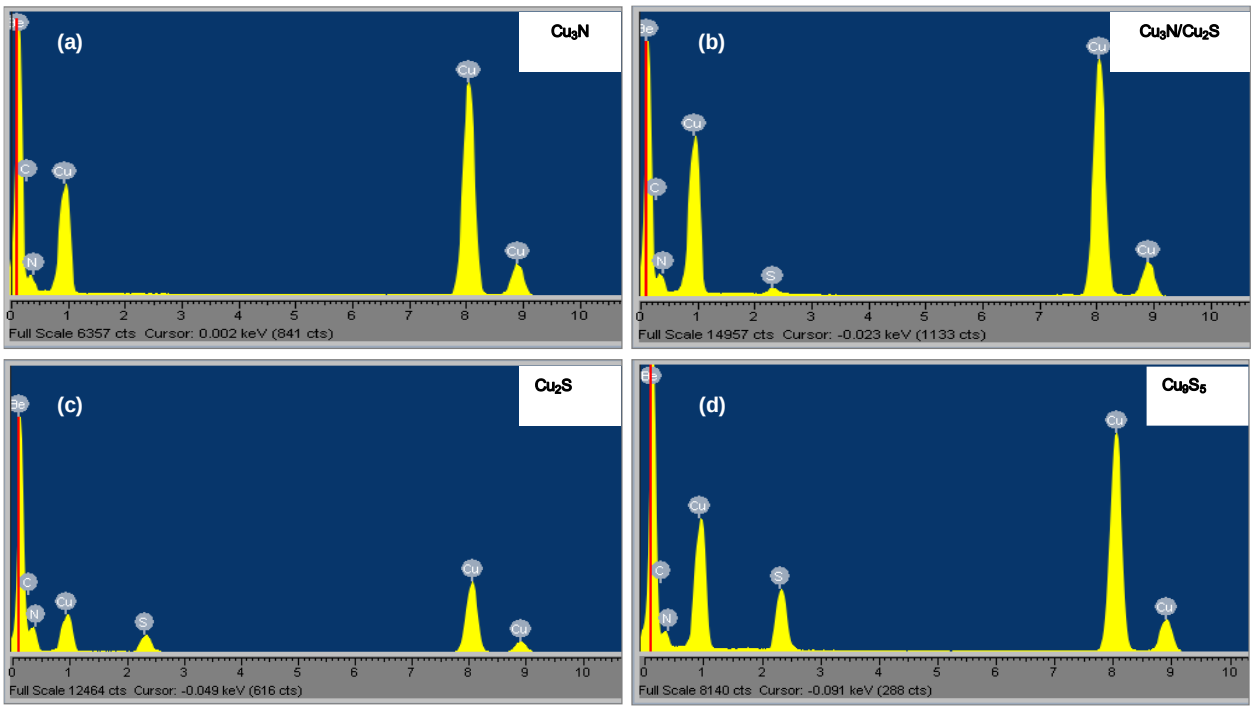

Fig. 3: EDX spectra of (a) Cu_3N NCs and sulfidation products after (b) 2.5, (c) 5 and (d) 10 min in HDA/DDT mixture at 230 °C.

To verify if the as-synthesized nanocrystals were capped or not, the particles were dissolved in $CDCl_3$ and analyzed using ^{1}H-NMR which revealed that the copper nitride and sulfide nanocrystals were all capped by the coordinating ligands (Fig. 4). Cu_3N NCs were synthesized in HDA and Cu_2S and Cu_9S_5 were obtained in a mixture of HDA and DDT. It is interesting to note that the raw HDA spectrum shows the presence of amine protons ($-NH_2$) indicated by the broad shoulder peak resonating around 1.28 ppm and the adjacent α-methylene protons on C2 at 2.68 ppm. These protons were not detected in the spectra of the HDA-capped Cu_3N NCs. The same scenario was depicted in the spectra of the sulfide nanocrystals. The spectrum for DDT shows the presence of the thiol proton (-SH) as a broad shoulder peak around 1.29 ppm and the adjacent α-methylene protons on C1 resonate at 2.50 ppm. In the resultant chalcocite and digenite NCs, these protons

were not detected. The loss of these protons could be due to the coordination that occurs between the N and S on the HDA and DDT respectively to the nanosurfaces. This resulted in the peak shifts that were observed on the β-methylene protons found on C3 of HDA and C2 of DDT. C3 peak in HDA shifted from 1.41 to 1.58 ppm in HDA-capped Cu_3N NCs whilst the C2 peak in DDT was displaced from 1.58 to 1.54 and 1.53 ppm in Cu_2S and Cu_9S_5 respectively. A similar trend was observed by Brust *et al.* [28] when they used DDT as a capping agent in controlling the size of Au nanoparticles. Although it cannot be concluded whether the sulfide NCs are only capped by the HDA, DDT or both, it is clear that all the nanoparticles obtained were capped.

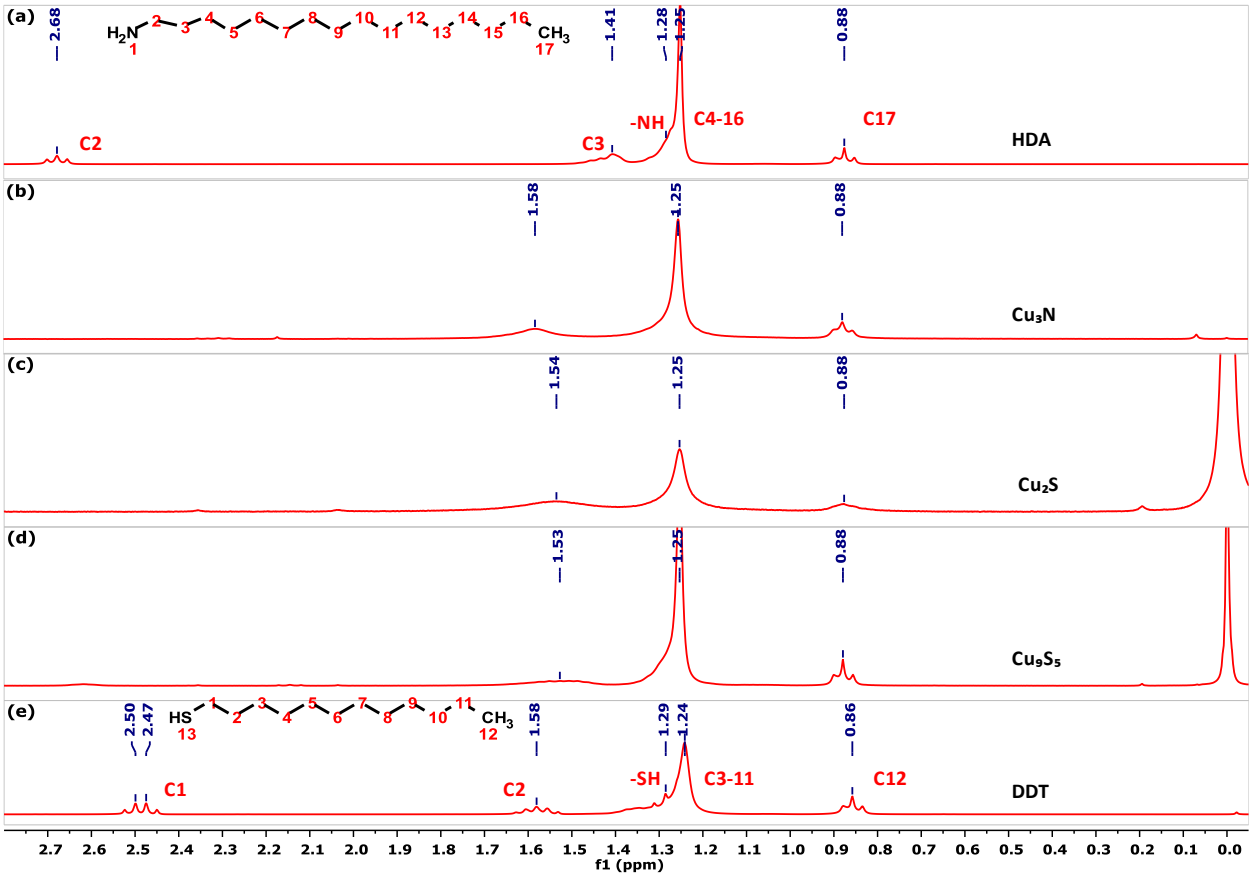

Fig. 4: ^{1}H-NMR spectra of (a) HDA, (b) Cu_3N in HDA, (c) Cu_2S and (d) Cu_9S_5 in HDA-DDT and (e) DDT.

To further understand the capping, FTIR spectroscopy was done as shown in Fig. 5. The two peaks of interest for DDT were located at 1467 cm^{-1} and 1290 cm^{-1} corresponding to the H_2C-S and C-S stretching frequencies respectively. For the HDA spectrum, four peaks of interest were identified, N-H stretching frequency at 3258 cm^{-1}, the N-H bending mode at 1613 cm^{-1}, the C-H and C-N stretching frequencies at 1460 cm^{-1} and 1063 cm^{-1} respectively. The Cu_3N showed the significant peaks for HDA however they were slightly shifted suggesting that the particles were capped by HDA. The Cu_2S NCs showed evidence of being capped by both HDA and DDT. This is supported by the observation of the amine peak at 3308 cm^{-1} and the H_2C-S at 1518 cm^{-1}. These peaks are red-shift from the unbound capping agents suggesting bonding has occurred. The Cu_9S_5 NCs show evidence of only HDA capping with no peak from DDT being detected. This further cement the idea that DDT gradually decomposes over time to become the sulfur source for the copper chalcogenides.

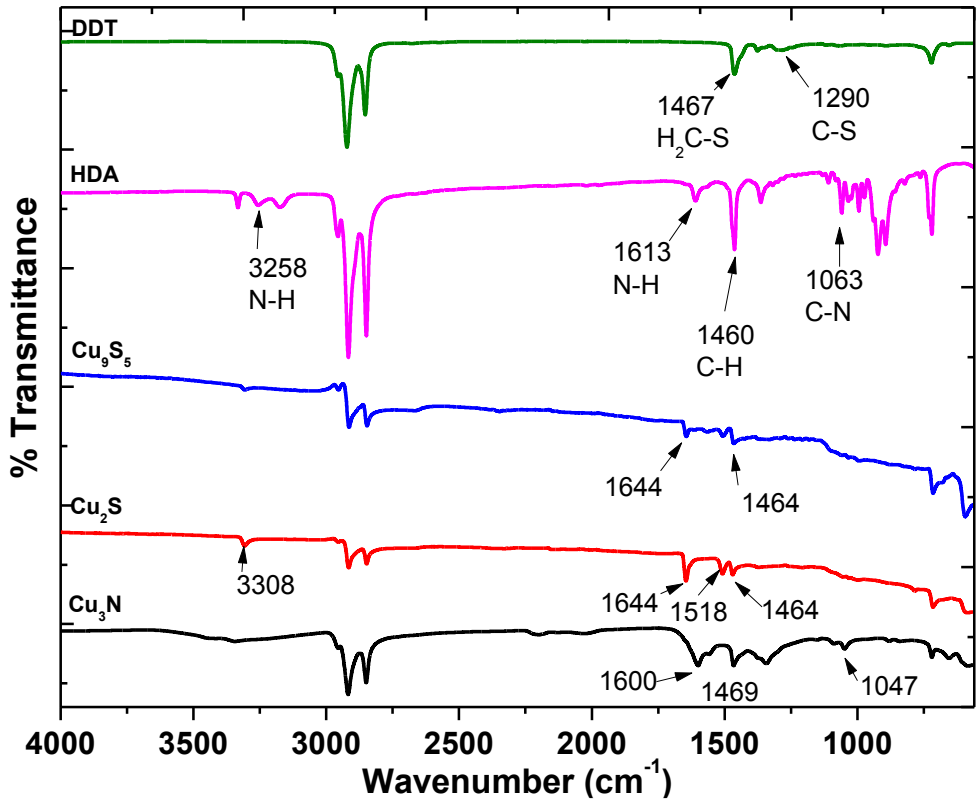

Fig. 5: FTIR spectra of DDT, HDA, Cu_3N in HDA, Cu_2S and Cu_9S_5 in HDA-DDT.

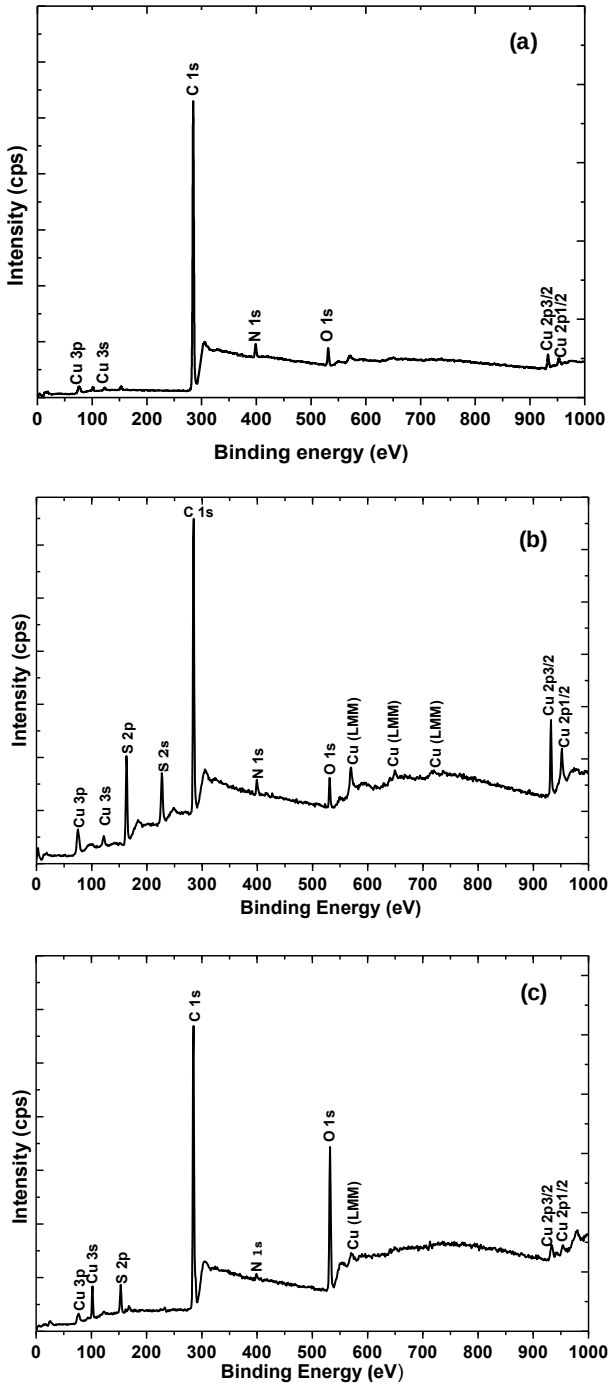

Fig. 6: XPS survey spectra of (a) Cu_3N NCs and sulfidation products after (b) 7.5 and (c) 10 min in HDA/DDT mixture at 230 °C.

To evaluate the surface chemistry as well as the bonding in the resultant particles, XPS was used. The XPS survey spectra of the as-synthesized NCs show the expected elemental compositions and the respective binding energies (Fig. 6). The Cu_3N spectrum shows the presence of Cu, N, C and O. The C is due to the capping agent and the O is as a result of the oxidation of the capping agent as previously reported [11]. Upon the addition of DDT, the 5 min and 10 min samples show the presence of S indicative of the formation of the copper chalcogenides. The presence of N can be attributed to the capping agent as it is a long-chain amine. This would be in agreement with the XRD data where for these samples no presence of the Cu_3N was detected. The evident Auger lines Cu LMM at 569.7, 649.2 and 720.0 eV in the 5 min sample and 569.9 eV in the 10 min sample are indicative of the existence of Cu^+ oxidation state [29-31].

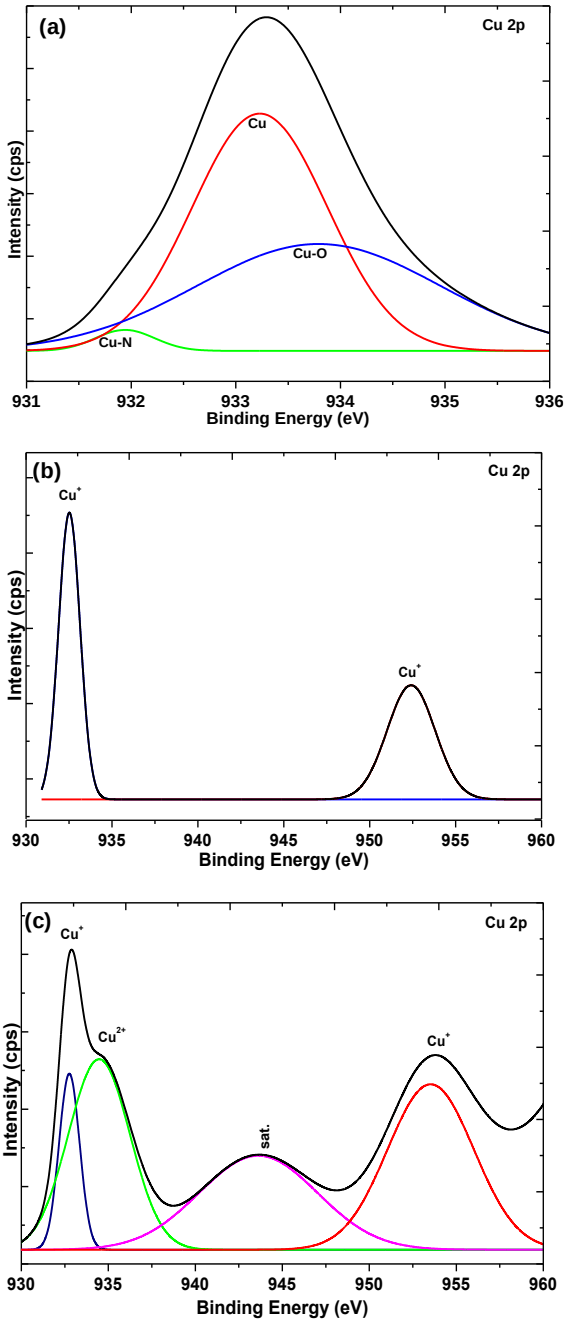

Fig. 7: High resolution Cu 2p XPS spectra of (a) Cu_3N NCs and sulfidation products after (b) 5 and (c) 10 min in HDA/DDT mixture at 230 °C.

The high resolution spectra with respect to Cu 2p were undertaken to establish the oxidation state of copper and confirm the composition of the NCs as shown in Fig. 7. The Cu 2p core-level spectrum emanating from the Cu_3N sample was deconvoluted to three sub-peaks corresponding to Cu–N (932 eV), Cu 2p3/2 (933.2 eV), and Cu–O (933.8 eV). These peaks confirm the formation of Cu_3N as well as the interaction of the particles with atmospheric oxygen. Fig. 7(b) shows the core level spectrum of the sulfidation product formed after 5 min of DDT addition. The spectrum shows two peaks at 932.5 and 952.4 eV characteristic of the Cu^+ state hence confirming the composition as Cu_2S. There were no satellite peaks that were detected and this suggests the presence of a fully filled $3d^{10}$ shell of Cu^+ in the chalcocite [24]. The high resolution Cu 2p spectrum for the 10 min sample showed four deconvoluted peaks as shown in Fig. 7(c). The peaks at 932.7 and 953.5 eV were characteristic of the Cu^+ oxidation state. In addition, a satellite peak was observed at 943.6 eV. This suggests the presence of unfilled Cu $3d^9$ shell of Cu^{2+}. Additionally, the peak at 934.6 eV implies the existence of Cu^{2+} in Cu_9S_5. As such, both Cu^+ and Cu^{2+} species are present in the Cu_9S_5. This is consistent with previous studies that have shown the existence of both Cu^+ and Cu^{2+} in Cu_9S_5 [24]. The binding energy values in Cu_2S and Cu_9S_5 are very similar hence additional information like the detection of Auger peaks and satellites peaks come in handy in determining the existent of additional oxidation states. Therefore, we can clearly follow the change in the oxidation states in the Cu species.

To further understand the copper chalcogenides, high resolution S 2p spectra were done as depicted in Fig. 8. Peak fitting revealed two peaks on the S 2p spectrum for the Cu_2S NCs at 161.8 and 163.0 eV corresponding with the S $2p_{3/2}$ binding energy. These main peaks were indicative of the presence of Cu-S-Cu bonding in chalcocite hence the presence of S^{2-} ions [24]. The Cu_9S_5 spectrum

displayed three peaks at 162.6, 164.0 and 165.0 eV representing the S^{2-} $2p_{3/2}$, $(S_2)^{2-}$ $2p_{3/2}$ and $(S_2)^{2-}$ $2p_{1/2}$ as previously reported in digenite [32]. This, therefore, implies the transition of the -2 oxidation state of some S^{2-} ions in the chalcocite to -1 in the Cu_9S_5. As such, both the S^{2-} and $(S_2)^{2-}$ species exist in the Cu_9S_5. From the peak areas, there is about 15.8 % of the S^{2-} ions in the Cu_9S_5 sample and the rest are disulfide ions.

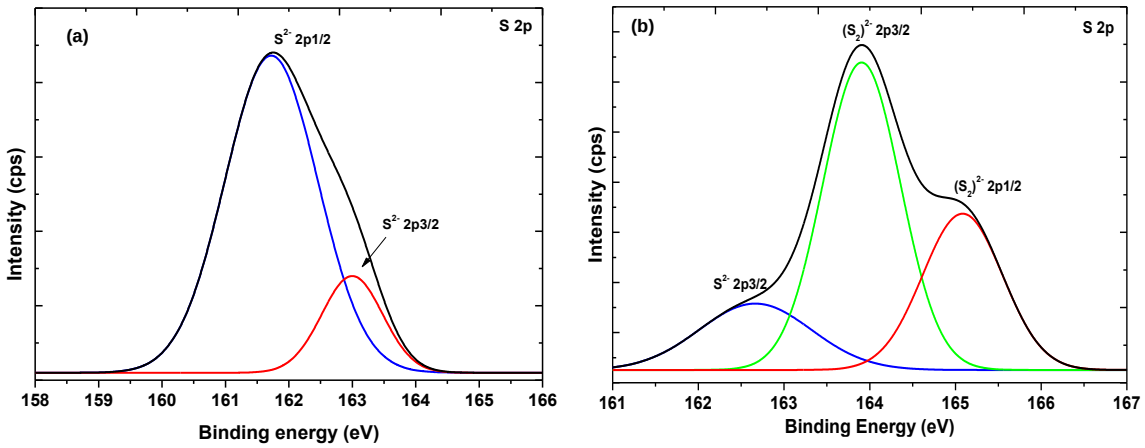

Fig. 8: High resolution S 2p XPS spectra of the sulfidation products after (a) 5 and (b) 10 min in HDA/DDT mixture at 230 °C.

To study the optical properties of the resultant NCs, UV-Vis absorption and photoluminescence spectroscopy was undertaken and the results are shown in Fig. 9. The Cu_3N and the mixture (Cu_3N/Cu_2S) spectra showed no clear excitonic peaks. The shape of the absorption spectrum is usually determined by electronic transitions and the distribution of band gaps in the system. Polydispersed samples, be in terms of size or composition will tend to have a spectrum absent of an excitonic peak as well as tailing. The Cu_2S and Cu_9S_5 NCs show broad excitonic peaks, typical of copper chalcogenide NCs [7]. To extract the band gaps of the Cu_3N NCs and the resultant copper

chalcogenide NCs, Tauc plots were done using the UV-Vis absorption spectra as shown in Fig. 10 [33].

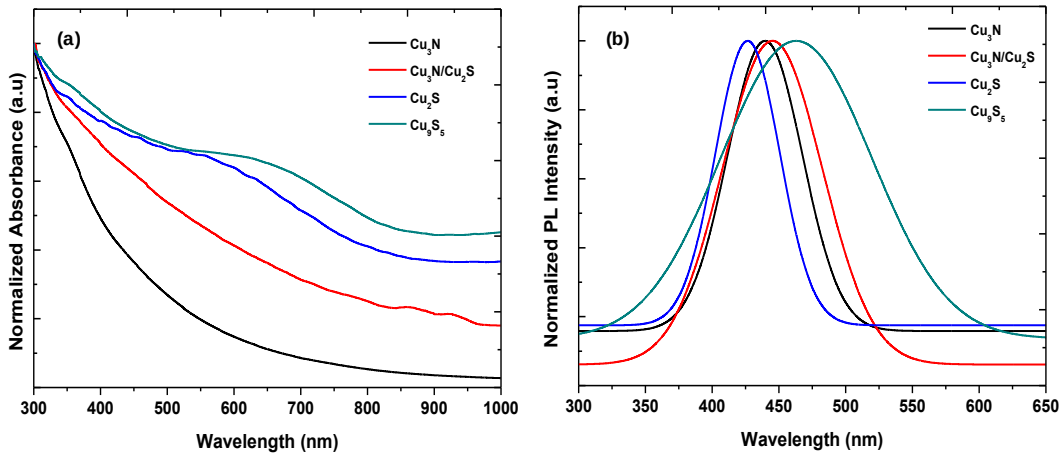

Fig. 9: UV-Vis absorption spectra of (a) and photoluminescence spectra (b) of Cu_3N and the different sulfidation products.

Well-defined linear regions were obtained for the plots of $(\alpha h\nu)^2$ vs. hν as displayed in Fig. 10. A straight line was drawn tangent to the point of inflection and the x-intercept (hν) was taken as the direct band (E_g) in eV. The bulk band gap for Cu_3N is reported to be 2.06 eV [11]. Shown in Fig. 10(a), a direct band gap of 2.92 eV corresponding to 425 nm is observed for Cu_3N NCs. This is blue-shifted from the bulk band-gap due to quantum confinement effects. As the size is reduced, there is the discretization of the energy band resulting in the increase of the band gap energy. The band gap energy for Cu_2S was found to 2.03 eV; a large blue-shift from the reported bulk band gap of 1.2 eV. A large blue-shift can result from surface traps and impurities. The 10 min sample corresponding to Cu_9S_5 NCs showed the band gap energy of 1.85 eV. The corresponding bulk band gap has been reported to range from 1.2 to 2.4 eV. The resultant band gap of 1.85 eV seems to lie

in the middle of the range. Nevertheless, the resultant band gaps in Fig. 10 seem to further suggest that DDT was progressively decomposing over time to produce the desired sulfur ions and this markedly influenced the resultant composition of the chalcogenides, thus corroborating the XRD and XPS results.

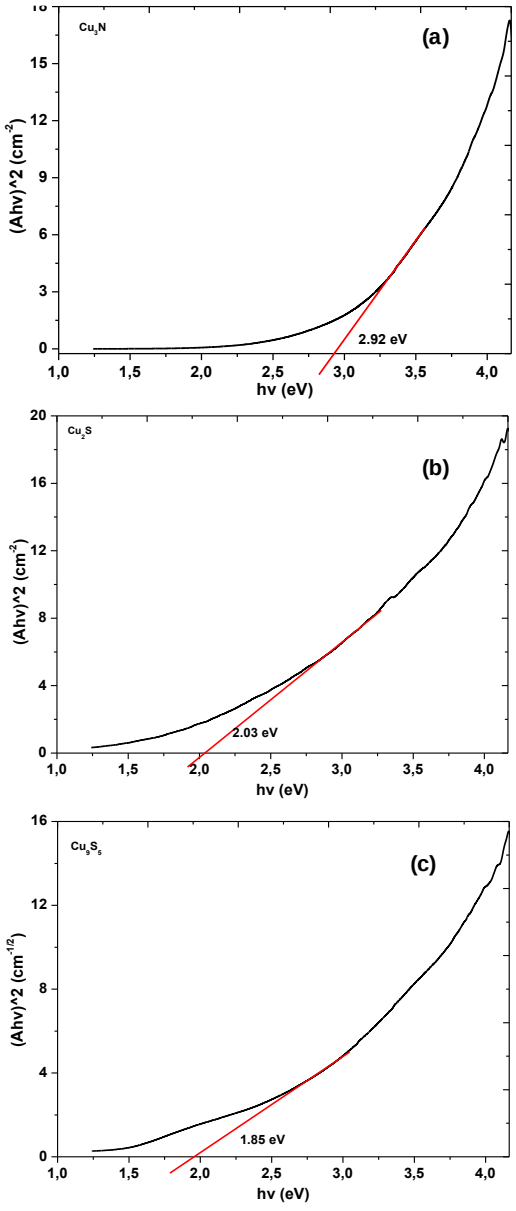

Fig. 10: Tauc plots showing the extrapolated band-gaps of (a) Cu_3N NCs and sulfidation products after (b) 5 and (c) 10 min in HDA/DDT mixture at 230 °C.

Copper nitride and the copper chalcogenides are p-type semiconductors and therefore their emission spectra can be studied. Shown in Fig. 9(b) are the photoluminescence (PL) spectra of the different NCs. The PL emission energy of 2.82 eV was obtained for the Cu_3N NCs. The emission energy is red-shifted from the band gap energy due to radiative energy losses and this is a usual phenomenon on NCs [34, 35]. After 5 and 10 min of DDT addition, as summarized in Table 1, a blue-shift in the emission energy is observed resulting in an up-conversion process. This is an unusual occurrence in copper chalcogenide NCs, however, welcomed as this has implication in an application such as up-conversion photovoltaics. Evidently, the substitution of the N^{3-} ions by the sulfur species S^{2-} and $(S_2)^{2-}$ has a significant impact on the optical properties of the NCs.

Table 1: Summary of the optical properties

Sample	Band Gap (eV)	λ_{max} (eV)
Cu_3N	2.9	2.8
Cu_2S	2.0	2.9
Cu_9S_5	1.8	2.7

Shown in Fig. 11 is the proposed substitution of the nitride ions by the sulfide ions generated from DDT. The decomposition of DDT to the sulfide species happens rapidly as within 10 min the composition of the copper chalcogenide is Cu_9S_5 and this does not change as the time is increased as reported in the XRD results. The emergence of the Cu_2S phase soon after the addition of DDT is as a result of the soft Cu^+ species preferring to bond to the soft S^{2-} species thus substituting some of the nitride ions. The existence of a mixture of Cu_3N and Cu_2S at 2.5 min suggests that at 2.5 min, partial decomposition of DDT has occurred and the amount of the S^{2-} ions is not enough to

replace all the N^{3-} ions. As time is prolonged to 5 min, complete substitution of the N^{3-} ions occurs and a single phase Cu_2S is obtained. After 10 min, there is an abundance of the sulfur ions and this results oxidation species Cu^{2+} and $(S_2)^{2-}$ forming together with the low valent Cu^{+} and S^{2-}. This results in the formation of Cu_9S_5 evident in the XRD and XPS results.

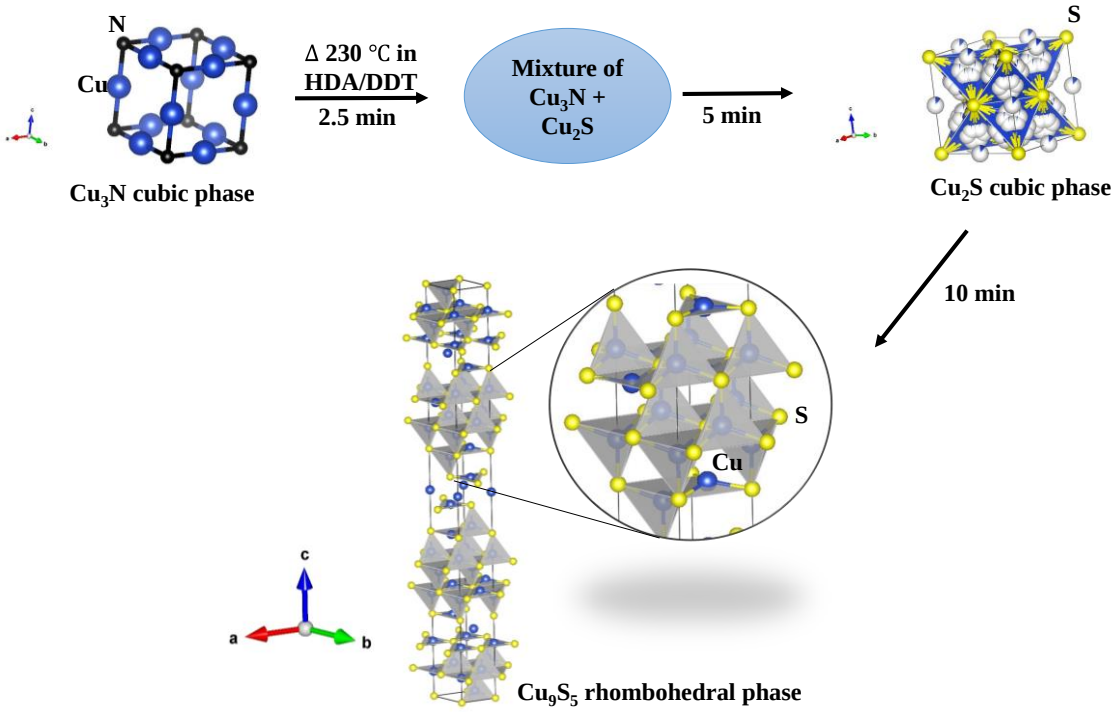

Fig. 11: Schematic of the sulfidation of Cu_3N NCs.

4. Conclusions

Herein the sulfidation of Cu_3N NCs to Cu_2S and Cu_9S_5 NCs using DDT as the sulfidation agent was demonstrated. The DDT did not act as a co-surfactant as previously seen by other authors but acted as a sulfur precursor. The DDT decomposition mechanism showed that at very short times (2.5 min), only a small amount of DDT has decomposed to the S^{2-} ions hence resulting in the mixture of Cu_3N and Cu_2S nanocrystals. This was corroborated by the XRD and XPS results. As the time was prolonged to 7.5 min, pure Cu_2S NCs were obtained both at 5 and 7.5 min. Further

extending the time to 10 min, the reaction system had an excess of sulfur thus resulting in the oxidation of some of the already existing Cu^{+} and S^{2-} ions to Cu^{2+} and $(S_2)^{2-}$ thereby resulting in the formation of Cu_9S_5. The existence of the different copper and sulfur species was confirmed by XPS and the resultant stoichiometry/phase of copper sulfide was confirmed by XRD. Further extension of time, showed no changes in composition and properties of the NCs therefore suggesting that the decomposition of DDT was complete and that no new sulfur ions were formed. The resultant morphologies were polydispersed particles for Cu_3N, nearly monodispersed hexagonal particles for Cu_2S (5 min) and monodispersed small spherical particles for Cu_9S_5 (10 min) NCs. The optical properties showed the transition of the band-gap from that of Cu_3N to Cu_2S and ultimately Cu_9S_5. The photoluminescence spectra of both Cu_2S and Cu_9S_5 showed an up-conversion process with the emission energy blue-shifted from the band gap energy.

References

[1] M.E. Leitch, E. Casman, G.V. Lowry, *Journal of Nanoparticle Research*, 14 (2012) 1283.

[2] F. Piccinno, F. Gottschalk, S. Seeger, B. Nowack, *Journal of Nanoparticle Research*, 14 (2012) 1109.

[3] M. Salavati-Niasari, F. Davar, *Materials Letters*, 63 (2009) 441-443.

[4] V.V.T. Padil, M. Černík, *International Journal of Nanomedicine*, 8 (2013) 889.

[5] A.S. Lanje, S.J. Sharma, R.B. Pode, R.S. Ningthoujam, *Advances in Applied Science Research*, 1 (2010) 36-40.

[6] P. Sutradhar, M. Saha, D. Maiti, *Journal of Nanostructure in Chemistry*, 4 (2014) 86.

[7] S.S.M. Nelwamondo, M.J. Moloto, R.W. Krause, N. Moloto, *Materials Research Bulletin*, 47 (2012) 4392-4397.

[8] M. Mousavi-Kamazani, Z. Zarghami, M. Salavati-Niasari, *The Journal of Physical Chemistry C*, 120 (2016) 2096-2108.

[9] Y.-I. Lee, *Materials Chemistry and Physics*, 180 (2016) 104-113.

[10] R. Juza, H. Hahn, *Zeitschrift für anorganische und allgemeine Chemie*, 239 (1938) 282-287.

[11] R.K. Sithole, L.F. Machogo, M.A. Airo, S.S. Gqoba, M.J. Moloto, P. Shumbula, J. Van Wyk, N. Moloto, *New Journal of Chemistry*, 42 (2018) 3042-3049.

[12] M.A. Airo, R. Rodrigues, S. Gqoba, N. Ntholeng, F. Otieno, M.J. Moloto, M.W.C.C. Greenshields, I.A. Hümmelgen, N. Moloto, *Sensors and Actuators B: Chemical*, 236 (2016) 116-125.

[13] M.S. Bakshi, *Crystal Growth & Design*, 16 (2) (2016) 1104-1133.

[14] M. Kruszynska, H. Borchert, A. Bachmatiuk, M.H. Rümmeli, B. Büchner, J.r. Parisi, J. Kolny-Olesiak, *American Chemical Society Nano*, 6 (2012) 5889-5896.

[15] X. Ding, D. Fu, Y. Kuang, Y. Zou, X. Yang, L. Feng, X. Sun, H. Wu, J. Jiang, *American Chemical Society Applied Nano Materials*, 1 (7) 2018 3303-3311.

[16] Y. Wang, X. Ai, D. Miller, P. Rice, T. Topuria, L. Krupp, A. Kellock, Q. Song, *Crystal Engineering Communications*, 14 (2012) 7560-7562.

[17] Y. Jiang, X. Zhang, Q.Q. Ge, B.B. Yu, Y.G. Zou, W.J. Jiang, W.G. Song, L.J. Wan, J.S. Hu, *Nano Letters*, 14 (2014) 365-372.

[18] J.R. Vegelius, K. Kvashnina, H. Hollmark, M. Klintenberg, Y. Kvashnin, I.L. Soroka, L. Werme, S.M. Butorin, *The Journal of Physical Chemistry C*, 116 (2012) 22293-22300.

[19] H.R.M. Frøkiær, T.E. Warner, *Solid State Sciences*, 70 (2017) 74-80.

[20] C. Marcos, A. Paniagua, D. Moreiras, S. García-Granda, M. Diaz, *Acta Crystallographica Section B: Structural Science*, 52 (1996) 899-904.

[21] S.W. Goh, A.N. Buckley, R.N. Lamb, *Minerals Engineering*, 19 (2006) 204-208.

[22] J. Folmer, F. Jellinek, *Journal of the Less Common Metals*, 76 (1980) 153-162.

[23] I. Nakai, Y. Sugitani, K. Nagashima, Y. Niwa, *Chemischer Informationsdienst*, 9 (36) (1978).

[24] M. Nagamori, *Metallurgical Transactions B*, 7 (1976) 67-80.

[25] L. Liu, H. Zhong, Z. Bai, T. Zhang, W. Fu, L. Shi, H. Xie, L. Deng, B. Zou, *Chemistry of Materials*, 25 (2013) 4828-4834.

[26] G. Donnay, J. Donnay, G. Kullerud, *American Mineralogist: Journal of Earth and Planetary Materials*, 43 (1958) 228-242.

[27] C.J. Thompson, R.A. Meyer, J.S. Ball, *Journal of the American Chemical Society*, 74 (1952)3287-3289.

[28] M. Brust, M. Walker, D. Bethell, D.J. Schiffrin, R. Whyman, *Journal of the Chemical Society, Chemical Communications*, (1994) 801-802.

[29] S.Y. Kang, K. Kim, *Langmuir*, 14 (1998) 226-230.

[30] S. Palchoudhury, Y. Xu, W. An, C.H. Turner, Y. Bao, *Journal of Applied Physics*, 107 (2010) 09B311.

[31] F. Laffineur, J. Delhalle, S. Guittard, S. Geribaldi, Z. Mekhalif, *Colloids and Surfaces A: Physicochemical and Engineering Aspects*, 198 (2002) 817-827.

[32] L. An, P. Zhou, J. Yin, H. Liu, F. Chen, H. Liu, Y. Du, P. Xi, *Inorganic Chemistry*, 54 (2015) 3281-3289.

[33] J. Tauc, R. Grigorovici, A. Vancu, *Physica Status Solidi (b)*, 15 (1966) 627-637.

[34] N. Moloto, M.J. Moloto, N.J. Coville, S.S. Ray, *Journal of Crystal Growth*, 324 (2011) 41-52.

[35] T. Xaba, M.J. Moloto, N. Moloto, *Materials Letter*, 146 (2015) 91-95.

Chapter 7

One-step synthesis of Cu_3N, Cu_2S and Cu_9S_5 and their photocatalytic degradation of methyl orange and methylene blue

Abstract

Herein we report on a simple one-step synthesis of copper-rich Cu_3N, Cu_2S and Cu_9S_5 nanoparticles by using the surfactant dodecanethiol as a sulfur source to substitute the nitrogen in Cu_3N using the HSAB theory. The resultant particles are characterized using XRD, TEM, and UV-Vis and PL spectroscopies. Cubic Cu_3N nanoparticles as well as hexagonal Cu_2S, and elongated Cu_9S_5 nanoparticles are formed. These nanoparticles have direct band-gap transitions in the visible region. The nanoparticles are then used as photocatalysts to degrade methyl orange and methylene blue dyes. The Cu_3N photocatalyst degrades 89% of the methyl orange dye in a 1^{st} order reaction with the degradation products being aniline and $C_5H_6N_2SO_3^-$ fragments whilst the Cu_9S_5 is the best catalyst at degrading methylene blue (79%). The methylene blue degradation follows a 2^{nd} order reaction and aniline is the only detectable degradation product.

Keywords: Cu_3N; Cu_2S; Cu_9S_5; photocatalysis; methyl orange; methylene blue

1. Introduction

Photocatalysis based on semiconductors has over the years shown potential in energy production through water splitting for H_2 generation as well as in water purification through the degradation of organic contaminants. Among the various semiconductor photocatalysts, TiO_2 and ZnO are the most studied due to their properties such as long-term stability towards the photo and chemical corrosion, low cost and non-toxicity [1, 2]. However, their major drawbacks are large energy band-gaps, 3.2 eV and 3.37 eV respectively and fast recombination rates [2]. To circumvent this, several strategies have been employed. From using supports such as carbon nanomaterials to prevent fast recombination rates, by using plasmons as well as doping with metals and non-metals to shift the band-gap energy [3-5]. Also, the use of co-catalysts has been extensively reported [6-8]. An alternative to these strategies is to use semiconductors with different chemical compositions that can absorb in the visible region of the solar spectrum and have low recombination rates while maintaining the costs relatively low. Apart from composition, material properties are strongly dependent on the size and morphology [9, 10]. The size of the nanoparticles can affect the overall surface area of the material whilst the morphology can potentially increase the exposure of active sites [11, 12]. These are some of the crucial parameters in photocatalysis.

Herein, we report on the one-step synthesis of Cu_3N, Cu_2S and Cu_9S_5 nanoparticles (NPs) and their use as catalysts in the degradation of methyl orange (MO) and methylene blue (MB) organic dyes. The synthesis of Cu_3N NPs is quite complex as the copper is being forced to acquire the +1-oxidation state with nitrogen where ideally it is more stable in a +2-oxidation state where it can form Cu_3N_2. This lack of stability readily results in uncapped Cu_3N NPs to easily disproportionate in air due to the presence of oxygen to form the more stable Cu (0) and Cu (II) species [13]. To

circumvent the oxidation, surfactant molecules have been used and these are often functionalized long-chain alkanes or alkenes. The surfactants play a critical role in nanoparticle syntheses as they control the resultant size and morphology of the NPs, they stabilize and protect the NPs and they can act as reducing agents and solvents. However, overlooked, is their potential role as precursors and monomers in the reaction mixture. Herein, we show that dodecanethiol can result in the conversion of Cu_3N NPs to Cu_2S and Cu_9S_5 through the donation of sulfur ions over time, therefore, resulting in the one-step synthesis.

Cu_3N is a semiconductor with band-gap values ranging from 0.23 eV and 2.06 eV [13]. Barman *et al.* reported on the catalytic activities of Cu_3N and Cu_3N decorated with Au NPs towards the degradation of MO and MB with rather modest degradation efficiencies, most likely due to the morphologies [14]. Copper sulfides are semiconducting chalcogenides. A wide range of copper sulfides have been reported from the Cu-rich chalcocite (Cu_2S) [15] to the less Cu-rich djurleite ($Cu_{1.97}S$), digenite (Cu_9S_5), geerite ($Cu_{1.6}S$) till the sulfur-rich covellite (CuS) [16] and villamaninite (CuS_2) [17]. There are many reports on the synthesis of copper sulfides, but the main challenge still lies in obtaining the stoichiometric sulfides especially the intermediates between Cu_2S and CuS. Different studies have shown that the oxidation state of Cu in chalcocite is +1 and the S carries a -2 charge [17-20]. On the other hand, Liu *et al.* [21] are of the view that the formula for $Cu_{1.8}S$ (Cu_9S_5) can be expressed as $[(Cu^{+})_8Cu^{2+}(S^{2-})_5]$. Both chalcocite ($Cu_2S$) and digenite ($Cu_9S_5$) are a p-type semiconductor with a bulk band-gap of 1.2 or 1.8 eV (direct and indirect) and 1.5 eV respectively [22, 23]. Zhao and co-workers reported on the use of Cu_2S microspheres and microrings as photocatalysts for the degradation of MB. The microrings had a better degradation efficiency [24]. A study on CuS-Cu_2S photocatalyst showed poor performance towards the

degradation of MB (61.95%) and MO (9.39%) [25]. There are no reported studies on the use of digenite as a photocatalyst in the degradation of MO and MB, however, $Cu_{1.8}S$-passivated carbon dots showed higher photoreduction efficiency for 2-tert-butyl-1,4-benzoquinone as compared to pristine carbon dots [26].

2. Experimental section

2.1 Materials

Copper (II) nitrate trihydrate (puriss p.a., 99-104%), octadecylamine (ODA) (99% (GC)), dodecanethiol (DDT) (≥ 98%), methyl orange (MO) (analyticatical grade), methylene blue (MB) (analytical grade), ethanol (absolute, ≥99.8% (GC)) and chloroform (anhydrous, ≥99%, contains 0.5-1.0% ethanol as stabilizer were all purchased from Sigma-Aldrich and were used without further purification.

2.2.1 Synthesis of Cu_3N, Cu_2S and Cu_5S_9 nanoparticles

The one-pot synthesis of Cu_3N, Cu_2S and Cu_5S_9 NPs was achieved following a procedure that was reported previously with some modifications. In a typical synthesis, $Cu(NO_3)_2.3H_2O$ (1 mmol) and ODA (10 mL) were mixed in a three-necked round-bottomed flask and degassed using N_2 gas at 115 °C. After an hour under magnetic stirring, the reaction temperature was raised to 240 °C and an aliquot (2 mL) was extracted after 15 min to obtain Cu_3N NPs. After the extraction, DDT (1 mL) was immediately injected into the remaining mixture. This was consequently followed by a temperature drop which was then raised back to 240 °C and maintained for the rest of the experiment. After 10 min and 20 min, aliquots of Cu_2S and Cu_5S_9 respectively were extracted and washed a couple of times in ethanol and then dried under nitrogen.

2.2.2 Photocatalytic degradation of methyl orange and methyl blue

A stock solution of methyl orange or methylene blue was prepared in deionized water to make a 20 ppm solution. About 0.1 g of Cu_3N, Cu_2S and Cu_9S_5 NCs were separately added to 50 mL of the 20 ppm solution. The mixtures were placed in the dark for an hour to allow equilibration. The catalyst-MO/MB solutions were then irradiated using a solar simulator (AM 1.5G 100 mW/cm^2) and aliquots were extracted and filtered before analysis.

2.3 Characterization techniques

The powder X-ray diffractograms (XRD) of the as-synthesized nanoparticles were recorded on a Bruker D2 phaser D2-205530 diffractometer using CuKα radiation (λ=1.5418 Å) at 30 kV/10 mA. The XRD data was acquired using a Bruker Lynxeye PSD detector set to measure at 5^o 2θ and all measurements were acquired at room temperature. The data was analyzed using Bruker AXS Evaluation package. The particle sizes and morphology were studied using a FEI Spirit 120 kV transmission electron microscope (TEM) equipped with an EDX detector operated at an acceleration voltage of 200 kV with a beam spot size of 20-100 nm in TEM mode. The particles were dispersed in chloroform and drop-casted onto a lacey carbon nickel grids. The solvent was then evaporated at room temperature. ImageJ software was employed in order to determine the size of particles. HPLC analyses were carried out with a pump Thermoquest Model TP 4000, an AS300 autosampler and a Thermoquest UV 6000 diode array detector. Separations were obtained under isocratic conditions using a RP-C18 column (Lichrospher RP-18, 250 mm × 4.6 mm; 5 mm particles, Merck, Darmstadt, Germany) and a mobile phase composed of acetonitrile–ammonium acetate 10 mMpH 6.8 (24/76 (v/v)); flow rate 0.8 $mLmin^{-1}$. The eluent from the chromatographic

column successively enters the UV-Vis diode array detector, the ESI interface, and the quadruple ion trap mass analyzer. Compass DataAnalysis software was used to process the acquired data.

3. Result and discussion

3.1 Characterization of the photocatalysts

To study the crystal structure and confirm the formation of the products, XRD is undertaken and the results are shown in Fig. 1. The Cu_3N NPs are indexed to an anti-ReO_3 cubic phase (card: PDF 00-055-0308) and the common oxide impurities are not detected. After extracting the Cu_3N aliquot, DDT is added and after 10 min, pure Cu_2S NPs are obtained. This is evidenced by the obtained X-ray diffractogram where all peaks are indexed to the alpha low cubic phase of Cu_2S (card no. PDF 00-009-0328) and there are no observable Cu_3N peaks. This suggests that the N in the nitride has been substituted by S. DDT continues to decompose and this leads to an increase in the uptake of sulfur resulting in the evolution of the rhombohedral phase of Cu_9S_5, belonging to the space group $R\bar{3}m$ (card no. 00-047-1748). Just like the nitride and the chalcocite, all the peaks in the obtained diffractogram are indexed to digenite and no impurities are observed. The obtained crystal structures are shown in *Scheme 1*.

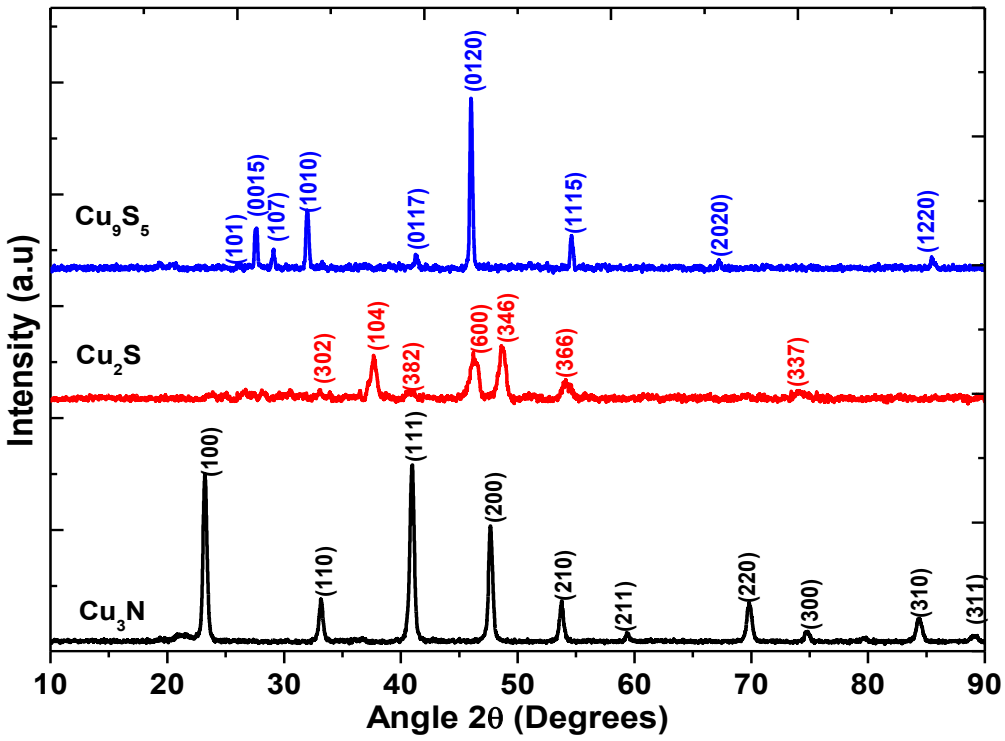

Fig. 1: X-ray diffractograms of (a) Cu_3N NCs in ODA, (b) Cu_2S, and (c) Cu_5S_9 NPs in ODA/DDT mixture.

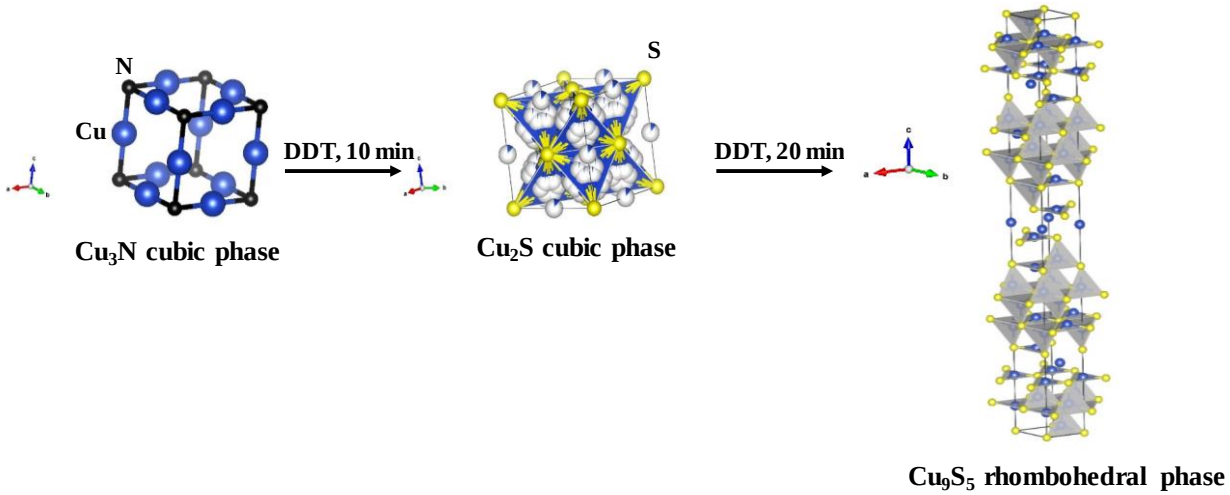

Scheme 1: Crystal structures of Cu_3N, Cu_2S and Cu_9S_5 NPs.

The different morphologies of the NPs obtained before and after the addition of DDT are shown in Fig. 2. In ODA, copper (II) nitrate decomposes anaerobically to give well-defined Cu_3N nanocubes. The cubes self-assemble in a brick-like layered manner even though the population is polydispersed. The average sizes of the nanocubes are 41 nm. After the extraction of the nitride NPs, DDT is added, and this results in the displacement of nitrogen in favor of sulfur thus forming chalcocite (Cu_2S) nanohexagons. Previous studies have shown that alkanethiols such as dodecanethiol can act as capping agents, reducing agents and/or solvents without releasing sulfur [253, 254]. However, herein, in keeping with the Pearson acid-base concept, Cu^+ in Cu_3N, is a soft acid and easily releases the intermediate donor nitrogen in favor of sulfur which is a soft base. Dodecanethiol, therefore, acts as a sulfur source and leads to the colloidal sulfidation of the Cu_3N nanocubes, resulting in Cu_2S after 10 min and eventually Cu_9S_5 after 20 min. The resultant chalcocite NPs are populated by nearly regular-shaped hexagons with an average diameter of 27 nm. Although the sample shows mostly well-dispersed nanoparticles, some regions show a level of agglomeration which is not seen in Cu_3N. The formation of Cu_9S_5 NPs after 20 min of DDT addition, is evident by the change in morphology. As shown in Fig. 2, the digenite NPs are oval to elongated shapes with an average aspect ratio of 1.3.

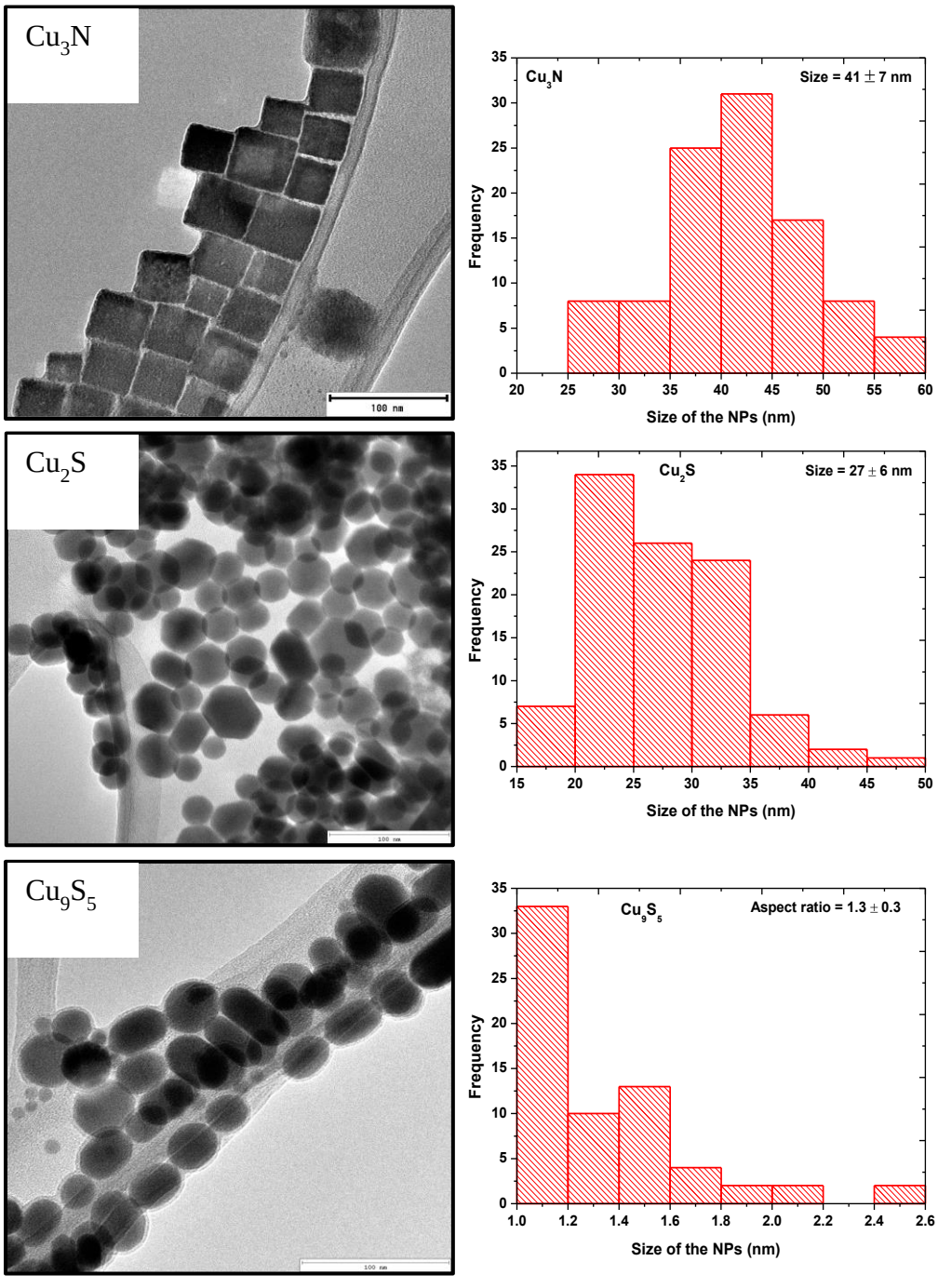

Fig. 2: TEM images and size distribution of Cu_3N, Cu_2S and Cu_9S_5 nanoparticles. (All scales are 100 nm).

In photodegradation, photocatalysts must absorb light preferably within the visible or infra-red range of the electromagnetic spectrum as they are the largest regions of the solar spectrum. To investigate the optical properties of the as-synthesized NPs, the absorbance of each was measured using a UV-Vis spectrometer and the corresponding Tauc plots are illustrated in Fig. 3.

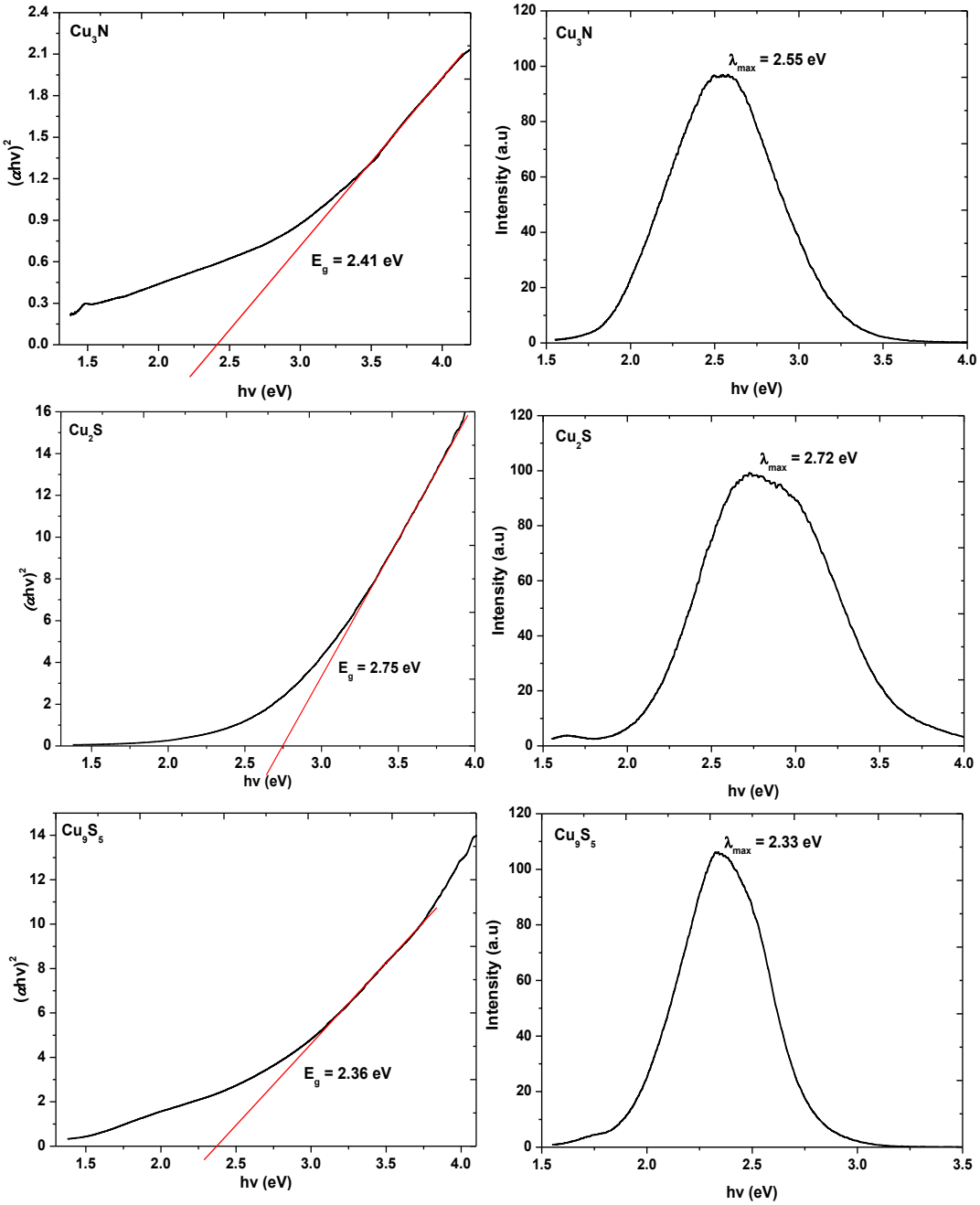

Fig. 3: Tauc plots extracted from UV-Vis absorption spectra for band-gap estimation and PL spectra of Cu_3N, Cu_2S and Cu_9S_5 nanocrystals.

A Tauc plot is used to derive the band-gap energy of a semiconductor with an indirect or direct transition using the relationship below where *h* is the Planck's constant, *v* is the frequency of light, and E_g is the band-gap energy. The value of the exponent *n* is related to the electronic nature of the band-gap, with values of 3, 2, 3/2, and 1/2 corresponding to indirect forbidden (IF), indirect allowed (IA), direct forbidden (DF), and direct allowed (DA) transitions, respectively [29].

$$\alpha h\nu \propto (h\nu - E_g)^n \qquad (1)$$

There is generally inconsistent information about the optical properties of bulk Cu_3N. This complexity is most probably amplified in nanomaterials where size and shape can influence the optical properties. The optical properties of Cu_3N have been the subject of controversy with regards to the bulk band-gap values as well as the nature of the transition. The band-gap values are said to vary between 0.23 eV and 2.06 eV, and the nature of the band-gap transition has been reported as direct and indirect [13]. From band structure calculations, three transitions have been reported, one indirect and two direct band gaps at the Γ and R points [30]. The indirect band-gap is usually associated with small band-gap values and direct band-gap transitions are in the visible region. From Fig. 3, the band gap of Cu_3N is found to be 2.41 eV corresponding to a blue-shifted direct band-gap (bulk band gap is 2.06 eV). The blue-shift of the band-gap is associated with quantum confinement effects. As the size of the nanoparticles become smaller than the Bohr exciton radius of the material, there is discretization of the density of states which increases the

band-gap. Also, as further evidence of the direct band-gap nature, is the observed emission. The emission peak is however blue-shifted from the band-gap (2.55 eV); this may be due to the poor surface passivation which result in surface traps. Cu_2S is both a direct and an indirect band-gap material, with E_g bulk ≈ 1.2 eV and 1.8 eV, respectively [22]. Herein, the observed band-gap of 2.75 eV is blue-shifted from the bulk direct band-gap. This is because the particles are in the nanosized regime. The PL spectrum shows a maximum emission at 2.72 eV, this is indicative of a near band-edge emission. Similarly, the bulk direct band-gap of Cu_9S_5 is reported as 1.5 eV [23]. The as-synthesized NPs as shown in Fig. 3 has a band-gap of 2.36 eV which is blue-shifted from the corresponding bulk band-gap due to quantum confinement effects. The corresponding PL spectrum is slightly red-shifted from the band-gap of the NPs and the near band-edge emission is indicative of impurity-free NPs.

3.2 Photocatalytic activity

The photocatalytic activity of the as-synthesized Cu_3N, Cu_2S and Cu_9S_5 is studied using two dyes, namely methyl orange (MO), which is an anionic dye and methylene blue (MB), which is a cationic dye. Fresh solutions of the dyes (20 ppm) are prepared in deionized water. UV-Vis spectra are acquired in order to monitor the photocatalytic process. Comparisons are done using the wavelength that shows maximum absorbance for each dye and these correspond to 464 nm and 666 nm for MO and MB respectively. The absorbance is then monitored against irradiation time.

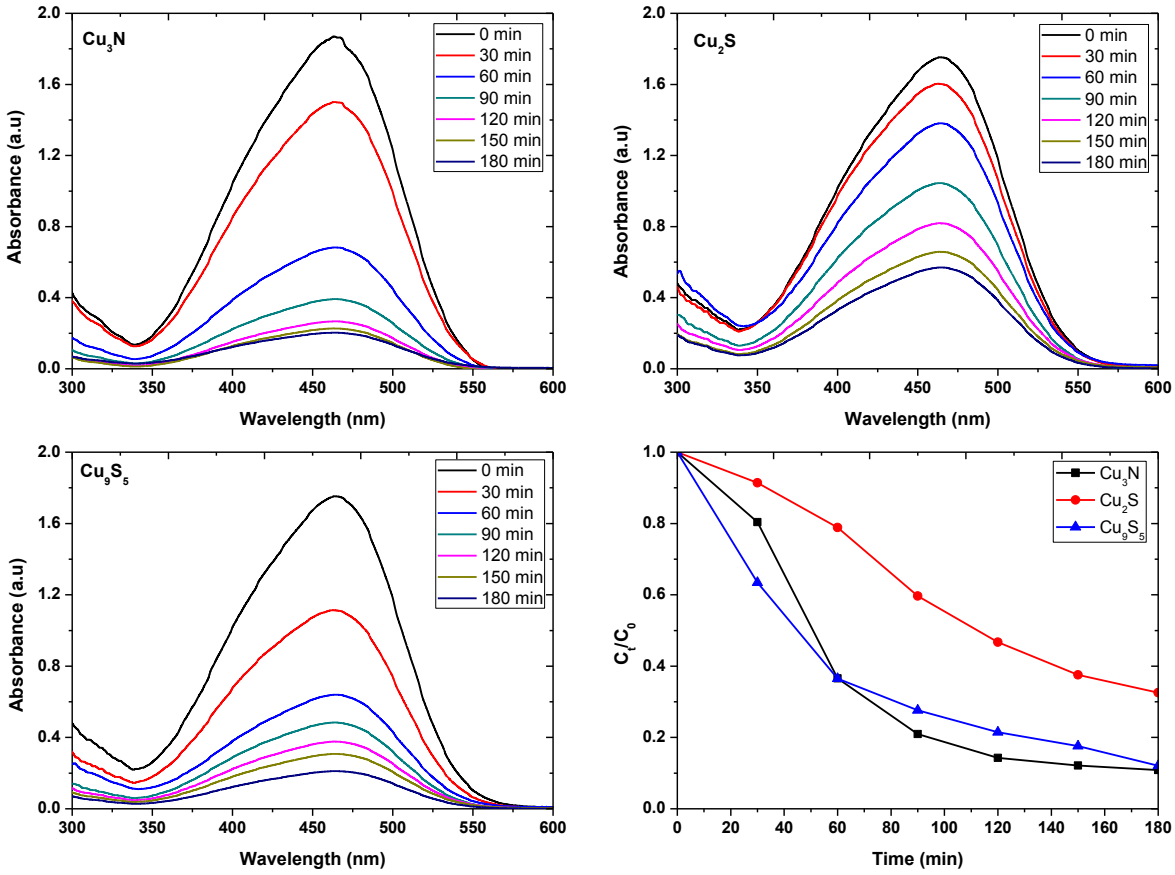

Fig. 4: Absorption spectra of MO under AM 1.5G solar irradiation in the presence of Cu_3N, Cu_2S and Cu_9S_5 nanoparticles and their photodegradation.

After the blank experiments, 0.1 g of each catalyst is added to the dyes and these were then evaluated separately, in MO then in MB for 180 min and 240 min respectively. Shown in Fig. 4 are the UV-Vis absorption spectra of the MO under solar illumination in the presence of Cu_3N, Cu_2S and Cu_9S_5 catalysts. For all catalysts, the characteristic absorption peak of MO diminishes with prolonged solar irradiation. From the degradation curves, Cu_3N and Cu_9S_5 nanoparticles has degraded 63% of the MO dye after an hour whilst Cu_2S has only degraded 21%. After 180 min,

Cu_3N has performed better than the chalcogenide catalysts with 89% degradation efficiency as compared to 88% and 67% for Cu_9S_5 and Cu_2S respectively as shown in Fig. 6.

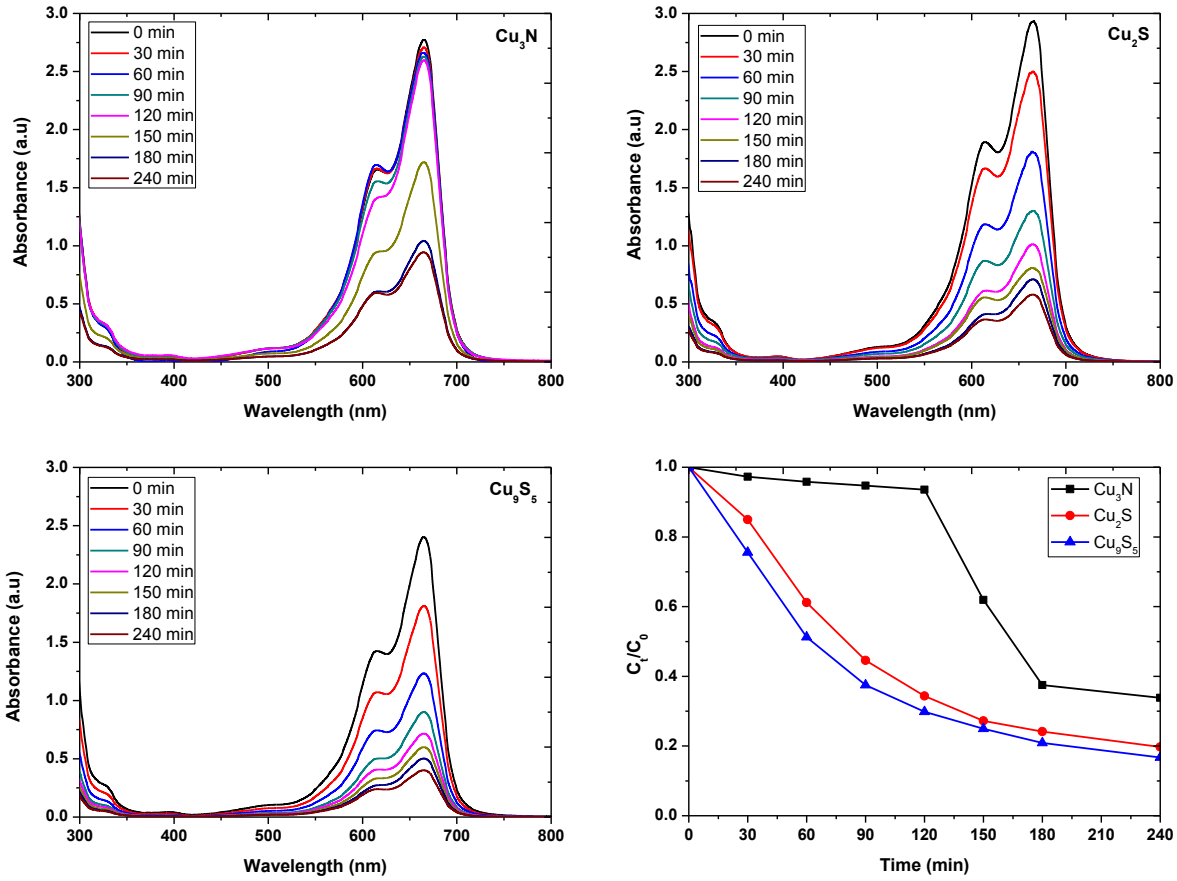

Fig. 5: Absorption spectra of MB under AM 1.5G solar irradiation in the presence of Cu_3N, Cu_2S and Cu_9S_5 nanoparticles and their photodegradation.

Methylene blue absorption peaks show moderate decrease in absorbance with increasing time (Fig. 5). Nevertheless, the degradation efficiencies are obtained in the order of Cu_9S_5 > Cu_2S > Cu_3N as shown in Fig. 6. From the obtained results, it is quite clear that the catalysts perform relatively better in an anionic dye versus a cationic dye. The structures of the dyes are shown in *Scheme 2* and *Scheme 3*. The intrinsic properties of the photocatalyst, such as the surface area, active sites,

light absorption range, redox potential, charge separation efficiency, and stability, strongly affect the photodegradation activity. In addition, the interaction of the dye with the catalyst also influences the degradation efficiency. From the TEM images, Cu_9S_5 has more anisotropic particles and most likely has a higher surface area and more active sites hence its overall better catalytic performance.

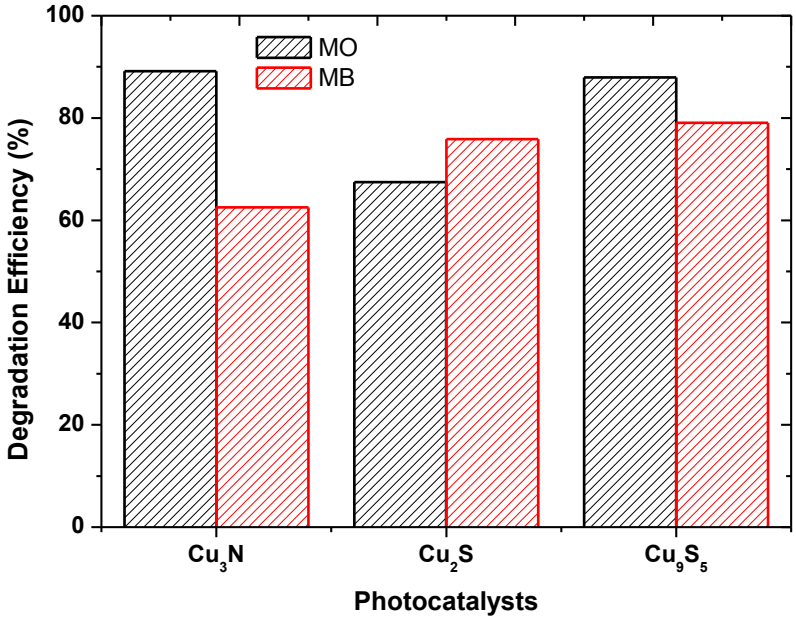

Fig. 6: MO and MB degradation efficiencies using Cu_3N, Cu_2S and Cu_9S_5 as photocatalysts.

The photocatalytic degradation of dyes needs simultaneous participation of organic and oxygen molecules. Because oxygen is generally abundant, its concentration can be considered constant during photocatalysis. According to the law of mass action, the photocatalytic reaction is a quasi-first-order reaction, and the photocatalytic rate is found as follows [31]:

$$r = -\frac{dC}{dt} = kC \qquad (2)$$

Where, *k* is a rate constant and C is the concentration of the dye that adsorbs on the photocatalyst surface at time t. The adsorption of the dye on the semiconductor photocatalyst surface is necessary for the photocatalytic reaction. The adsorption–desorption (A–D) equilibrium is considered to follow a Langmuir isotherm. If the A–D equilibrium is still satisfied during photocatalytic reactions under illumination, Eq. (2) can be changed to,

$$r = -\frac{dC}{dt} = \frac{kKC}{1+KC} \qquad (3)$$

This is the Langmuir–Hinshelwood (L–H) model. In the equation, K is the A–D equilibrium constant, and C is the reaction concentration in solution at time t. By integrating Eq. (3) from time 0 to t, another form of the Langmuir–Hinshelwood model (L–H model) can be found:

$$-ln\frac{C_t}{C_0} = k_1 t + b \qquad (4)$$

Where, k_1 *is* the apparent 1st order rate constant, which is the product of *k* and *K*. C_0 is the initial concentration of the dye before photocatalysis, and C_t is the reactant concentration at time t during the photocatalytic reaction. Equation (4) can easily be used to calculate the k_a values of different photocatalytic reactions. The rate constants for the degradation of MO using Cu_3N, Cu_2S and Cu_9S_5 are -0.01354 min^{-1}, -0.00675 min^{-1} and -0.01125 min^{-1} respectively as extracted from the linear curves in Fig. 7. The rate constants are consistent with the degradation efficiency data where Cu_3N is found to be the best photocatalyst.

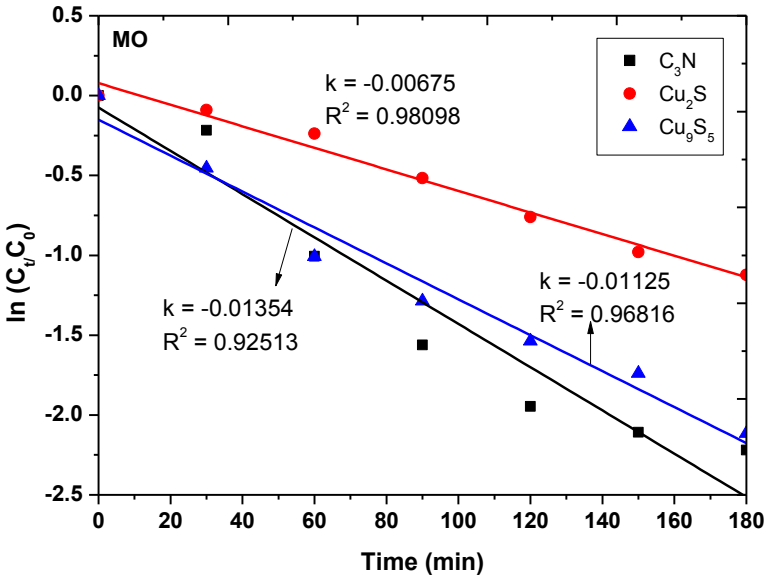

Fig. 7: Kinetics for MO degradation using Cu_3N, Cu_2S and Cu_9S_5 nanoparticles as photocatalysts.

The kinetics of the degradation of MB are shown in Fig. 8. Generally, the photocatalytic reaction is known to follow a pseudo-first-order reaction. Shown in Fig. 8 and summarized in Table 1, the resultant 1st order rate constants trend is Cu_2S > Cu_9S_5 > Cu_3N corresponding to -0.0073, -0.0070 and -0.00502 min^{-1}. The rate order is slightly different from the observed degradation efficiency trend where the Cu_9S_5 catalyst shows slightly better efficiency at degrading MB than the Cu_2S catalysts. Also, the observed R^2 value for Cu_3N is particularly low (0.76378) and this prompted the investigation into the reaction proceeding through either zero-order or 2nd order reaction pathways. The zero-order photocatalytic rate can be found using Eq. 5, where k_0 *is* the apparent zero-order rate constant, C_0 is the initial concentration of the dye before photocatalysis, and C_t is the reactant concentration at time t during the photocatalytic reaction.

$$C_t - C_0 = -k_0 t \qquad (5)$$

The rate constants trend for the zero-order reaction is Cu_2S > Cu_9S_5 > Cu_3N which is similar to the 1st order rate trend. There is an increase in the R^2 value of Cu_3N; however, the R^2 values for Cu_2S and Cu_9S_5 show a significant decrease. The 2nd order reaction pathway can be described using Eq. 6 where k_2 *is* the 2nd order rate constant, C_0 is the initial concentration of the dye, and C_t is the reactant concentration at time t.

$$\frac{1}{C_t} = k_2 t + \frac{1}{C_0} \qquad (6)$$

The rate constants as shown in Table 1 are 0.0091, 0.00622, 0.00318 min^{-1} corresponding to Cu_9S_5 > Cu_2S > Cu_3N. This observed trend is consistent with the observed degradation efficiency shown in Fig. 6. The R^2 value for Cu_3N is 0.73296, slightly lower than the values in zero-order and 1st order reactions. However, the R^2 values for Cu_2S and Cu_9S_5 are significantly better. This, in combination with the degradation rate trend corresponding to the efficiency trend, suggests that the reaction pathway for the degradation of MB by all the photocatalysts is following a 2nd order reaction pathway.

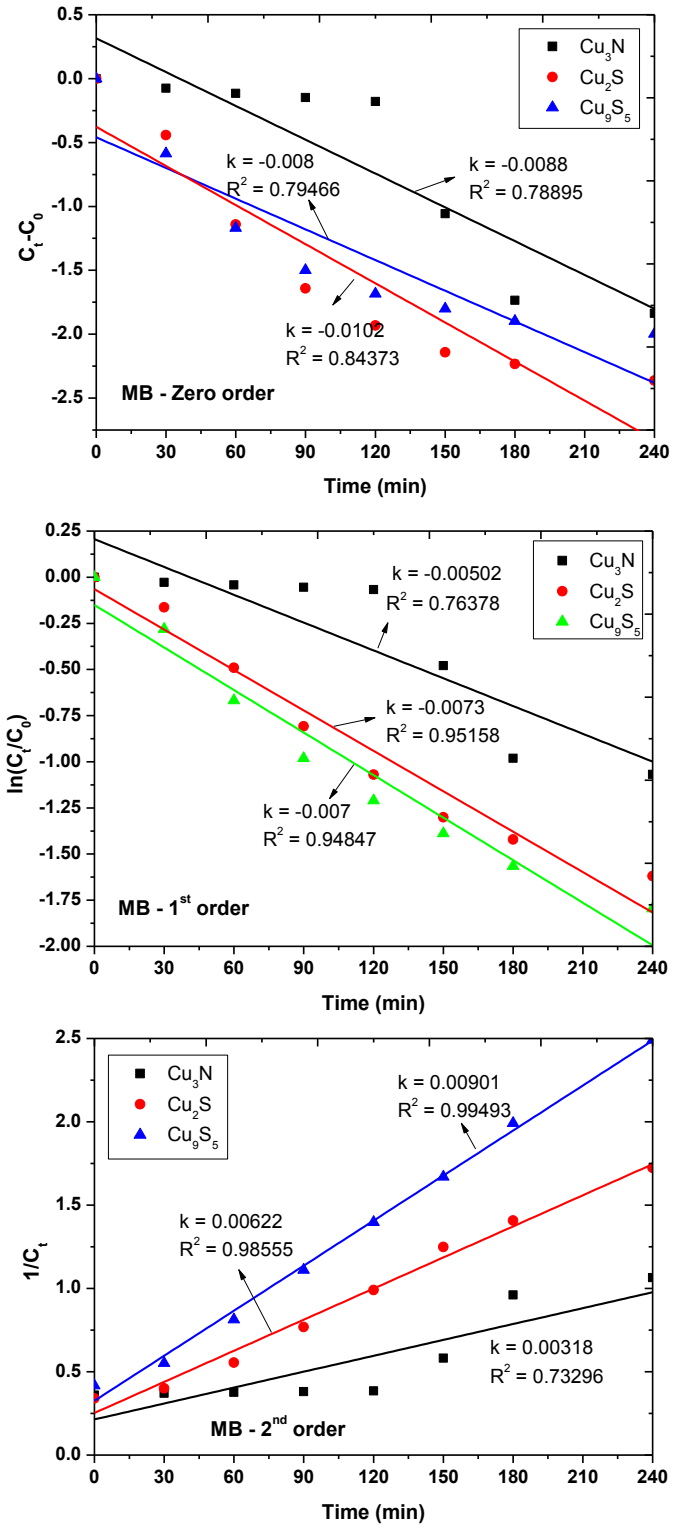

Fig. 8: Kinetics for MB degradation using Cu_3N, Cu_2S and Cu_9S_5 nanoparticles as photocatalysts.

Table 1: Kinetics constants of photocatalytic degradation of MB by the different catalysts

Catalyst	Zero-order		1st order		2nd order	
	k_0	R^2	k_1	R^2	k_2	R^2
Cu_3N	-0.0088	0.78895	-0.00502	0.76378	0.00318	0.73296
Cu_2S	-0.0102	0.84373	-0.0073	0.95158	0.00622	0.98555
Cu_9S_5	-0.008	0.79466	-0.007	0.9447	0.0091	0.99493

To study the degradation paths of MO and MB, the most efficient catalyst for each dye is used, namely Cu_3N for MO and Cu_9S_5 for MB. The photocatalytic process mainly involves the absorption of light which provides enough energy to generate electrons (e^-) and holes (h^+). The charges separate and electrons migrate to the conduction band and the holes move to the valence band. On the surface of the catalysts, the electrons reduce dissolved oxygen in the reaction mixture generating the $O_2^{\cdot -}$ radicals. On the other hand, the holes oxidize H_2O molecules to form $OH^{\cdot}$ radicals. The formed radicals are highly reactive and attack the dye molecules resulting in degradation [14]. To study the degradation products, HPLC equipped with a UV-Vis detector is used. The HPLC results of the degradation of MO and MB by Cu_3N is shown in Fig. 1S. The intensities of all the chromatographs are set to the same scale, hence it can be seen that the intensity of the MO peak is decreasing with increasing irradiation time, thereby indicating the depletion of MO dye in the reaction mixture. On the other hand, the extent of the degradation of MB using Cu_3N as a photocatalyst in the same amount of time is less pronounced as evident by the peak intensity. This is consistent with the observed UV-Vis absorption data and the corresponding degradation efficiency graph in Fig. 5. Although the depletion of MO is observed, there is a need to try and establish what the possible degradation products are. To achieve this, mass spectrometry

of the aliquots up to 180 min is done and the results are shown in Fig. 2S. Methyl orange ($C_{14}H_{14}N_3NaO_3S$) has a molar mass of 327.33 g/mol and at 0 min it appears as a peak $[MO + H]^+$ at m/z = 328.25. The $C_{14}H_{14}N_3O_3S^-$ ion (sulfonate), with a molar mass of 304,34 g/mol is thought to take up H^+ ion in the reaction mixture, hence resulting in m/z = 306.09 which is the most intense peak. In the beginning (0 min), the MS spectrum shows two peaks corresponding to the masses of MO and sulfonate ion but as time progresses other peaks start to emerge. The emergence of new hydrogenated species, for example at m/z = 122.08 and 186.20 indicate the formation of by-products during the degradation. Using the acquired results, the formed degradation products are shown in *Scheme* 2. These results suggest that the C-N group was attacked by the radicals resulting in the formation of smaller molecules namely aniline and $C_6H_5N_2SO_3^-$ fragments.

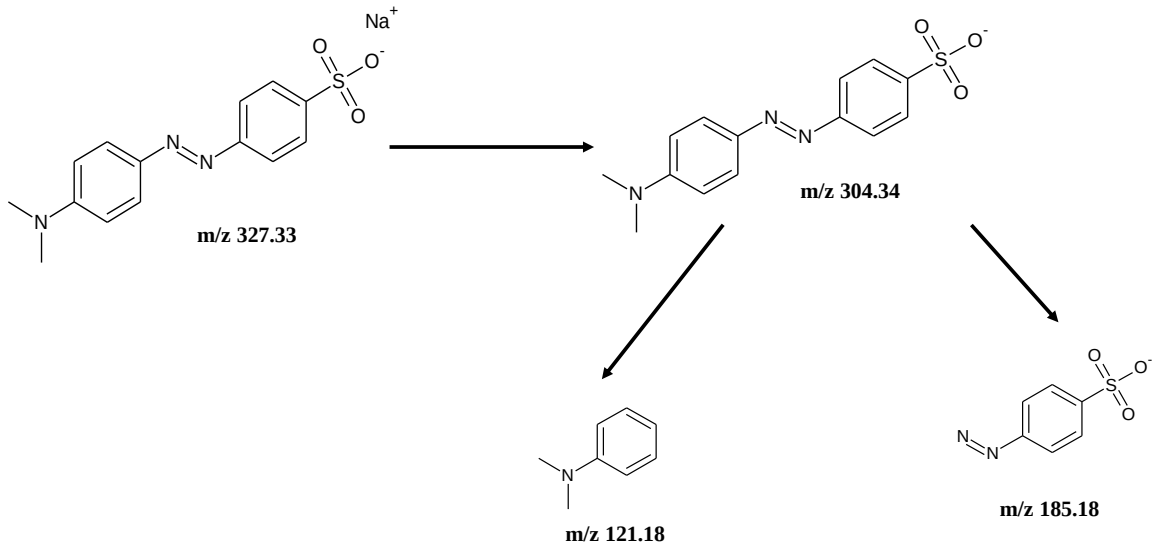

Scheme 2: Degradation products of MO using Cu_3N as a photocatalyst determined by mass spectrometry.

The HPLC results for the degradation of MO and MB by Cu_9S_5 are shown in Fig. 3S. The MO peaks diminish completely within 300 min as compared to the MB. Nevertheless, the Cu_9S_5 catalyst seems to degrade MB much better than the Cu_3N catalyst and this is consistent with the results reported in Fig. 6. The corresponding mass spectra in Fig. 4S, largely show one peak at m/z = 284 corresponding to the dye cation after the loss of chlorine (MB is $C_{16}H_{18}ClN_3S$ with a molar mass of 319.8522 g/mol) and only after 240 min, a small peak is observed corresponding to m/z = 121.1796 which is assigned to aniline. The degradation products are therefore shown in *Scheme* 3.

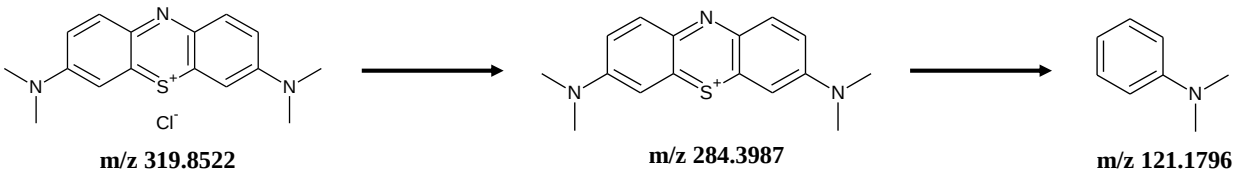

Scheme 3: Degradation products of MB using Cu_5S_9 as a photocatalyst determined by mass spectrometry.

4. Conclusions

Herein the sulfidation of Cu_3N NPs to Cu_2S and Cu_9S_5 using DDT as the sulfidation agent is demonstrated. The Cu_3N NPs are cubic in shape with an average size of 41 nm whilst Cu_2S NPs are hexagonal with an average size of 27 nm and Cu_9S_5 has an elongated shape with an aspect ratio of 1.3. The three nanoparticles are then used as photocatalysts to degrade MO and MB. The Cu_3N photocatalyst has the greatest efficiency in degrading MO (89%) whilst the Cu_9S_5 is the best at degrading MB (79%). The degradation path of MO involves the cleaving of the C-N to form aniline and $C_5H_6N_2SO_3^-$ fragments whilst the MB degradation product is aniline only.

References

[1] K. Nakata, A. Fujishima, *Journal of Photochemistry and Photobiology C: Photochemistry Reviews*,13 (2012) 169-189.

[2] S.S. Nkabinde, X. Mathebula, Z. Tetana, N. Moloto, *MRS Advances*, 3 (2018) 2653-2665.

[3] S.U.M. Khan, M. Al-Shahry, W.B. Ingler, *Science*, 297 (2002) 2243-2245.

[4] W.Y. Choi, A. Termin, M.R. Hoffmann, *Journal of Physical Chemistry*, 98 (1994) 13669-13679.

[5] M. Anpo, *Pure and Applied Chemistry*, 72 (2000) 1787-1792.

[6] J. Yang, D. Wang, H. Han, C. Li, *Accounts of Chemical Research*, 4(8) (2013) 1900-1909.

[7] X. Chen, S. Shen, L. Guo, S.S. Mao, *Chemical Reviews*, 110 (2010) 6503-6570.

[8] X. Zong, H.J. Yan, G.P. Wu, G.J. Ma, F.Y. Wen, L. Wang, C. Li, *Journal of American Chemical Society*, 130 (2008) 7176-7177.

[9] N. Moloto, N.J. Coville, S.S. Ray, M.J. Moloto, *Physica B: Condensed Matter*, 404(22) (2009) 4461-4465.

[10] S.M.M. Nelwamondo, M.J. Moloto, R.W. Krause, N. Moloto, *Materials Research Bulletin*, 47(12) (2012) 4392-4397.

[11] T.L. Hsiung, H.P. Wang, H.P. Lin, *Journal of Physics and Chemistry of Solids*, 69 (2008) 383-385.

[12] Y. Inaki, H. Yoshida, T. Hattori, *The Journal of Physical Chemistry B*, 104 (44) (2000) 10304-10309.

[13] R.K. Sithole, L.F. Machogo, M.A. Airo, S.S. Gqoba, M.J. Moloto, P. Shumbula, J. Van Wyk, N. Moloto, *New Journal of Chemistry*, 42 (2018) 3042-3049.

[14] D. Barman, S. Paul, S. Ghosh, S.K. De, *ACS Applied Nano Materials*, 2 (2019) 5009-5019.

[15] Y. Jiang, X. Zhang, Q.Q. Ge, B.B. Yu, Y.G. Zou, W.J. Jiang, W.G. Song, L.J. Wan, J.S. Hu, *Nano Letters*, 14 (2014) 365-372.

[16] J.R. Vegelius, K. Kvashnina, H. Hollmark, M. Klintenberg, Y. Kvashnin, I.L. Soroka, L. Werme, S.M. Butorin, *The Journal of Physical Chemistry C*, 116 (2012) 22293-22300.

[17] H.R.M. Frøkiær, T.E. Warner, *Solid State Sciences*, 70 (2017) 74-80.

[18] C. Marcos, A. Paniagua, D. Moreiras, S. García-Granda, M. Diaz, *Acta Crystallographica Section B: Structural Science*, 52 (1996) 899-904.

[19] S.W. Goh, A.N. Buckley, R.N. Lamb, *Minerals Engineering*, 19 (2006) 204-208.

[20] J. Folmer, F. Jellinek, *Journal of the Less Common Metals*, 76 (1980) 153-162.

[21] I. Nakai, Y. Sugitani, K. Nagashima, Y. Niwa, *Chemischer Informationsdienst*, 9(36) (1978).

[22] M. Nagamori, *Metallurgical Transactions B*, 7 (1976) 67-80.

[23] L. Liu, H. Zhong, Z. Bai, T. Zhang, W. Fu, L. Shi, H. Xie, L. Deng, B. Zou, *Chemistry of Materials*, 25 (2013) 4828-4834.

[24] B. Zhao, S. Li, Q. Zhang, Y. Wang, C. Song, Z. Zhang, K. Yu, *Chemical Engineering Journal*, 230 (2013) 236-243.

[25] U. Shamraiza, A. Badshaha, R.A. Hussaina, M.A. Nadeemb, S. Saba, *Journal of Saudi Chemical Society*, 21 (2017) 390-398.

[26] Q. Chang, X. Han, C. Xue, J. Yangab, S. Hu, *Chemical Communications*, 53 (2017) 2343-2346.

[27] M.A. Airo, R. Rodrigues, S. Gqoba, N. Ntholeng, F. Otieno, M.J. Moloto, M.W.C.C. Greenshields, I.A. Hümmelgen, N. Moloto, *Sensors and Actuators B: Chemical*, 236 (2016) 116-125.

[28] S.Y. Moon, S-i. Tanaka, T. Sekino, *Nanoscale Research Letters*, 5 (2010) 813-817.

[29] J. Tauc, R. Grigorovici, A. Vancu, *Physica Status Solidi B*, 15 (1966) 627-637.

[30] M. Mikula, D. Búc, E. Pincik, *Acta Physica Slovaca*, 51 (2000) 35-43.

[31] T. L. Villarreal, R. Gómez, M. Neumann-Spallar, N. Alonso-Vante, P. Salvador, *Journal of Physical Chemistry B*, 108 (2004) 15172-15181.

Chapter 8

Thesis conclusions and recommendations

1. Conclusions

Wet chemical synthesis of Cu_3N and Zn_3N_2 nanoparticles is still one of the least explored areas in nanotechnology. Oxidation during colloidal nanosythesis of the metal nitrides poses a huge challenge as both copper and zinc have a higher affinity for O than for N. The study carried out in this thesis has demonstrated the colloidal synthesis of Cu_3N NPs using single-source precursors. Pyrroylaldiminato copper and zinc complexes were synthesized and characterized using powerful techniques such as single crystal X-ray diffraction and nuclear resonance spectroscopy respectively. Different synthetic methods were then employed, namely colloidal synthesis, microwave-assisted synthesis and chemical vapor deposition in an attempt to make copper and zinc nitride nanoparticles. All attempts to synthesize zinc nitride using different single-source precursors proved futile in both solution and solid-state methods of synthesis. In the precursors, Zn^{2+} has a very high affinity for oxygen hence zincite (ZnO) was obtained. Zn_3N_2 was only obtained through ammonolysis of zinc powder using chemical vapor deposition.

We reported for the first time, the use of a Schiff-base complex, bis(2-pyrrolecarbald-propyliminato) copper(II) (PPC) as a single-source precursor in the synthesis of stable copper(I) nitride NPs in organic solvents. Using the conventional colloidal method, thermolysis of PPC in an inert environment resulted in the formation of Cu_3N NPs. In this work, we showed for the first time that the microwave is a potential tool that can be used to synthesize Cu_3N NPs. Spherical Cu_3N NPs were obtained from the microwave synthesis although after 5 min, PXRD showed a

peak at about 2θ = 42˚ which was assigned to Cu_2O. The peak eventually intensified and other Cu_2O peaks emerged with time as the N_2(g) depleted in the vessel. We therefore proposed that if an inert atmosphere can be maintained, then microwave synthesis can be employed to synthesize Cu_3N and avoid oxidation. Synthesis using CVD resulted in the decomposition of the complex to give Cu NPs. Hence, in this study, the best method of synthesis of Cu_3N using PPC as a single-source precursor proved to be the colloidal method.

A comparative study showed that changing the precursor can result in different optical and morphological properties of the NPs. Thermolysis of PPC in octadecylamine resulted in the formation of spherical nanocrystals with an average diameter of 2.8 ± 0.6 nm. The NPs were optically active, having a band gap of 2.21 eV indicating a very significant blue shift compared to the bulk band gap of 0.23 [256]. TEM images of NPs obtained from using copper(II) nitrate as a source of Cu and N showed nanocubes with an average length size of 19 ± 4 nm and a band gap of 1.89 eV. Of interest was that both the band gaps of the nanospheres and the nanocubes were blue shifted compared to bulk and their emission spectra showed anti-Stokes shifts hence setting them as good candidates for up-conversion optoelectronic devices.

The study then went on to embark on studying the morphological and optical changes that occur as Cu_3N NPs are being formed in coordinating ligands. $Cu(NO_3)_2.3H_2O$ was thermolyzed in ODA and HDA at 260 ^oC and time effects were investigated. Nucleation was evident after 5 min in both ODA and HDA as nanocubes could be seen forming in a dense mass of very tiny NPs (nuclei) displayed in the TEM micrographs. Formation of the nanocubes continued and eventually near-perfect nanocubes were obtained after 15 min with no observable presence of the nuclei. The

nanocubes showed good stability but started decomposing to form Cu at 20 and 30 min in ODA and HDA respectively. Complete decomposition was detected after 60 min yielding Cu NPs with no proof of the presence of the nitride NPs. All the acquired nanomaterials showed absorbance within the visible region of the electromagnetic spectrum. This study can aid in employing colloidal Cu_3N in the fabrication of metallic links and write once optical recording devices. Furthermore, this study reported for the first time the contribution that capping agents, ODA and HDA make during the synthesis of Cu_3N. FTIR spectra showed that the nanoparticles were capped with the amine ligands. We then discovered that during the reaction, the alkylamine ligands did not behave as passive solvents or capping agents, but lost 4 protons each from their H_2N-CH_2-groups and were converted to nitriles. The deprotonation enabled oxygen to be released from the nitrate leading to the formation of the nitride NPs and water molecules.

We then probed the effect of introducing a small quantity of a thiol coordinating ligand in the synthesis of colloidal Cu_3N. This study proved to be very interesting as it revealed how three different chalcogenide NPs can be obtained in a one-pot synthesis. Following our normal colloidal synthesis of Cu_3N NPs, a small amount of dodecanethiol (DDT) was introduced into the reaction vessel resulting in the formation of chalcocite and digenite NPs after 5 and 10 min respectively at 230 $^{\circ}$C. The not so well defined Cu_3N NPs were transformed to well dispersed Cu_2S and eventually to Cu_9S_5 nanohexagons. The introduction of DDT did not just result in changes in the morphology of NPs but caused the displacement of N by S species. This came about as a consequence of the high affinity that Cu has for S compared to N atoms. Herein, we reported for the first time the colloidal sulfidation of Cu_3N to get optically active Cu_2S and Cu_9S_5 NPs in a one-pot synthesis.

This phenomenon can come in handy in cases where the copper sulfides are required but only Cu_3N is available hence saving institutions of buying more chemicals.

The optical properties of the Cu_3N nanocubes, Cu_2S hexagons and oval shaped Cu_9S_5 synthesized at 240 ^oC were interrogated by studying their photocatalytic activities. Following the one pot synthesis, optical properties of the NPs were analyzed using their absorption and emission spectra. Cu_3N NPs presented a direct band gap of 2.41 eV and, Cu_2S and Cu_9S_5 NPs showed direct band gaps of 2.75 and 2.36 eV respectively. The photocatalytic activities of the as-synthesized NPs were then evaluated using methyl orange (MO) and methylene blue (MB) azo-dyes. 89%, 88% and 67% degradation of methyl orange was achieved after 3 hours using Cu_3N, Cu_9S_5 and Cu_2S NPs respectively. Although there was not much difference with the Cu_9S_5, the nitride proved to the best catalyst in degrading MO and HPLC results suggested the presence of two degradation byproducts at m/z of 121.18 and 185.18. A different scenario was observed in the degradation of MB. The percentage degradation of Cu_3N was the lowest at 63% and that of Cu_9S_5 was the highest at 79% after 3 hours. The digenite proved to be consistently high in its photocatalytic activity despite the change in the organic dyes where the MO and MB are anionic and cationic respectively in nature. Degradation of MB in the digenite led to degradation byproducts being detected at m/z of 284.40 and 121.18. From kinetic studies, use of the Langmuir–Hinshelwood model resulted in linear curves proposing that the three chalcogenide NPs followed a 1^{st} order reaction pathway in degrading MO. Further investigation revealed that the degradation of MB by all the as-synthesized nanophotocatalysts followed a 2^{nd} order reaction pathway. In this chapter, we presented for the first time the kinetics of photodegradation of colloidal Cu_3N NPs and that the particles showed the best photocatalytic activity in the anionic dye. Only one report has been published on the

photodegradation activity of copper(I) nitride hence, this investigation will shade more light into the application of the colloidal Cu_3N NPs in photocatalysis. Treatment of polluted water is of paramount importance especially in drought stricken and 3rd world countries with few sources of fresh and clean water. Copper and Cu-based NPS have been used in water treatment hence, this study can make a plausible contribution that can help societies.

2. Recommendations and future work

Synthesis and characterization of Cu_3N NPs

There is a lot of work that still needs to be done on the colloidal synthesis, characterization and application of Cu_3N NPs as they present interesting semiconducting properties. An avenue is open to investigate the effects of using other Schiff-base single-source precursors to get the nitride NPs. Other properties of the colloidal NPs still need to be investigated, such as magnetic properties.

Capping agents

We suggest studies that are linked to the effect of chain length of the alkylamine ligands to determine if they can influence the size, morphology and optical properties of the NPs. Functionalization of the synthesized colloids can allow the NPs to be used as supports during heterogeneous catalysis and drug delivery in the body.

Reduce the degradation time

Near complete degradation times went up to 5 hours in this current study hence, there is a need to probe how it can be made to occur at a faster rate reducing the time. We recommend exchanging

the long ligands for shorter ones after synthesis and doping the Cu_3N NPs in order to facilitate charge separation hence avoid recombination of holes and electrons during photocatalysis.

Other applications

The as-synthesized copper(I) nitride NPs presented very interesting optical properties. They were optically active, absorbing within the visible region and as such, we highly recommend their use in fabricating optoelectronic devices such as solar cells and gas sensors.

References

[1] U. Hahn, W. Weber, *Physical Review B*, 53 (1996) 12684.

Appendix

Chapter 3: Supporting information

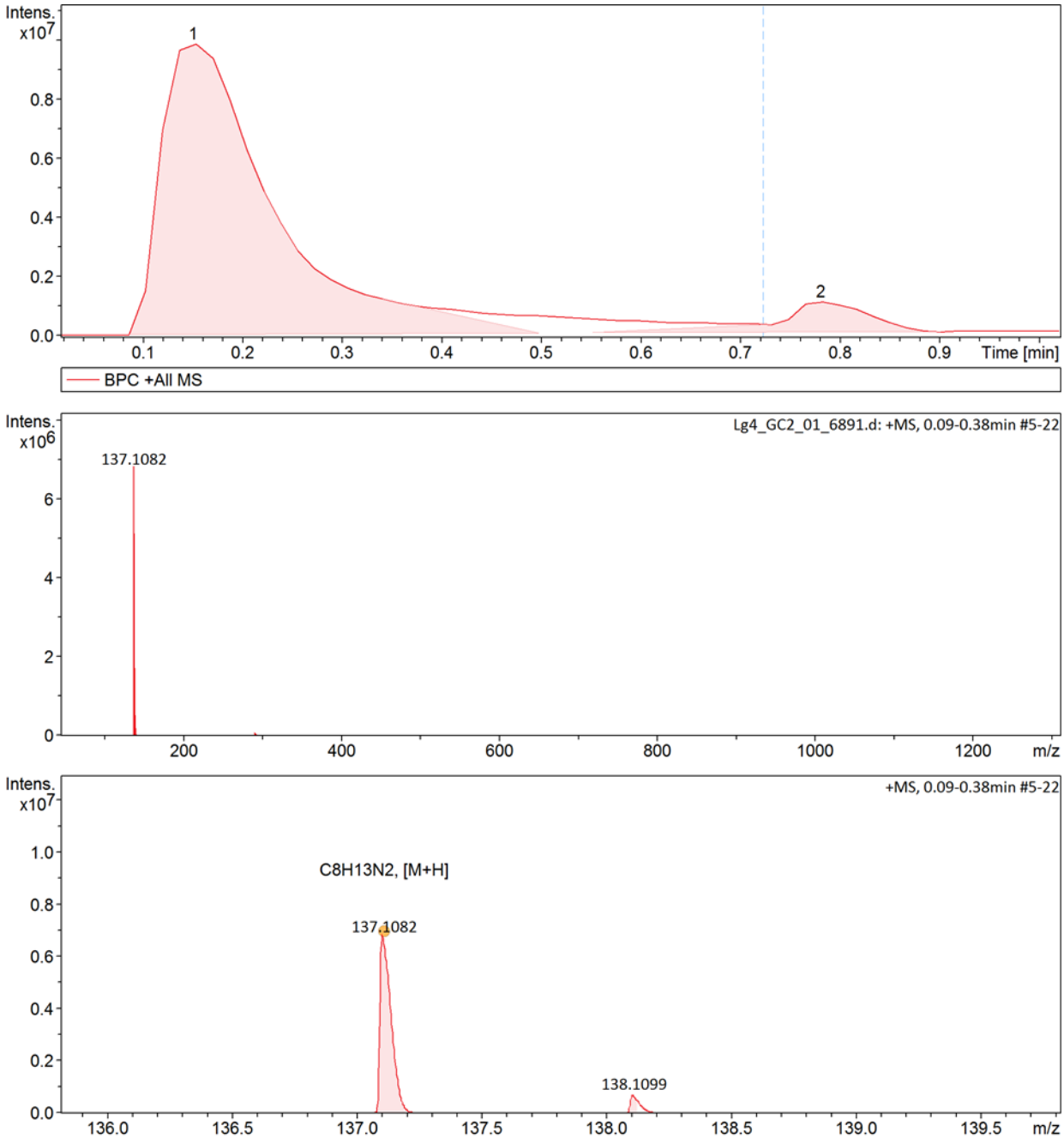

Fig. S1: Mass spectrum of the PP ligand.

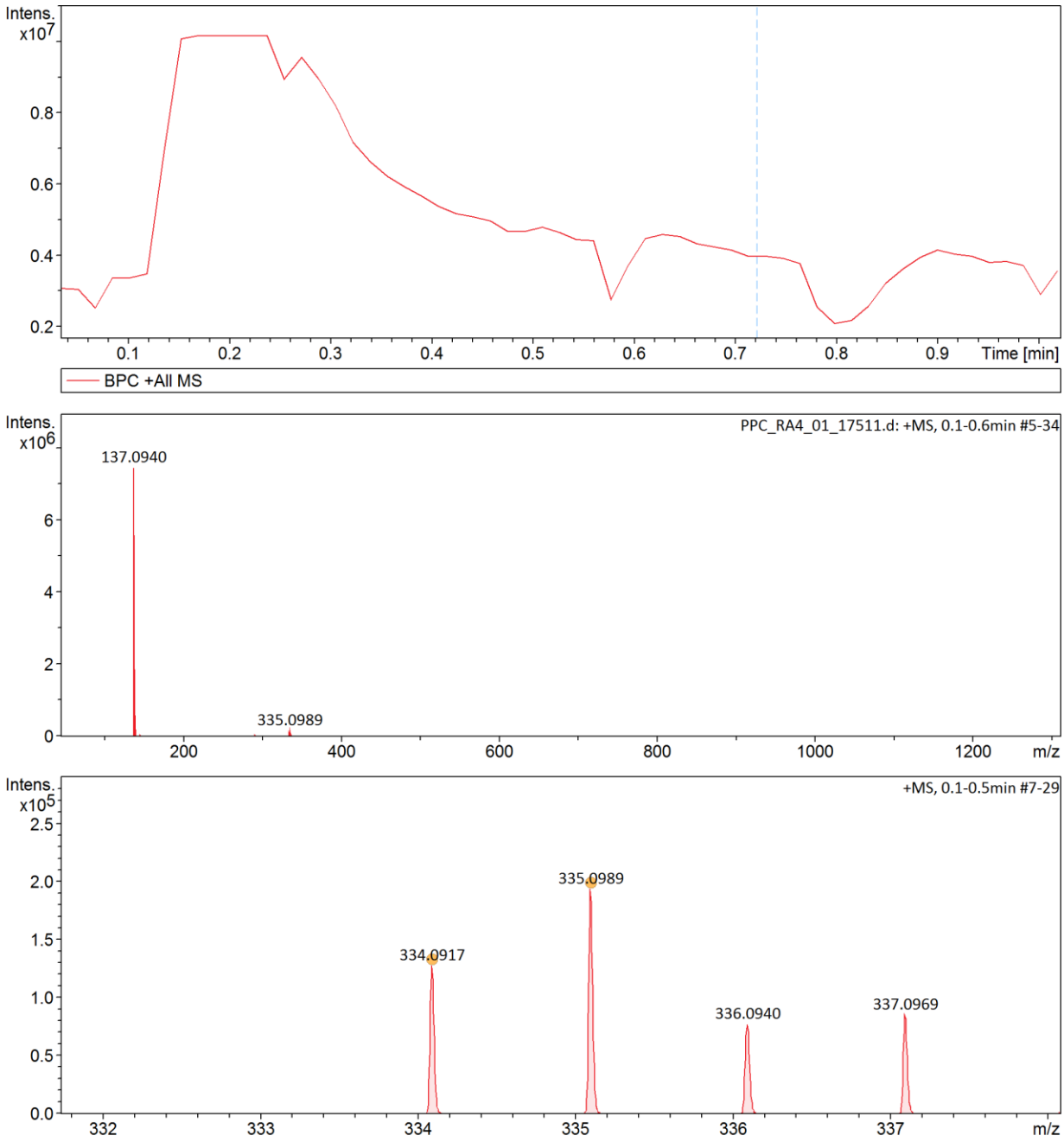

Fig. S2: Mass spectrum of the PPC complex.

Table S1: Elemental analysis: PPC complex

PPC	C	H	N	S
Calculated	57.55	6.69	16.78	-
Found 1	57.36	6.911	16.58	0.53
Found 2	57.51	7.012	16.63	0.306

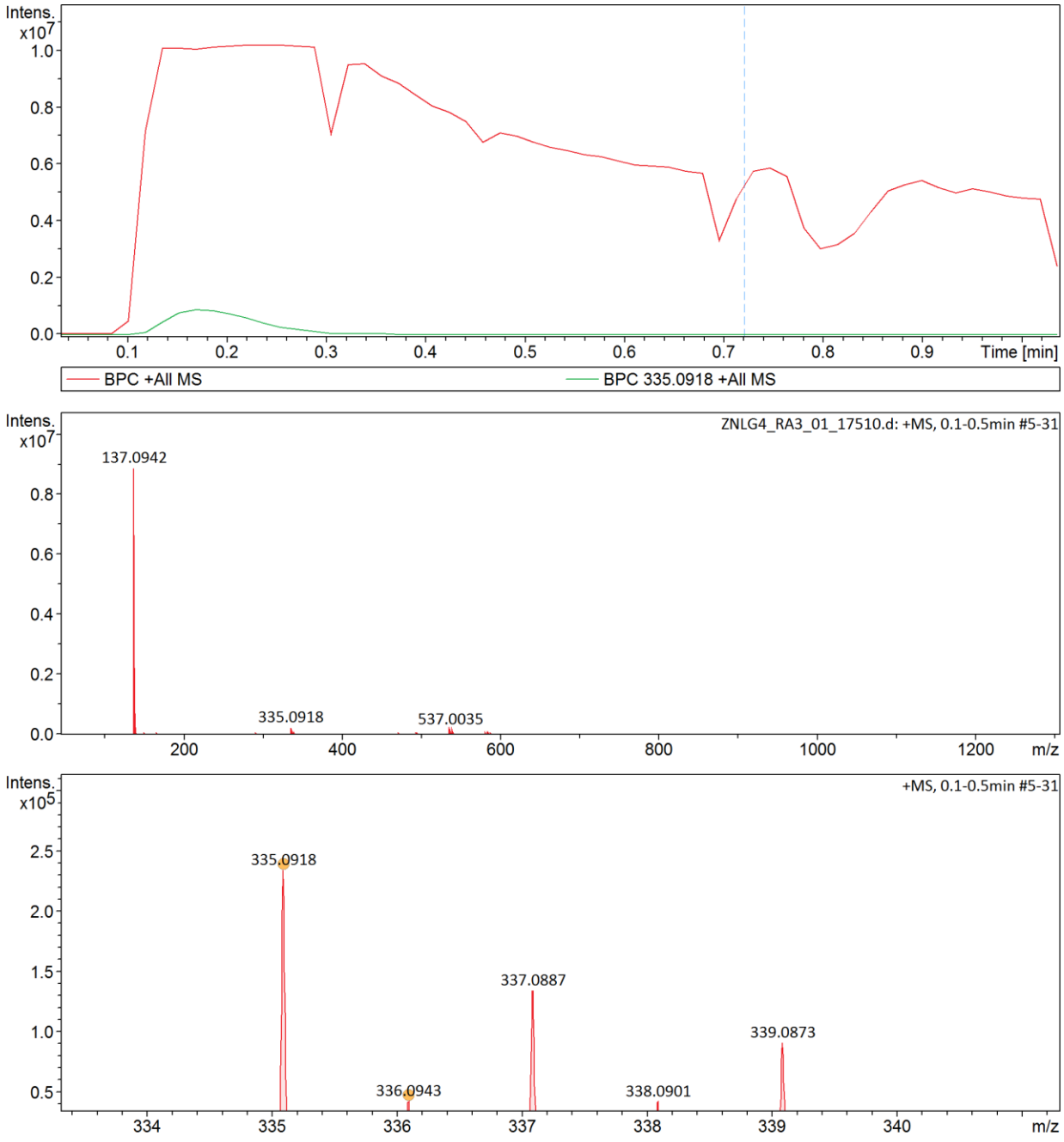

Fig. S3: Mass spectrum of PPZ complex.

Chapter 4: Supporting information

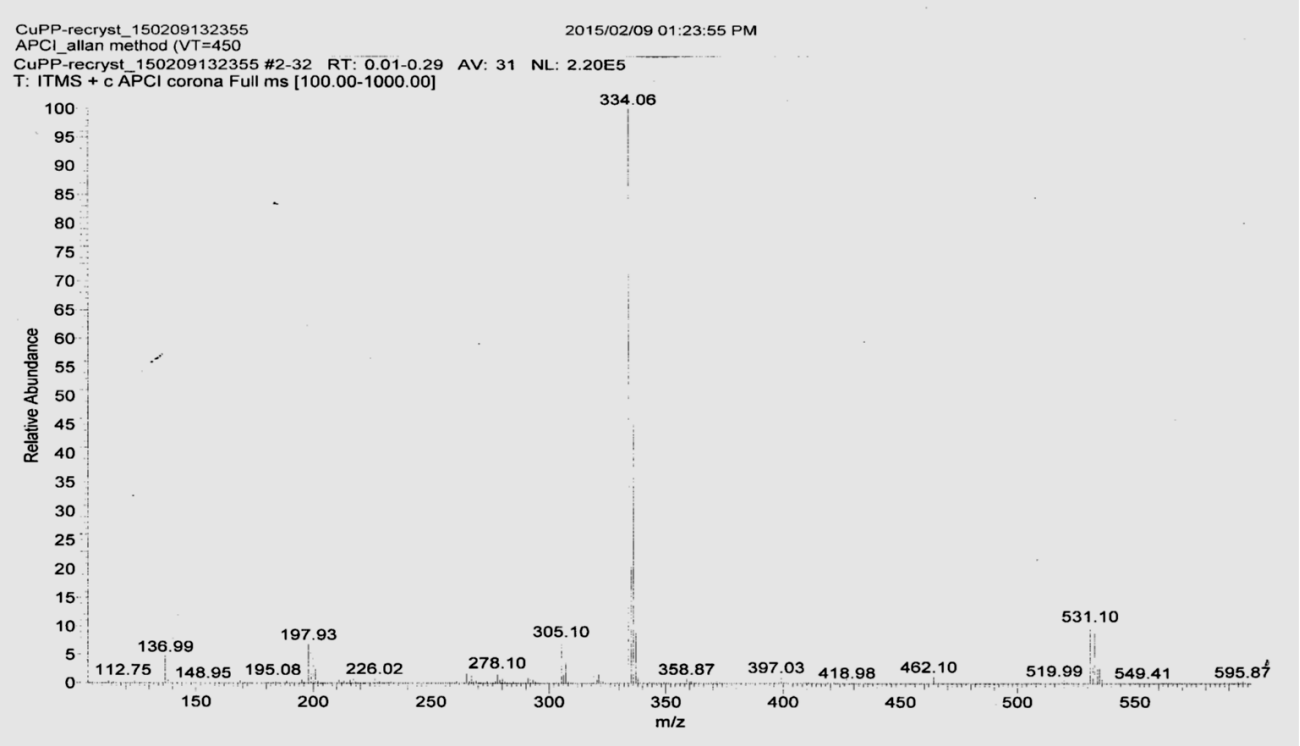

Fig. S1: Mass spectrum of the PPC complex.

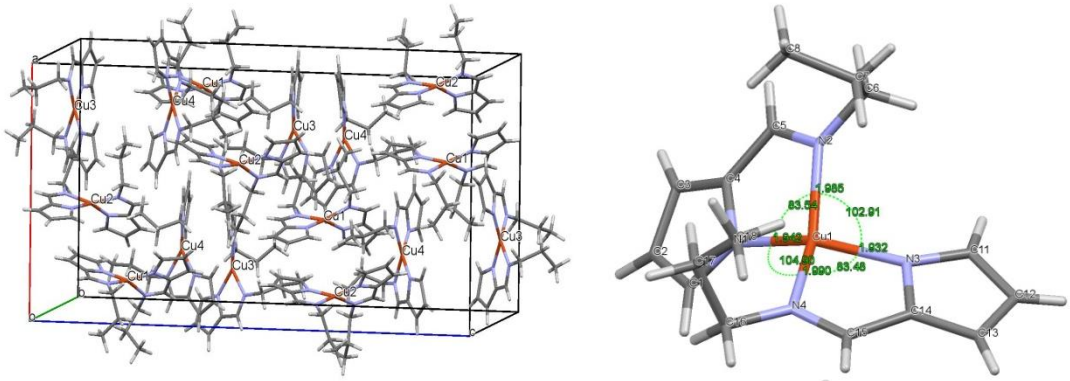

Fig. S2: Crystal structure showing (a) packing of the four different molecules (b) central bond angles and distances on a molecule of the synthesized PPC complex.

Table S1: Crystal data and detailed structure refinement for synthesized and published complex [1].

	Synthesized	**Published**
Empirical formula	$C_{16}H_{22}N_4Cu$	$C_{16}H_{22}N_4Cu$
Formula weight	333.93	333.93
Temperature (K)	293	293
Wavelength (Å)	0.71073	0.71073
Crystal system	orthorhombic	orthorhombic
Space group	P $2_12_12_1$	P $2_12_12_1$
Unit cell dimensions		
***a* (Å)**	14.6108(5)	14.6053917)
***b* (Å)**	15.9605(7)	15.9508(19)
***c* (Å)**	28.9556(11)	28.957(3)
***β* (°)**	90	90
Volume (Å^3)	6752.3(5)	6746.0(13)
Z	16	16
***D*$_{calc}$ (g/cm^3)**	1.314	1.315
Absorption coefficient (mm^{-1})	1.293	1.009
***F*(0 0 0)**	2800	2800
Crystal size (mm)	0.30 × 0.20 × 0.03	0.39 × 0.40 × 0.42
***θ* Range for data collection (°)**	1.406–27.998	1.41–28.32
Index ranges	$-19 \leqslant h \leqslant 19$, $-21 \leqslant k \leqslant 20$, $-38 \leqslant l \leqslant 33$	$-19 \leqslant h \leqslant 16$, $-20 \leqslant k \leqslant 19$ $-20 \leqslant l \leqslant 38$
Reflections collected	54 025	44605
Independent reflections (*R*$_{int}$)	16 264 (0.057)	16033 (0.0490)
Completeness to *θ* (%)	100.0 (θ = 25.242°)	97.1 (θ = 28.32°)
Maximum and minimum transmission	-	0.8237 and 0.6884
Goodness-of-fit on *F*^{2}	0.886	1.031
Final *R* indices	R_1 = 0.0322, wR_2 = 0.0580	R_1 = 0.0496, wR_2 = 0.1135
***R* indices (all data)**	R_1 = 0.0541, wR_2 = 0.0545	R_1 = 0.0787, wR_2 = 0.1285

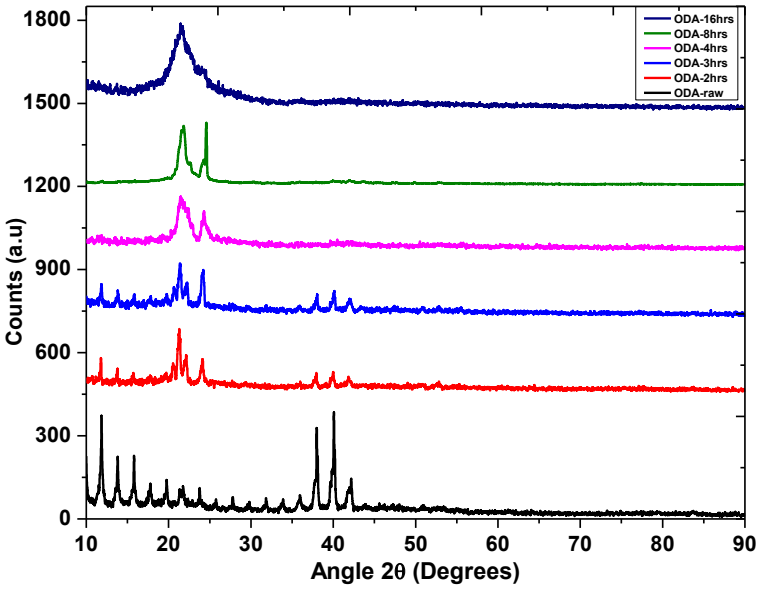

Fig. S3: XRD patterns of products of decomposition of octadecylamine at 260 °C under N_2 (g) flow.

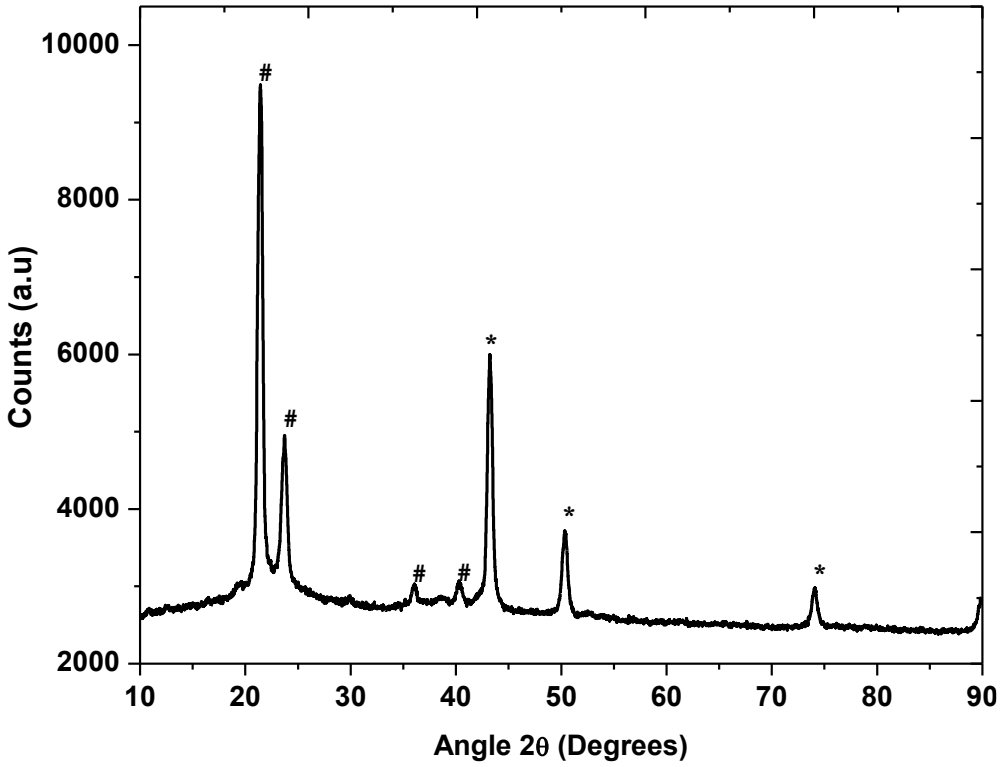

Fig. S4: XRD pattern of a product obtained from the thermolysis of $Cu(CO_2CH_3).H_2O$ in ODA at 260 °C (# ODA and * Cu) JCP2.2CA:01-070-3038.

References

[1] Cambridge Crystallographic Data Centre CCDC-241810.

Chapter 5: Supporting information

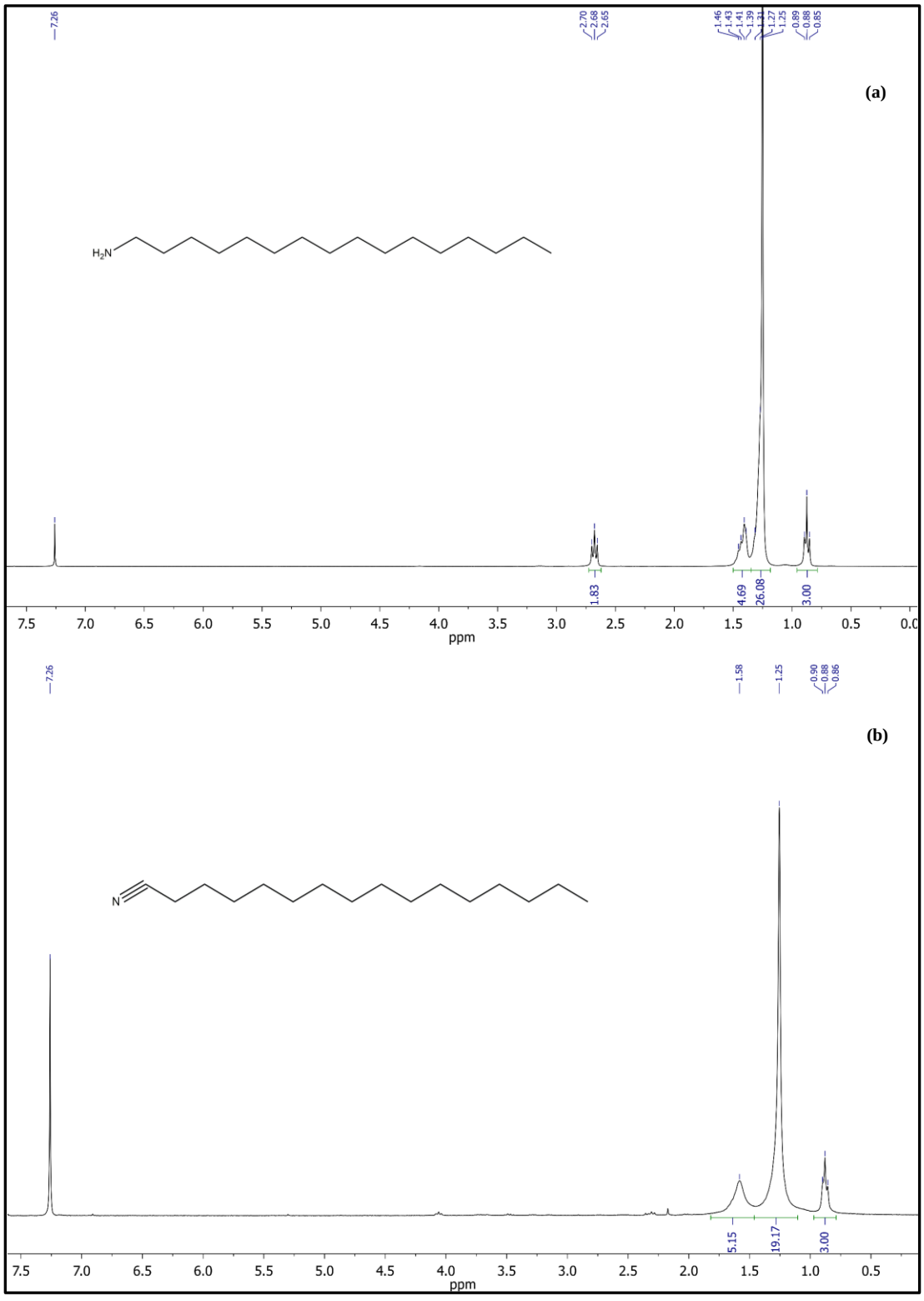

Fig. 1S: ^{1}HNMR spectra of (a) HDA and (b) Cu_3N nanocubes in $CDCl_3$ (15 min sample).

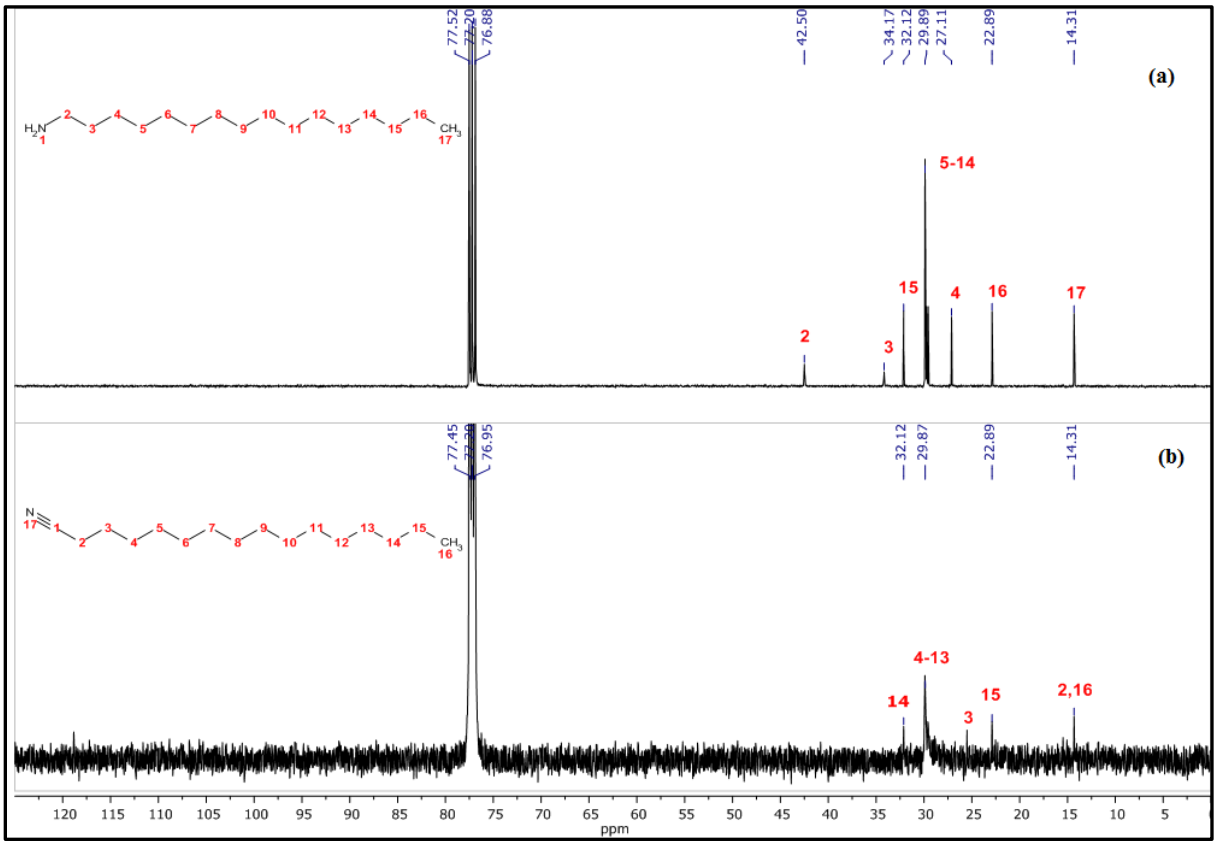

Fig. 2S: ^{13}C NMR spectra of (a) HDA and (b) Cu_3N nanocubes in $CDCl_3$ (15 min sample).

Chapter 7: Supporting information

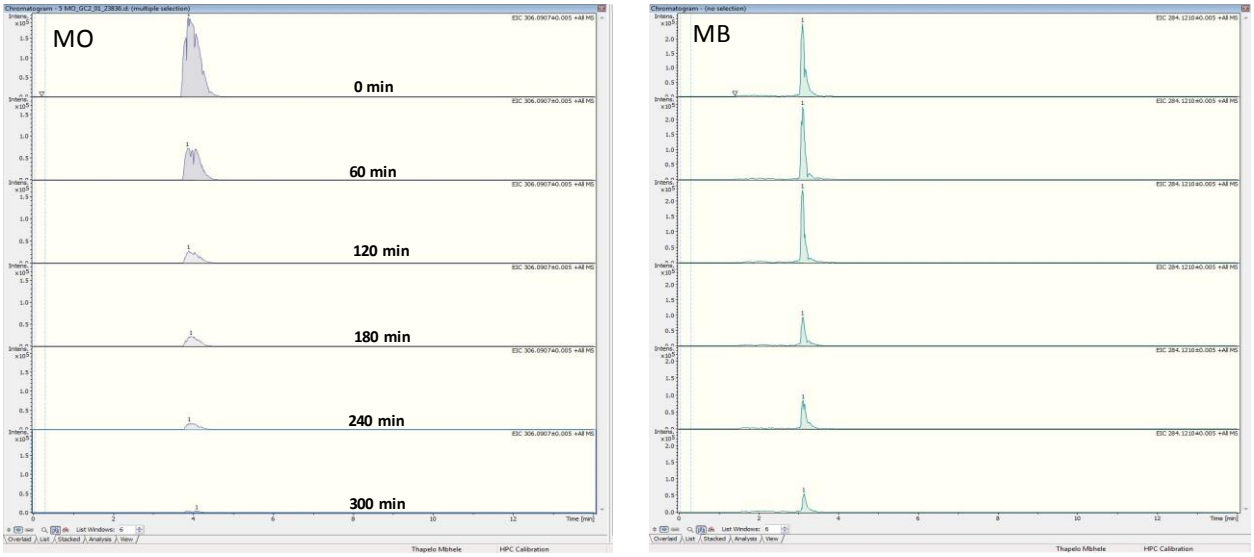

Fig. 1S: HPLC analysis of MO and MB after 5 hours of using Cu_3N NPs as a photocatalyst.

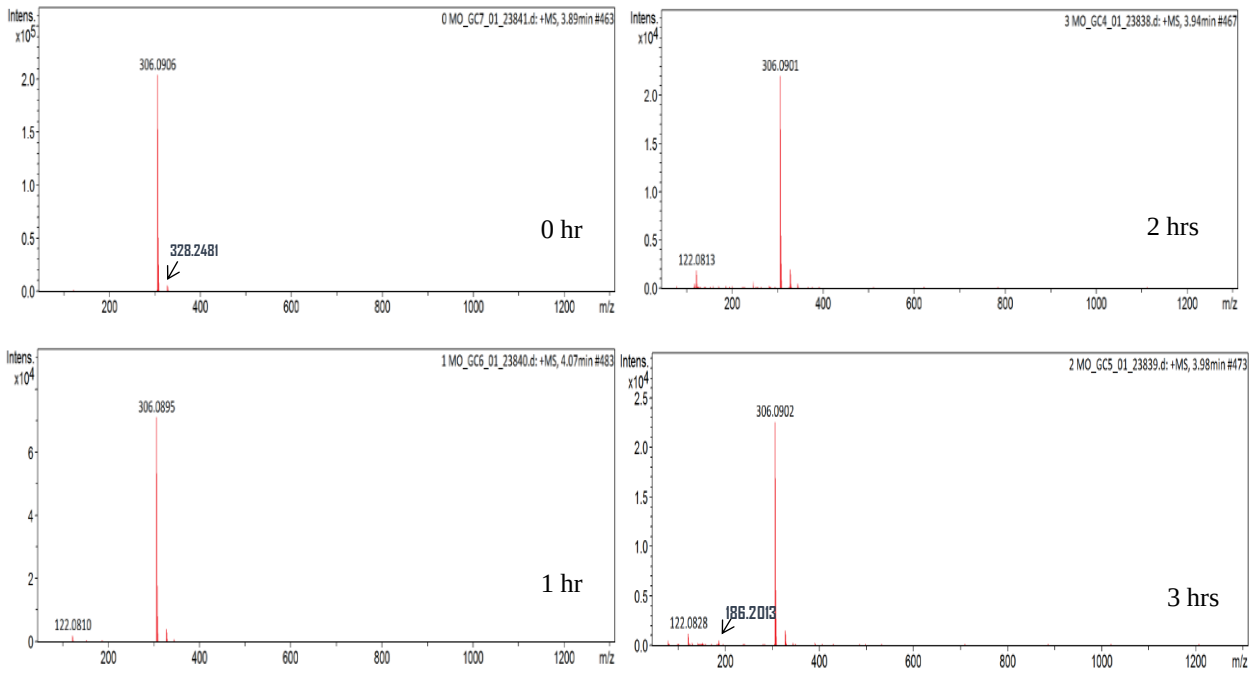

Fig. 2S: Mass spectra of degradation products of MO using Cu_3N as a photocatalyst.

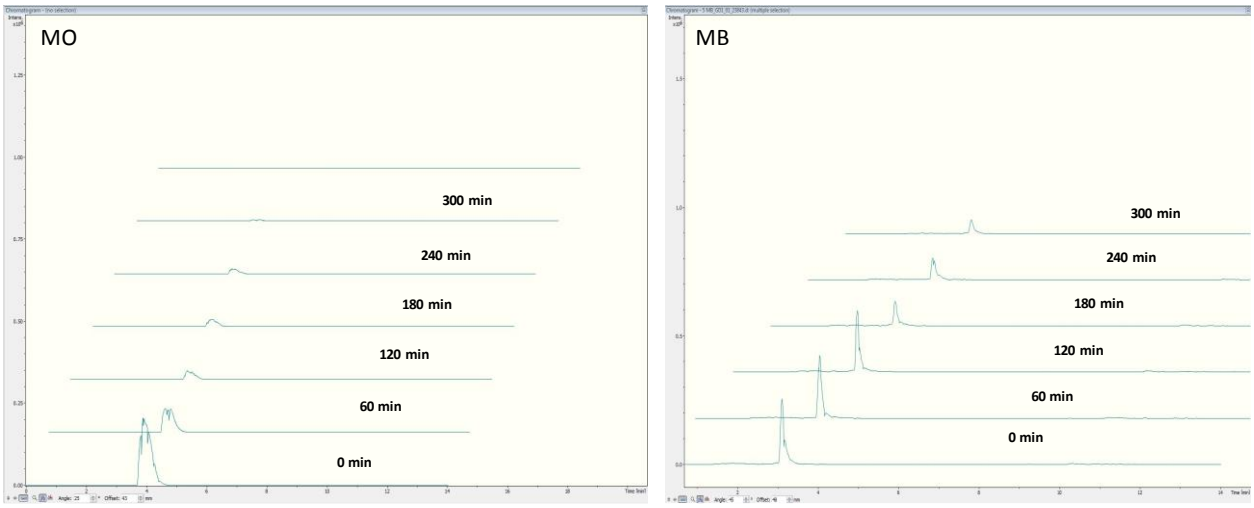

Fig. 3S: HPLC analysis of MO and MB after 5 hours of using Cu_9S_5 NPs as a photocatalyst.

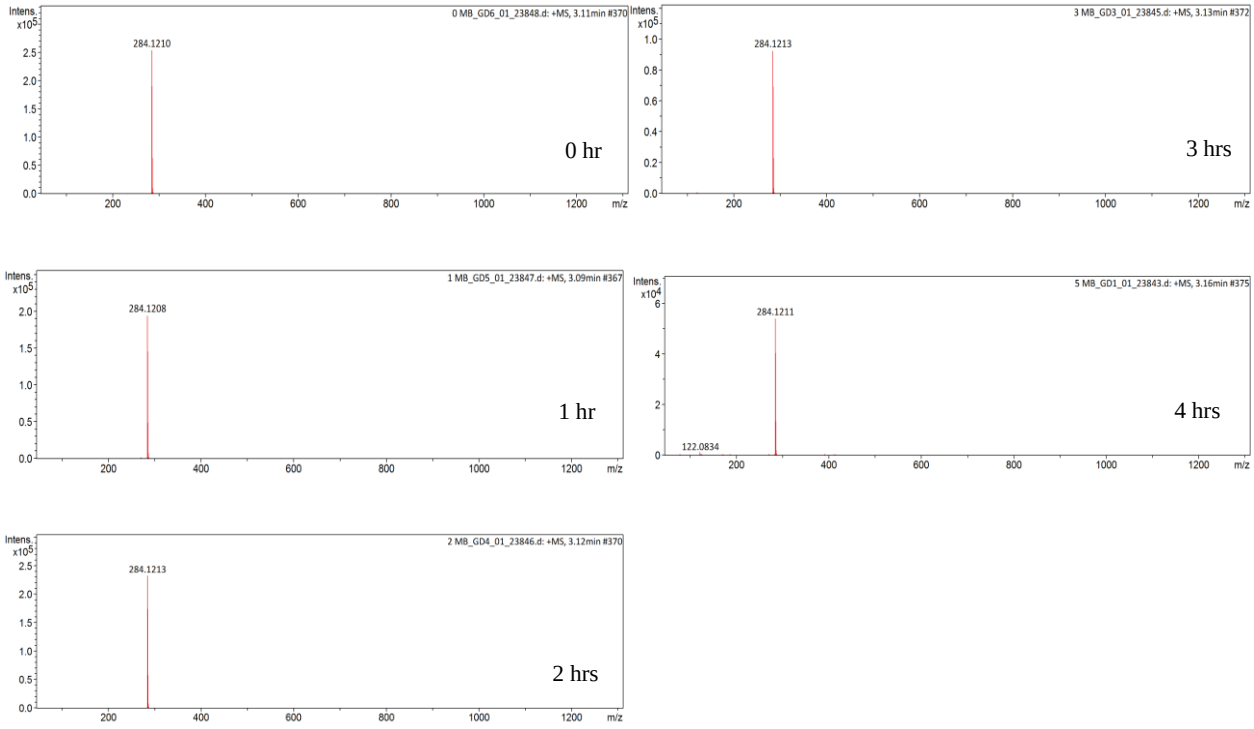

Fig. 4S: Mass spectra of degradation products of MB using Cu_5S_9 as a photocatalyst.